Development of front-end pre-analytical modules for integrated blood plasma separation

Md Ehtashamul Haque

Submitted for the degree of Doctor of Philosophy

Heriot-Watt University

School of Engineering and Physical Sciences

March 2022

ABSTRACT

Blood plasma separation is a fundamental step in numerous biomedical assays involving low abundance plasma-borne biomarkers. The interest in microscale blood plasma separation solutions has emerged with the development of microfluidic technologies in the early 2000s and has continued in recent years as few solutions have so far achieved both high yield and high purity without sample dilution, in volumes compatible with current clinical assays. Hydrodynamic or acoustic blood plasma separation microdevices have attracted considerable attention from the microfluidic community in the continuous separation of blood samples with a volume of a few mL due to their high throughput and insensitivity to clogging. However, obtaining a high yield from whole blood is challenging because the volume of red blood cells or hematocrit typically rises above physiological levels after each separation region, following plasma extraction. Some key parameters that influence the microfluidic blood plasma separation efficiency and yield of such devices have been investigated in this project. In particular, this project sought to establish experimentally, for the first time, the maximum hematocrit level and flow rate achievable in a microchannel, without hemolysis. Furthermore, the influence of flow fluctuation in syringe pumps, which are commonly employed in microfluidic setups, on the separation performance of blood plasma separation devices was investigated. These studies not only reveal the reasons behind the slow progress in the development of high-throughput microfluidic blood plasma separation devices capable of handling whole blood samples but also provides a framework for the design optimisation of future microfluidic blood plasma separation devices. While for low to mid-volume clinical sample volume (<4 mL), microscale solutions are viable, for high clinical sample volume (>4 mL) blood plasma separation traditional centrifugation approach remains the gold standard but is currently cost-prohibitive. In the third part of this thesis, a low-cost and open-source centrifugation setup for clinical blood sample volume has been developed. This centrifugation system capable of processing clinical blood tubes could be valuable to mobile laboratories or low-resource settings where centrifugation is required immediately after blood withdrawal for further testing.

DEDICATION

This book is dedicated to my father and mother,
MD KHIJERUL HAQUE & REBAKA SULTANA
with love.

You taught me to be an independent and determined person. Without you, I would never be able to achieve my objectives and succeed in life.

ACKNOWLEDGEMENTS

All praise to God Almighty, the Most merciful, the most compassionate, and the sustainer of the worlds who blessed me with the strength, ability and competence to complete my studies and, humblest and deepest gratitude to the greatest educator of mankind, the Holy Prophet MUHAMMAD (S.A.W).

Throughout this research, I've worked with a large number of people, each of whom deserves special recognition for their contribution to the thesis work. Without their help, it would not be possible to conduct the work presented here.

My deepest and most sincere gratitude goes to my supervisor, Prof. Maïwenn Kersaudy-Kerhoas, for giving me the opportunity to pursue a PhD at Heriot-Watt University under her supervision. Having her advice, support, and time was invaluable to the development of this thesis. Furthermore, I am pleased that I was given the freedom to pursue my study and, more importantly, I would like to thank her for the patience she showed towards me at all levels.

I would like to thank my other two supervisors, Dr Lynn Paterson (Heriot-Watt University) and Dr Miguel O. Bernabeu (University of Edinburgh) for providing useful feedback throughout my PhD to improve my research.

Furthermore, I would like to thank my colleagues and friends in IB3 at Heriot-Watt University. In particular, I would like to thank Dr Alvaro Conde, Dr Alfredo Ongaro, and Dr Antonio Liga for their engineering support, suggestions, and discussions. As well as that, I would like to express my gratitude to the rest of the team Linda Marriott, Dr Ieva Keraite, Dr Conni McCarthy, Dr Franceso Lopresti, Damaso Sanchez Carrera, Adelaide Lety-Stefanska, Mhairi Clark, Marilena Stamouli, Dr Rhiannon Grant, Ana Martinez Lopez and others at Royal Infirmary of Edinburgh, who made me feel like I belonged there.

My acknowledgement would be incomplete without thanking the biggest source of my strength, my family. The blessings of my parents and the love and care of my brother and sisters have all made a tremendous contribution in helping me reach this stage in my life. Finally, I'd want to express my gratitude to my beloved wife, Rimmi, for being the good-humoured, peacekeeping force at the front line of my emotional struggle with this work, as well as my son Rihan, without whom my PhD life would have been extremely hard. Your understanding and support have given me the inner peace without which I wouldn't be at this level today.

Research Thesis Submission

Name*:*	Md Ehtashamul Haque		
School:	Institute of Biological Chemistry, Biophysics and Bioengineering School of Engineering and Physical Sciences		
Version: *(i.e. First, Resubmission, Final)*	Final	Degree Sought:	Doctor of Philosophy

Declaration

In accordance with the appropriate regulations I hereby submit my thesis and I declare that:

The thesis embodies the results of my own work and has been composed by myself
Where appropriate, I have made acknowledgement of the work of others
The thesis is the correct version for submission and is the same version as any electronic versions submitted*.
My thesis for the award referred to, deposited in the Heriot-Watt University Library, should be made available for loan or photocopying and be available via the Institutional Repository, subject to such conditions as the Librarian may require
I understand that as a student of the University I am required to abide by the Regulations of the University and to conform to its discipline.
I confirm that the thesis has been verified against plagiarism via an approved plagiarism detection application e.g. Turnitin.

ONLY for submissions including published works

Where the thesis contains published outputs under Regulation 6 (9.1.2) or Regulation 43 (9) these are accompanied by a critical review which accurately describes my contribution to the research and, for multi-author outputs, a signed declaration indicating the contribution of each author (complete)
Inclusion of published outputs under Regulation 6 (9.1.2) or Regulation 43 (9) shall not constitute plagiarism.

Signature of Candidate*:*		Date:	03.03.22

Submission

Submitted By *(name in capitals):*	MD EHTASHAMUL HAQUE
Signature of Individual Submitting:	
Date Submitted:	03.03.22

For Completion in the Student Service Centre (SSC)

Limited Access	Requested	Yes		No		Approved	Yes		No	
E-thesis Submitted (mandatory for final theses)										
Received in the SSC by *(name in capitals):*						Date:				

Inclusion of Published Works

Declaration

This thesis contains one or more multi-author published works. In accordance with Regulation 6 (9.1.2) I hereby declare that the contributions of each author to these publications is as follows:

Citation details	Md Ehtashamul Haque, Amirali Matin, Xu Wang, and Maïwenn Kersaudy-Kerhoas, "Effects of syringe pump fluctuations on cell-free layer in hydrodynamic separation microfluidic devices", Physics of Fluids 33, 073317 (2021)
Author 1	Conceived and designed the study, performed all experiments except the video processing and video data acquisition, analysed the data and wrote the original draft of the manuscript except the optical setup part in materials and methods.
Author 2	Performed video processing and video data acquisition. Wrote the optical setup part in materials and methods.
Author 3	Read, edited and approved the final manuscript.
Author 4	Contributed to conceiving the project and analysing data. Read, edited and approved the final manuscript.
Signature:	
Date:	03.03.22

Citation details	Md Ehtashamul Haque, Linda Marriott, Noman Naeem, Taygan Henry, Alvaro J. Conde, Maïwenn Kersaudy-Kerhoas, "Design, 3D-printing, and characterisation of a low-cost, open-source centrifuge adaptor for separating large volume clinical blood samples", bioRxiv, 10.19.464959 (2021)
Author 1	Contributed to conceiving the project. Designed and carried out the experiments except for the cfDNA extraction and power load measurement, analysed the data and wrote the original draft of the manuscript.
Author 2	Carried out the cfDNA extraction and contributed to the protein load experiment.
Author 3	Contributed to finding pieces of literature about hemolysis detection.
Author 4	Contributed to simulation work.
Author 5	Contributed to conceiving the project and read, edited and approved the final manuscript.
Author 6	Contributed to conceiving the project, performed the power load measurement and analysed data. Read, edited and approved the final manuscript.
Signature:	
Date:	03.03.22

TABLE OF CONTENTS

Lists of figures

Lists of tables

Abbreviations

POCT- Point-of-care Testing

LOC- Lab-on--chip

μTAS- micro total analysis systems

RBC- Red Blood Cell

WBC- White Blood Cells

cfDNA- cell-free deoxyribonucleic acid

NIPT- Non-Invasive prenatal testing

ctDNA- Circulating tumour DNA

PCR- Polymerase chain reaction

BPS- Blood Plasma Separation

HCT- Hematocrit

CFL- Cell-free Layer

CFZ- Cell-free Zone

CFZW- Cell-free Zone width

BAW- Bulk Acoustic Waves

SAW- Surface Acoustic Waves

SSAW- Standing Surface Acoustic Waves

PMMA- Poly(methyl methacrylate)

PDMS- Polydimethylsiloxane

PBS- Phosphate-buffered saline

CCRM- coded compressive rotating mirror

UV- Ultraviolet

NIR- Near-infrared

DLS- Dynamic Light Scattering

CFD- Computational Fluid Dynamics

RPM- Revolutions Per Minute

RCF- Relative Centrifugal Force

FDM- Fused Deposition Modeling

PLA- Polylactic acid

HGB- Hemoglobin

List of publications by the candidate

Peer-reviewed journal publications

- Md Ehtashamul Haque, Amirali Matin, Xu Wang, and Maïwenn Kersaudy-Kerhoas, "Effects of syringe pump fluctuations on cell-free layer in hydrodynamic separation microfluidic devices", Physics of Fluids 33, 073317 (2021) https://doi.org/10.1063/5.0057415

- Md Ehtashamul Haque, Linda Marriott, Noman Naeem, Taygan Henry, Alvaro J. Conde, Maïwenn Kersaudy-Kerhoas, "Design, 3D-printing, and characterisation of a low-cost, open-source centrifuge adaptor for separating large volume clinical blood samples", bioRxiv, 10.19.464959 (2021) https://doi.org/10.1101/2021.10.19.464959 (Under review)

Peer-reviewed conference publications

- Md Ehtashamul Haque, Krystian Wlodarczyk, Duncan P. Hand, Miguel O. Bernabeu, and Maïwenn Kersaudy-Kerhoas, "The effect of elevated hematocrit on human blood flow in a microchannel", μTAS 2020 24th International Conference on Miniaturized Systems for Chemistry and Life Sciences, 2020, Virtual preceding.

- Md Ehtashamul Haque, Amirali Matin, Krystian L. Wlodarczyk, Duncan P. Hand, Miguel O. Bernabeu, Xu Wang and Maïwenn Kersaudy-Kerhoas, "The underlying issues affecting the efficiency and yield of microfluidic blood plasma separation", Emerging Investigators in Microfluidics (EIMC), 2021, Virtual preceding.

- Md Ehtashamul Haque, Henry Tygan, and Maïwenn Kersaudy-Kerhoas, "Design, Fused Filament Fabrication, and characterization of a low-cost micro-centrifuge adaptor for separating large volume clinical blood samples in low resource settings", International Conference on Additive Manufacturing, 2021, Anaheim, USA.

Chapter 1: Introduction

1.1 Point of care testing

The medical industry has been reaping the benefits of Point-of-care Testing (POCT), a simple delivery option for performing medical testing closer to the patients since its inception in the 1990s. POCT devices usually do not require permanent dedicated space and therefore enable testing to be done outside the physical facilities of a traditional clinical laboratory. To date, many POCT devices have established their place in the market and are capable of performing numerous tests such as (but not limited to) pregnancy tests, infectious disease tests, sexually transmitted disease tests, cardiac tests, drug abuse tests, alcohol tests, blood glucose test [1], [2]. During the recent outbreak of coronavirus disease in 2019, the necessity of POCT was emphasized as the medical industry throughout the world began to collapse owing to a lack of adequate testing facilities. Hundreds of POCT Covid-19 detection devices, such as Abbott ID NOW, have been commercialized, played an important role in meeting the demand for millions of tests per day. Another significant advantage of POCT devices is their rapid performance which helps clinical personnel or physician, without minimal laboratory science knowledge, to quickly diagnose patients, and potentially treat more patients within a reduced time frame. Moreover, the immediate availability of test results helps the clinicians to test their patients on a regular basis which has proven advantageous for the detection of diseases at an early stage [3], or in repeated sampling and testing. However, precise test results are required for POCT devices since tests with inaccurate test performance may result in inappropriate treatment, increasing healthcare expenses and putting the patient in danger [4].

Microfluidic lab-on-a-chip (LOC) technologies, also sometimes called micro total analysis systems (μTAS), can meet the requirement of the POCT because of their capability of miniaturising and integrating analytical modules used in central libraries into a small chip that ranges in size from millimetres to a couple of square centimetres. These LOC devices have several advantages such as the minimum requirement in terms of reagent volume which eventually reduces the cost of mass production, shorter reaction and analysis time, portability and automation [5]. Numerous POCT based LOC devices and tests that are available in the market have one commonality: they all rely on the correct identification of biomarkers.

1.2 Biomarkers in disease diagnosis

A biomarker is a measurable indicator of a particular disease. Hulka *et al*. defined biomarkers as "cellular, biochemical or molecular alterations that are measurable in biological media such as human tissues, cells, or fluids" [6]. Molecular biomarkers, such as proteins or nucleic acids, are among the several types of biomarkers that can aid in the diagnosis of a variety of diseases and are well suited for POCT-based LOC devices. They are extracted from biological fluids such as plasma, serum, cerebrospinal fluid, or urine. Molecular biomarkers have a wide spectrum of uses, and they are further classified based on their use, such as monitoring biomarkers that provide information on the status of a disease or medical condition, diagnostic biomarkers that detect or confirm a specific disease, response biomarkers that demonstrate a patient's biological response after using a medical product, and so on [7]. Because of the large range of applications and the demand for POCT, numerous research studies have been undertaken to maximise the performance of extraction and processing of biomarkers from biofluids.

Among all the biological fluids in the human body, blood is the most abundant and can provide a universal reflection of a person's health condition or phenotype [8]. It has three cellular components: erythrocytes (Red Blood Cells or RBCs, ~45%), leukocytes (White Blood Cells or WBCs, ~0.7%), thrombocytes (Platelets, ~1%) and a liquid portion called plasma (~55%). Plasma contains around 4000 different components, including lipids, sugars, cell-free deoxyribonucleic acid (cfDNA) fragments, vitamins, minerals, enzymes, hormones, antibodies, and other proteins, in addition to cellular components. Because blood's cellular components cause discrepancies in biological analysis, separating plasma from whole blood has become a prerequisite in diagnostic tests [9]. Several biomarkers have been identified in the blood that has been employed in a variety of applications spanning from diagnosis to prognosis. Table 1.1 summarises some of the applications of blood-based molecular biomarkers. Among these various biomarkers accessible in the blood, cfDNA has been analysed in different applications such as diagnosis, prognosis, monitoring of different diseases or health conditions like Non-Invasive Prenatal Testing (NIPT), immune diseases, organ transplantation and cancer.

Table 1.1: Different applications of molecular biomarkers available in the blood

Application	Task	Example with required blood volume	Uses	Reference
Diagnostic Biomarker	Detection of a disease	Estimated Glomerular filtration rate (eGFR), 4 mL volume	Measuring the working condition of kidneys	[10]–[12]
		Blood sugar or hemoglobin A1c, Finger-prick volume	Type 2 diabetes mellitus (DM) detection	[13]–[15]
		cell-free DNA (cfDNA), Finger-prick to 10 mL volume	The non-invasive approach in cancer diagnosis, detection of immune diseases, determination of fetal sex in non-invasive prenatal testing (NIPT)	[16]–[25]
Monitoring Biomarker	Inform the status of a disease or medical condition	Monoclonal protein, ~1 mL volume	Showing signs of progressing to other disorders after being diagnosed with monoclonal gammopathy	[26]–[29]
		Prostate-specific antigen, 1 mL volume	Monitoring a patient condition during prostate cancer	[30]–[32]
		Cancer antigen 125, <3 mL volume	Monitoring a patient condition during ovarian cancer	[33]–[35]
		cell-free DNA (cfDNA), 1-8 mL volume	Rapid, non-invasive monitoring for cancer	[36]–[43]

			progression, monitoring organ transplantation	
Prognostic Biomarker	provides information on the likely patient health outcome	prostate-specific antigen (PSA), 1 mL volume	Evaluation of patients with prostate cancer in determining the likelihood of cancer progression	[32], [44]–[46]
		Plasma fibrinogen, 2-5 mL volume	Access the patient condition during different stages of cancer	[47]–[50]
		cell-free DNA (cfDNA), 3 mL volume	Predicts overall survival in cancer patients	[51]–[53]
Predictive Biomarker	Provides information about the effect of a therapeutic intervention	Human leukocyte antigen allele (HLA), ~10 mL volume	Predicts the risk of skin reaction during abacavir treatment of HIV patients	[54]–[57]
		cell-free DNA (cfDNA), 2-8 mL volume	Predicts the treatment response of cancer patients	[58]–[61]
Risk Biomarker	Informs the potential for developing a disease	C-reactive protein (CRP) level, Finger-prick volume	Identification of patients with a greater risk of coronary disease	[62]–[65]
		Apolipoprotein E (APOE) gene, 1-10 mL volume	Identification of patients with a higher risk of Alzheimer's disease	[66]–[70]

1.3 Cell-free DNA (cfDNA)- a potential biomarker

cfDNA has emerged as a potential biomarker in the diagnosis, prognosis, or monitoring of a variety of diseases, including fetal chromosomal abnormalities, malignancies, infectious diseases, trauma, myocardial infarction, stroke, and organ transplants [71], [72]. These are the released small (50-200 bp) fragments of DNA from cells into the circulating body fluids throughout the body and were first discovered by Mandel and Métais in 1948 in blood plasma [73]. Usually, these fragments are originated from the hematopoietic system in healthy individuals [74] however during physiological or

pathological conditions such as pregnancy, organ transplantation and cancer they can be released from the affected cells or tissues [20], [39], [51]. These released sub-classes of cfDNA such as circulating tumour DNA or ctDNA from cancer cells, donor-derived cfDNA or dd-cfDNA after organ transplantation, circulating cell-free mitochondrial DNA or ccf mtDNA released during stress or other damaging or pathological events and Cell-free fetal DNA or cffDNA that circulates freely in the maternal blood are the main point of interest during disease diagnosis as they carry significant information about the disease condition and can be used in various non-invasive procedures. Two of such widely used non-invasive techniques for cfDNA testing from blood samples are NIPT and liquid biopsy where the former applies in the prenatal diagnosis while the latter is used in cancer diagnosis which saves the patients from the pre-and post-therapeutic discomfort and a great deal of time. However, the extraction of cfDNA from the blood sample is very challenging because of its low concentration in the plasma (average 30 ng/mL, range 1.8–44 ng/mL) [75], [76]. Elevated concentration of cfDNA has been reported to be present during disease conditions [77]–[79] as for cancer patients the concentration goes up to 180 ng/mL which is nevertheless difficult to detect [40], [80], [81]. These released sub-classes of cfDNA from disease cells or tissues are distinct from an individual's normal cfDNA and can therefore be analysed to identify mutations using a variety of methods, such as PCR-based sequence-specific detection or DNA sequencing [82]. However, they are extremely rare which make the detection procedure more complex [83]. For example, ctDNA is of particular importance in cancer detection because it contains genetic information about the disease despite accounting for only 0.01% of total cfDNA. According to Emergen Research, the market for cfDNA testing will be valued at 22.41 billion USD by 2027, up from 3.80 billion USD in 2019 [84]. Researchers have been investigating novel methods to extract cfDNA utilising simple and less expensive techniques in the last 10-15 years. Microfluidic techniques have become popular because they allow non-conventional approaches to be carried out without the use of complicated and expensive instruments.

1.4 Microfluidics for the extraction of plasma borne molecular biomarkers

Microfluidic POCT technology proved great potential in detection and monitoring various diseases by analysing a wide range of plasma borne molecular biomarkers. Conventionally these analyses are performed on plasma by tests like polymerase chain reaction (PCR), enzyme-linked immunosorbent assay (ELISA), western blotting, flow cytometry and a wide range of other complex techniques, which takes a long time to

complete and requires expensive and bulky instruments. Microfluidics technology, as a solution, provides simple operation with less reagent, high throughput, cheap cost, and rapid diagnosis. As a result, over the last two decades, there has been a significant amount of research into the potential of microfluidic technology in detecting molecular biomarkers, resulting in the development of a wide range of successful microfluidic detection systems. While many of the studies focused on different proteins detection from blood samples such as prostate-specific antigen (PSA) detection [85]–[87], C-reactive protein (CRP) detection [85], [88], cancer antigen 125 (CA125) detection [89], others looked into genomic biomarker detection (DNA, RNA) [40], [90]–[95], lipids (cholesterol, acylglycerols, fatty acids) detection [96]–[99] and carbohydrates (glucose) detection [100], [101].

Blood Plasma Separation (BPS) is the pre-analytical step that separates the plasma from cellular components for the detection of various low abundant biomarkers available in plasma. Traditionally, this separation is accomplished using centrifugation, which necessitates the use of expensive and large apparatus, making it unsuitable for low-resource environments. In this case, microfluidics offers a rapid and inexpensive solution that also considerably reduces the sample preparation stages associated with centrifugation. Despite these developments in microfluidic BPS solutions, centrifugation remains the gold standard for separating higher amounts of blood than the finger-prick volume. This is due to the fact that contemporary microfluidic BPS devices that ensure near 100% separation performance have a substantially lower yield (1-15%) and flow rate (6-10 mL/h) [102], [103]. For example, if a downstream study requires 1 mL plasma from a blood sample with a 50% hematocrit (volume fraction of RBCs), a microfluidic device with a 15% yield and 10 mL/h flow rate will need to process at least 13mL of blood for more than 1 hour. The centrifugation procedure, on the other hand, can produce the same volume of plasma in 10 minutes with only <3 mL of the same blood sample. Another major limitation of currently available microfluidic BPS devices is the need for blood dilution to maintain high separation efficiency, which results in further dilution of existing rare biomarkers, such as cfDNA [104]. Devices that do not require blood dilution, on the other hand, have produced poor plasma yield and separation [105]. The maximum achievable plasma yield and flow rate of current BPS devices must be significantly increased in order to develop a new fully automated, high throughput microfluidic platform that integrates the BPS module with further downstream analysis modules on a single chip, which is the project's ultimate future goal.

1.5 Aim and scope of this thesis

The goal of this thesis was to investigate the current microfluidic BPS devices' limitations in handling whole blood samples and delivering high separation efficiency and yield. Many of the current blood-based biomarkers, such as blood sugar, cfDNA, M-protein, PSA, and eGFR, require low to mid-volume (<4 mL) blood samples to produce statistically significant results, as shown in Table 1.1. Despite the success of the microfluidic approach in processing finger-prick volume (<0.5 mL) whole blood, no high throughput (>20 mL/h) microfluidic blood plasma separation device has delivered enough yield and efficiency suitable for integration within a biomarker detection assay that requires more than 1 mL plasma (mid-volume BPS: 1 mL to 4 mL blood) in the last one and a half decades. The overarching goal of this thesis was to investigate the reasons behind this stunted development to explore the feasibility of a microfluidic approach through two independent studies in the first and second years. These studies will aid in the development of a microfluidic BPS device with high throughput, efficiency, and yield. Separation efficiency is critical for downstream analysis purity, so 100% efficiency in the future device is desirable, while yield and throughput can be targeted at 70% and 20 mL/h, respectively, because exceeding this limit could cause enough shear stress inside the channel to lyse the RBCs.

While a developed high throughput microfluidics BPS device with a high yield could be able to serve a large portion of downstream biomarker assays in the future, during the first two investigations, I came to the conclusion that centrifugation will continue to be the gold standard for assays requiring high volumes of un-diluted plasma (>2 mL) in applications such as Apolipoprotein E and HLA detection, early cancer detection, NIPT, and liquid biopsy. This is because the required high volume plasma separation will take a long time even with high throughput (20 mL/h) microfluidic BPS device, making the entire process tedious and unfeasible. Therefore, a parallel study with the microfluidic approach was undertaken to serve the high-volume BPS following the centrifugation approach. There is currently no low-cost centrifugation equipment available for large volumes of clinical samples. Large-volume centrifuges are bulky and expensive, making them unsuitable for a resource-constrained setting. Despite the availability of a wide range of cost-effective microcentrifuges on the market, these instruments can only handle 0.2-1.5 mL volume and hence cannot solve the challenge of separating large volumes of whole blood. Thus, in this final part of this thesis, a microcentrifuge rotor was customised as a cost-effective, and portable alternative to the widely used refrigerated centrifuge. As

well as solving the issue of large volume clinical samples centrifugation, the adapted centrifuge could be implemented in resource-limited labs at a cost of 140 USD.

Chapter 2: State of the art

Since the previous four decades, particle separation at the micron and sub-micron scale has become an integral aspect of chemical and biological analysis, diagnostics, and chemical processing [106]. As a result, advanced particle separation research has attracted a lot of attention. Many different separation techniques have been developed and investigated in a variety of research fields, including the detection of viral particles [107], separation of cancer cells from normal cells [108], virus cells from healthy cells [109], malaria-infected cells from healthy cells [110] and plasma from blood [103], [111]–[113], with the main goal of shifting particles from their original input trajectory in a microfluidic channel and collecting them at predefined outlets [114]. Among these diverse study domains, blood plasma separation (BPS) is very important in the analysis of blood since it is the first step in most diagnostic studies in this regard, where plasma, the liquid portion of the blood that contains wide ranges of biomarkers (e.g., proteins and cell-free nucleic acid), is separated from the blood cells. As mentioned earlier, traditionally this step is accomplished using the centrifugation technique, which has several drawbacks. In order to overcome the issues, microfluidic approaches for BPS came into play.

2.1 Microfluidic Blood Plasma Separation (BPS) techniques

Microfluidic-based BPS can be achieved with active or passive separation techniques. In the active separation techniques, an external field (e.g., electric, magnetic or acoustic) is used for particle sorting, whereas passive separation techniques rely solely on particle interaction, the microfluidic channel, and the flow field. Figure 2.1 shows a list of microparticle separation strategies that have been reported in the literature. Because we are interested in BPS at low to high volumes (usually 0.5-10 mL excluding finger-prick volume) in this study, the literature review will concentrate on approaches that have been used in BPS and are applicable to volumes of more than 0.5 mL of blood.

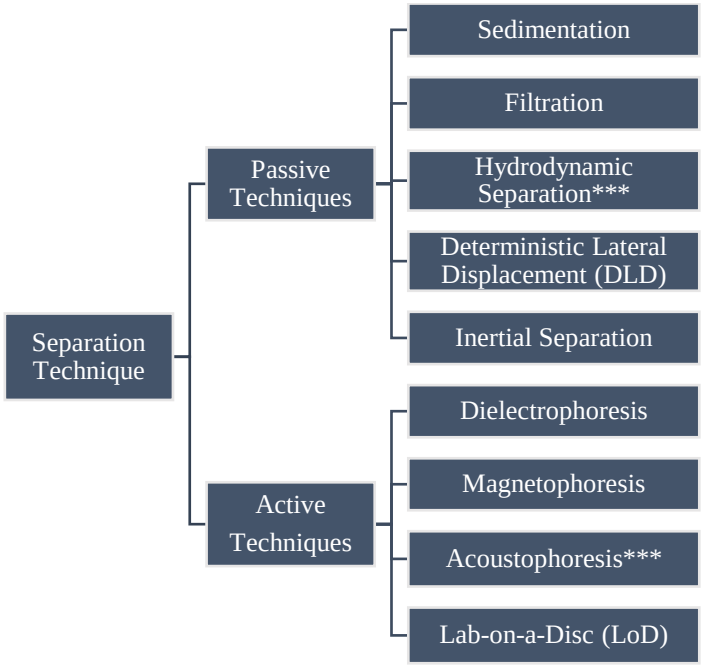

Figure 2.1: Classification of existing microfluidic separation techniques. The star rating systems were found to be effective in processing large volumes of blood samples in a continuous manner and will be discussed extensively.

2.1.1 Passive techniques

- ***Filtration***

The filtration technique is commonly used for size-based separation of particles and has evolved into an acceptable separation technique for BPS at low volumes [115]–[119]. Microfabricated filters are employed in this technique so that only plasma can flow through the membrane and the cells are segregated from it. However, the method is very prone to clogging due to the tiny pore size of the membrane and, therefore, only suitable for very small volumes, such as finger-prick volumes. Plasma yields in this approach typically vary from 200 nL and 300 µL [116], [118], [120], [121]. Hemolysis, or the destruction of red blood cells (RBC), is another disadvantage of the technique caused by elevated stress at the membrane. Several investigations have reported this, leading researchers to prefer to deal with diluted samples [116], [122]–[124]. One conceivable application for this technique in high-volume BPS devices is at the downstream part of the device, where it can be employed on plasma with low hematocrit (HCT) to improve separation efficiency.

- ***Sedimentation***

Sedimentation is a slow process by definition. Without any external force, and depending on the HCT, it can take a long time for cells to aggregate at the bottom of their container

and for plasma separation to occur. In a study conducted by Maria *et al.*, it required almost 30 minutes of sedimentation time (on the bench) to collect 1.6 µl of plasma from an 8 µl whole blood sample in a cylindrical well [125]. Many researchers have embraced this technology to process finger-prick volume samples because no external pumps are required for blood infusion into the device [125]–[127]. When dealing with large samples, however, this technology has been integrated with other separation techniques, resulting in successful hybrid BPS devices [117], [128].

- ***Hydrodynamic Separation***

Hydrodynamic separation is a term that refers to all techniques that rely on inertial or viscous effects, as well as intelligent manipulation of microchannel geometry, to extract a substantial volume of plasma from diluted or undiluted blood samples [112], [113], [129], [130]. Only BPS studies based on this passive technique will be reviewed in depth because it is apparent that this technique can handle large volumes of blood samples continuously and is not prone to clogging.

In passive hydrodynamic separation techniques, microchannels can be designed to take advantage of biophysical effects such as the cell-free layer effect [131], [132], and bifurcation effects [120], [133] as illustrated in Figure 2.2. According to the Fahraeus-Lindqvist law, when a mixture of fluid and particles, such as blood flows through a tube with a diameter of smaller than 300 µm, the viscosity starts to decrease with a decreasing tube diameter [133], [134]. At these small diameters, cell migration to the centre of the tube can be observed [135], [136]. The cell migration can be explained as an effect of two different forces: shear gradient lift force and wall induced lift force. While the shear gradient lift force tries to move the cells towards the walls of the channel, the wall induced lift force acts oppositely and move the cells away from the wall. The net lift force from these two determines the equilibrium position of the cells somewhere in the middle of the channel and therefore a cell-free layer (CFL) forms at the tube wall [137]. The hydrodynamic technique also sometimes utilises constriction-expansion regions, comparable to stenosis, to create additional lift forces and displace cells to desired streamlines, enabling separation at bifurcations or diverging outlets. The effect occurring at a bifurcation is sometimes described as Zweifach-Fung bifurcation law [113], [120], [121]. Utilising these effects ensures the generation of cell-free zones (CFZ) at the bifurcations, from where the liquid portion is extracted through daughter channels.

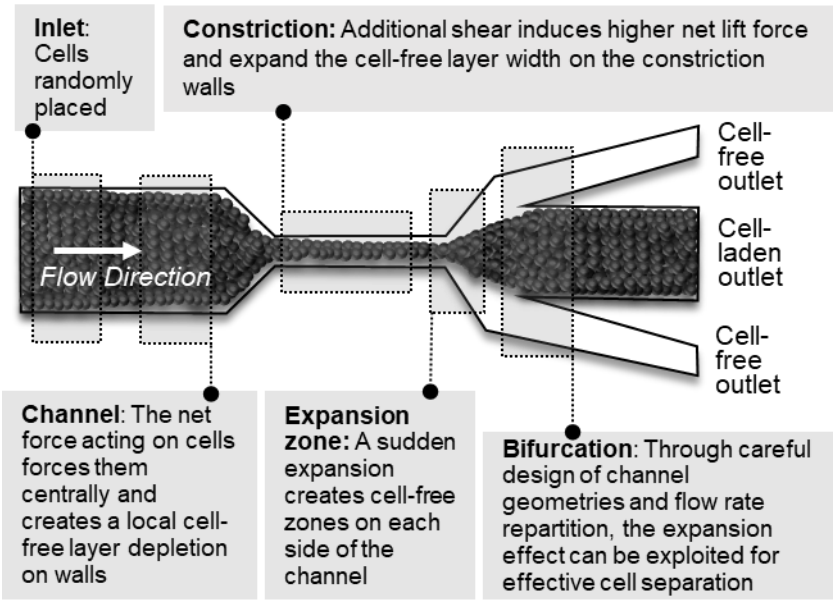

Figure 2.2: Graphical illustration of cells, fluid and structure interactions in microfluidic hydrodynamic separation devices. Reproduced from [138]**.**

The inlet flow rate, among many other flow parameters, is fundamental for hydrodynamic separation. When employing a low inlet flow rate, many researchers have been able to get a considerably greater yield. Yang *et al*. developed a microfluidic device (Figure 2.3.A) for continuous, real-time BPS and obtained plasma yields ranging from 15% to 25%. They characterized this device using the sheep blood sample having 10% to 35% HCT and found that when a 1:6 flow rate ratio was maintained between the plasma and blood collecting channels, the separation efficiency was 100% after around 30 minutes of continuous blood infusion [139]. Human blood has a lower viscosity than sheep blood at higher shear rates due to the higher flexibility of RBCs in human blood [140]. Therefore, the device could be capable of flowing blood with much higher HCT. The flow rate of 0.01 mL/h utilised in their experiment, on the other hand, is extremely low and unsuitable for practical applications. Similarly, Faivre *et al*. also incorporated a low flow rate of 0.2 mL/h in their investigation where for the first time they introduced a constriction region in their device before the bifurcation region and achieved a diluted plasma yield of about 24% [131]. Although these two devices produced substantial plasma yields, a device capable of extracting plasma from several mL should be able to operate at a much higher flow rate while maintaining high separation efficiency.

Development of devices having higher flow rates also have been reported but failed to yield any promising results. Jaggi *et al*., for example, employed a three-dimensional microchannel network to operate with high flow rates of 120 and 300 mL/h [141]. When working with 45% feed HCT, however, the separation efficiency was as low as 30%

(Figure 2.3.B) and the yield of the device has not been reported. Tripathi *et al*. developed a microdevice that could flow undiluted blood samples at a rate of 30 mL/h in another investigation [112], although the yield was low (1%-6%) (Figure 2.5.B).

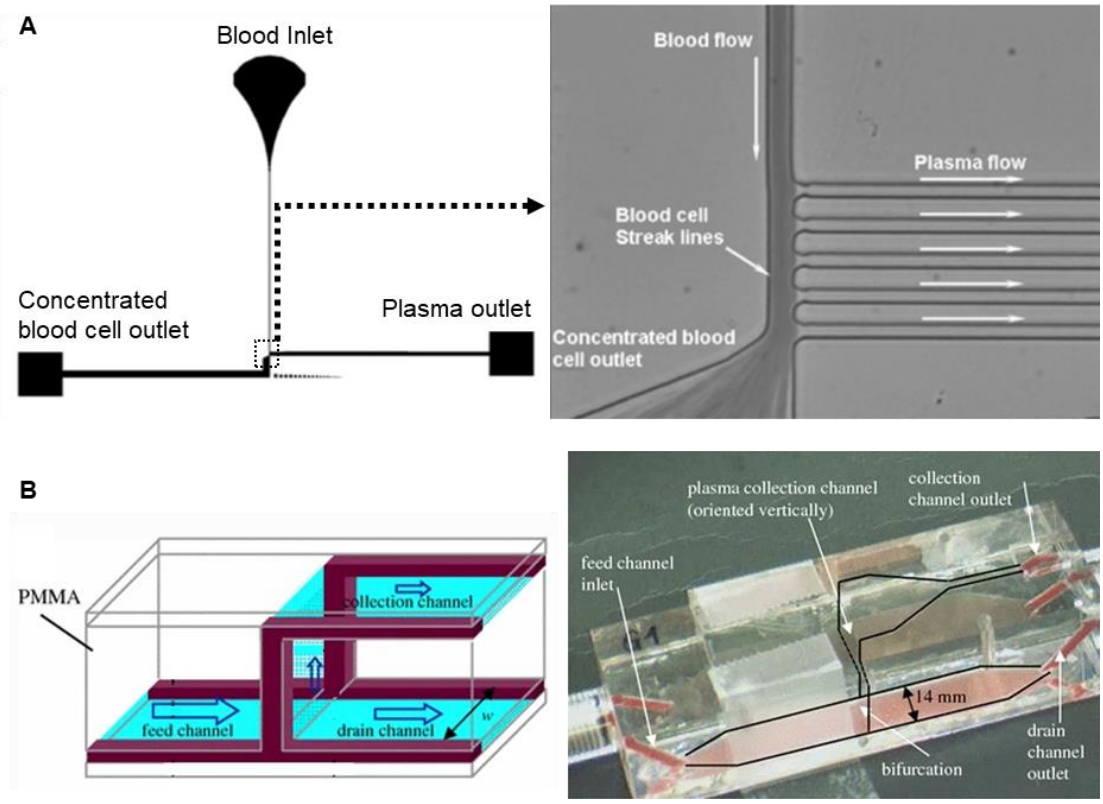

Figure 2.3: Hydrodynamic BPS devices developed by Yang et al. and Jaggi et al. (A) (Left) An overview of the separation device developed by Yang et al. which is designed to have a whole blood inlet, a purified plasma outlet, and a concentrated blood cell outlet. Each channel is 5 mm in length. (Right) Snapshot of the zoomed part showing plasma flow through the side channel [139]***; (B) (Left) schematic of a three-dimensional, high aspect ratio microdevice developed by Jaggi et al. (Right) A snapshot of the separation device with high-aspect-ratio channels. Channel boundaries are outlined with black lines*** [141]

Aside from the inlet flow rate, there are several other variables that can be tweaked to improve BPS efficiency, including the constriction-expansion region, microchannel geometry, feed HCT, and the number of constrictions. Tripathi *et al*. compared their designed microdevice's performance as a function of dependent governing parameters such as flow rate, feed HCT, and microchannel geometry [130]. Two distinct expansion ratios (width of the constriction to the width of the blood outlet channel), 1:4 and 1:8, were tested in various designs, and the device with the higher expansion ratio had a lower efficiency. They concluded, however, that even with a model with a high expansion ratio, efficiency may be improved by using a much higher flow rate. But the high shear stress

generated inside the channel due to such high flow rates might increase the likelihood of cell damage. The maximum separation efficiency achieved in their study was over 90% for the blood with 7% HCT with a plasma yield of 4.5%. High HCT blood, on the other hand, reduced efficiency. In another design, the authors added cascading microchannels to the plasma extraction channel to further separate the cells from the collected plasma and improve separation efficiency. However, the boost in efficiency came at the expense of plasma yield (1.2%).

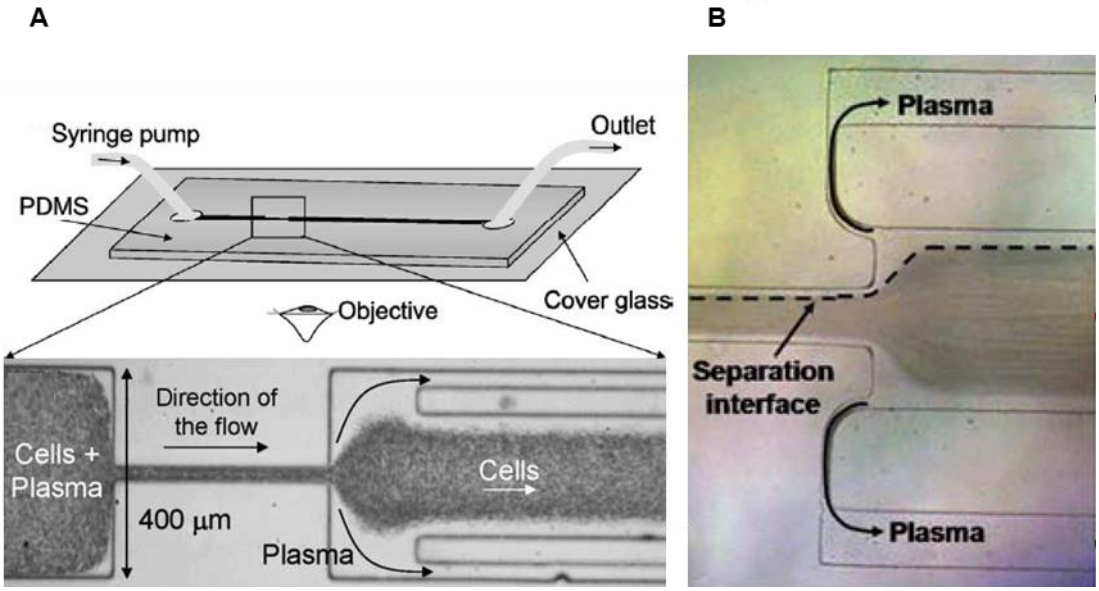

Figure 2.4: Hydrodynamic BPS devices developed by Faivre et al. and Sollier et al. (A) Geometrical focusing of cells in the constriction-expansion microdevice from [131]***; (B) Single constriction developed by*** [132] ***where plasma is taken out from the cell-free zone at the bifurcation.***

Many studies have used a constriction region before the bifurcation to improve cell-free zone width (CFZW) by focusing the cells on the middle of the channel, or at one side of the bifurcation channel. As previously mentioned, Faivre *et al*. reported the first comprehensive study using single constriction-expansion, in which they found that the enhancement of the CFZ is dependent on several factors, including the length of the constriction region, the viscosity of the suspending fluid, the concentration of the cells, the deformability of the cells, and the width of the constriction [131]. Plasma yield during their experiment was comparably higher, almost 24%. However, they worked with diluted blood of 16% HCT and most importantly, as discussed in an earlier section, with a very low flow rate of 0.2 mL/h. The BPS device used in their study is shown in Figure 2.4.A. Sollier *et al*. tested several passive geometries to characterise the influence of geometric singularities and constriction in the BPS device, and with their final design which has a single constriction region (Figure 2.4.B), they were able to achieve a greater plasma yield

of 17.8% with 1:20 diluted blood [132]. The samples they collected throughout their experiment were scientifically validated, and there was no evidence of protein loss or hemolysis. The authors also stated in their concluding remarks that cascading of such bifurcation could result in a substantially greater yield. Similarly, Rodrguez-Villarreal *et al*. designed another single bifurcation device that can handle whole blood and along with the constriction effect, they evaluated the effect of temperature (as high as 50°C) on the CFZW, concluding that temperature can play a substantial role in this type of arrangement [142]. The separation efficiency in their experiment reached up to 97% at 37°C with a high flow rate of 12 mL/h, with no sign of hemolysis. Reduced blood viscosity at high temperatures may have aided in achieving improved efficiency in this study. The device schematic is shown in Figure 2.5.A. Although the blood can be damaged at temperatures exceeding 50°C [143], no cell damage was observed in this investigation. This could be due to the cells' brief exposure period to high temperatures as a result of high flow rates.

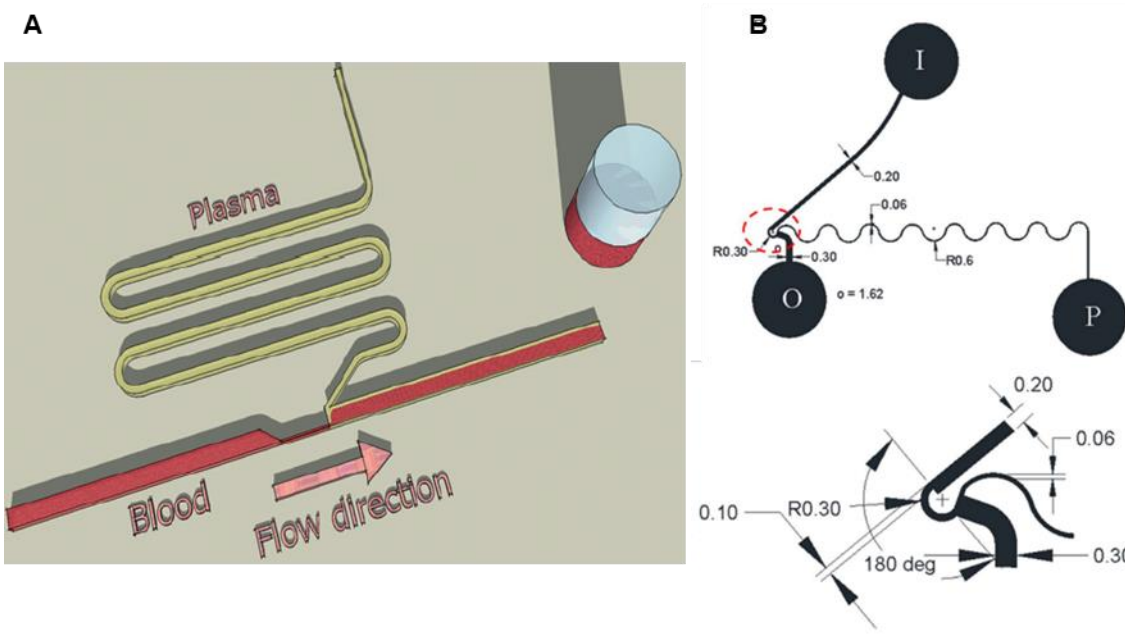

Figure 2.5: Hydrodynamic BPS devices developed by Rodrguez-Villarreal et al. and Tripathi et al. (A) Schematic showing the direction of the flow and separation of the plasma after the constriction [142] ***(B) Device with a bent constriction tested with blood having 62% HCT*** [112]

In another work, Tripathi *et al*. [112] demonstrated separation of blood with up to 62% HCT, which is much higher than HCT recorded in prior investigations [105], [144], [145]. Their design included a constriction before the single bifurcation, as well as a bend before the constriction to bring the centrifugal effect into account. The schematic of this device is shown in Figure 2.5.B. They achieved nearly 100% separation efficiency with a yield ranging from 1 to 6%, depending on the HCT and the plasma channel resistance utilised, using raw blood with 42% HCT at a 30 mL/h flow rate. Furthermore, the separation

efficiency was 95.3% for blood with 50% HCT, and for 62% HCT, with no visible CFZW, the separation efficiency came down to nearly 84%. Shatova *et al*., on the other hand, designed a constriction−expansion BPS device that they claimed achieved 99.96% purity. Instead of sudden increase as in prior designs, this design used a progressive expansion after the constriction. The device (Figure 2.6.A) was tested with a range of whole blood samples (40-50% HCT), and the yield was 9% [144]. However, when using this undiluted blood, the device's plasma throughput of 0.3 mL/h makes it less appealing in assays that require large volumes of plasma in a short time period. Namgung *et al*. also designed a biomimetic microfluidic BPS device with arteriolar Y shaped bifurcation and tested with 40% HCT blood. They were able to attain 99.9% separation efficiency with a greater bifurcation angle (Θ=60°). It will be difficult to design cascading bifurcation in such setting which will result in poor plasma yield.

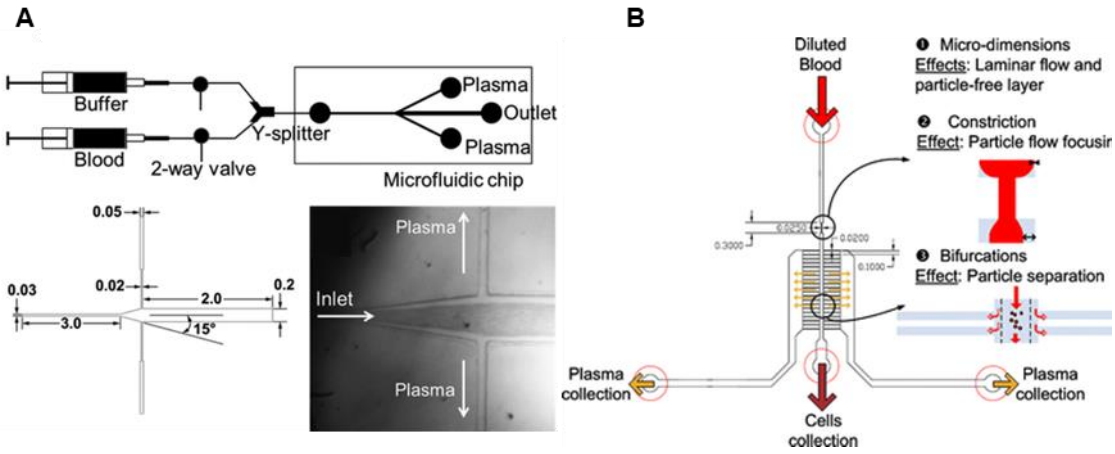

Figure 2.6: Hydrodynamic BPS devices developed by Shatova et al. and Kersaudy-Kerhoas et al. (A) (Top) Schematic of the experimental setup; (Bottom left) Schematic of the BPS device design, device dimensions in mm; (Bottom right) Microscope image of the device with gradual expansion for separation of plasma from undiluted blood [144]***; (B) Hydrodynamic BPS device having several bifurcations after a single constriction region [105]***

Kersaudy-Kerhoas developed a BPS device (Figure 2.6.B) with a series of bifurcations and a single constriction region, which was only tested with diluted blood samples [105], but the results were not satisfactory. Following that, several constrictions rather than a single one helped to boost plasma yield (Figure 2.7.A). This new design increased the purity to 100% while increasing the yield to 8% [113]. Finally, in his PhD research, Mielczarek improved the previous device [113], increasing the yield from 8% to nearly 14% when dealing with non-diluted blood with HCT ranging from 38% to 42% [102]. When the inlet flow rate was 5-9 mL/h, his device's separation efficiency was about 95% with whole blood (Figure 2.7.B), while a 1:1 blood dilution resulted in 100% efficiency

(HCT 23%). A downstream sedimentation module has been further incorporated with the hydrodynamic BPS part to remove the cells remaining in the plasma.

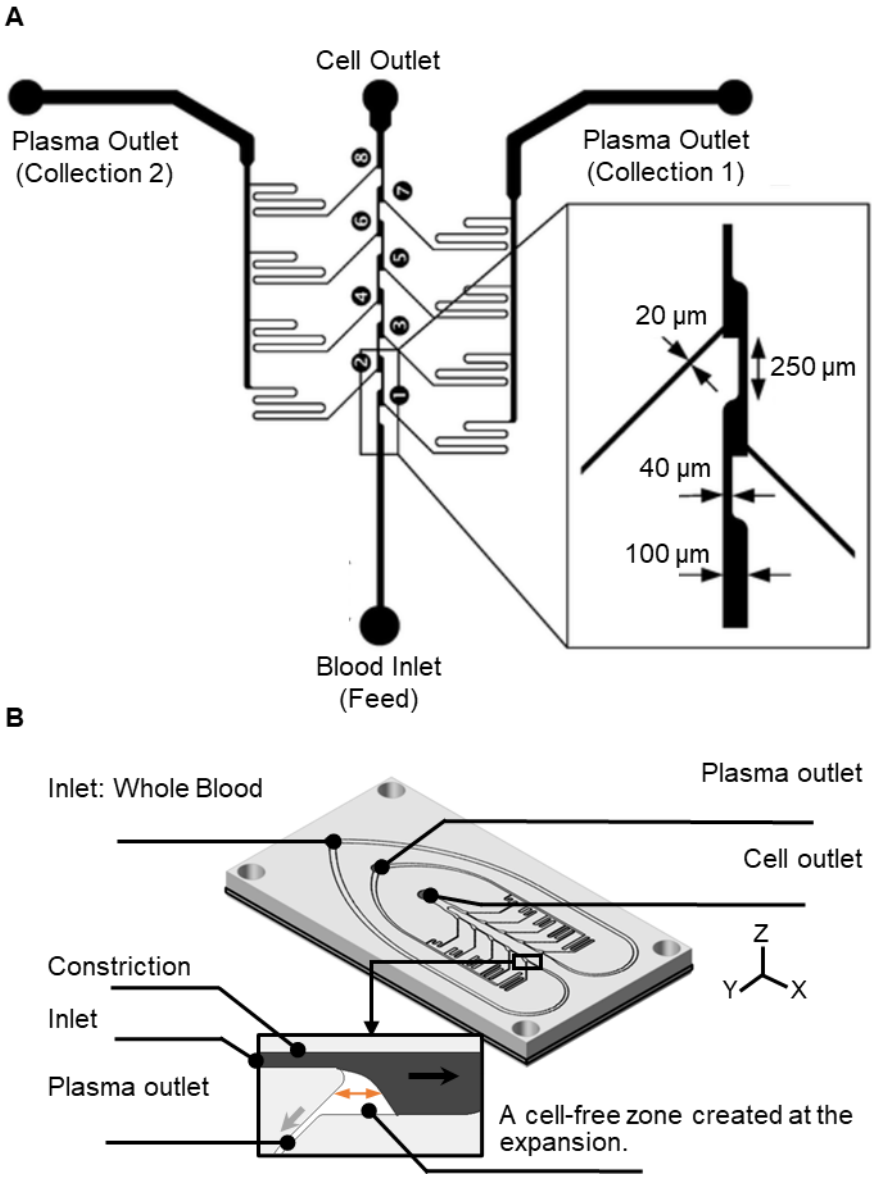

Figure 2.7: Hydrodynamic BPS devices developed by Kersaudy-Kerhoas et al. and Mielczarek (A) BPS device having constriction region before each bifurcation [113]***; (B) (inset) Photograph of cell separation at a bifurcation, (top) Isometric view of a hydrodynamic BPS device developed by Mielczarek [102].***

- ***Deterministic lateral displacement (DLD)***

Deterministic lateral displacement (DLD) can be understood as a sub-category of hydrodynamic separation. This size-based cell or particle sorting technique uses "bump arrays" to separate streamlines in a flow [146]. These are the arrays of obstacles with gaps larger than the particle size and particles select their path deterministically based on their size and deformability [147]. Despite the success of this technique in successful cell sorting [148], [149], it still needs blood dilution, a pre-requisite for this technique.

Furthermore, because this technique frequently results in limited throughput, it is not well suited to huge volume samples of complex matrices like whole blood [63]– [65].

- ***Inertial separation***

The inertial technique, which is also widely regarded as a side branch of hydrodynamic separation and is capable of dealing with large volumes of samples, has gained a lot of attention in the microfluidic community in recent years as a novel method for controlling and governing particles in microfluidic channels [152], [153]. In this technique, the net inertial lift force (the difference between shear-gradient lift and wall-induced lift force) and dean drag force are primarily used, and a balance between these forces determines the route and magnitude of particle movement across the channel, depending on particle size [154]. The key reason behind not acknowledging this approach in our project is that blood dilution is a precondition in this technique because treating a rich quantity of cells would be impossible by the inertial forces and thus the technique has mainly been used in cell sorting, particularly for low-concentration samples [155]–[159].

2.1.2 Active Techniques

- ***Dielectrophoresis (DEP)***

Dielectrophoresis (DEP) phenomenon occurs when there is a difference in the permittivity between the particle and the surrounding medium. During this phenomenon, a force is exerted on a dielectric particle when it is subjected to a non-uniform electric field [160]. The size of the particle, the electrical characteristics of the particle and the medium, and the amplitude and frequency of the applied electric field all influence the magnitude and polarity of DEP [161]. Among the two types of DEP, positive and negative DEP, negative DEP is preferable for cell separation in biomedical and chemical analysis because of the safety of the cell function [160] where particles move away from the electrode. However, this method is flawed because of the longer time requirement of particles to go through the electric field to obtain higher separation accuracy and, therefore, often reported as a low throughput technique [68]–[72]. Moreover, due to the long operating time, mostly it is used to deal with micro-volume of blood samples [145], [165].

- ***Magnetophoresis***

The magnetophoretic method of separation is based on the difference of magnetic susceptibility in cells by applying a magnetic field around the microfluidic channel [167]. The associated setup cost to this technique is cheaper compared to other active separation

techniques [105]. However, this technique has not been used widely in BPS, and the flow rate of 0.6 mL/h used in blood plasma extraction by Kim *et al*. is very low and not viable for practical applications [168]. It takes a long time to focus the cells, similar to the dielectrophoretic approach, resulting in a low flow rate and generally dealing with low volume samples. Vemulapati and Erickson recently developed their High-Efficiency Rapid Magnetic Erythrocyte Separator (H.E.R.M.E.S) sleeve, which employs magnetic beads to efficiently separate plasma from a 1mL whole blood sample with an average purity of 99.9% and a yield of 77% [169]. However, the equipment is not cost-effective, and processing a 10 mL undiluted blood sample will most likely cost more than $100.

- ***Acoustophoresis***

Acoustic based separation techniques utilize the interaction of the acoustic waves and cells to separate cells from the sample [170], [171]. Transducers composed of piezoelectric materials are commonly utilised to produce acoustic waves in this technique. These piezoelectric materials produce an electric current when they are placed under mechanical stress, called the direct piezoelectric effect [172]. It is also possible to create a converse piezoelectric effect, which is the production of mechanical strain in the crystal induced by applying an electric field and is mainly used in acoustophoretic separation.

Bulk Acoustic Waves (BAW) and Surface Acoustic Waves (SAW) are the two main categories of the acoustophoretic technique. Inverse piezoelectricity causes a mechanical strain when an electrical field is formed at the electrodes on the substrate. As a result, the frequency of the AC signal causes piezoelectric materials to vibrate. The entire piezoelectric material vibrates in BAW, and the generated waves propagate through the bulk of the substrate [173]. Acoustic waves in SAW, on the other hand, only travel through the surface of the piezoelectric material [174]. SAW can be further subdivided into standing surface acoustic waves (SSAW) [175], where the acoustic waves from two different opposite facing interdigital transducer (IDT) meet each other to generate a standing acoustic wave on the surface and travelling surface acoustic waves(TSAW), in which only one IDT is used to create a travelling acoustic wave on the surface [176]. Here, IDT is the widely used configuration of electrodes to generate SAW on the surface of a piezoelectric crystal firstly reported in 1965 by White and Voltmer [177].

The working principles for SAW and BAW are quite different. In SAW, two identical IDTs are fabricated on a piezoelectric substrate, and a microfluidic channel is aligned between the IDTs. Each IDTs comprise an array of metal electrodes with a signal input port and ground port. Therefore, two neighbouring electrodes have opposite polarities in

their electric field when radio frequency (RF) signals of equal amplitude are applied to the electrodes. Because of the inverse piezoelectric effect, periodic elastic stresses can be generated along the surface by the periodic electrical field, which finally results in acoustic waves propagating away both sides from the IDTs [174], [178]. In this same way, applied alternating voltage on the other sided IDT generates another SAW. As a result, these two waves with the same frequency and amplitude propagate in opposite directions toward the particle solution inside the microfluidic channel and create a standing wave field at the centre. Whereas, in BAW devices, microfluidic channels are made of materials with high acoustic impedances like glass or stainless steel to provide a significant impedance mismatch between the fluid medium and channel material [179]. Therefore, when the acoustic waves travel inside the channel, the channel walls serve as reflectors. By adjusting the width and depth of the channel, it is possible to generate standing acoustic waves inside the microfluidic channel [180].

The standing acoustic waves created either by SAW or BAW provide a periodic distribution of pressure nodes (minimum pressure amplitude) and anti-nodes (maximum pressure amplitude) inside the microfluidic channel. The generated force in these periodic fluctuations is used in cell separation. Cells with different sizes experience varying degrees of radiation forces and move toward the pressure node. Figure 2.8 explains the principle of free flow acoustophoresis in multiplex mode separation [181]. Two main forces are considered during acoustophoretic separation, namely acoustic radiation forces and acoustic streaming induced drag forces [182], [183].

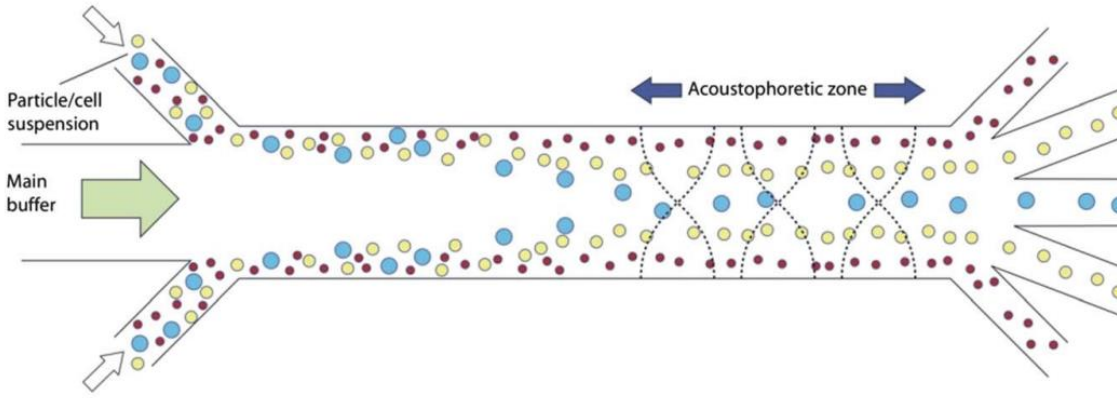

Figure 2.8: Schematic of free flow acoustophoresis for multiplex separation of mixed suspensions where the blue particles experience a larger force than the smaller yellow and red ones and are thus moving faster to the central pressure node. The yellow ones experience less force, therefore, they moved a little bit towards the pressure node while the smallest red particles do not experience any force [181]**.**

The primary acoustic radiation force (F_r) and the viscous force (F_v) on a particle can be expressed as [184]–[187]:

$$\boldsymbol{F_r = -\left(\frac{\pi p_0^2 V_c \beta_w}{2\lambda}\right)\phi(\beta,\rho)\sin(2kx)} \tag{2.1}$$

$$\boldsymbol{\phi = \frac{5\rho_c - 2\rho_w}{2\rho_c + \rho_w} - \frac{\beta_c}{\beta_w}} \tag{2.2}$$

$$\boldsymbol{F_v = -6\pi\mu r u_r} \tag{2.3}$$

Where, $p_0, V_c, \lambda, k, x, \rho_w, \rho_c, \beta_w, \beta_c, \mu, r,$ and u_r correspond to pressure amplitude, particle volume, ultrasonic wavelength, wave vector, distance from a pressure node, density of the medium, density of particles, compressibility of the medium, compressibility of particles, viscosity (dynamic) of the medium, particle radius, and relative velocity, respectively. The acoustic radiation force is dominant compared to the viscous drag force. ϕ denotes the acoustic contrast factor in Equation (2.1) which depends on both ρ_c and β_c, in relation to the corresponding properties of the medium (ρ_w,β_w). The relationship can be found in Equation (2.2). If $\phi < 0$, particles will gather at the anti-node, but if $\phi > 0$, particles will move toward the pressure node. Both of these cases depend on the relative density and compressibility between the particles and the medium [188]. Generally, most biological particles in the liquid medium are moved toward the pressure node [189].

As the acoustic radiation force is proportional to the volume of the cells and viscous drag force is proportional to the radius of the cells, cells with different sizes will arrive at the pressure node at different speeds. Such as, for a blood sample, WBCs will move faster compared to the RBCs with a smaller size. Because acoustophoresis has the ability to handle large volumes of samples while maintaining a continuous flow separation, it is our preferred approach among active techniques.

The acoustophoretic technology for separating blood components has a large literature base and a lot of attention. The majority of researchers incorporated this technique in cell sorting, and only a few of them used it in BPS. Also, blood dilution was a prerequisite in almost all of them. Peterson *et al*. demonstrated an acoustophoretic separation device (Figure 2.9.A) using BAW, which can separate lipid emboli from the shed blood sample recovered during cardiac surgery [190]. Initially, lipid particles were mixed with the blood which were later on removed through the designated side outlet. However, to

achieve acceptable separation efficiencies, sample concentrations of around 5-10% by volume were necessary. The study ensured that applied ultrasound during acoustophoretic separation does not hamper the sample quality. In a similar study, Urbansky *et al*. used a two-stage BAW device (Figure 2.9.B) and separated low abundant mononuclear cells (MNCs), part of the white blood cell population, from RBC with a 2800-fold enrichment and 88% recovery rate [191]. Nonetheless, the central buffer inlet present in their design plays a crucial part during the separation process and makes it less attractive for undiluted samples.

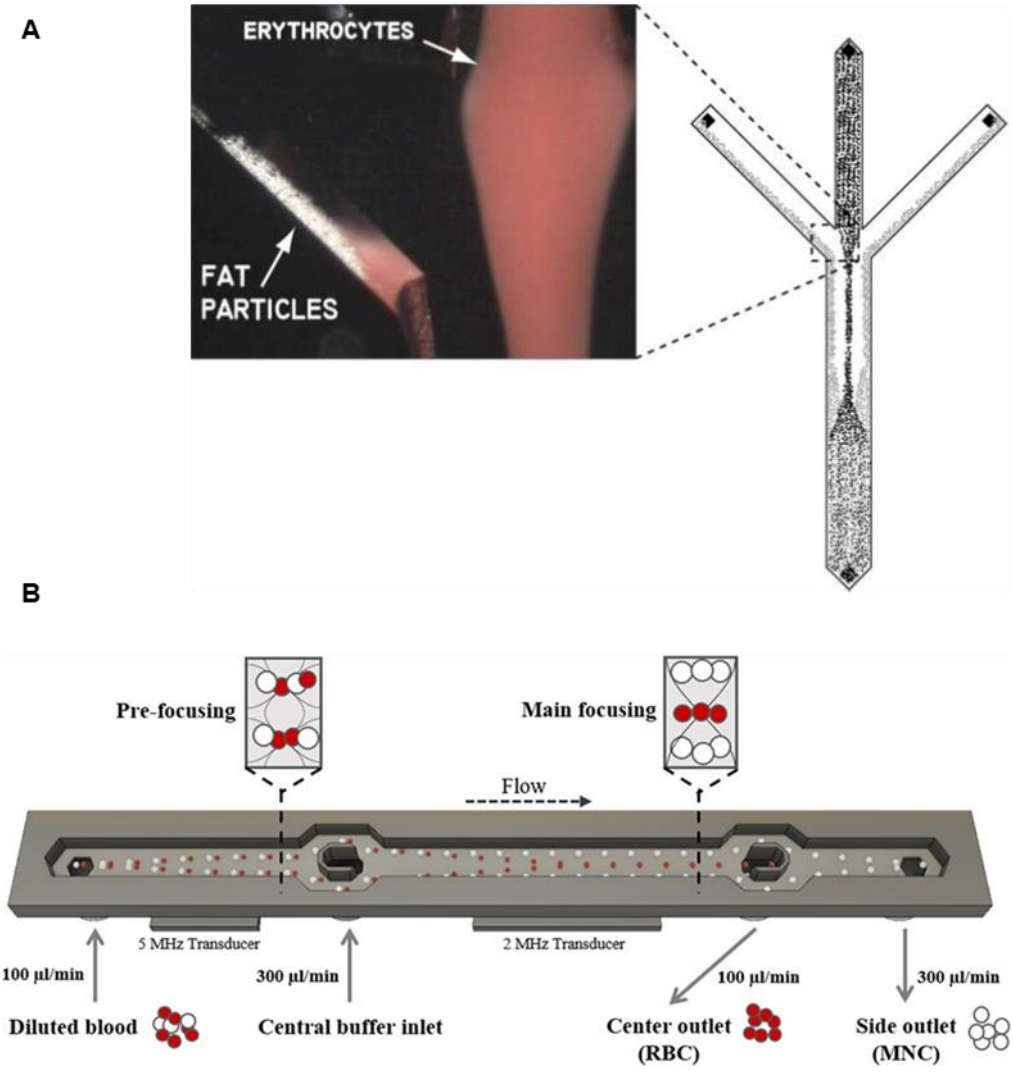

Figure 2.9: Acoustophoretic separation devices developed by Peterson et al. and Urbansky et al. (A) Lipid particles separated from erythrocytes at the trifurcation of 350 mm separation chip with ultrasound turned on [190]***; (B) Separation of mononuclear cells (lymphocytes and monocytes) from blood using a two-stage acoustofluidic separation device*** [191]

Microfluidic based platelet separation from blood has become a topic of great importance in biochemical analyses and clinical diagnosis because the conventional method used to separate platelet using high-speed centrifugation might lead to platelet activation caused

by mechanical shear stress [192], [193]. Nam *et al*. presented SSAW based separation method to separate platelets with a 98% purity from undiluted whole blood [194]. To avoid platelet activation due to shear, they added a sheath flow from two side-inlets (Figure 2.10.A), which hydrodynamically concentrated the blood sample before entering the active zone. Their technique could be effective in BPS, where a constriction zone could take the place of the current cell focusing mechanism. However, due to the small active region in the microchannel provided by the IDTs, the device has a low flow rate (0.015 mL/h), which may be difficult to enhance using SSAW. To ensure high throughput, Chen *et al*. have come up with their BAW based separation device (Figure 2.10.B) where they increased the performance to 600 mL/h and achieved more than 80% RBC/WBC removal and platelet recovery from whole blood [195]. Despite using a dextrose buffer from the top input, the researchers kept mixing to a minimum by matching the acoustic impedances of the two fluids and putting a pump with the same inlet flow rate at the top outlet. However, matching the impedance is challenging and yet very crucial because a slight difference in impedance, e.g., 0.1% between two fluids, can induce fluid mixing in a resonant acoustic field [196]. In a recent study, the same group improved their device even further, achieving a sample throughput of 1200 mL/h while increasing platelet recovery and RBC/WBC clearance to nearly 90% with this new device built entirely of plastic [197].

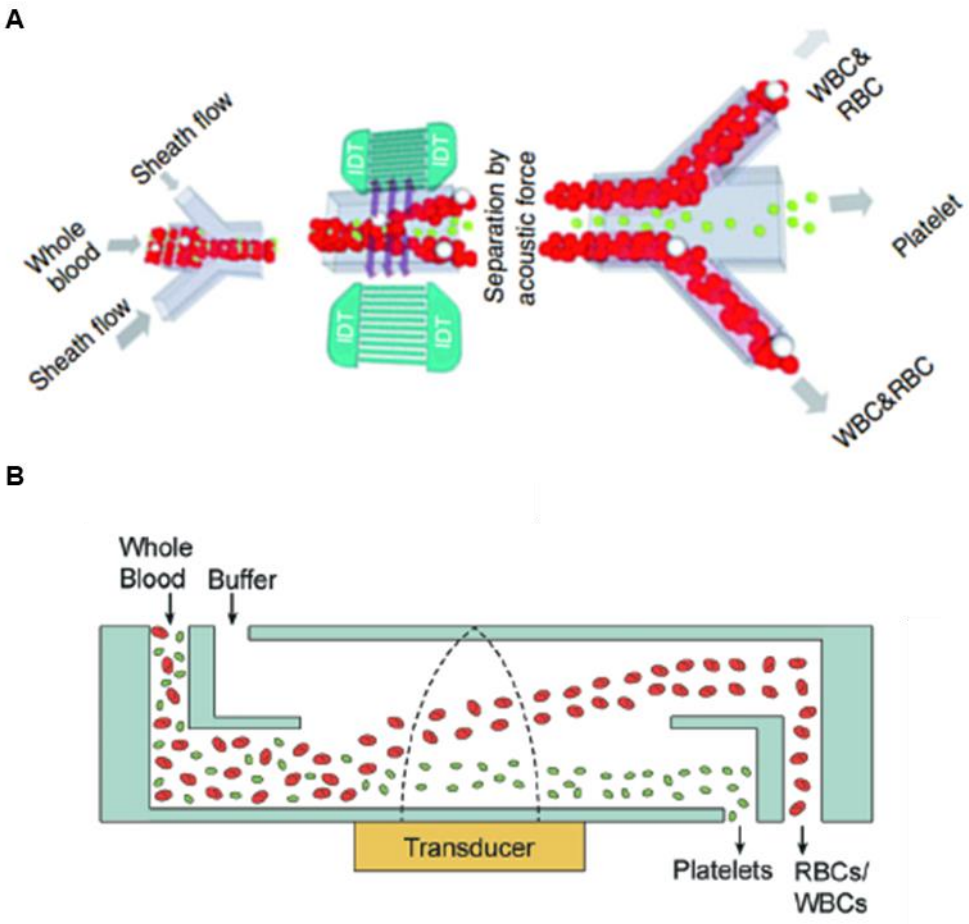

Figure 2.10: Acoustophoretic separation devices developed by Nam et al. and Chen et al. (A) Separating platelets from blood cells by a SSAW device [194]***; (B) High-throughput separation of platelets and blood cells using a BAW technique*** [195]**.**

Back in 2009, Lenshof and his colleagues presented the first acoustofluidic-based BPS device capable of handling whole blood with a high HCT (40%) [111] and a sequential blood cell removal technique. Processing whole blood using active techniques is difficult, as previously stated because focusing cells from a sample with a higher concentration inside the limited active region of a BPS device takes a long time. Furthermore, concentrating such a large number of cells at the pressure node is difficult. The study examined four different designs with different separation channel lengths to overcome the first problem. The 224 mm long device with four meanders was able to remove 12.5% of plasma volume while retaining 100% separation efficiency. Several extra cell outlets were placed in the centre of the separation channel to help the cells focus on their design, as illustrated in (Figure 2.11), which gradually reduces the HCT level. Later in 2013, the same group modified their previous design in order to boost plasma yield which recovered 33% plasma volume [198]. However, the inlet flow rate of 3 mL/h achieved in their experiment needs to be increased further. Later, Karthick *et al*. improved the design of

[111] by increasing the dimension of the channel near the cell-extraction outlet to reduce the effect of shear-induced diffusion, which is the diffusive mobility of microparticles in a shear flow due to hydrodynamic interactions, between the neighbouring particles [103]. Furthermore, in their proposed design, cell extraction outlets were decreased from four to three, allowing for a higher plasma flow rate. They were able to separate plasma at a rate of 1.32 mL/h while using whole blood (40% HCT) at a flow rate of 6 mL/h.

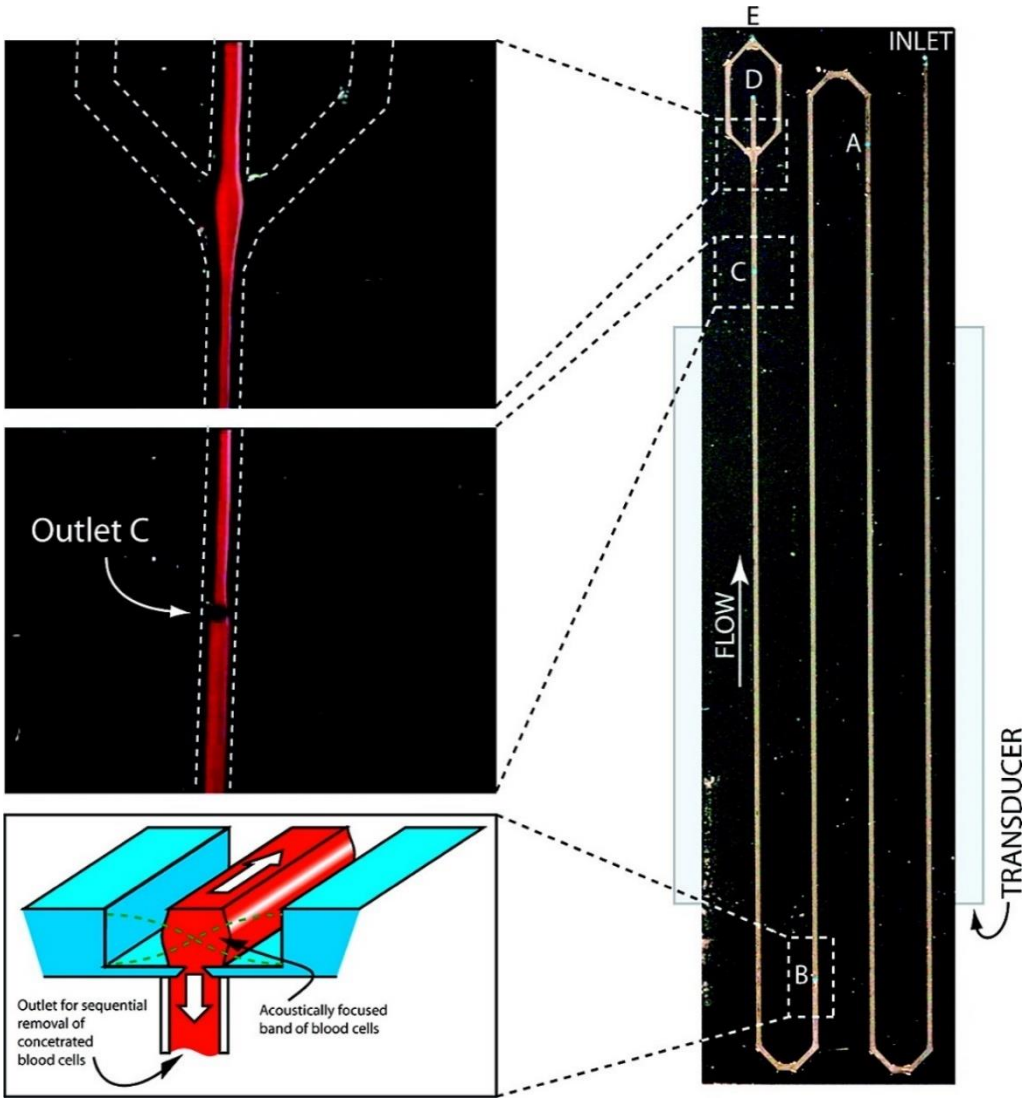

Figure 2.11: Acoustophoretic BPS device developed by Lenshof et al. (A) Plasmapheresis Chip developed [111] ***where the enriched blood cell fractions are taken out through outlets A-C which helps decrease the HCT gradually in the channel. The remaining focused blood cells exit through outlet D while the clean plasma fraction is withdrawn from exit E.***

- ***lab-on-a-disc (LoD)***

Over the last two decades, centrifugal microfluidic devices, also known as lab-on-a-disc (LoD) systems, have become increasingly popular, with the fluidic platform taking the shape of a compact disc and fluidic channels and chambers arranged on the surface.

During the operation, the created centrifugal force assists in moving the sample from the centrally placed input to the designated outlets on the disk's edge via microfluidic channels, where particles of various densities are then separated from their liquid mixture by precise design choices. This approach has several advantages, including the fact that it does not require an external pump and that numerous blood analysis processes can be combined onto a single disc [199]. The method's primary downside is that it has mostly been used for finger-prick volume blood separation [199]–[203], and the separation performance is strongly dependent on blood dilution [204]. Li *et al*. recently reported that their centrifugal microfluidic system successfully isolated 1.6 mL of plasma from a 4 mL whole blood sample (Figure 2.12). Later, using immiscible phase filtration, the collected plasma was used to isolate cfDNA quickly [205].

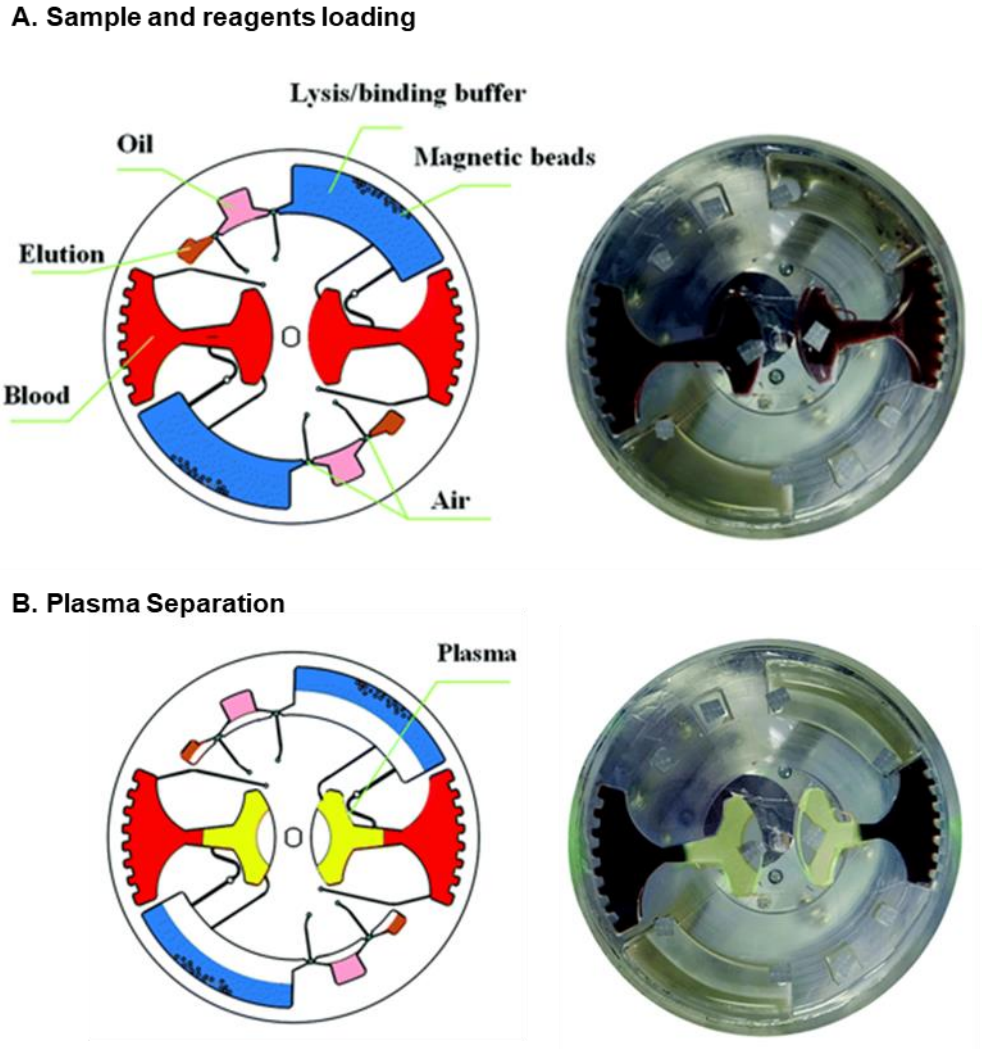

Figure 2.12: Centrifugal microfluidic system developed by Li et al. Plasma separation protocol: (A) the whole blood and DNA extraction reagents were first added into the chamber. (B) The disk was then accelerated to 120 rpm and then to a sedimentation frequency of 3600 rpm where it remained for 4 min for plasma separation.

2.2 Open-source centrifugal procedures

While traditional centrifuge systems have a number of fundamental drawbacks, such as cost and size, centrifugation remains an appealing approach, especially when dealing with high volumes samples (>4 mL) and minimum downstream processing integration is required. Unlike microfluidic solutions, it does not clog and is rather easy to use. However, cost remains an issue, which is why academic researchers have tried to develop open-source microcentrifuges using additive manufacturing and have achieved very promising results by overcoming the limitations of traditional centrifuges. A number of research groups have focused their efforts of DIY and open-source on minute sample amounts [206], [207]. However, here I will only discuss some of the open-source microcentrifuge systems where researchers have been able to process at least 4 ml of a sample through their developed devices and the production cost is less than $150.

Patel *et al*. constructed a portable, low-cost microcentrifuge that achieved speeds of up to 7000 rpm (~550×g) utilising a DC motor, as illustrated in Figure 2.13.A [208]. Although the achievable speed is very high, the usage of glass test tubes in their microcentrifuge will increase the blood handling step. They were able to remove zinc oxide nanomaterial from deionized water using this 3D printed device. The gadget has not been tested on biological samples, and their publication lacks further performance analysis. With a constructed hand-powered centrifuge, Sule *et al*. have been able to achieve the relative centrifugal force (RCF) of up to 700×g where their entire device costs just $27 [209]. They also employed glass test tubes in their device (Figure 2.13.B) and most importantly, the device is not safe to use with biological samples because it lacks a protective cover. Typically, plasma separation requires at least 10 minutes of centrifugation with a refrigerated centrifuge with a capacity of around 2000×g and maintaining that time with a hand-powered microcentrifuge will be challenging.

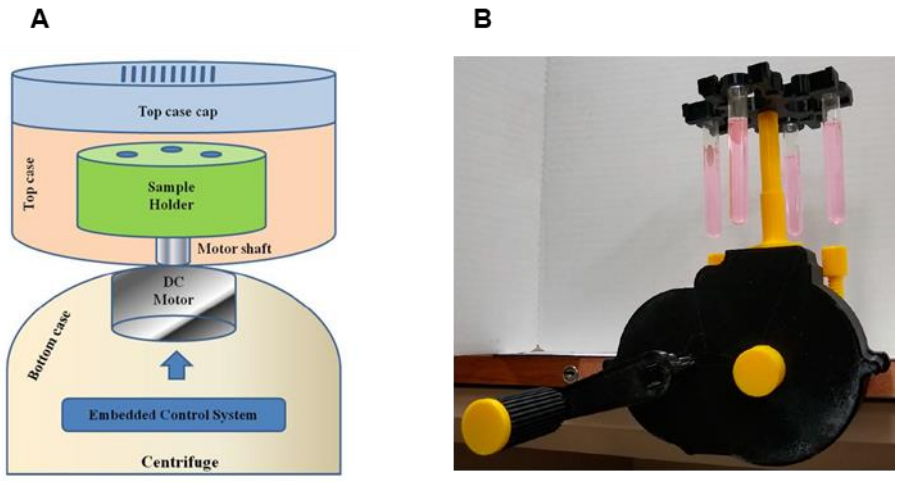

Figure 2.13: 3D printed centrifuges for high volume sample separation (A) Block diagram of 3D printed centrifuge includes the embedded system, DC motor, power supply and speed regulator [208] ***(B) Fully assembled open source hand-powered centrifuge*** [209]**.**

In addition to these open-source microcentrifuges, there are some low cost (<$150) CE marked commercial alternatives available in the market, from SciQuip (SciSpin MINI Microfuge) and Camlab (Camlab D1008 Mini Centrifuge). The major limitation is that they can only manage a maximum volume of 1.5 ml sample.

2.3 Conclusion

From the cited literature, it can be concluded that passive techniques are preferable for efficient microfluidic BPS because of their high flow rate. Active devices are appealing in terms of purification efficiency, but because they require a longer residual time to expose cells to a physical field for successful sorting, it is difficult to achieve a high flow rate with them. Passive approaches are also simple and inexpensive to manufacture.

Acoustic separation stands out from the rest of the active techniques for BPS. It can process whole blood while maintaining high separation efficiency and recovering a significant amount of plasma, resulting in a higher device yield. However, the flow rate achieved in [103], [111], 5 mL/h, and 6 mL/h, respectively, appear to be low. But, this technique could be integrated at the downstream part of the passive hydrodynamic BPS device where the volume fraction of RBC will be much higher. This high HCT blood can be separated using acoustophoresis with a higher frequency piezoelectric transducer, increasing the hybrid device's yield.

After analysing the hydrodynamic based BPS designs discussed earlier, it can be noticed that the number of bifurcations along with a constriction region before each bifurcation improves the separation efficiency and yield [102], [113], [130]. This is due to the fact that when working with a high flow rate, one bifurcation is insufficient to remove a large

volume of plasma. Also, it has been noticed that the CFZW decreases gradually at each subsequent bifurcation [102], [113] and blood HCT typically increases above physiological levels after each separation region, following plasma extraction. Therefore, as the channel progresses the CFZW gets smaller at each subsequent bifurcation because of the increasing volume of cells. As this CFZW highly depends on the flow rate ratio of the plasma and cell primary channel [131], a gradual increment in the flow rate ratio between these two outlets at each bifurcation could help to maintain a constant CFZW throughout all the expansion regions. Along with these discussed design considerations, the following aspects from prior studies should be considered while designing a high yield BPS device in the future.

- Length of the constriction region [131]
- Number of bifurcation [102]
- An expansion ratio between the width of the blood and plasma channels [130]
- Gradual increase of the expansion region after the constriction [144]

One common concern in the majority of the cited literature is that most techniques require blood dilution in order to circumvent the cell-cell interaction which is detrimental to the device's performance. These hydrodynamic interactions between the cells deviate the cells from their particular trajectory in a sample with a high HCT, resulting in decreased separation efficiency. Another reason to use diluted blood is to avoid hemolysis caused by high shear stress inside the channel when dealing with high HCT blood samples. When shear rates exceed 200 to 300 per second, blood viscosity reaches its lowest constant plateau [210]–[213]. As an example, a shear rate of ~1100s^{-1} can be calculated for a microfluidic channel having a cross-section of 200 µm × 50 µm with at a 1 mL/h flow rate. In our lab, we are primarily interested in flow rates greater than 5 mL/h in our pursuit to design a high yield and throughput BPS device, and the cross-section of the main channel of such devices will be similar to or smaller than the example provided. As a result, in future experiments, the viscosity of blood should remain constant, similar to that of a Newtonian fluid, and the pressure gradient should maintain a linear relationship with the flow rate. This increment of pressure gradient will eventually increase the wall shear stress which could lead to hemolysis. While hemolysis could be neglected by maintaining a minimum flow rate, such a low flow rate is not desirable in future studies. Therefore, before designing a BPS device capable of handling whole blood, it is crucial to understand why diluted blood is used, which is a major drawback of most existing devices. Additional factors that could limit the efficiency or yield of the BPS device will also be investigated.

The following chapter (Chapter 3) will primarily focus on the underlying issues influencing the efficiency and yield of microfluidic BPS, as well as possible solutions.

Syringe pumps are commonly employed in microfluidic devices to maintain steady flow rates. The fact that these extensively used stepper motor driven low-cost syringe pumps exhibit flow fluctuation is a major drawback. This fluctuation can have an impact on a BPS device's separation efficiency. The impact of these flow fluctuations on the separation performance of hydrodynamic devices will be investigated in Chapter 4.

The previous chapter emphasized our lab's future aim to develop a microfluidic-based plasma separation method with high throughput, yield, and efficiency. However, several studies have demonstrated that simultaneously increasing the flow rate and efficiency of the BPS device is difficult. Based on this prior research and the fact that blood cells may be damaged by higher shear stress at high flow rates in a tiny microfluidic channel, it can be estimated that the flow rate of our future designed device will be around 20 mL/h. Although this high flow rate will be beneficial in many studies that require low to mid-volumes of plasma (<2 mL), many others that require much larger volumes of plasma (~5 mL) will opt for the centrifugation method over the microfluidic BPS because extracting such large volumes of plasma will require a lot of time. The fundamental problem with commercial refrigerated centrifuges is that they are extremely expensive, and the less expensive options, such as microcentrifuges, can only handle a small volume sample. Chapter 5 presents the design of a low-cost centrifuge solution as an alternative to microfluidic techniques in high volume BPS. The primary outcomes of this research study are presented in Chapter 6, as well as the study's future prospects. A diagram linking all chapters of this thesis is presented in Figure 2.14.

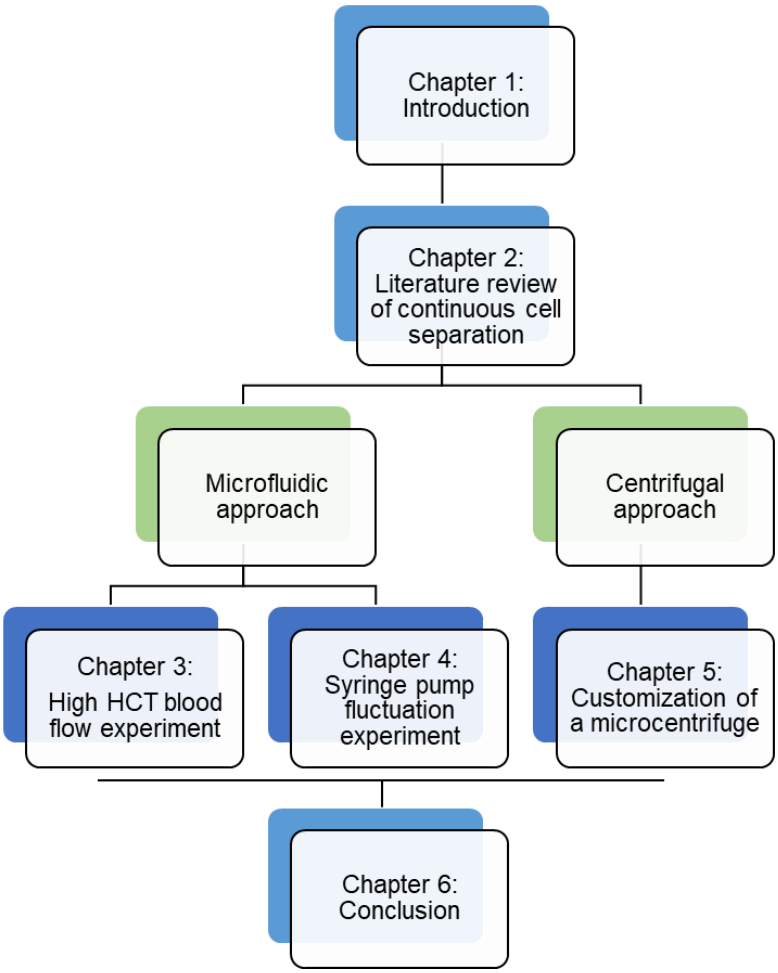

Figure 2.14: Diagram of the thesis customisation

Chapter 3: The effect of elevated hematocrit on human blood flow in a microchannel

3.1 Introduction

A comprehensive literature review (Chapter 2) of active and passive microfluidic blood plasma separation (BPS) techniques to separate plasma from whole or diluted blood samples has highlighted a major concern for higher than finger-prick volume (typically > 0.5 mL) BPS. Most techniques require blood dilution which results in further dilution of the already rare biomarkers available in plasma and therefore greatly affects the sensitivity of the downstream analysis. This dilution is often necessary to reduce the interaction between blood cells. For a sample with a high-volume fraction of erythrocytes, or hematocrit (HCT), the interaction between the cells may deviate the cells from their particular trajectory and result in poorer separation efficiency. Another reason for dilution is to avoid hemolysis of erythrocytes, or Red Blood Cells (RBCs), due to high shear stress inside the microchannel.

Hemolysis can be defined as the destruction of red blood cells which leads to the release of hemoglobin from within the red blood cells. *In vitro*, outside the body, hemolysis can occur during the collection of blood specimens or by the effects of mechanical processing of blood during sample preparation. For example, mixing samples too vigorously can cause hemolysis due to cells being exposed to larger shear stress for a certain time [214], [215]. When blood with high HCT is required to flow with a certain flow rate, the pressure gradient inside the channel will be higher compared to what is needed for low HCT blood. This high shear stress can be a cause of hemolysis inside the microchannel. Shear stress as low as 0.15 KPa has been reported to lyse RBCs in less than 100 seconds [216]. If hemolysis occurs inside a microfluidic device, the released contents will mix with the plasma and degrade the purity of the plasma, resulting in low selectivity, sensitivity, and erroneous results in subsequent diagnostic tests [217]–[219].

The hydrodynamic separation technique, which does not require external fields and has a high throughput and separation performance, was highlighted in the previous chapter as the most suitable passive separation technique for processing higher volume of blood volume than finger-prick volume (usually > 0.5 mL). As stated previously, the technique mainly uses two bio-physical effects called the cell-free layer (CFL) effect [220], [221], and bifurcation effects [120], [133] along with the constriction-expansion regions to separate RBCs from the liquid plasma part Despite the fact that this technique has been demonstrated to be successful in separating large volumes of plasma, the separation yield

is currently quite low, with a maximum of 14% at a relatively high flow rate (~9 mL/h) [102]. The most likely solution to this problem is to increase the number of constriction and bifurcation regions, which will result in a substantially higher plasma yield by directing a larger quantity of plasma to the specified side outlet. However, integrating a large number of bifurcation channels on the sides of the main channel to improve plasma yield might raise a number of issues, which will be discussed in the following paragraphs with the help of Figure 3.1.

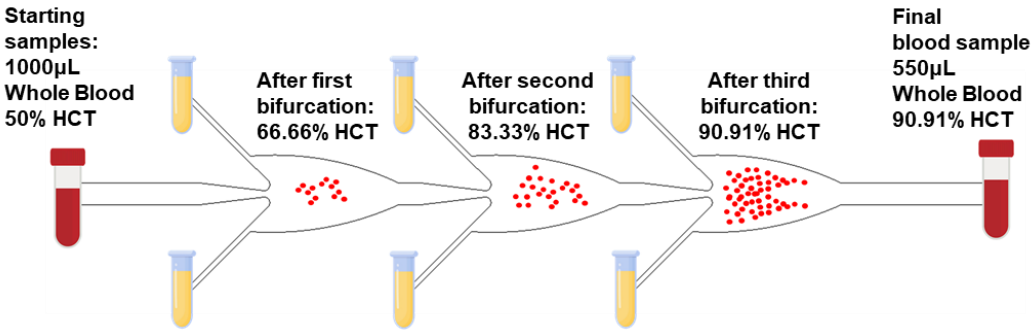

Figure 3.1: Schematic of a hydrodynamic BPS device illustrating the increment of the volume fraction of RBC (HCT) after each bifurcation (NB: This is not an actual device schematic, only a visualization). In this theoretical projection, plasma outlets are assumed to have 100% purity (no red blood cells).

In a hydrodynamic BPS device, when plasma is extracted from the cell-free zones (CFZ) via daughter channels, HCT in the main channel increases after the bifurcation. Therefore, providing a higher number of plasma extraction channels by increasing the number of bifurcations will increase the HCT after each bifurcation. As an example, the BPS device presented in Figure 3.1 has three bifurcation regions with six plasma extraction channels. If 1000 µL of whole blood with 50% HCT is processed by the BPS chip and 250 µL of plasma is transported through the first bifurcation's plasma extraction channels, the blood with 66.66% HCT will be delivered to the second bifurcation region. Blood will flow through the remaining bifurcation regions in the same way, and if 150 µL of plasma and 50 µL of blood travel through the extraction channel at the second and third bifurcations, respectively, the output will have 550 µL of blood with an HCT of 90.91%. Because plasma is the main carrier fluid for blood cells, it is essential to figure out if such high HCT blood can be processed down a microfluidic channel. If this high HCT blood sample clogs the main channel, cells will begin to invade the plasma extraction channel, reducing separation efficiency. Hemolysis, as previously mentioned, could be a subject of concern. Blood viscosity rises with increasing HCT for a given shear rate [212]. As a result, with higher HCT blood at different bifurcations, a higher force will be required to maintain a

consistent flow rate. This will raise the pressure gradient within the microchannel, perhaps resulting in hemolysis. Therefore, two research problems have evolved in designing a viable BPS device with high purity, yield, and no dilution:

• First research question: What is the highest volume fraction of RBC that can be flowed through a microfluidic channel that is similar in size to what is used in a BPS device without clogging it? The answer to this question will provide an upper limit of separation yield for such devices. This upper limit has never been established before.

• Second question: With such a high HCT, what is the maximum blood inlet flow that can be delivered while avoiding cell damage? This answer will reveal the highest flow rate that the future BPS device can achieve, and it has never been investigated previously.

The technical work included in this chapter focuses on answering these two questions and has been presented at International Conference on Miniaturized Systems for Chemistry and Life Sciences (microTAS 2020) and Emerging Investigators in Microfluidics Conference (EIMC 2021). Experiments have been carried out with straight microchannels. To answer the first question, blood with HCT varying between 60% and 90%, was flowed through the microchannel at various flow rates while measuring the pressure inside the channel. The post HCT measurement of each trial has provided the answer for the second question. Prior to discussing the materials and methods utilised in these experiments, the next part introduces additional theoretical concepts that are necessary to comprehend the underlying principles involved in blood flow through microchannels.

3.2 Theoretical Concepts About Blood Flow in Microchannels

3.2.1 Fluid flow in microchannels

To effectively experiment with blood having different HCT, it is necessary to understand the fundamental mechanisms involved in fluid and blood flow through the microchannel. Any fluid flowing through a microchannel behaves differently than any other media. The flow of fluid through a microfluidic system is influenced by a number of factors. It is primarily characterized by the laminar or turbulent flow profile in a system. However, microfluidic flows inside BPS devices are mostly laminar, meaning that two or more layers of fluid can flow side by side with no mixing other than diffusion. Diffusion is a slow mechanism that makes reactions within microfluidic devices easily controllable. As an example, 5000-base-pair DNA molecules in water ($D \sim 2\times10^{-9}$ m^2s^{-1}) take almost 3 hours to cross a microfluidic distance of 100 μm by diffusion [222]. Therefore, the predictability of flow patterns during laminar flow is being exploited to regulate the flow

of particles, cells, and droplets in a growing number of cell biology, biomedical, and pharmaceutical protocols. In order to forecast flow behaviour, the Reynolds number (Re) is the most significant dimensionless number which is the ratio of inertial forces to viscous forces in a fluid, and it may be calculated using the formula below.

$$R_e = \frac{\rho u l}{\mu} = \frac{u l}{v} \tag{3.1}$$

Here, ρ is the density of the fluid (kgm^{-3}), u is the velocity of the fluid with respect to the object (ms^{-1}), l is a characteristic linear dimension (m), μ is dynamic viscosity of the fluid (kg. $s^{-1}m^{-1}$) (for simplicity the dynamic viscosity will be addressed as viscosity throughout the chapter) and v is the kinematic viscosity of the fluid (m^2s^{-1}). For homogeneous fluid, at low Reynolds number, *Re* < 2300 (for rectangular microchannel approx. 700), laminar flow occurs where viscous force is the dominant one and is characterized by continuous and smooth fluid motion as mentioned earlier. Whereas, when *Re* > 4000, microfluidic flows are turbulent where inertial forces dominate and is characterized by the presence of chaotic eddies, vortices, and other so-called flow instabilities. Both laminar and turbulent flows are possible in the interval between 2300 and 4000 and are called 'transition' flows [223], [224]. Table 3.1 depicts different flow patterns inside a microchannel.

Table 3.1: Flow patterns inside a microchannel. Adapted from [225]

Flow	Reynolds number	Pattern
Turbulent	>4000	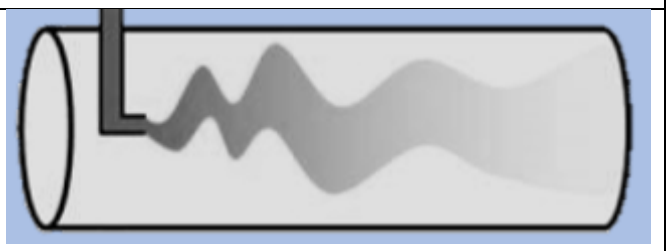
Transitional	2300-4000	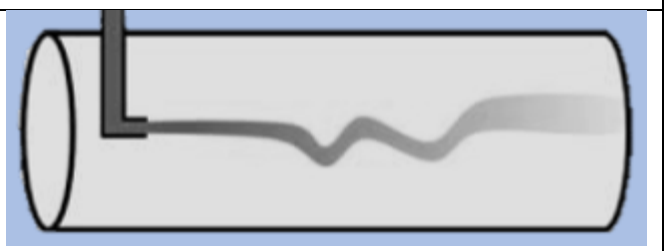
Laminar	<2300 For rectangular microchannel, <700	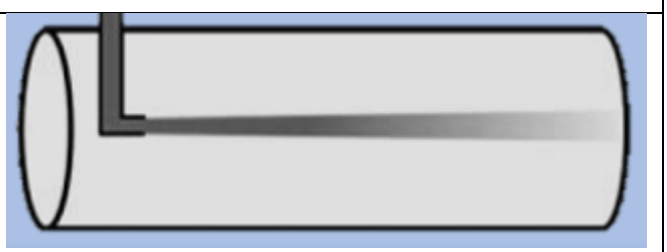

In any microfluidic experiment, pressure drops inside the microchannel are a vital parameter to monitor. Theoretically, Resistance (R) of a rectangular channel is given by:

$$R = \frac{12\mu L}{\{1 - 0.63\left(\frac{h}{w}\right)\}} \frac{1}{h^3 w} \tag{3.2}$$

Here, *L*, *h*, and *w* are the length, depth, and width of the microchannel, respectively, and μ is the viscosity of the liquid sample. Furthermore, the pressure inside a microchannel can be defined by the following formula,

$$\Delta P = Q \times R \tag{3.3}$$

Where ΔP, *Q*, and *R* are pressure, volumetric flow rate, and resistance of the channel, respectively. According to equations (3.2) & (3.3), pressure drops inside the microchannel will solely depend on the flow rate for Newtonian fluids with constant viscosity and will increase linearly with increasing flow rate, however non-Newtonian fluids with non-constant viscosity will exhibit non-linearity.

The flow rate is simply the multiplication of the area and velocity of flow. Therefore, for a rectangular microchannel, the flow rate can be described as,

$$Q = w \times h \times u \tag{3.4}$$

Where *Q*, *w*, *h*, and *u* are the flow rate, the width of the channel, the height of the channel, and velocity in the microchannel, respectively. The maximum shear rate in a rectangular channel can be approximated by [226]:

$$\gamma = \frac{QP\partial}{8A^2} \tag{3.5}$$

Where *Q* is the volumetric flow rate, *A* is the cross-sectional area of the channel and *P* is the wetted perimeter, and where the shape factor ∂ is given by:

$$\partial = [(1 - 0.351b/a))(1 + b/a)]^2 \tag{3.6}$$

Here *b* represents the short side of the rectangle and *a* represents the long side.

3.2.2 Blood flow in microchannels

Understanding the blood flow behaviour inside a microchannel necessitates a thorough understanding of the unique features of blood. Blood is classified as a complex non-

Newtonian fluid. It can, however, change its nature from non-Newtonian to Newtonian or vice versa depending on the shear rates. Newton's law of viscosity is used to distinguish Newtonian and non-Newtonian fluids.

$$\tau = \mu \frac{du}{dy} \tag{3.7}$$

Where τ is the shear stress, μ is the viscosity, and *du/dy* is the shear rate (often represented by γ), with velocity *u* and position *y*. Newtonian fluids have the constant viscosity. The viscosity of non-Newtonian fluids, on the other hand, varies with the rate of shear. Non-Newtonian fluids are further separated into shear-thinning and shear-thickening fluids based on whether the viscosity increases or decreases with the shear rate. The viscosity of the shear-thinning fluid, like blood, will decrease as the shear rate increase whereas viscosity changes oppositely for the shear-thickening fluid. At relatively low shear rates, blood viscosity is at its maximum. Then it starts to drop at moderate shear rates (non-Newtonian behaviour) until it finds a constant lowest plateau (Newtonian behaviour) [210], [212]. This is illustrated in Figure 3.2 where Brooks *et al*. measured the viscosity of different blood samples with varied HCT throughout four decades of shear rate (0–1000 s^{-1}) using a viscometer [227]. It is apparent from the figure that viscosity for all the different HCT samples comes to the lowest constant plateau after a shear rate of almost 300 s^{-1}. Several studies have been carried out to understand this dual behaviour of blood in different regions. In particular, blood was shown to exhibit Newtonian behaviour at zero HCT, and thus plasma is often regarded as Newtonian fluid [228]. Therefore, at higher HCT, the blood cells, mainly the RBCs, are responsible for its dual Newtonian and Non-Newtonian behaviour [212], [228]. This is possible because of the deformation capabilities of RBCs, which is discussed elaborately in the following two sections. It also helps blood to flow with a very HCT. Without the deformation, it would be impossible to circulate high HCT blood due to clogging.

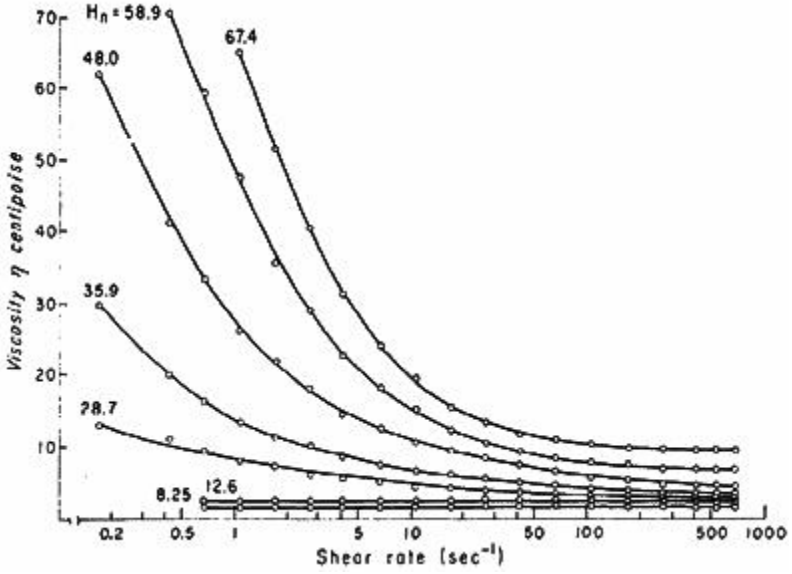

Figure 3.2: Relationship between viscosity and the rate of shear for human red blood cell suspension in homologous ACD-plasma at 25°C for various volume concentrations of the erythrocytes [227] ***The viscosity becomes independent of the shear rate (Newtonian behaviour) at high shear rates, typically >300 s-1.***

3.2.3 Individual RBC behaviour

Depending on the shear rate inside the microchannel, individual RBCs can move in three manners, known as tumbling, swinging, and tank-treading [229]–[231]. These three RBC motions have been classified in Table 3.2. RBC maintains its tumbling pattern when the shear rate is very low and the Reynolds number is very high, but the flow is in the laminar flow regime. In this condition, they can flip around themselves and have almost no deformation. They travel in a transitional swinging motion as shear rates increase, undergoing quasi-deformation and oscillations around their stationary orientation [105]. Finally, at very high shear rates, RBC motion develops into a tank-treading motion [232], in which the largest dimension of the RBCs remains parallel to the flow direction.

Table 3.2: Exemplary cross-sections of rotating RBC during the tumbling, swinging, and tank-treading motion have been taken and reproduced from [232]**.**

RBC Motion	Condition	RBC Pattern
Tumbling	Shear Rate low with high viscosity	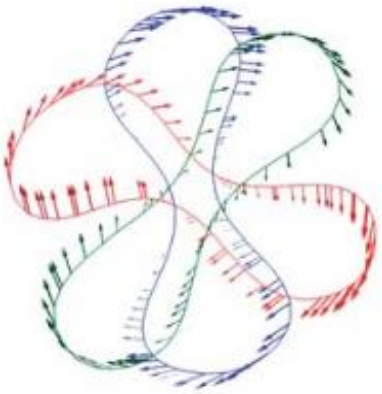
Swinging	Transitional	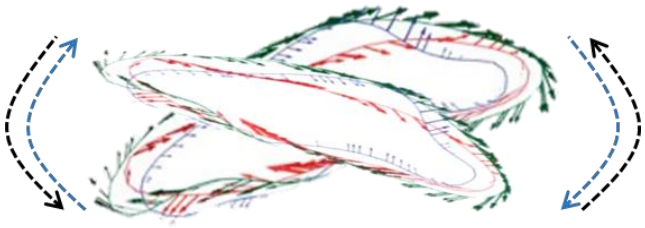
Tank-Treading	Shear rate high with very low viscosity	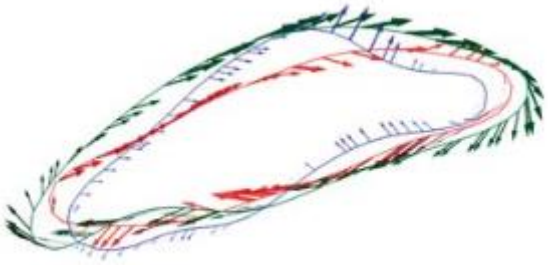

3.2.4 Collective RBC behaviour

At very low shear rates, the flipping of RBCs around themselves often favours the formation of stacks (rouleaux) which results in increased viscosity [233]. However, at higher shear rates when a tank treading motion is formed, the number of aligned cells in the microchannel increases, which helps to minimize the viscosity to its lowest value [234], and blood maintains its lowest viscosity from this stage on [212]. In other words, this flexibility and tendency of RBCs to align with the flow make blood a shear-thinning fluid. The graphical representation and explanation about the blood flow behaviour in a

hydrodynamic BPS device can be found in section 2.1.1 (Hydrodynamic separation, Figure 2.2).

3.3 Materials and Methods

3.3.1 Design of the micro-channel

Channels were designed with AutoCAD (2018, student edition) with a simple straight channel design to test the flow of different HCT blood samples through the microchannel. To carry out unique experiments, the length of the microfluidic channel was adjusted from 11 mm to 47 mm, while a single straight line was common in all configurations to cut a 150 μm width channel.

3.3.2 Device fabrication

In literature, many of the developed microfluidic devices incorporated glass [235], [236], silicon [237], polydimethylsiloxane (PDMS) [112], [144], poly(methyl methacrylate) (PMMA) [105], paper-based [238], [239], and hybrid devices [240], [241]. Of these, paper-based devices are not viable when dealing with large volume samples, and glass and silicon are expensive and not flexible to be dealt with, making the polymers like PDMS and PMMA suitable for the manufacturing of medical-grade devices [242]. Although PDMS is widely used for research purposes, many researchers have adopted PMMA in manufacturing devices because PDMS has been reported to absorb small hydrophobic molecules like biomolecules and proteins from the samples [243]. PMMA prototypes can also be easily scaled up to high-volume production.

PMMA sheets of 2.0 mm thicknesses from Weatherall Ltd (UK) (Clarex® cast) have been used to manufacture the devices. Each of the devices comprises two PMMA slides with the size of 75mm×25mm×2mm. Microchannels were fabricated by the IPAQS group (HW) on the top slide using a customized laser micromachining system based on a 50 W picosecond laser (Trumpf TruMicro 5×50). The system provides approximately 6-ps pulses (measured at full-width-half-maximum) with a maximum pulse repetition frequency (PRF) of 400kHz. The laser spot diameter used for machining PMMA was approximately 24μm (measured at 1/e2 of its peak intensity). The other laser machining parameters were as follows: pulse energy of 15.4μJ, PRF of 20kHz, a scan speed of 40mms-1, and hatch distance of 6μm. A 3D surface Profilometer (Alicona IFM G4) has been used for the measurement of the manufactured micro-channels where the width and depth were found to be 130 μm and 62±2 μm, respectively.

Access holes were created in the other PMMA slides with a 30W CO_2 commercial laser cutter (Epilog Mini 18, 30 W, Epilog). During this double cut process, the speed and power was 25% and 80%, respectively. The schematic of the manufactured microchannel with the measurements is provided in Figure 3.3. From 5 mL/h to 30 mL/h, the Reynolds number calculated for the devices might range from 3 to 90.

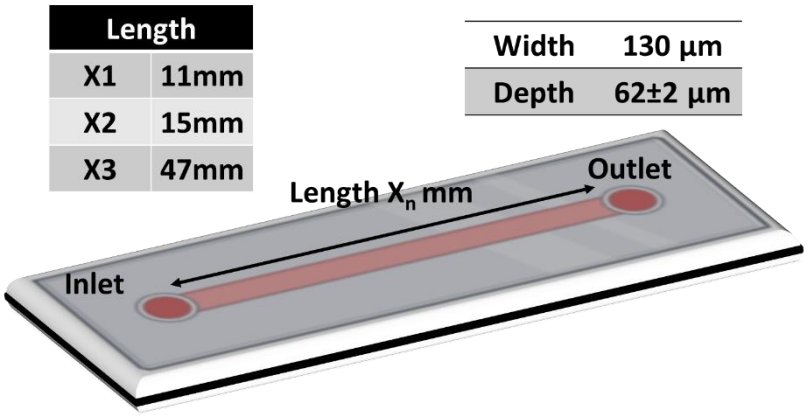

Figure 3.3: Schematic of the single micro-channel devices used in the experiment with the parameters. Three different devices with lengths ranging from 11 to 47 mm have been used while the width and depth were kept constant.

3.3.3 PMMA bonding

Before the bonding process, both layers of PMMA slides were thoroughly cleaned with clean-room tissue and ethanol to remove dust. UV-assisted pressure bonding was used to bond the PMMA slides, as previously described by several groups [244], [245]. The PMMA slides with the bonding surface on top were exposed for one minute under a custom-made UV lamp in our lab during the process. Both slides were immediately aligned in the proper order and placed inside a custom-made heating plate, which kept the layers at the proper temperature during bonding. Finally, the PMMA chips were bonded for 7 minutes at 85°C and 3.5 metric tonnes of pressure using a Bonny Doon Classic 20-Ton Manual Press (Rio Grande, USA). The PMMA chip's engraved channels are extremely narrow. Therefore, excessive heat could result in significant wall deformation and channel collapse [244]. It has been verified that pressing the PMMA chip for more than 7 minutes at 90°C causes microchannel deformation, which demands a higher amount of pressure to flow liquid than an undamaged channel. Therefore, care has been taken to ensure that the time and temperature did not exceed this limit.

3.3.4 Sample preparation

The blood used in the research was collected under local ethical approval from the Scottish National Blood Transfusion Service (contract #18~06; refrigerated at 2°-8°

degrees) and according to the Declaration of Helsinki. Because the volume of blood samples required for this thorough investigation was quite high, blood samples from the same group (O positive) were requested, and when they arrived, they were gently mixed to prevent the RBCs from being damaged by high shear stress. The appropriate plasma was thereafter removed in order to produce the required HCT samples for each experiment.

3.3.5 Experimental setup

All the experiments regarding this project were performed at the Department of Infection Medicine (IM), University of Edinburgh (Royal Infirmary of Edinburgh, Little France, Edinburgh) in a level II biosafety facility. The blood samples with artificially high HCT were loaded into 1 mL syringes (BD Plastipak, Fisher Scientific) and injected by a syringe pump (Aladdin, WPI, USA) into the devices at 1-30 mL/h flow rate by an increment of 3mL/h (except 47 mm long devices where the measurements were done for 0-21 mL/h because of the limitation of the pressure sensor). Same length Polytetrafluoroethylene (PTFE or Teflon) tubing (ID 1 mm) has been used as inlet and outlet tubing which adds a negligible amount of resistance (<10 KPa) to the fluidic network. The pressure was monitored by an inline pressure sensor (uPS1800-T116-10, Labsmith). It should be noted that the measured pressure in this experiment is the pressure measured at the sensor (not to be confused with the standalone pressure at microchannel). However, for simplicity, this pressure at the sensor will be considered as the microchannel pressure. Pre-and post-passage hematocrit values (HCTinitial and HCTpost) were measured on a hematology analyser (ActDiff2, Beckman Coulter). All data points were averaged from triplicate measurements. The schematic and photograph of the full experimental setup are shown in Figure 3.4.

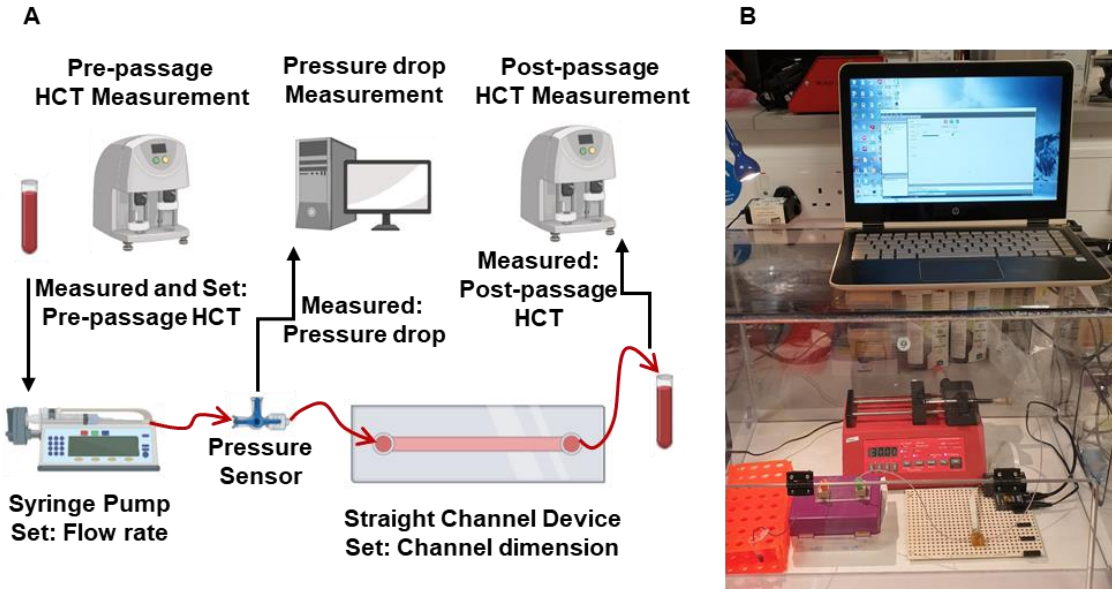

Figure 3.4: Experimental setup in high HCT blood flow experiment (A) Schematic of the experimental set-up. HCT values are collected using ActDiff2 hematology analyser (Beckman Coulter) before injection of the (1mL) blood sample into the channel, and after the passage of the sample to assess hemolysis. A pressure sensor (uPS1800-T116-10, Labsmith) is used to measure the pressure drop in the microchannel. (B) Photograph of the experimental setup (Hematology analyser measurement is not shown).

3.3.6 Statistical Analysis

Statistical significance was determined by an unpaired parametric Student t-test. Unless specified, the p-value significance threshold was set at 0.05. When reporting on statistical significance symbols '*ns*' is used to indicate non-significance ($p>0.05$), while *, **, *** denotes $p<0.05$, $p<0.01$, $p<0.001$ as per conventional practice.

3.4 Results and discussion

3.4.1 Pressure gradient inside the microchannel

Although blood is considered a non-Newtonian fluid, it exhibits Newtonian characteristics at higher shear rates, thanks to the deformation capabilities of RBCs, which allow blood to flow with very high HCT while maintaining a constant viscosity. Therefore, the pressure gradient of all the blood samples inside the microchannel with various HCT was increased linearly (Figure 3.5) with all increments of flow rates (R^2 >0.98), just as Newtonian fluids. According to Poiseuille's equation, for a specific channel, an increment in the blood viscosity will result in a linear increment of pressure gradient inside the channel. Therefore, the slope of the pressure gradient curve was

observed to increase for all devices throughout the experiment as the volume fraction of the blood sample was elevated.

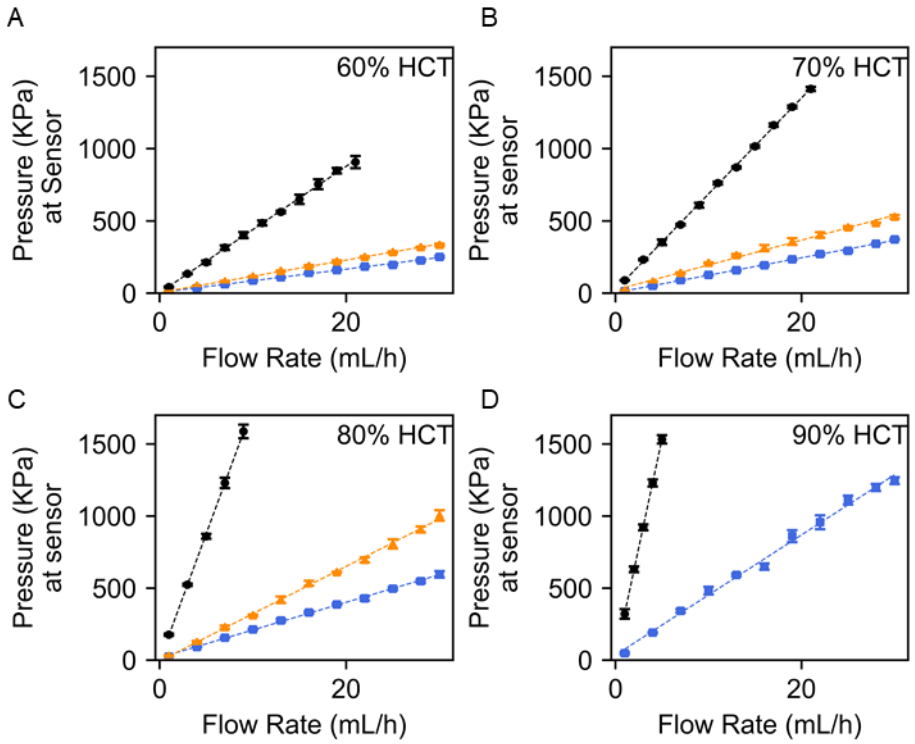

Figure 3.5: Effect of elevated HCT in microchannels. Pressure drops (at sensor) versus flow rate for (A) 60%, (B) 70%, (C) 80%, and (D) 90% HCT blood in 11 (■), 15 (▲) and 47 (●) mm channels. The pressure sensor used has a limit of measurement up to 1700 KPa. Therefore, it was not possible to conduct the full experiment up to 30 mL/h with 80% and 90% HCT blood.

3.4.2 Hemolysis in microchannels

The previous section addressed the study's first research question, demonstrating that blood samples with up to 90% HCT can flow through microfluidic channels with diameters equivalent to previously developed BPS devices. However, because of the increased cell interaction, the pressure gradient inside the channel was extremely high for samples with higher volume fraction of RBCs. The effects of these increased pressure gradients on hemolysis have been investigated in this section.

Figure 3.6 shows the normalised HCT for different sized channels with different HCT samples over a range of flow rates from 0 to 30 mL/h. The difference between the initial and post HCT of each sample used in each experiment was divided by the initial HCT value to calculate the normalised HCT. In this way, only the hemolysed samples will show a positive value, while the non-hemolysed sample will maintain their zero value as there will be no difference between their initial and post HCT values. Figure 3.6 illustrates that there was no trace of hemolysis in any of the different sized channels for 60% and

70% HCT samples. There was also no trace of hemolysis in the 80% sample for 11 mm and 15 mm channels, but the cell started to get damaged after 9 mL/h with a 47 mm long channel, where the difference between the initial and post HCT reached over 30% at 15 mL/h. For 90% HCT, cell damage was persistent for all sized devices (80% HCT sample data not achieved). For a 47 mm long channel, hemolysis occurred after 5 mL/h, and the difference increased to nearly 50% at 15 mL/h, but cells survived up to a flow rate of 19 mL/h for an 11 mm long channel. Therefore, cells are expected to survive a flow rate smaller than 19 mL/h for a 15 mm long channel.

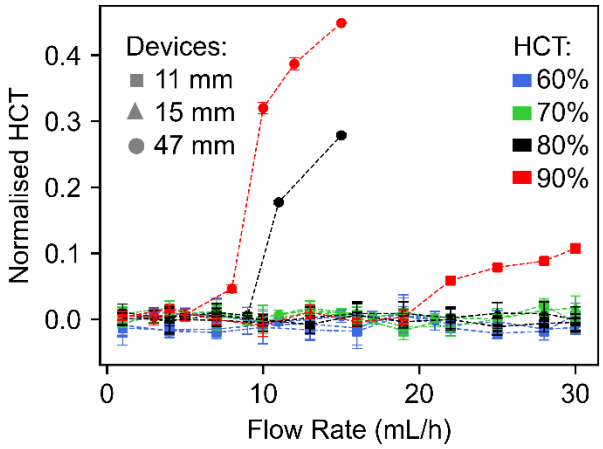

Figure 3.6: Normalised HCT (HCTinitial-HCTpost/HCTinitial) versus flow rates after passage in the microchannel. A positive value indicates the presence of hemolysis after the passage of the sample in the microchannel. In some points, the error bar becomes smaller than the respective point.

To find out the effect of exposure time of the cells inside the microchannel on hemolysis, the wall shear stress on the cells at each experiment was calculated and plotted against their respective exposure time. It can be seen from Figure 3.7 that RBCs started to damage when flowing with a shear stress of 1KPa for over 160 ms. RBCs, on the other hand, can withstand nearly double the shear stress during shorter exposure times (e.g., 17ms).

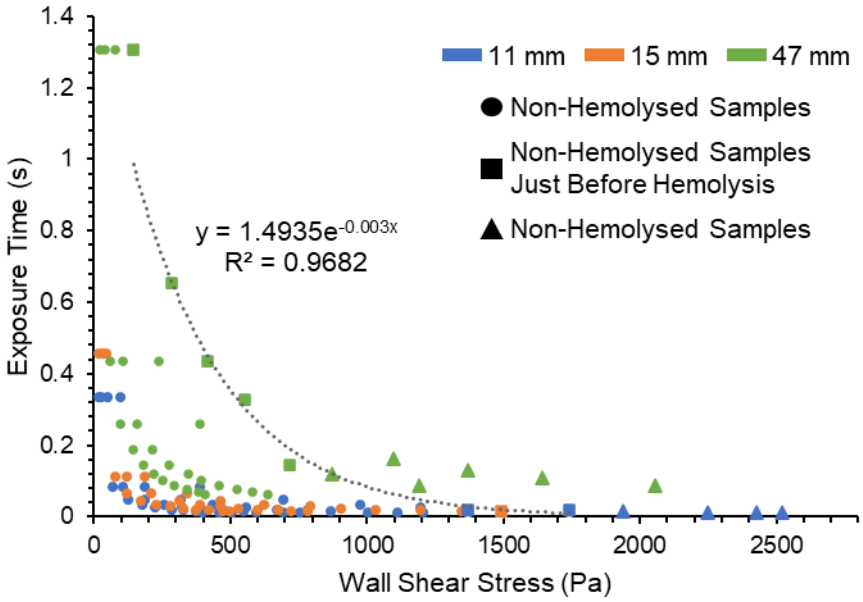

Figure 3.7: Wall shear stress versus exposure time. The Circular points shows the non hemolysed samples after full operation. The triangular points represents where hemolysis has occurred (points where we got a positive normalised value in Figure 3.6). Squared points represents the border non-hemolysed points just before the hemolysis. The exponential trend line is drown using those border non-hemolysed points of all the different devices indicates that there could be an exponential relationship between the wall shear stress inside the microchannel and the cell exposure time.

3.4.3 Microchannel acting as a viscometer

In the next set of results, the dynamic viscosity of various HCT samples was calculated from the measured pressure gradient using equations (3.2 and (3.3 and compared to values obtained from other literature. These calculated viscosities were plotted against the haematocrit value of the sample and compared to historical literature data available on high haematocrit samples, of interest in the present study. Closer inspection of Figure 3.8 shows that viscosity for 60% and 70% HCT is almost similar for each of the three devices tested and matches the viscosity measured using a rheometer in [211], [227]. However, for blood with 80% HCT, calculated viscosity became 13cP, 15cP and 21cP for 11mm, 15mm and 47mm channel devices, respectively, higher than the values reported in [211].

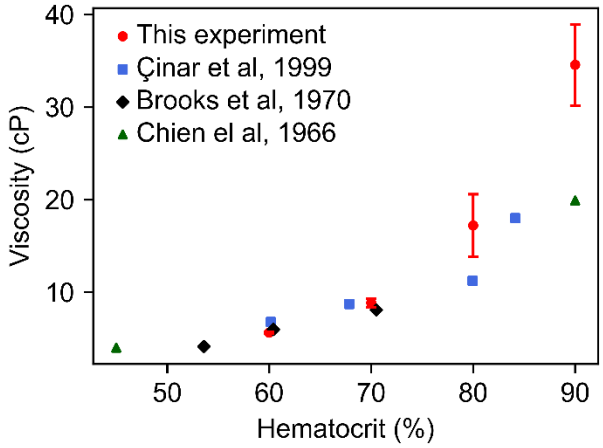

Figure 3.8: Viscosity calculated from experimental data (11,15,47 mm) is compared to experimental data obtained on rheometers in literature [211], [227], [228]**.**

3.5 Discussion

As previously stated, depending on the shear rate, blood can behave like both Newtonian and Non-Newtonian fluids. With a 1 mL/h flow rate, the predicted minimum shear rate in this work was roughly $1011s^{-1}$ using equation (3.5). Blood viscosity reaches its lowest plateau and behaves like a Newtonian fluid from 300 s^{-1} shear rate [134], [210], [212], [213], so does the blood sample in the following experiments because of its much higher shear rates throughout the experiment. This viscosity is determined by several factors, including RBC deformability [246], protein structure and amount [247], erythrocyte and leukocyte masses [211], and, most importantly, HCT [211], [246], which alone has been reported to increase viscosity by 20% with an increase of 10% HCT in the range of 60.16% and 25.32% [211]. This increase in viscosity with higher HCT can be attributed to increased cell-cell interaction, resulting in a high-pressure gradient within the microchannel that could damage RBCs (increase hemolysis).

From Figure 3.5.D, it can be noted that at the highest surviving flow rates, the pressure gradient for 11 mm and 47 mm long channels was about 1000 and 1600 KPa, respectively. Because the cells in the 11 mm long channel appeared to be damaged at a much lower pressure, there must be a definite link between hemolysis and the exposure time of the cells in the microfluidic channel. This has been investigated further and established an exponential relationship between wall shear stress and exposure time, similar to what [216] reported using a viscometer previously.

Blood viscosity represents the ability of blood flow through blood vessels in the human body and its precise assessment is critical in cardiovascular illnesses including stroke and myocardial infarction [248], [249]. For example, during the Covid-19 pandemic, monitoring blood viscosity became significantly vital because many patients began to

develop atypical blood clotting despite taking anti-clotting medicine [250], [251]. Traditionally, these measurements are performed using different types of viscometers such as the capillary viscometer, falling ball viscometer, and rotating viscometer [252] which necessitate bulky and expensive instruments, vast quantities of samples, and longer experimental times [253]. Therefore, many alternative microfluidic approaches using microchannel array [253], micro-cantilever [254] have been reported by many research groups. Although these approaches have made measuring viscosity considerably easier and less expensive, they are not simple to manufacture. In contrast, the straight microchannel device utilised in this project can be used in conjunction with a syringe pump and a pressure sensor to detect the viscosity of any sample. The calculated viscosity with different sized devices up to 70% HCT blood was comparable with the literature value. However, the calculated viscosity of 80% HCT blood was different than the previously measured ones via viscometer which seemed increasing with the channel length. This is counterintuitive with the theory because viscosity is always constant for a certain volume fraction of RBC. When testing with 90% HCT blood, the same type of viscosity difference was observed for 11mm and 47mm long devices, and the values were significantly greater than those reported in the literature [228]. This discrepancy was attributed to manufacturing defects and this phenomenon can be described with the cell-cell and cell-uneven surface interaction of RBCs that introduced flow resistance while flowing with a high-volume fraction. Any blockage or resistance in the flow path can raise the pressure gradient inside the channel, resulting in higher viscosity values than those recorded with a rheometer, which is unaffected by blockages.

3.5.1 A possible explanation for the different viscosity for blood with the same HCT

In the previous section, inconsistencies in measured viscosities for high HCT (80% and 90%) blood were identified, and two hypothetical barriers that could have increased the resistance during the flow and caused these discrepancies were outlined. The first is the uneven surface, which was introduced by a manufacturing flaw during the microchannel's laser cutting. Figure 3.9 presents the surface profile of the 47mm long microchannels employed in the experiment (at three different locations). One can see that the surface of the laser-cut channels was not completely smooth (Same for the 11mm and 15 mm channels).

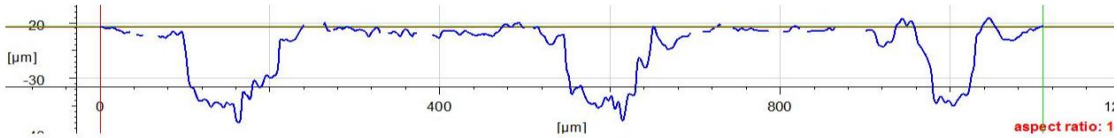

Figure 3.9: Surface profile of the 47mm long microchannel used in the experiment at 3 different locations (Measured with Alicona profilometer).

The ferrule-based connection that was employed to connect the tubing with the microchannel outlet could also be a major contributor to the increased resistance. Because there is an abundance of plasma available when blood has a low HCT, it does not encounter any barriers on its flow path. A sample with a high HCT, on the other hand, has less available plasma and interacts in the opposite way to the obstacles because of the difficulties in flowing through the microchannel. During the experiments, even though the surface was not completely smooth, or the ferrule connection tried to restrict the flow, when blood flowed up to 70% HCT, it did not encounter any impediments on its flow path since there was enough plasma available. During the flow of blood with a high HCT, however, the situation would have been entirely different. The phenomenon is visually described with the help of a diagram in Figure 3.10. During the high HCT blood flow (>80%), some RBCs would have gathered at the asperities inside the channel because of the lack of plasma. But it has been assumed that the main flow resistance was introduced from the contact region of the ferrule and the outlet hole, where the cells faced maximum resistance due to the blockage, as opposed to the low HCT samples, which had a little blockage. Due to the high cell-cell interaction of RBCs at the flow path, more cells would have travelled to the already gathered RBC's position at the ferrule connection. This could explain why, in earlier investigations, higher pressure was required to flow blood with high HCT, resulting in high calculated viscosity values with high HCT samples.

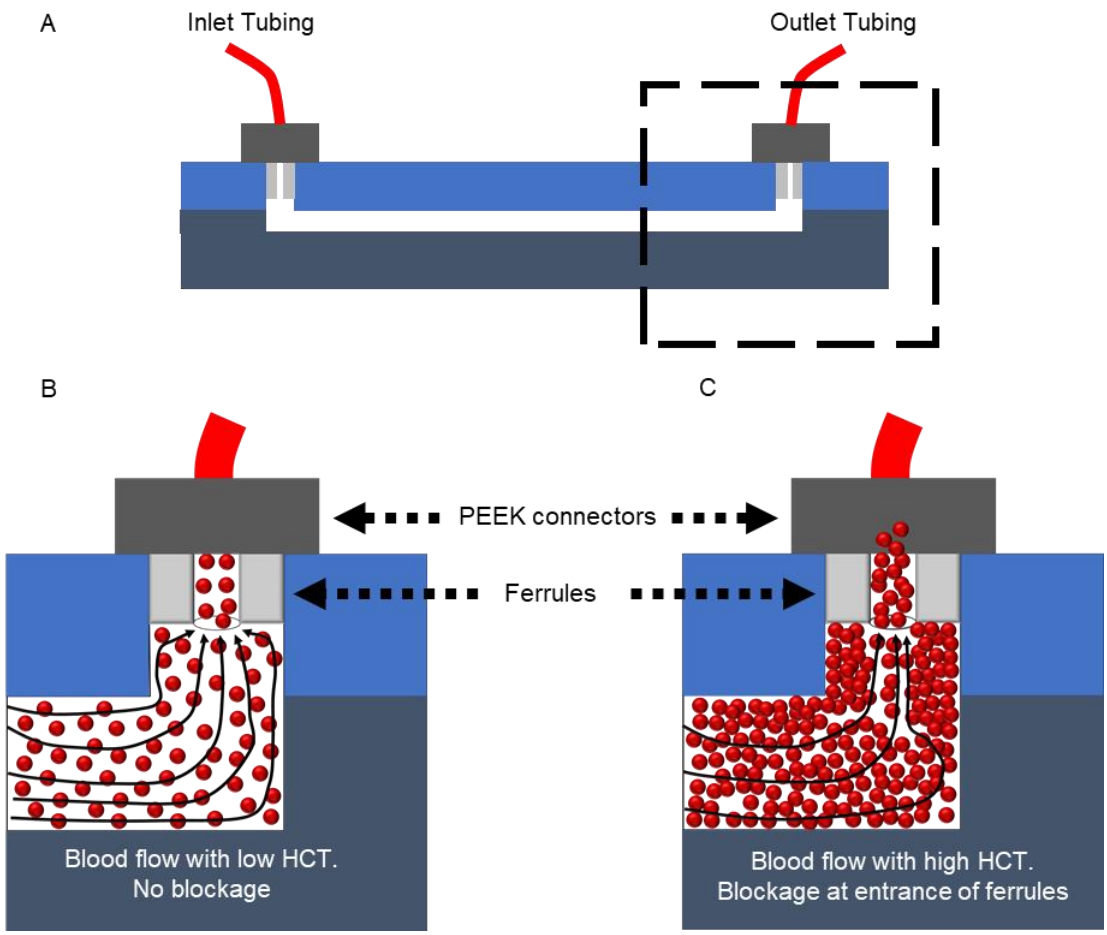

Figure 3.10: Illustration of the effect of the ferrule (OD:1.6mm, ID: 0.5mm) on blockage in high HCT set-up (A) full microchannel showing the ferrule based connection of the tubing and microfluidic inlet/outlet; (B) zoomed section of the outlet showing blood flowing out through the ferrules without any resistance with a low volume fraction of RBCs; (C) zoomed section of the outlet showing blood flowing out through the ferrules with high resistance and blockage with a high volume fraction of RBCs; [Cartoon produced to explain the reason behind the varying viscosity in ferrule based setup]

To evaluate the effect of the ferrule connection at the outlet, the ferrules were removed from the outlet of a previously utilised 11 mm long channel device and through which 90% of HCT blood flowed. The result from this experiment is shown in Figure 3.11 from where it can be observed that the measured viscosity from this experiment has reduced to almost 20 cP, almost similar but slightly higher than the viscosity measured with the rheometer [211]. However, due to the increased pressure measured at some flow rates, viscosity is still higher in the range of 26-28 cP at some points. Although the reason for this abrupt increase of viscosity at particular flow rates is unknown, the surface unevenness issue mentioned previously could be a contributor. Furthermore, there was no cell damage or hemolysis up to 30 mL/h in this experiment, whereas hemolysis occurred after 19 mL/h in the previous experiments.

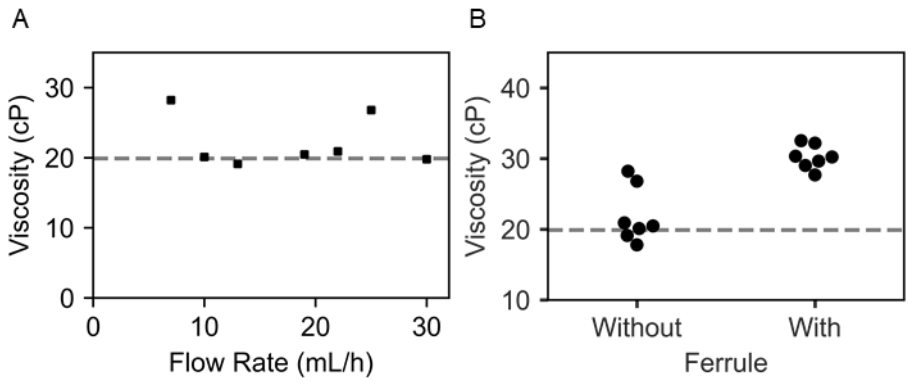

Figure 3.11: Calculated viscosity without ferrule system (A) Calculated viscosity from the measured pressure data against different shear rates (11mm long channel device without outlet ferrule). Due to the device shortage, only one set of data has been achieved (B) Comparison between viscosity with and without ferrule showing significant viscosity difference between two systems. The grey dashed line indicates the 90% HCT blood viscosity from literature [228]**.**

Despite the fact that the effect of surface roughness could not be examined in the same way because all of the laser engraved microchannels in our lab have certain asperities, measured viscosity was almost identical to the literature after removing the ferrules. Therefore, it can be concluded that the ferrule-based connection between the outlet and tubing is the primary cause of the high pressure that leads to higher measured viscosity values while working with high HCT blood samples in this experiment. However, the same experiment should be carried out using the long channel device, which has a significantly larger surface area, allowing the effect of surface roughness to be observed. RBCs gathering at the asperities is a slow process because these asperities are distributed over a large surface area, and this can be avoided by increasing the frequency of the cleaning process. Here, the device was cleaned frequently with the Phosphate-buffered saline (PBS) after each experiment. On the other hand, cells start to gather immediately at the ferrule connection after starting the high HCT blood flow which acts as a blockage at certain points and increases the pressure. This cannot be avoided without stopping the use of the ferrules. But in a high-pressure setup, the ferrules play a crucial role in the connection between the microfluidic channel and tubing. Therefore, to solve this issue a three-part, three-step PMMA bonding process was proposed.

3.5.2 Proposed new ferrule system.

During the initial device manufacturing, two PMMA slides were employed, one with the engraved microchannel and the other with the inlet-outlet holes. However, it was explained in the previous section with the help of Figure 3.10 that ferrules connected at the outlet may impede high HCT blood flow to the point where considerably higher

pressure is necessary to flow the blood than is required for low HCT blood. This will result in a higher viscosity, which could easily damage the cells. Therefore, it is essential to construct the device in the three steps depicted in Figure 3.12 to eliminate the likelihood of obstructions forming at the output ferrule. At the first step, the channel will be engraved on a PMMA slide. The inlet and outlet through holes will be cut into another PMMA slide in the second step. The diameter of the through-holes will be the same as the inner diameter of the ferrule. Finally, the third step will be identical to the second, but the diameter will be equal to the ferrule's outer diameter. The full-cut profile should be circular, not cone-shaped which is often the case because of the laser beam shape. This is necessary to prevent the ferrules from being squeezed. This can be accomplished in a number of ways, including altering the laser pointer's focus or using a tape attached to one side of PMMA.

Figure 3.12(b & c) presents the zoomed section of the outlet showing blood flowing through the outlet of the new ferrule system with low and high HCT blood. Because of the placed ferrules, there will be no obstacles, and as a result, there will be no room for RBCs to congregate and block the flow of the high HCT blood.

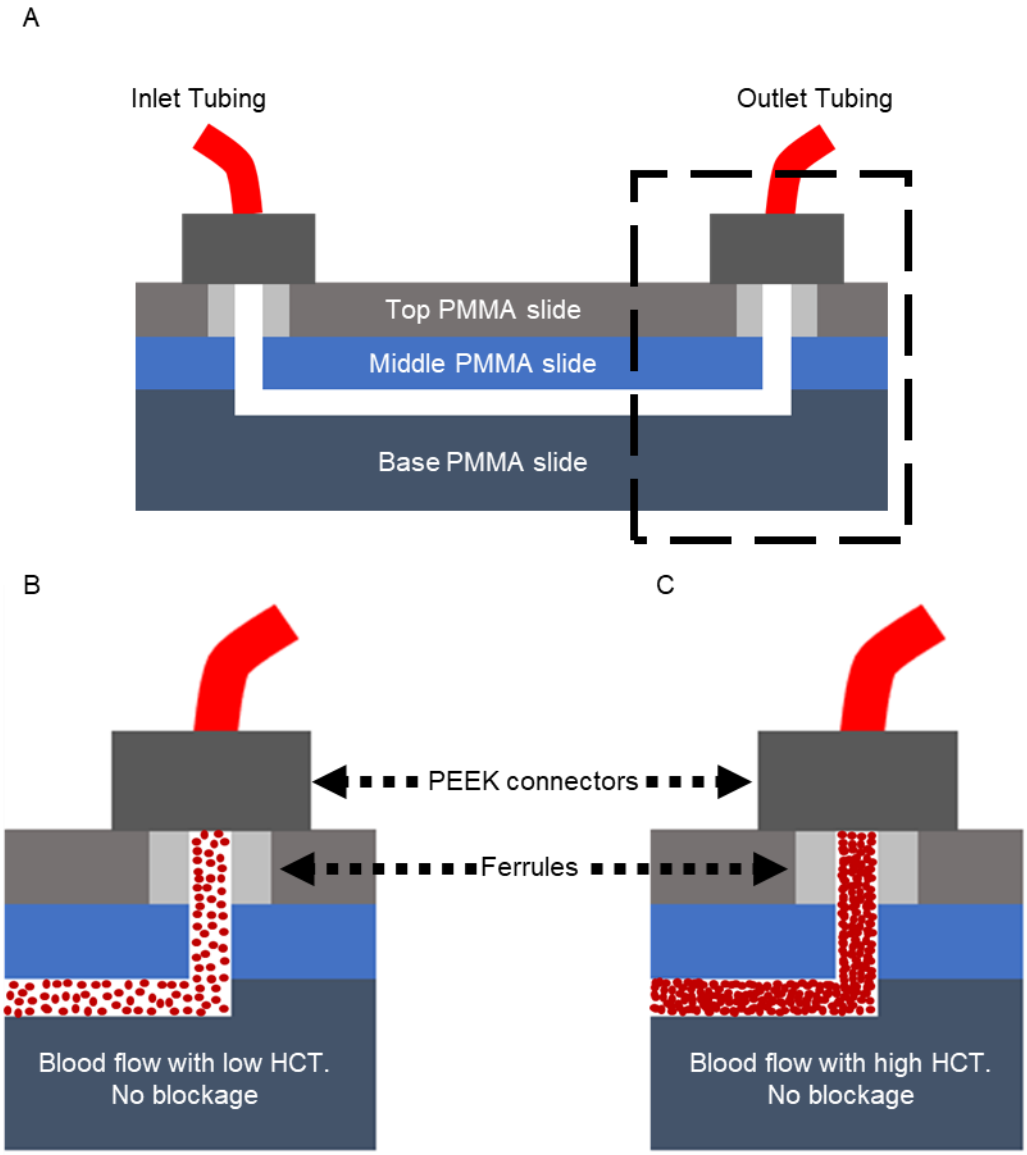

Figure 3.12: Proposed new ferrule system to reduce blockage at the outlet (A) Proposed new ferrule system for high HCT blood sample where the base PMMA slide has the engraved microchannel. The middle PMMA slide has the inlet and outlet connection holes equal to the diameter of the ferrule ID. Finally, the top PMMA slide has the inlet and outlet holes equal to ferrule OD; (B) zoomed section of the outlet showing low HCT blood flowing out through the ferrules (C) zoomed section of the outlet showing high HCT blood flowing out through the ferrules; in both cases, there are no obstacles at the ferrule connection and therefore no pressure increment is expected. [Cartoon produced to explain the reason behind the varying viscosity in ferrule-based setup]

3.6 Conclusion

While many studies have deciphered the behaviour of red blood cells in a confined environment, few studies have studied bulk blood flow, especially at high HCT flow in microchannels. In this study, it has been established that blood can flow through

microchannels of the size employed in the BPS device with an HCT of up to 90%. However, it has also been noted that flowing blood samples with high HCT can potentially damage RBCs depending on their residence time in the microchannel. The existing ferrule-based method has been recognised as the source of cell damage in high HCT blood flow, and a new ferrule-based system has been proposed as a solution, involving device manufacturing segmented into three parts rather than two. Furthermore, for viscosity measurement, this device can be a low-cost microfluidic alternative to the traditional bulky, high-cost viscometer, and it is much easier to manufacture than the other currently available microfluidic viscometers. Most importantly, this study provides a framework for the design of future blood plasma separation devices or the study of neonate circulation [134].

Chapter 4: Effects of Syringe Pump Fluctuations on Cell-Free Zone in Hydrodynamic Separation Microfluidic Devices

4.1 Introduction

Precise and accurate control of flow rates is essential in many microfluidic-based experiments such as droplet generation [255], [256], particle separation [257], [258], cell manipulation [259], [260], sample processing [261], [262], and chemical and biomolecular sensing [263]. Three types of systems are used to control the liquid motion in microfluidic devices: (i) hydrostatic pressure and capillary action, which do not require external forces, (ii) pressure control via pressure generators, and (iii) flow rate control via syringe pumps. Among them, syringe pumps are widely used for flow rate control because of their availability, user-friendliness, cost-effectiveness, and their capability to control the flow rate across micro-channels independently of the fluidic resistance. Additionally, syringe pumps are ubiquitous equipment in medical settings, which makes them particularly suitable for medical applications and medical staff. However, stepper motors inside syringe pumps can be an unwanted source of flow fluctuations. These flow instability has been demonstrated to be a serious concern for droplet microfluidics, where flow fluctuations have been confirmed to increase polydispersity [264], [265]. Because of the pulsation of the stepper motor from the syringe pump, Li *et al*. observed a 13 μm radial variation of 435 μm sized formed jet at the meeting point of the two fluids flowing from different capillaries in their droplet microfluidics experiment [264]. They discovered that the calculated frequencies of mechanical oscillation from the syringe pump are consistent with the measured frequency of ripples and are linearly related to the driving flow rate, similar to the findings of Zeng *et al*., who compared the measured frequencies of induced pressure fluctuation in their device [266]. The difference between these two frequencies was less than 10%, according to this later study, and smaller diameter syringes provide higher frequency fluctuation, while the amplitude of fluctuation is higher for larger diameter syringes. Researchers have devised methods for dealing with fluctuations. The use of elastomeric tubing before the microfluidic network is a straightforward approach that does not necessitate the use of any additional fluidic components [267]. However, this solution is not compatible with high-pressure microfluidic applications and creates an additional surface that increases non-specific binding. Microfluidic stabilizers using air bubbles have been proven attenuating 46% flow fluctuation with one stabilizer by expanding and shrinking the trapped air volume

[268]. Most recently Zhou *et al*. developed similar air bubble based hydraulic capacitors that can minimize the flow pulses by 75.3% [269]. The drawback is that a separate unit is required to dampen the fluctuation induced by the syringe pump. Naive systems (non-damped) are common in research settings and warrant further investigations. No study is yet to investigate the effects of these flow fluctuations on the microfluidic-based particle separation technique. Therefore, here in this chapter, I will rigorously focus on flow fluctuation effects on microfluidic-based passive separation techniques, specifically on hydrodynamic separation techniques.

Amongst techniques that are particularly susceptible to pump fluctuations, are hydrodynamic separation techniques. Microfluidic-based passive separation techniques use specific channel geometries to separate particles in designated outlets and harvest pure particle-free liquid into the remaining outlets. These passive techniques have been applied for cell separation [270]–[272], blood plasma separation (BPS) [112], [113], [129], [130], algae separation [273], [274], and other applications [275]–[277]. Flow stability is crucial in these techniques because instabilities can cause particles or cells to travel in the wrong flow streams and thus lead to poor separation efficiency [278], [279]. Particularly, it is of utmost importance in BPS, to ensure no cells travel to the plasma outlet because of lower efficiency as this can lead to further disturbances in biomarker detection during downstream analysis. It is hypothesized that there is an ample chance of unwanted migration of blood cells to the plasma outlet as a result of flow fluctuation induced from the syringe pump's mechanical oscillation. This study set out to evaluate the impacts of syringe pump fluctuations on hydrodynamic separation structures, utilising a novel high-speed imaging technique called a coded compressive rotating mirror (CCRM) camera. The findings of the study were characterised in the context of milk fat separation, where separation efficiency was investigated against the pump fluctuations. The technical work included in this chapter has been presented at Emerging Investigators in Microfluidics Conference (ICAM 2021) and published in the journal Physics of Fluids [138].

4.2 Materials and methods

4.2.1 Hydrodynamic Separation Technique

Microfluidic passive separation techniques use particle-particle interaction, microfluidic geometry and particle's flow field for the separation of particles from their liquid mixture. As mentioned before, hydrodynamic passive separation techniques are advantageous over the other techniques because of their capability of processing large volume samples with

a considerable high flow rate. All the available hydrodynamics techniques and the full working principle of this technique have been discussed elaborately in Chapter 2. In summary, this technique uses several biophysical effects such as the cell-free layer effect [220], [221], and bifurcation effects [120], [133] to ensures the generation of cell-free zones at the bifurcation from where the liquid portion is extracted through daughter channels. The stability of the cell-free zones positioning is crucial to maintain the high separation efficiency of these devices.

4.2.2 Microfluidic chip design and fabrication

The hydrodynamic separation device (Aug 15 C1) used in this experiment was previously developed and tested by our lab group in the context of BPS where a separation efficiency of 95% with 14% yield has been reported [102]. This device comprises one inlet and two outlets, one outlet for particle-free liquid and one outlet for particle-enriched liquid, as illustrated in Figure 2.7.B. The main inlet channel separates into two units where each unit comprises five constriction-expansion regions, followed by a bifurcation into a daughter channel collecting the particle-free liquid and the particle-laden main channel. The main channel width varies from 100 to 150 μm, whereas the constriction width varies from 35 to 37.5 μm. The devices were fabricated commercially in a proprietary Bisphenol A Novolac epoxy resin (SU8), on a Polymethyl methacrylate (PMMA) substrate (Epigem, UK). A PMMA holder and Polyether ether ketone (PEEK) connectors were machined in-house to enable standard HPLC-type fittings to be connected to Luer-lock syringe connections for safe, high-pressure fluid actuation. This device has been used in all the experiments except the one where different syringe pumps have been compared (Section 4.3.5).

In certain studies, two other BPS devices with very similar channel sizes, the Nov 09 and Feb 16 B1 (Figure 4.1), were used to assess the impact of fluctuations from different commercial and open-source syringe pumps. In section 4.3.1 (Figure 4.5), both Nov 09 and Feb 16 B1 along with Aug 15 C1 and the straight microchannel device were utilised to examine the relative fluctuation change with various channel geometry. The Feb 16 B1 device was also used to compare different syringe pumps (section 4.3.5). Although the three BPS devices have comparable channel diameters and manufacturing processes, their device geometry is different, which will aid in providing a clear depiction in the comparison. Main difference between device Aug 15 C1 and Feb 16 B1 is the inlet placement. The Aug 15 C1 device has all the inlet, particle/cell laden fluid outlet and particle/cell free liquid outlet on the same side of the device to ensure longer relaxation

time for the particles/cells before entering the constriction-extraction region. But for the Feb 16 B1 device the inlet is placed on the opposite side of the both outlets. Instead of dividing the inlet into two separate units (where each unit comprises five constriction-expansion regions), device Nov 09 has only single inlet channel with eight constriction-expansion regions. In addition, a straight microchannel device, used in the experiment in Chapter 3, has been employed to observe the fluctuation effects on a device without any complex geometry.

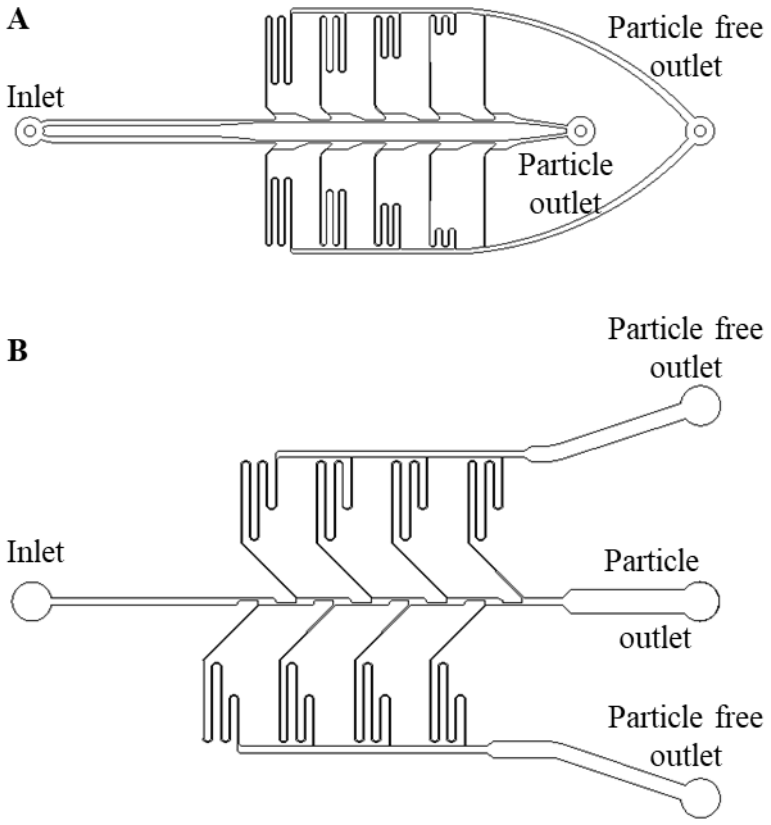

Figure 4.1: Schematic of the hydrodynamic BPS device used in section 4.3.1 and 4.3.5 (A) Feb 16 B1 (B) Nov 09.

4.2.3 Fluid flow actuation

An overview of the experimental setup is shown in Figure 4.2.A. The milk sample was injected into the device by a syringe pump (Aladdin Single-Syringe Pump, model: AL-1000HP, pitch S=1.27 mm). With every step generated by the stepper motor inside the syringe pump, the pushing block moves forward, forcing the syringe to flow the liquid into the system. For a specific flow rate, the pushing block covers a fixed distance by a step originated by the motor. The generated pulse during each step has been identified as a source of disturbance in the flow initiated by the syringe pump [264]. Three other

syringe pumps were used in the last section when the performance of different syringe pumps was compared. The pulseless mid-pressure pump used was the neMESYS 1000N (Cetoni, Germany). The commercial KD Legato 130 (KD Scientific, USA) and an open-source pump built by Baas and Saggiomo from a standard fused deposition modelling (FDM) 3D printer (Creality Ender3) were the two other stepper motor-based pumps used in that comparison [280]. Luer-lock plastic syringes (1mL: 4.78 mm ID and 5 mL: 12.06 mm ID, Fisherbrand) have been used in all experiments. An inline pressure sensor (LabSmith uPS-series pressure sensor, model: uPS1800-T116-10**) was used to record the pressure fluctuations originating from the syringe pump. All experiments described in this chapter were run in triplicate or otherwise stated.

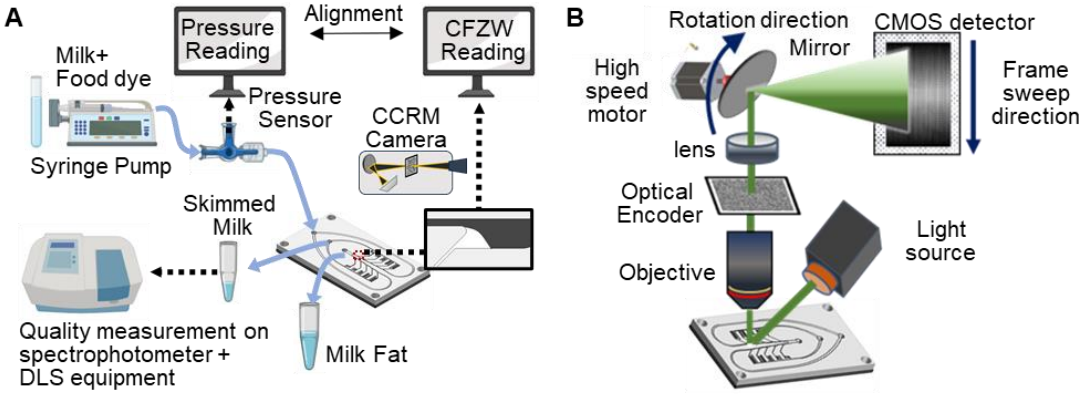

Figure 4.2: Experimental Setup in syringe pump fluctuation study: (A) Microfluidic setup. Samples were injected by a syringe pump. An inline pressure sensor was used to record pressure fluctuations. A high-speed CCRM camera capturing at the rate of 220 frames per second recorded the cell-free zone position for the full run. The pressure sensor data and cell-free zone width data from the video file were aligned manually and compared to establish the relationship between the syringe pump fluctuation induced pressure fluctuation and CFZW. Extracted samples collected from the daughter channel were examined with a spectrophotometer and Dynamic Light Scattering (DLS) equipment to study the effect of fluctuation on separation efficiency. (B) Optical (CCRM) set-up. The sample was illuminated using a halogen lamp where the reflected light was collected using a set of objective and relay lens systems which was then encoded via an optical encoder. The encoded scene was collected via a lens and focused on the rotating mirror. The reflected light from the mirror was continuously swept across a CMOS detector and was collected by the processing unit for applying the reconstruction algorithm.

4.2.4 Optical set-up and image processing

The effects of the fluctuation on the width of the cell-free zone were quantified by using the optical setup. The optical setup of the CCRM camera [70] is shown in Figure 4.2.B.

The high-speed CCRM camera recorded images of the interrogation window (approximately 400 μm × 350 μm, centred on the first bifurcation) at the rate of 210 frames per second (7× faster than the acquisition rate of the pressure sensor). The dynamic scene was first collected by an infinity-corrected microscopic objective and directed towards the lens tube. The 2D image was focused onto an optical encoder. The encoder pattern was printed on a soda-lime glass with a 1:1 ratio between the blocked and transparent pixels. The encoded image was then collected by an ordinary convex lens and focused on the surface of the rotating mirror. The rotation of the mirror was controlled by an off-the-shelf low-cost electric motor [281]. Lastly, the reflected light from the rotating mirror was swept across the surface of the detector (low-cost CMOS module) [281]. The continuous sweeping from the mirror overlapped the individual encoded frames based on their time of arrival hence applying optical compression on the frames. The optically encoded and compressed observed frame from the detector can be reconstructed via an optimisation algorithm that produces a series of individual frames based on the capture rate of the system. Converting these images to grayscale provided the white solid lines for the milk particles and the side walls of the device while the background remained black. Furthermore, because we are solely interested in the mobility of milk fat particles, soft thresholding on images was employed to reduce noise from the casein particles in milk as well as suppressing the imaging noise. Finally, image processing function with the prior knowledge about the scene (detector pixel size, optical magnification factor, physical dimensions of the chip etc) was used to process each individual frame, and an interactive line (Red line, Figure 4.3) was placed 20 μm away from the sidewall using the imdistline function. This function includes a distance tool as well as a text level that shows the distance between line endpoints. The distance of 20 μm was picked at random since, in this case, any distance will suffice because we are computing relative fluctuation value. Amir Matin and Xu Wang (IPAQS, Heriot-Watt University) were in charge of developing the optical setup and processing the recorded footage.

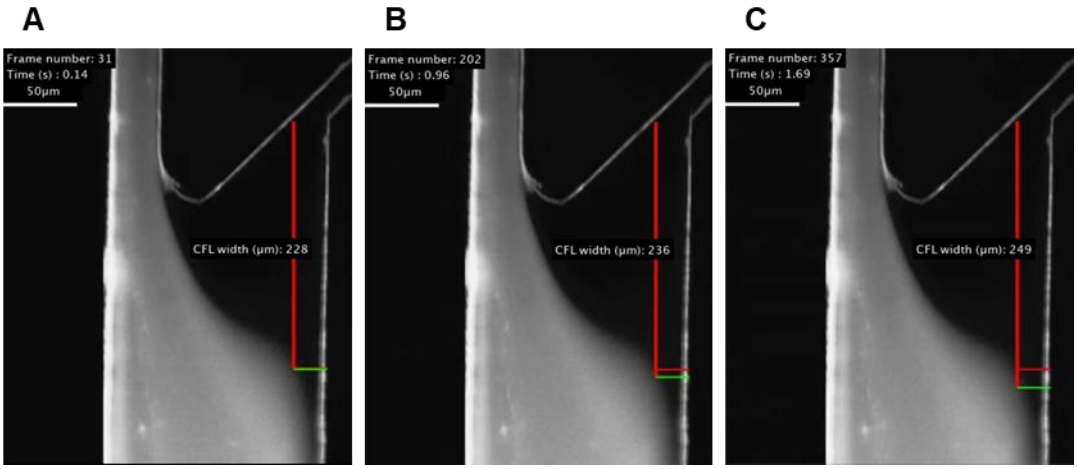

Figure 4.3: Measuring the CFL width or CFZW where (A), (B) and (C) shows three different frames during the measurement using MATLAB.

4.2.5 Sample material

While the chip was designed for BPS, full-fat milk (Tesco Whole Milk (homogenised), 7.4g fat/200 mL) was used in lieu of blood to enable the experiments to be performed in an optical laboratory with a low biosafety level. Milk and blood share useful properties for the purpose of these experiments. Milk fat takes the shape of large fat globules. Like red blood cells, these globules are soft and deformable in a water-based liquid. The composition of milk has been extensively studied. While the average size of the fat droplet is 1.6 – 10 µm in non-homogenised milk, following homogenisation, the size of the fat globules is around 0.2-2 µm, not far from the smallest dimension of red blood cells (RBCs) (2-3 µm in their smallest dimensions). In addition, there are casein micelles (<0.2 µm in size) in the milk as well as various smaller molecules. There are approximately 1.5×10^{10} fat globules present per mL of milk [282]–[284], compared to $4\text{-}6\times10^{9}$ red blood cells in plasma. However, milk fat globules and red blood cells significantly differ in density. The density of RBCs is 1.11 g/mL and higher than their surrounding plasma (1.025 g/mL) [285], while milk fat density is 0.9 g/mL and less dense than its surrounding liquid (1.029 g/mL) [286]. Despite their density differences, it is possible to observe milk fat separation in devices designed for BPS from cells. Due to the higher shear rate, a CFL is enhanced at the constriction walls. At the expansion-bifurcation, milk fat globules maintain their initial spatial distribution: the fat particles remain on their streamlines and flow into the channel with a higher flow rate. The water-based fat-poor fluid formed at the expansion of the channel can be harvested through the daughter channel. To observe the behaviour of different dilution samples during experiments, whole milk samples were

diluted with Phosphate-buffered saline (PBS, pH= 7 to 7.6, Fisher Scientific) to maintain physiological conditions.

4.2.6 Computational Flow Dynamic (CFD) study

To plot the fluid streamlines, the full device (August 15 C1) was simulated using the finite element analysis from COMSOL Multiphysics software (v5.3). The 3D separation model designed by AutoCAD (2019 edition) was imported as the device geometry in COMSOL. Water was used as the fluid material, but the density and viscosity were changed to 1033 kg/m3 and 2 cP, respectively, to match milk parameters. To save the computational time fine meshing was preferred throughout the whole device which resulted in a total of 525628 domain elements, 142918 boundary elements, and 20355 edge elements. To better comprehend the laminar flow regime, a stationary solver was used to simulate laminar flow physics with two outputs and one pressure-driven inlet. To simulate the average pressure of different samples used in section 4.3.3, the viscosity and density of material water has been replaced by the calculated one from specific samples (e.g., glycerol, milk etc.) and 10 mL/h has been used as the inlet flow rate. After computing, the average pressure throughout the device has been calculated from the pressure field. Finally, to simulate the streamlines in section 4.3.4, the minimum, average and maximum pressure fluctuation value from the experiment was used as the inlet pressure. A no-slip boundary condition was applied to all sidewalls. After computing, flow streamlines were plotted from specific locations from the internal constriction wall to infer expected particle locations. To accomplish so, the co-ordinates of the constriction edge were first determined using the measure function from the geometry tab. A streamline plot has been constructed from the velocity 3D plot group. The streamline positioning and entry method have been set as start point controlled and co-ordinates, respectively, in the streamline plot. The x-coordinates of the previously measured constriction edge were maintained the same, but the y and z coordinates were varied (y: 1.5, 2.5, and 3.5 μm away from the edge, z: 10 and 6).

4.2.7 Characterisation of hydrodynamic separation performance via spectrophotometry

The effect of syringe pump pressure fluctuations on the separation efficiency has been characterized using spectrophotometry. A spectrophotometer (Jenway 7315) was used to measure absorbance from 198 to 1000 nm wavelengths. The limit of the equipment photometric absorbance is -0.300 to 2.500. To be able to measure in this range, collected

milk samples were diluted to 1:250 in PBS before measurement in microcuvette (centre H 15 mm, Brand Gmbh + Co KG) cuvettes. In the ultraviolet (UV) spectrum, milk fat was previously reported to absorb strongly at 220 nm [287], [288] whereas in the near-infrared (NIR) spectrum, milk fat was previously reported to provide a peak at 968 nm [289]. However, absorbance values at 968 nm are very small compared to the 220 nm value because the water content present in milk interferes in this region and strongly absorbs the IR light [290]. Absorbance peaks at both 220 nm and 968 nm were measured from the sample collected from the inlet and both outlet samples after 1:250 dilution with PBS solution.

4.2.8 Dynamic Light Scattering

The size distribution of the particles presents in all the collected samples from the inlet and both outlets at different flow rates were determined using Dynamic Light Scattering (DLS) (Nanozetasizer, Malvern). All the collected samples were diluted to 1:250 in PBS before the measurements and the analysis was performed at 20 °C.

4.2.9 Statistical analysis

Statistical significance was determined by unpaired parametric Student t-test. Unless specified, the p-value significance threshold was set at 0.05. When reporting on statistical significance symbols ‘n.s’ is used to indicate non-significance ($p>0.05$), while *, **, *** denotes $p<0.05$, $p<0.01$, $p<0.001$ as per conventional practice.

4.3 Results

4.3.1 Comparison between of theoretical and measured syringe pump pressure fluctuation frequencies

The goal of this first experiment was to verify the previously established relationship between the measured frequency of the pressure fluctuation and the inherent mechanical frequency of the screw-driven syringe pump. The mechanical frequency can be calculated from the following equation, established by [291]:

$$f_m = \frac{4Q}{\pi D^2 S} \qquad (4.1)$$

Where Q represents the volumetric fluid flow rate, D is the internal diameter of the syringe which depends on the model and S is the pitch of the screw in the syringe pump. Different milk samples (10-50%) were flowed into the device at various flow rates, while the pressure sensor recorded the pressure fluctuations. The frequency of pressure

fluctuations was extracted from the experimental data and compared to the theoretical data calculated from Equation (4.1).

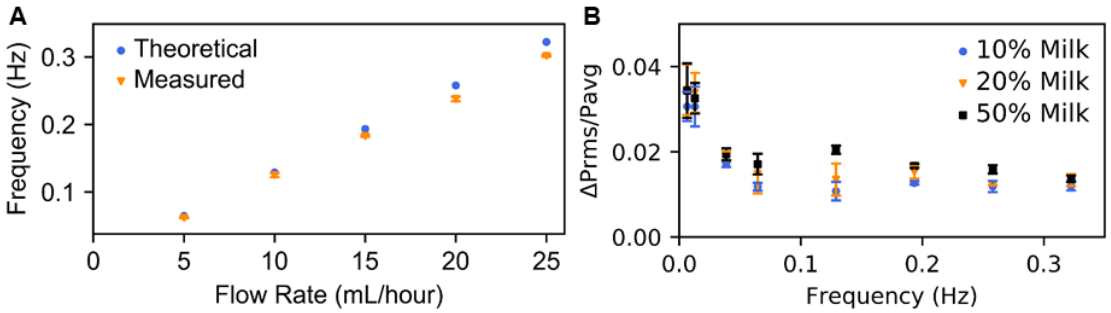

Figure 4.4: Pressure fluctuation data on various milk samples (A) Comparison between theoretical and measured frequency of syringe pump fluctuations in the function of flow rate. The measured frequency was obtained from the pressure sensor measurement while using a syringe with an Internal Diameter of 4.78 mm (50% milk sample, N=3). The error on the measured frequency is close to the point size. The theoretical syringe pump frequency is based on Equation (4.1) for a 1mL syringe, and the pitch of the screw in the syringe pump is 1.27 mm. There is no error on the theoretical value of the syringe pump fluctuation frequency (B) Relative fluctuation at various flow rates for 10, 20 and 50% milk samples. Up to 0.06 Hz, the linear decay of the relative fluctuation with the frequency corroborates other studies [266]***. However, from 0.06 Hz (corresponding to 5mL/h) it has been uncovered that the relative fluctuation reaches a plateau corresponding to a fluctuation with an amplitude of around 2% of the average pressure.***

Figure 4.4.A shows the theoretical and measured frequencies plotted against flow rates ranging from 5 to 25 mL/h. The correlation between the theoretical and measured frequencies is high (R^2=0.99). The deviation was more pronounced at a higher flow rate. The difference between theoretical and measured frequencies was found to be in the range of 4 to 8%, which is consistent with previous findings [266]. The relative amplitude of pressure fluctuations was plotted against the pump theoretical frequency (Figure 4.4.B). Here, P_{avg} is defined as the average pressure drop and ΔP_{rms} as the root mean square (RMS) value of pressure drop fluctuations. Similar to a previous study, from 0.5mL/h to 5mL/h, the relative fluctuations with this set-up were higher at low flow rates and decreased with an increment in flow rate [266]. However, in previous studies, the highest reported flow rate was 5 mL/h. Higher flow rates are desirable in microfluidic separation devices, as they lead to higher throughput. Thus, the effects of syringe pump fluctuations were investigated at higher inlet flow rates, ranging from 0.5-25 mL/h. The relative fluctuation maintains a plateau with an amplitude of about 2% of the average pressure at

flow rates >5mL/h (corresponding frequency 0.06 Hz), contrary to previously reported behaviour at lower flow rates.

Four different microfluidic devices were evaluated by flowing DI water at various flow rates to explore how this 2% relative fluctuation plateau changes with different microfluidic settings. Figure 4.5 compares the relative fluctuations of these devices, and it is worth noting that relative fluctuations maintain a plateau, approximately 2% of the average pressure fluctuations, starting at 0.06 Hz frequency (matching flow rate 5 mL/h) for all of the devices. One of the devices examined consisted of a straight microchannel with no sophisticated structure and exhibited the same relative fluctuation characteristics as the other BPS devices. In a broad sense, any type of microfluidic device with any channel geometry and sample at a higher frequency will have constant relative fluctuations. The relationship between this syringe pump induced pressure fluctuations and CFZW fluctuations at the expansion-bifurcation is investigated experimentally in the following section.

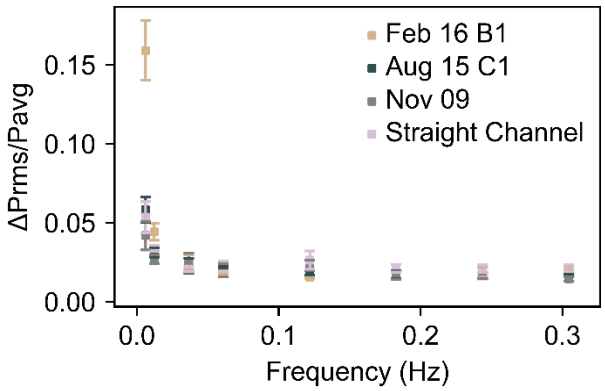

Figure 4.5: Using DI water, the relative pressure fluctuation of four different microfluidic devices at different flow rates. Regardless of the channel geometry, all devices retain a 2% plateau.

4.3.2 Relation between mechanical pressure fluctuations and cell-free zone width fluctuations

In the previous section, it has been demonstrated that the relative pressure fluctuation reaches a plateau, equal to 2% of the average pressure from 0.06 Hz (5mL/h). It is first necessary to relate the pressure fluctuations to CFZW fluctuations in order to understand how these fluctuations affect a hydrodynamic separation device since the CFZW dictates the location of the separation between cell or particle-free liquid and cell or particle-laden liquid, and thus the separation performance. An analysis of the relationship between cell-free zone fluctuations and pressure fluctuations in milk samples is presented in this section. Milk samples were flowed through the hydrodynamic separation device at 5, 10,

15, 20 and 25 mL/h and dilution of 10, 20 and 50% with PBS. The pressure and cell-free zone fluctuation were recorded respectively, via the inline pressure sensor and CCRM camera, as presented in the Materials and Methods section. Figure 4.6.A shows CCRM-acquired images of the first bifurcation for 15, 20 and 25 mL/h flow rates at 50% milk dilution. The measured average CFZW is indicated for each nominal flow rate.

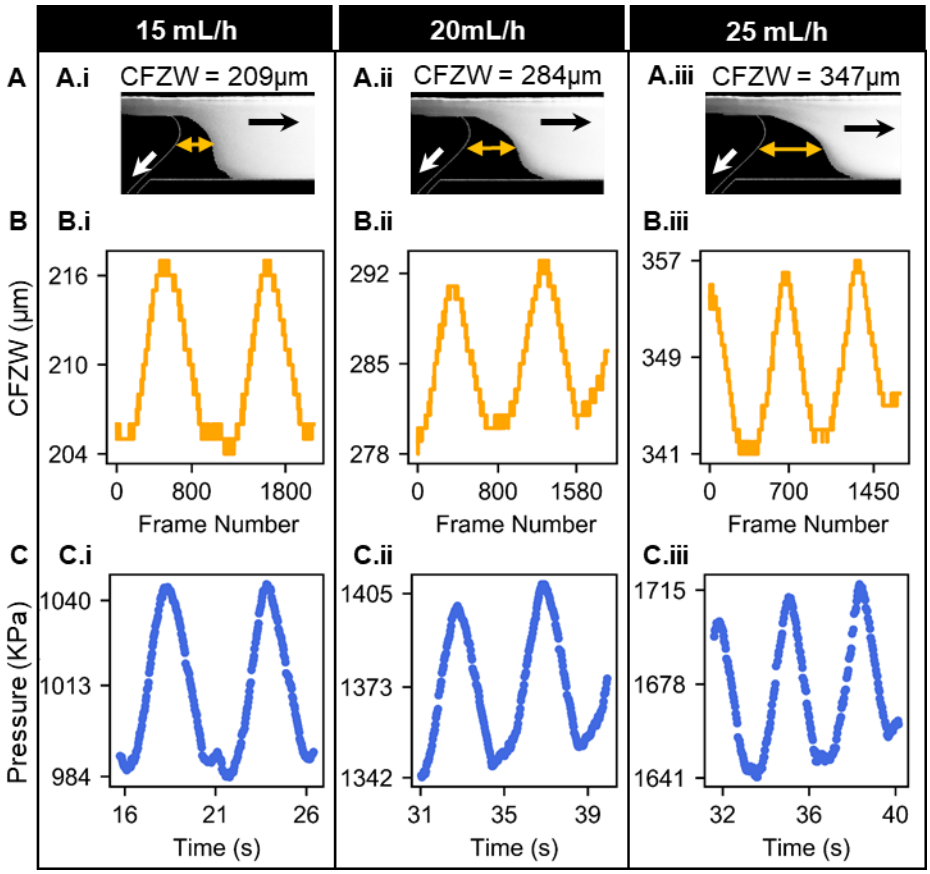

Figure 4.6: Relationship between CFZW fluctuation and pressure fluctuation (A) Photographs of the cell-free zone acquired by the CCRM set-up at 50% milk dilution and 15, 20 and 25mL/h. The yellow arrow indicates the position from which the width of the cell-free zone (CFZW) is acquired. The average of the CCRM-measured CFZW is indicated for each flow rate. (B) Raw data for CFZW (CCRM acquisition) and (C) Pressure fluctuations (LabSmith pressure sensor, c.f. method section) for 50% milk sample at 15, 20 and 25 mL/h flow rate. The pressure sensor provides 30 samples per second whereas the CCRM camera is able to capture 210 frames per second.

The measurement data of CFZW fluctuations for 50% milk at the first bifurcation are shown in Figure 4.6.B, while the pressure fluctuations are right at the bottom of each CFZW fluctuation data (Figure 4.6.C). The CFZW fluctuations were manually aligned to the pressure fluctuations since the image acquisition and the pressure acquisition could not be automatically synchronised. On these images, it can be observed that the CFZW fluctuations reproduce the pressure fluctuations. The full dataset of CFZW and pressure

fluctuation measurement for 50%, 20% and 10% milk can be found in appendix A, where the data corroborate with the discussed findings from 50% milk sample data.

As the pressure fluctuations increased in frequency and amplitude at higher flow rates, it has been observed that CFZW fluctuations also increased in frequency and amplitude. To investigate the correlation between the two sets of data, the measured frequencies of the pressure fluctuations were first plotted against the measured frequencies of the cell-free zone fluctuations. Figure 4.7.A shows a large correlation (R^2=0.994) and agreement between the frequencies of the CFZW and pressure fluctuations. It was also investigated if the pressure and cell-free zone fluctuations had any amplitude correlation. Figure 4.7.B illustrates that cell-free zone amplitude is linearly related to the pressure fluctuation amplitude (R^2=0.977).

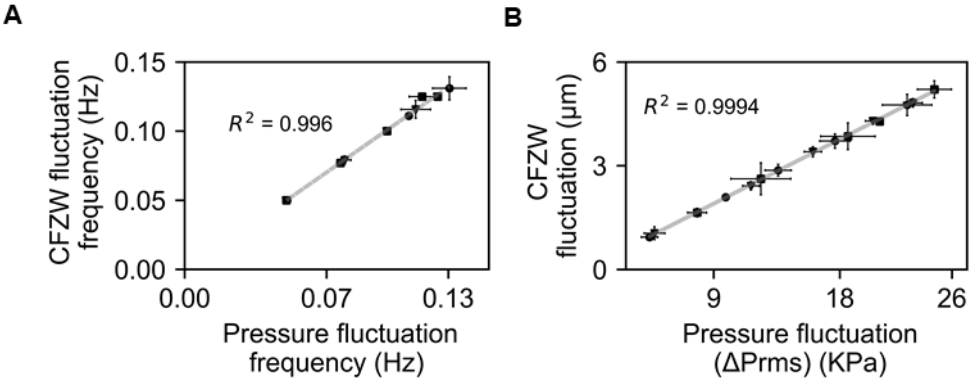

Figure 4.7: Relationship between CFZW and pressure fluctuation frequency and amplitude (A) Plot of frequency of pressure fluctuations versus frequency of cell-free zone fluctuations for 10% (●), 20% (▲), and 50% (■) milk dilution (B) Plot of the amplitude of pressure fluctuations versus amplitude of cell-free zone fluctuations for 10% (●), 20% (▲), and 50% (■) milk dilution (acquired in triplicate).

4.3.3 Effect of overall sample kinematic viscosity on pressure fluctuations

The amplitude of pressure fluctuations was linked to the amplitude of CFZW fluctuations in the preceding section. The pressure gradient inside a microchannel is directly proportional to the viscosity which varies from one sample fluid to another [226]. As a result, higher viscosity samples are expected to flow through the microfluidic network with a higher-pressure gradient. This will result in higher cell-free zone fluctuation which could further degrade the separation efficiency. The effect of pressure fluctuations on samples of various densities and viscosity has been examined in this regard. Since it was impossible to control both viscosity and density independently, these results are reported for kinematic viscosity (ratio of dynamic viscosity over density). The milk-PBS mixture is considered a binary mixture so that mixing the components does not produce any

volume change. The density of the mixture is calculated by dividing the total mass by the volume where the initial density of milk and PBS are taken as 1.033 kg/l and 1 kg/l, respectively. Finally using the viscosity of the mixtures are calculated using Arrhenius equation (for binary mixture),

$$\ln \mu_{12} = x_1 \ln \mu_1 + x_2 \ln \mu_2 \quad (4.2)$$

Here, x_1 and x_2 are the volume fraction of milk and PBS and $\mu_1$and μ_2 are the viscosity (dynamic) of the initial milk and PBS sample (2 and 1 cP). Whereas, the viscosity and density of the complex glycerol-water solution are calculated from an online calculator based on the viscosity and density of the glycerol water mixture model from [292], [293]. The calculated values of densities, dynamic and kinematic viscosities can be found in Table 4.1.

Table 4.1: Calculated densities, dynamic and kinematic viscosity for different mixtures

Samples	Density (g/cm^3)	Dynamic viscosity (cP)	Kinematic viscosity (cSt)
Water	0.997	1	0.997
Milk 50%	1.015	1.414213562	1.415062
Milk 20%	1.0042	1.1487	1.153525
Milk 10%	1.0006	1.0718	1.087877
Glycerol 6.67%	1.017585669	1.2383	1.260076
Glycerol 20%	1.056975506	1.985	2.098096
Glycerol 33.3%	1.095588698	3.482	3.81484

In a first instance, pressure fluctuations recordings were measured for three milk dilution samples (10, 20 and 50%) in the 5-25 mL/h range with a 5 mL/h increment. It was observed the absolute pressure fluctuations for 50% milk was occasionally marginally superior to that of 20% and 10% milk (Figure 4.8.A) because of its higher kinematic viscosity. It is noticeable from Figure 4.8.B that the CFZW fluctuations also match with the pressure fluctuation because of the correlation between the pressure and CFZW fluctuation proved in the previous section. As the kinematic viscosity of these three samples were very close to each other, it was difficult to determine clear trends. Therefore, the same experiment was performed with an additional four samples, three diluted glycerol samples (6.67, 20, 33.3%) and water at 5 and 10 mL/h. The variations of pressure at 10 mL/h and 5 mL/h were found to increase logarithmically with kinematic viscosity (Figure 4.8.C and E). Although the reason is unknown, I assume that the

particles present in samples might be a reason for this. This can be explained from the relative fluctuation of the samples.

Relative fluctuation for the sample samples can be seen increased to 2% of the average pressure for the milk samples Figure 4.8. D and F. However, when working with water or glycerol samples, a smaller value has been measured. From this I assume that the particles present in milk samples might influence the syringe pump fluctuation inside microfluidic channel. However, this needs to be clarified by further investigation.

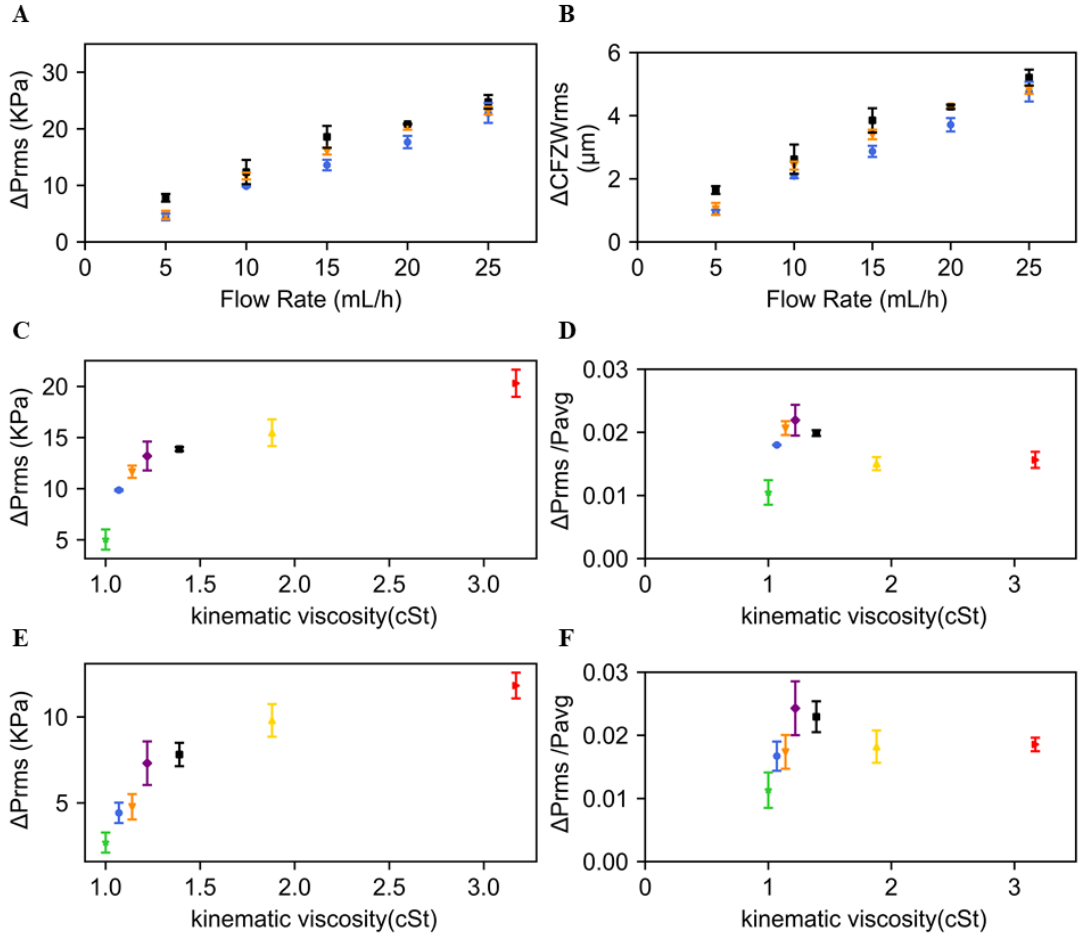

Figure 4.8: Effect of overall sample kinematic viscosity on pressure fluctuations (A) Pressure fluctuations at various flow rates and milk dilutions (B) CFZW fluctuations at various flow rates and milk dilution. (C) Pressure fluctuation for samples having different kinematic viscosities at 10 mL/hour (D) Relative pressure fluctuations for samples having different kinematic viscosities at 10 mL/hour. (E) Pressure fluctuation for samples having different kinematic viscosities at 5 mL/hour (F) Relative pressure fluctuations for samples having different kinematic viscosities at 5 mL/hour. Samples: ★water; ● 10% milk; ▼20% milk; ■50% milk; ◆6.67% glycerol; ▲ 20% glycerol; ► 33.33% glycerol.

Simulation using the compressible fluid module was carried out using the calculated viscosity and density. It can be seen that when pressure fluctuation amplitude is calculated using relative fluctuation measured from the experiment, the simulated pressure

fluctuation followed the similar trend like the experimental value with a high R^2 value (Figure 4.9. A and B). When taken independently, the milk samples provided very good linearity and high correlation and good agreement between the simulated and measured results (R^2=0.995) (Figure 4.9.C).

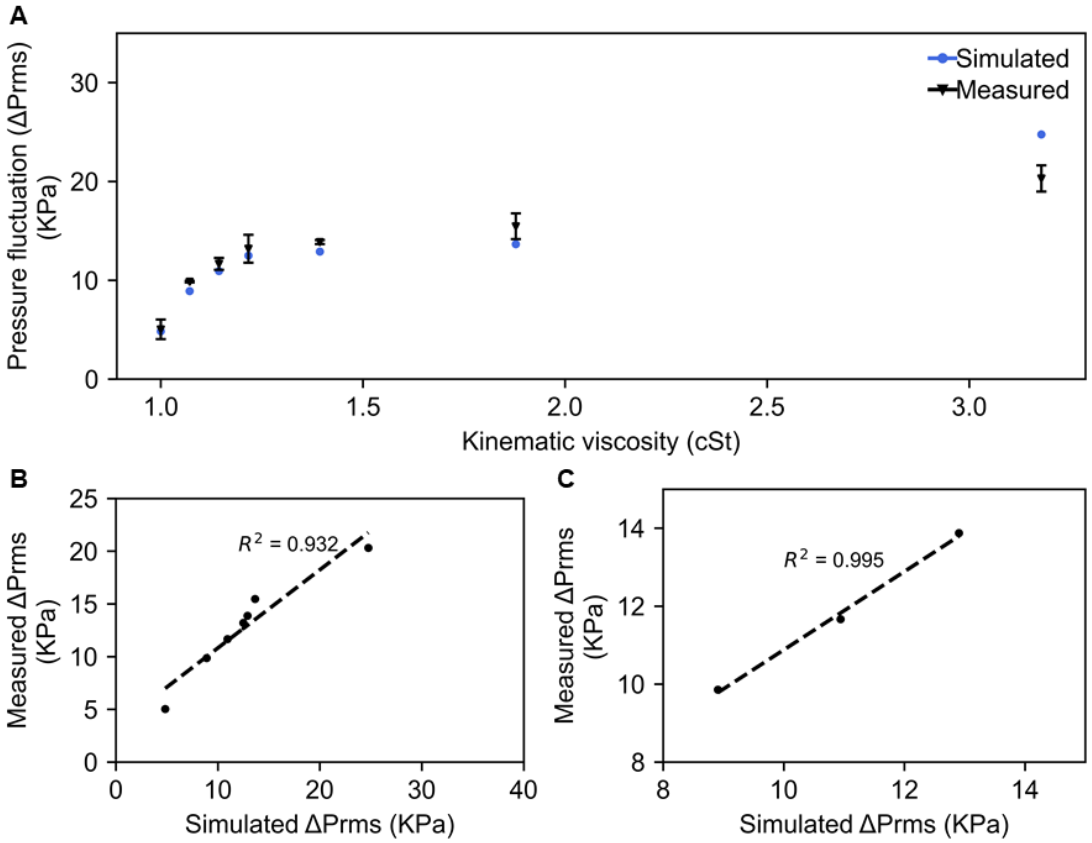

Figure 4.9: Simulated vs measured pressure fluctuations on samples with different kinematic viscosity (A) Pressure fluctuations vs kinematic viscosity for measured and simulated data. A good agreement exists between the measured and simulated milk samples exists, but deviations for the water sample and glycerol was observed. (B) Correlation between simulated and measured fluctuations (all samples) (C) Correlation between simulated and measured fluctuations (milk)

4.3.4 Effect of syringe-pump pressure fluctuations on hydrodynamic separation performance

It has been established in previous sections that the pressure fluctuations of the syringe pump introduce fluctuations in the CFZW, and both are linearly related in frequency and amplitude. In a hydrodynamic device, the fluctuations of the CFZW at the bifurcation might become large enough to drive particles in the cell-free outlet and hence reduce the separation efficiency of the device. Two different scenarios are possible: (i) The CFZW is very large and situated away from the daughter channel collecting particle-poor or particle-free fluid. In this case fluctuations in the CFZW are unlikely to lead to any

particles travelling to the skimmed milk outlet. The separation efficiency will remain unaffected by the pressure fluctuations (ii) The CFZW is relatively small and situated closely to the daughter channel. In this case, pressure fluctuations are most likely to affect the particle's path, deviating them from their original position leading to the particle-poor channel. Both of these theoretical situations are illustrated in Figure 4.10.A.

To analyse these scenarios, three distinct flow rates were identified: a lower flow rate (10 mL/h), to investigate the first scenario and two higher ones (20 and 30 mL/h) to investigate the second scenario. In addition, CFD simulation was run for the three flow rates.

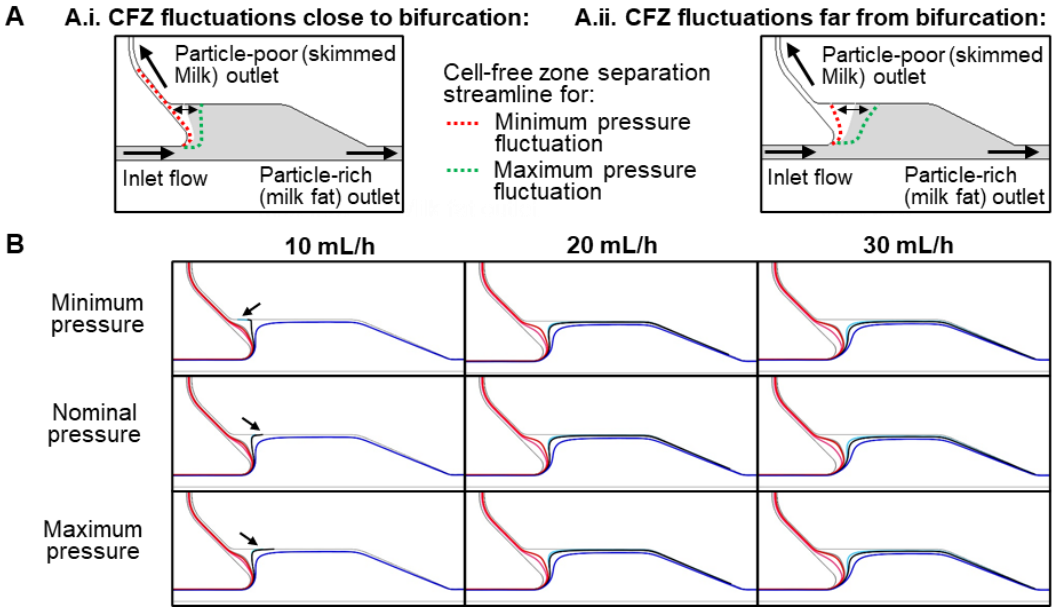

Figure 4.10: COMSOL simulation results to determine the effect of pressure fluctuation (A) Schematic explaining the effect of cell-free zone variation on separation efficiency (i) When the cell-free zone resides very close to the skimmed milk outlet at lower flow rates, fat particles have chances to travel to the skimmed milk outlet at minimum pressure fluctuation amplitude and degrade the separation efficiency (ii) When the cell-free zone resides far away from the skimmed milk outlet, fat particles mainly travel to the milk fat outlet even though the fluctuation is higher at higher flow rates (B) computed streamline which are: --- 1.5 µm, --- 2.5 µm and --- 3.5 µm far from the constriction upper boundary are presented for 10,20 and 30 mL/h. The dark coloured streamlines are simulated from the channel centre (Z=10 µm, 20 µm total depth) and light-coloured ones are 4 µm bottom from the channel centre (Z=6 µm) At 10 mL/h, particles which are present at the midplane (Z=10) and 2.5 µm far away from the constriction upper boundary have the tendency to travel to the skimmed milk outlet when the pressure fluctuation amplitude is minimum. For a different depth (Z=6), this distance can go up to 3.5 µm. Whereas for 20 and 30 mL/h, fat particles reside at least around 2 µm (For Z=10) and 3 µm (For Z=6) far away from the upper boundary have no chance to travel to the skimmed milk outlet.

For the mid-plane scenario (z =10), the CFD simulations in Figure 4.10.B. showed that for any flow rates (10, 20, 30 mL/h), all particles situated 1.5 μm from the edge of the constriction will travel into the particle-free daughter channel (red traces). Whereas, particles situated from and beyond 2.5 μm (black trace) will travel to the particle-rich outlet except for the minimum pressure scenario for 10 mL/h when a "switching" event (indicated by an arrow on Figure 4.10.B) was observed. At this minimum pressure fluctuation for 10 mL/h, the streamlines starting 2.5 um from the wall, switch from the particle–rich channel to the particle-poor channel. A similar switching event at 10 mL/h (minimum pressure fluctuation) was observed when the streamlines were computed 4 μm away from the z-mid-plane and 3.5 μm away from the constriction sidewall. For this z plane, all the particles reside within this 3.5 μm distance follows the particle-poor channel, no matter what the flow rate is.

Before explaining the experimental result, it is worth noting again that the device used in this experiment was designed to separate blood plasma and does not have 100% separation efficiency for milk fat. Therefore, some fat particles will end up at the skimmed milk outlet without any fluctuation effect. The lowest amount of fat that could travel through the skimmed milk outlet will be at higher flow rates (e.g., 20 mL/h) which might be because of the remaining smallest fat particles (0.2-0.5 μm) within the CFL as confirmed and explained in the simulation result in the previous paragraph. To further verify the effect of pressure fluctuations on the separation performance, milk (50%) was flowed into the device at 10, 20 and 30mL/h. Absorbance measurements were acquired at 220 and 968 nm to characterise the presence of fat particles in particle-poor (skimmed milk) microfluidic extract and particle-rich (fat) microfluidic extract. All the absorbance measurements were acquired in triplicates on samples collected from extractions in three unique and previously unused, but identical, devices. For these experiments, the cell-free zone was imaged under a microscope (Dinolite, Premier AM7013MZT) (Figure 4.11.A) and the absorbance spectrophotometry was used to characterise the separation performance on the inlet (feed) solution. Both the absorbance spectrum from 190nm-1000nm for particle-poor and particle-rich outlets are shown in Figure 4.11. B and C. A higher 200 nm absorbance peak can be noticed at 10 mL/h for particle-poor skimmed milk outlet as a result of a large number of fat particles travelling to that outlet. A complete opposite trend was observed for the milk fat outlet because most of the fat particles travelled to the milk outlet at 20 and 30 mL/h. However, the trend at 968 nm is difficult to notice because of its lower value compared to 220 nm absorbance, as discussed earlier.

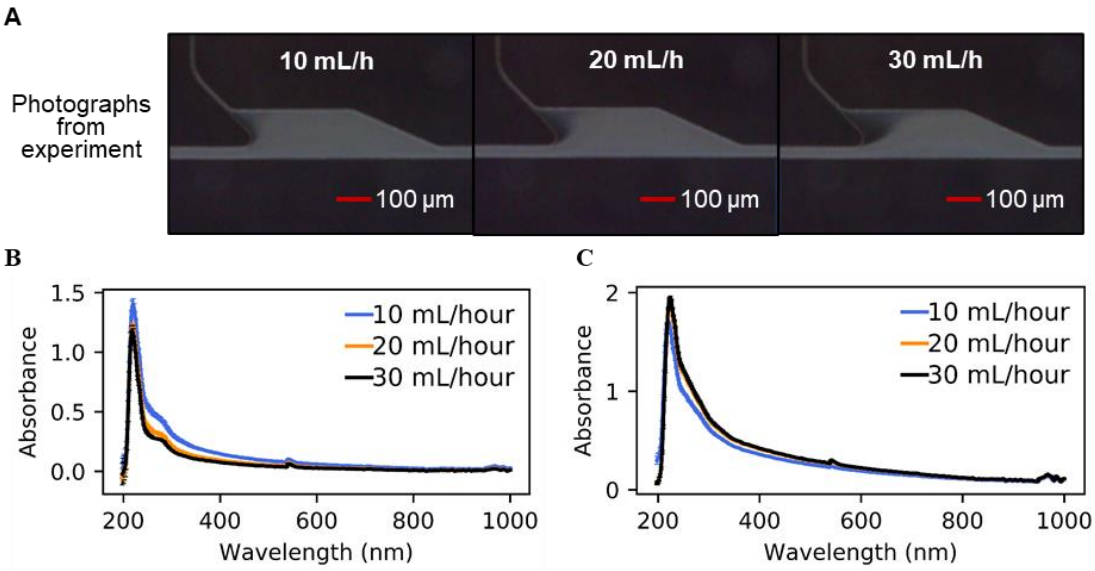

Figure 4.11: Spectrophotometry results for different milk samples (A) Photographs of the cell-free zone at 10,20 and 30 mL/h; (B) Absorbance spectrum of skimmed milk outlet sample after 1:250 dilution with PBS in range (190nm-1000nm) at different flow rates. It can be visible that at 220 nm, the sample collected from the low flow rate (10 mL/hour) provides a higher absorbance value compared to the other two (which are almost similar) due to the presence of a large number of fat particles. CFZW fluctuation is one of the major factors behind this fat particle movement to the skimmed milk outlet. Absorbance peak at 968 nm is very small compared to the 220 nm peak, therefore, is not visible here; (C) Absorbance spectrum of Milkfat outlet sample after 1:250 dilution with PBS in range (190nm-1000nm) at different flow rates. At higher flow rates (20 and 30 mL/hour) most of the fat particles travelled to the milk outlet hence showing a higher absorbance peak at 220 nm. 968 nm peak can be visible but difficult to quantify from the figure because of the large difference between the absorbance peak values.

To observe the trend clearly, the absorbance values at 220 nm and 968 nm are shown in Figure 4.12.A and B, respectively, for the inlet, and particle-poor (skimmed milk) and particle-rich (fat) outlets at various flow rates. The absorbance of separated centrifuged skimmed milk (at 16,000×g for 10 minutes) is also added as a control. In these experiments, the particle-poor, skimmed milk outlet sample absorbance for 10 mL/h was superior compared to the ones from 20 and 30 mL/h (respectively p= 0.0056, and p=0.024). This can be further understood by Figure 4.12.C and D from where it can be inferred that when the CFZW is increased to a certain point, there is no more influence of flow fluctuation on the separation efficiency, thus the absorbance values of the skimmed milk outlet achieve a plateau. A complete opposite relationship can be observed for milk fat outlet. Finally, the inlet and the extracted particle-poor samples were analysed by DLS. The DLS results (Figure 4.12.C) showed a relatively larger portion of the milk fat

globules (1-7 µm) in the 10 mL/h separations, which confirmed the spectrophotometric measurements.

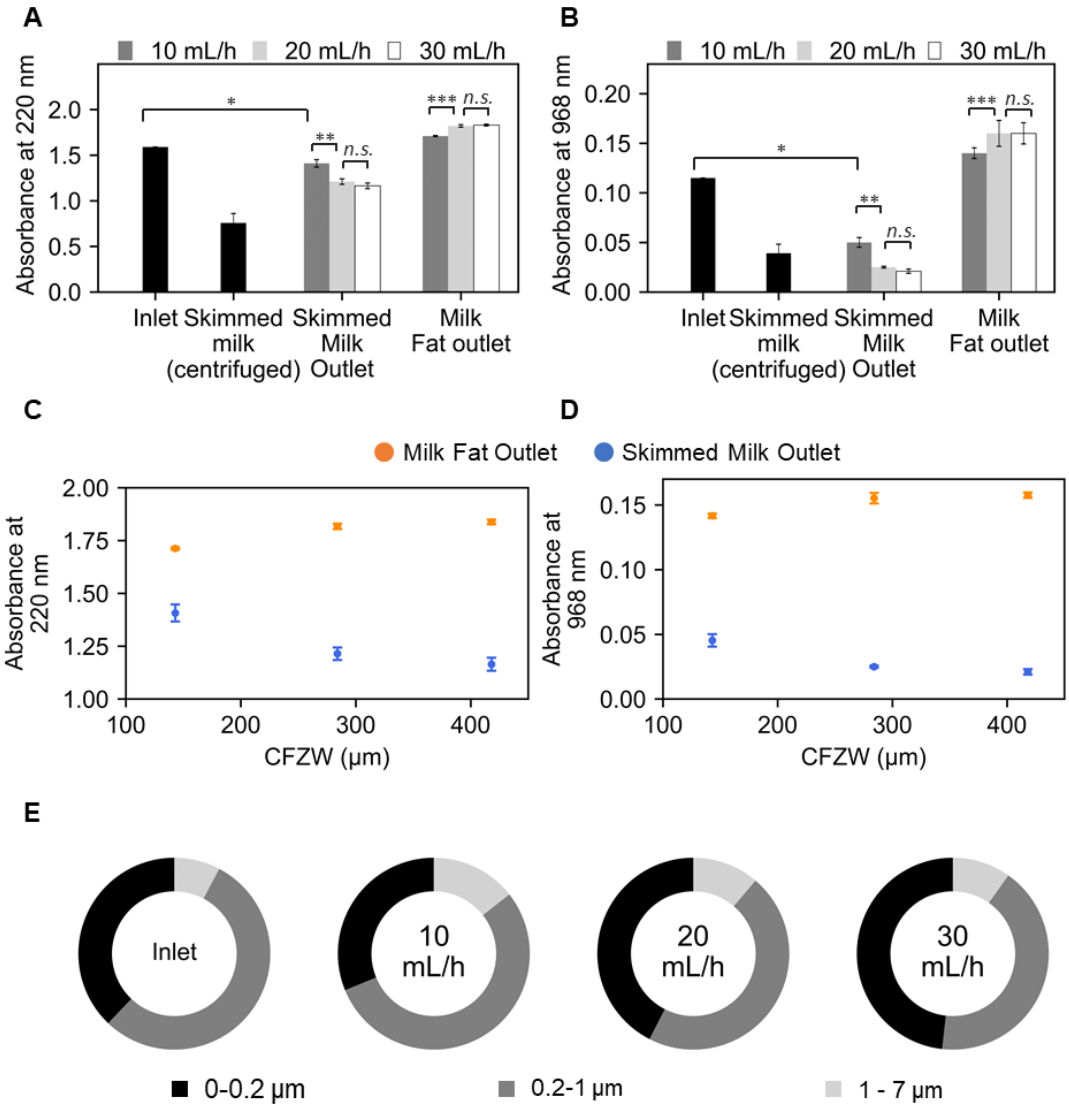

Figure 4.12: Detailed spectrophotometry and DLS results for different milk samples (A) Absorbance values for the sample collected from Inlet, skimmed milk (centrifuged at 16,000g for 10 minutes), skimmed milk outlet and milk fat outlet at 220 nm; (B) Absorbance values for the sample collected from Inlet, skimmed milk (centrifuged at 16,000g for 10 minutes), skimmed milk outlet and milk fat outlet at 968 nm; (C) CFZW vs the absorbance values for the skimmed milk outlet and milk fat outlet at 220 nm; (D) CFZW vs the absorbance values for the skimmed milk outlet and milk fat outlet at 968 nm; (E) Dynamic Light Scattering (DLS) data from the skimmed milk outlets show that the milk fat fraction (1-7 µm) is increased in the 10m/h experiments. However, due to the DLS data variability, statistical significance was not fully achieved.

4.3.5 Comparison between different syringe pumps

The results of earlier sections were obtained with Aladdin syringe pumps, demonstrating how syringe pump fluctuation influences the separation efficiency of a microfluidic BPS. There are a variety of commercial and open-source syringe pumps available, and it would be interesting to compare their performance in microfluidic settings, particularly in terms of fluctuations and their amplitudes. In this section, the fluid delivery performance of three commercial syringe pumps (neMESYS, KD Legato, and Aladdin) and one open-source syringe pump (Ender) have been compared. Figure 4.13 illustrates all of the pumps that were compared.

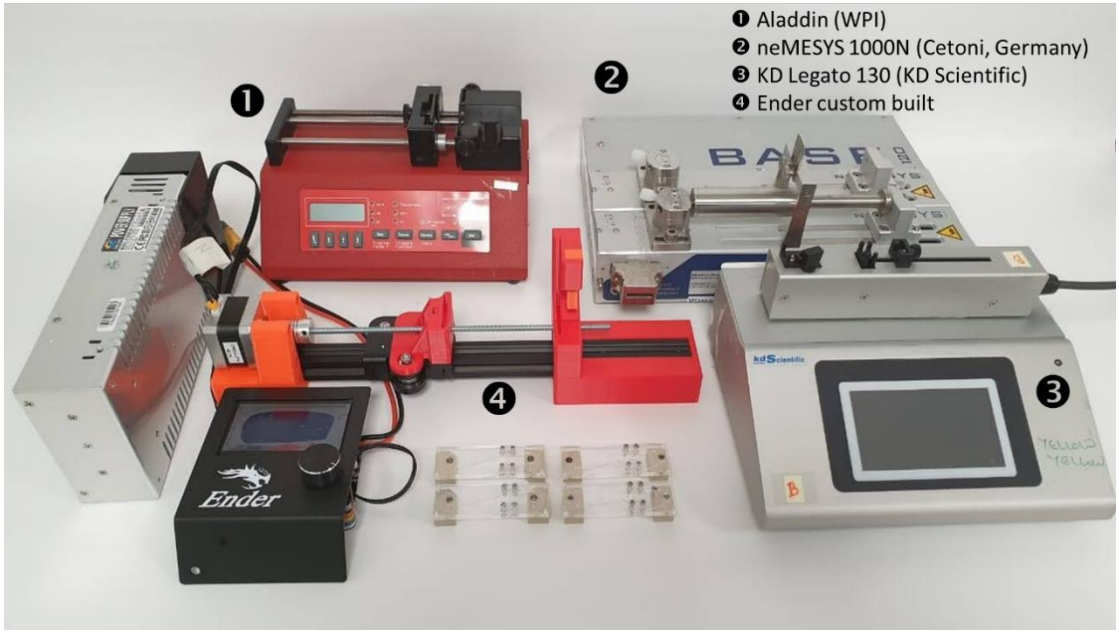

Figure 4.13: Photograph of the different syringe pumps used to compare the flow rate fluctuation. Except for the neMESYS 1000N pump, which is pulseless, all the other pumps are stepper motor-driven pumps.

When operated by a syringe pump, smaller diameter syringes should provide higher mechanical oscillation, according to Equation 4.1. The performance of three stepper motor-driven syringe pumps was investigated to observe the pressure fluctuation caused by this mechanical frequency. Figure 4.14. A depicts the relative fluctuation of different syringe pumps at 0.5 to 25 mL/h flow rates. Similar to the Aladdin syringe pump, the KD and Ender syringe pumps provide larger fluctuation at low flow rates and maintain a plateau with their lowest relative fluctuation amplitude at high flow rates (from 5 mL/h). The KD pump's plateau magnitude is roughly 0.2%, which is significantly less than the Aladdin and Ender pumps' relative fluctuation plateau magnitudes of 2% and 2.5%, respectively.

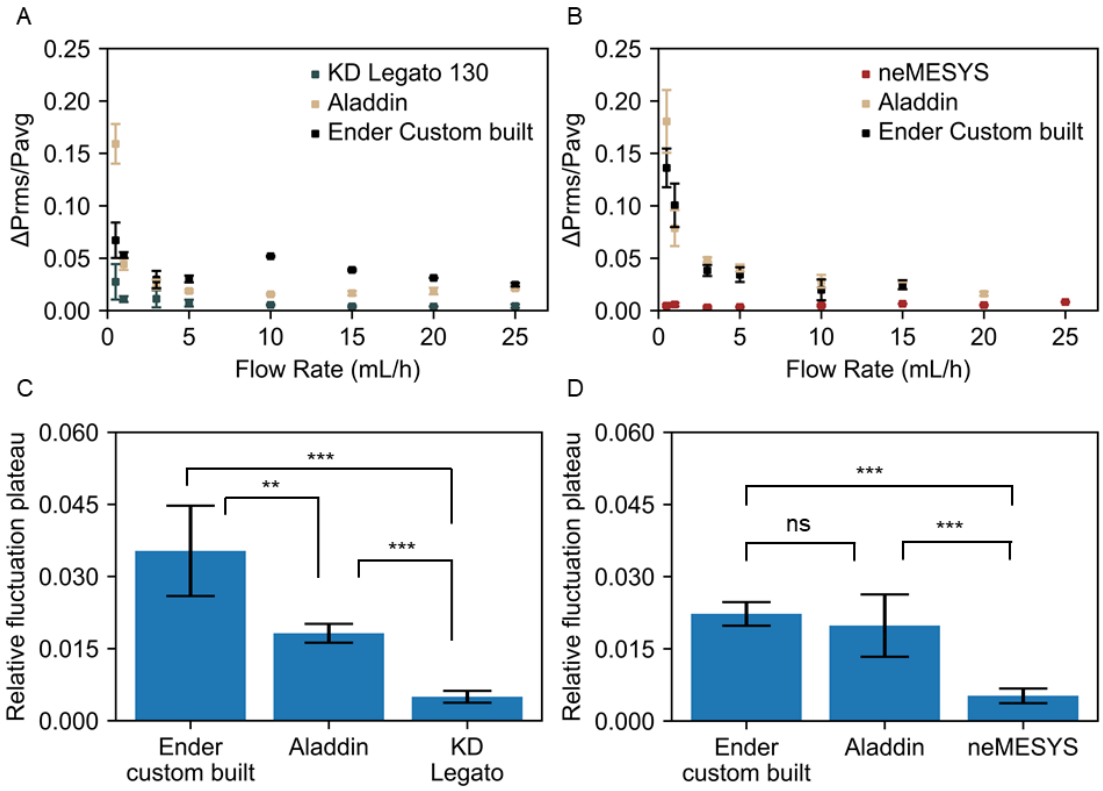

Figure 4.14: Characterization with different syringe pumps using Feb 16 B1 BPS device (A) Relative fluctuation of three stepper motor-based syringe pump at different flow rates using 1 mL syringe showing the KD pump which can take 3200 micro-steps per revolution provides much lower relative fluctuation compared to the Aladdin (400 micro steps) and Ender (200 micro steps) pump (B)Relative fluctuation comparison between pulseless neMESYS syringe pump and stepper motor based Aladdin and Ender pump using 5 mL syringe at different flow rates showing superior performance of neMESYS pump than the other two (C) Magnitude of relative fluctuation plateau for different pumps using 1 mL syringe confirms significant difference in performance between them (D) Magnitude of relative fluctuation plateau for different pumps using 5 mL syringe. The pulseless neMESYS pump maintains a plateau throughout the operation.

The pulseless syringe pump neMESYS performed the best with a 5 mL syringe, keeping the relative fluctuation amplitude within 0.1-0.7% throughout the operation (Figure 4.14.B). In the case of Aladdin and Ender pumps, on the other hand, the relative fluctuation was higher at low flow rates, and at higher flow rates, it attempted to reach the plateau at 2% of the average pressure for both of them, which has been already observed. Figure 4.14.C (for 1 mL syringe) and Figure 4.14.D (for 5 mL syringe) present a clear comparison of the plateau magnitude of different pumps.

4.4 Discussion

Unlike the previous studies, this study was conducted from low to very high flow rate (2-25 mL/h) and informed that at higher flow rates (>5 mL/h) the relative pressure fluctuation comes to a plateau magnitude of 2% of the average pressure with commercial Aladdin syringe pump. According to this, pressure fluctuations in the 50% milk sample using the August 15 C1 device can exceed ±40 KPa at 30mL/h. Previous studies have shown CFZW at an expansion-bifurcation to increase with the shear rate and the pressure gradient [113], [132]. As an extension, this study uncovered that the CFZW is also fluctuates with the same frequency as pressure gradient fluctuations and it directly copies the fluctuation nature of the pressure fluctuation. This can be seen even during minor secondary pressure fluctuations, for example, such as the secondary pressure fluctuations seen between the two peaks in Panel B of Figure 4.6 for 15mL recordings (first set), which could be due to temporary minor blockages in the device.

It has been previously shown that Polydimethylsiloxane (PDMS) and other rubber-based materials of low Young Modulus have damping properties, thereby reducing the amplitude of mechanical oscillations in a fluidic network [294], [295]. PDMS is a silicon-based organic polymer that is popular among academic microfluidics communities in the exploratory stages of research because of its straightforward fabrication, cost, robustness, flexibility and optical transparency [296]. Here both the chip and the tubing material are non-silicone; the chip is a composite of SU8 and PMMA and the tubing is polytetrafluoroethylene (PTFE). Therefore, most of the hydrodynamic instabilities are expected to be transmitted in the fluid and visible at the CFZW. The advantages of a SU8/PMMA approach include its suitability for industrial mass manufacturing, better chemical and mechanical stability, and lower absorption of small molecules, as also mentioned in Chapter 3.

The amplitude of pressure and CFZW fluctuation has also found to be linearly related. From this corelation it is possible to back-calculate a particular CFZW fluctuation for a given pressure fluctuation amplitude. For example, for a 10 KPa pressure fluctuation from the mean pressure, the CFZW will vary about 2 μm (this holds for 10-50% milk dilution). Since the best in-silico blood models, including the most recent Lattice-Boltzmann models, cannot yet resolve high haematocrit blood flow (or high-density particulates) or support the design of complex, high-density soft particulate flow, these experimental findings could be useful when designing hydrodynamic separation devices. By knowing the cell-free zone spatial fluctuations, designers and experimentalists can adjust devices to avoid cells or particles non-intentionally reaching undesired outlets.

The experiment was broadened for a wide variety of various kinematic viscosity samples, and it was discovered that samples with no cells or particles have lower relative fluctuation, and so the overall fluctuation appears to demonstrate a logarithmic relationship between samples. The reasons for the reduced relative fluctuation in the glycerol and water samples is unknown; however, cell-cell interactions have been postulated as a possible cause of the pressure fluctuations [297].

The initial streamline location for the CFD simulation was critical for observing the fluctuation effect, and it was carefully determined based on the forces and effects that are active in those regions. As mentioned earlier in section 4.2.1, three forces are mainly considered in inertial focusing to determine the ultimate position of a particle in a micro-channel named as shear gradient lift force, wall induced lift force and drag force. Based on the relative velocity around the particles, the shear gradient lift force moves the particles mainly towards the channel wall, while the wall induced lift force acts on the particles in the opposite direction. Counter interaction of these two forces determines the net lift force on a specific particle. However, mainly the wall induced lift force has been considered in determining the distance of the streamlines from the top constriction boundary because of its dominance on the particles that are initially moving close to the side walls. These particles will interact with the channel wall and because of the pressure build-up between the wall and the particles, they will move away from the wall. In this study, the primary focus was on the homogenised fat globules (typically 0.2-2 μm in size) present in the homogenised milk, although some unhomogenised and larger fat globules (~2-6 μm) were also expected to be present in the sample. In a rectangular channel, depending on the aspect ratio (channel width/channel depth) and Reynolds number, particle distribution pattern might lead to two to eight equilibrium positions near the walls [298]–[301]. Since the Reynolds number varies between 100 and 300 in this setting and the aspect ratio is nearly two, it was assumed for simplicity that there will be four equilibrium positions near the top-bottom and sidewalls, similar to [302]. Therefore, when predicting the positioning of particles at different distances from the sidewall, those particles' positioning in the z-direction (channel depth) have also been taken into account. According to the simplified net lift force near the sidewall [303] derived from [304], the larger sized particles which are close to the sidewall will experience higher wall induced force and move further away from the wall faster than the smaller sized ones. This will create the CFL near the side wall depending on the channel diameter, particle size and density [137], [305]. For a specific sized channel, the CFL usually decreases with an increment in the density of particles. As an example, for a channel with a 40 μm width,

the CFL decreased from 2.9 to 2 μm when the blood HCT rises from 40 to 45% [137], [306], [307]. This is because the degree of axial migration decreases with the aggregation of RBC at the core of the channel. However, the scenario will be different with milk. As it has been mentioned earlier that the smallest size of fat particles available in homogenised milk is much smaller than that of RBCs, the wall induced force exerted on those particles will be comparably very small and this will affect the migration significantly. Moreover, the comparably higher number of fat particles available in milk will further hinder this migration as a result of higher cell-cell interaction. Regardless of the presence of a cell-free layer, particles larger than 2 μm, cannot have their centre of mass between the streamline located at 1 μm from the wall. Smaller fat particles (0.2-0.5 μm) and casein particles (~100 nm) located within the 1.5 μm zone are expected to travel to the skimmed milk outlet, as the net lift force will be negligible for them. In general, the fat particles will try to move to the centre at different speeds depending on their size, which is related to the wall induced force and interaction with the already existing different-sized particles near the centre of the channel. The smallest fat particles (~ 0.2-0.5 μm) are expected to reside next to the casein particles layer after crossing the CFL boundary. However, some of them might remain within the CFL because of the smaller induced force and their interaction with the particles that will try to move to the sidewall from the centre because of the shear gradient lift force and reside at the CFL boundary. Whereas the biggest fat particles are predicted to cross the CFL boundary and remain at the furthest region from the sidewall. Flow streamlines were computed from precise starting locations from the constriction boundary side wall (1.5, 2.5 and 3.5 μm) at the closest to the daughter channel and for two z locations: one at channel centre and another one 4 μm away from the centre. A central shift of particles can be noticed by observing at the post- streamline placement after the constriction. This central shift of particles flowing through the particle rich channel is expected as the particles tend to move towards the channel centre near the top and bottom walls to attain their equilibrium position. It can be inferred from the CFD simulation that, although some fat particles will end up at the skimmed milk outlet because of the insufficient cell-free zone, the effect of pressure fluctuation will further degrade the separation efficiency.

Characterisation with the absorbance spectrophotometry and DLS shed light into the experimental effect of syringe pump fluctuation on the separation efficiency of the BPS device. Although the CFZW was large enough to be situated beyond the particle-poor channel at the nominal pressure, the pressure fluctuations due to the mechanical fluctuation of syringe pump led to more milk fat particles travelling into skimmed milk.

This study bears similarities with investigations into stenosed arteries under pulsatile flow and plasma skimming effect as a function of heart rate [308]–[310]. Since the results presented in this study do not allow direct comparison (data acquired on milk rather than blood), future work will be dedicated to investigating the fluctuations of the cell-free zones in blood flow under syringe pump-induced fluctuations. Vascularisation associated with cardio-vascular and cancer pathologies (respectively stenosis and abnormal vascular structure[311]) which operates under similar pulsatile conditions could inspire biomimetic structures (such as constrictions and bifurcation geometries) for optimal blood plasma separation.

Furthermore, various commercially available and open-source pumps were investigated to determine their mechanical fluctuation effects. The KD pump performed exceptionally well among the syringe pumps without feedback loops, as one could expect considering its higher cost (15 times that of Ender) and higher motor steps per revolution (3200 micro steps). One might expect higher motor steps per revolution (3200 micro steps) than the other two pumps. Pulseless nemesys pumps perform best at low frequency since they utilize feedback loops to keep pressure fluctuations to a minimum, but they are quite expensive.

Between the low-cost commercial Aladdin pump and open-source Ender pump, significant statistical difference in the plateau magnitude can be observed while operating with a smaller diameter 1 mL syringe. Whereas, for 5 mL syringe, there was no significant difference in plateau magnitude. While the main reason for this is unknown one reason could be the faulty setup of Ender pump. Ender pump is made up of three separate programable pumps, two of which were used in this study. Although it is assumed that these pumps operate identically (same diameter screws were used), this may not be the case, as the pump used in the 1 mL experiment had more fluctuation. This is most likely due to the fact that the screws required to push the syringes are manually attached, and some of them might not have been adequately connected. Another reason could be Ender pump's comparatively better performance at higher frequencies (mechanical frequency is higher when working with lower diameter syringe). Because of its fewer micro-steps per revolution, the Ender pump's performance may not be as good as the Aladdin pump at lower frequencies.

4.5 Conclusion

The effect of syringe pump fluctuations on the cell-free zones in the microfluidic hydrodynamic separation structure has been investigated. Using a CCRM imaging

approach, having reported for the first time, a direct relationship between the mechanical oscillation of the syringe pump and the width of the cell-free zone at an expansion region. The cell-free zone width at an expansion region has been observed to fluctuate with the same frequency and amplitude as the mechanical fluctuations of the syringe pump. To explore this effect in the context of high throughput applications, relevant to cell separation studies, the relative fluctuations of pressure and cell-free zone width have been measured in this study from moderate to high flow rates (from 5 to 25 mL/h). The relative pressure and cell-free zone fluctuation maintain a plateau with an amplitude of approximately 2% of the average value for this range (with Aladdin pump), which should hold for devices with any geometrical structure. Finally, the potentially damaging impact of pressure fluctuations on hydrodynamic separation has been demonstrated using milk fat separation. It has been proved, by simple simulation and experiment, that these pressure fluctuations degrade the particle flow path and the separation efficiency. It has also been demonstrated that absolute pressure fluctuations increase with kinematic viscosity, implying that the impacts of pressure fluctuations will become more severe for blood and other two-phase, or highly viscous flows. Furthermore, the performance of various commercial and open-source syringe pumps was evaluated using pressure fluctuation measurements, which revealed that employing a pulseless syringe pump or a high precision stepper motor-based pump (higher micro-steps) can greatly reduce these fluctuations. These high-precision pumps, however, are hugely expensive.

In conclusion, following these results, microfluidic designers may take two approaches. On one hand, using pulseless syringe pumps or damping solutions will overcome major fluctuation effects and improve the efficiency of separation devices. On the other hand, it is possible to take pressure fluctuations into account and design a hydrodynamic separation system for widely used conventional syringe pumps. Using the present findings, designers of bulk cell separation devices can ensure robust performances, independent of pressure fluctuations.

Chapter 5: Design, 3D-printing, and characterisation of a low-cost, open-source centrifuge adaptor for separating large volume clinical blood samples

5.1 Introduction

A centrifuge is one of the most frequently used instruments in laboratory diagnostic and molecular biology laboratories, where it is employed to extract particles having different densities from a variety of mediums, using centrifugal forces. The primary uses of a centrifuge in a laboratory include the separation of plasma from whole blood for immunoassays or hematocrit analysis [209], the separation of pathogens and parasites in biological fluids [312], and DNA extraction preparation steps [313].

In particular, blood plasma separation is essential, and often the primary step in numerous biomedical assays involving low abundance target molecules, such as cell-free nucleic acids. Conventionally, this separation process is performed using high-capacity refrigerated centrifuges which are capable of dealing with a large volume (>5-50 mL) of blood samples. These laboratory centrifuges are bulky (120 kg), usually work with 20–40 cm diameter rotors holding 20–100 sample vials, thus occupy a sizeable space in the laboratory space. Moreover, these large capacity centrifuges are expensive, (capital expenditure starts from $1,500) and have high operational costs associated with them [314]. There are commercially available micro-centrifuges that can be cost-effective whose price starts from $120, however their drawbacks are that firstly they cannot handle volume blood samples above 1.5 mL and secondly, they cannot handle routinely used clinical tubes such as S-Monovettes (Sarstedt, Germany) which introduces further preparation steps before the centrifugation. Many researchers have adopted microfluidic blood plasma separation to enable low-cost plasma separation; however, these systems still have yield and purity issues for extremely low abundance biomarker detection, and the low throughput (10 mL/h) of the developed high-purity ones makes them inadequate for practical high-volume blood processing applications. In many clinical applications, such as Apolipoprotein E and HLA detection [68], [70], early cancer detection [21], [315], and liquid biopsy [52], [53], large volumes of plasma (>4 mL) are required. Hence, there is a clear demand on the market for a centrifugation system that will at the same time be safe, low-cost, able to handle large volumes as well as work with routinely used clinical blood tubes. A system like this might be useful for mobile laboratories or low-budget labs

in underdeveloped nations when centrifugation is necessary immediately after blood collection for additional testing.

To reduce the cost of centrifugation, a number of so-called “frugal” solutions have emerged, as part of the open-source and open-science movement [316]–[318]. Centrifuges using hand powered rotary mechanism such as fidget spinners [319], [320], egg beaters [207], paper toy [206], hand crank torch lights [321], salad spinners [322] and centrifuges involving electric motor such as USB fans [323], [324], Dremel tools [325] have been proposed, amongst other solutions. However, all of these devices are only able to handle low volume samples typically from a few microliters to 2 mL. Only a few solutions have been proposed to meet the large volume centrifugation requirement. Patel *et al*. constructed a portable, low-cost 3D printed microcentrifuge with a DC motor that can accommodate special 4 mL glass tubes, which necessitates additional blood handling phases [208]. Sule *et al*. also designed a 3D printed hand-powered centrifuge for high volume centrifugation that costs only $27 in total. [209]. Because it lacks a protective cover, the gadget might not be suitable for use with biological samples. Plasma separation needs at least 10 minutes of centrifugation in a refrigerated centrifuge, which will be difficult to achieve using a hand-powered microcentrifuge. Most crucially, none of the abovementioned low or high-volume systems can employ clinical blood collection tubes (such as S-Monovette) straight after blood removal, resulting in further sample preparation steps. Figure 5.1.A shows the processing volume of available commercial and open-source academic microcentrifuges against their price. Figure 5.1.B illustrates the size difference between the blood handling tubes commonly used in microcentrifuges and the clinical S-Monovette collection tube. I have identified the need for a low-cost, yet automated, approach to the centrifugation of larger sample volumes. Such a device could facilitate access to relevant laboratory tools and expand scientific or medical research and practice.

In this work, I propose a novel approach to significantly reduce the cost of S-Monovette centrifugation by customising the rotor of a commercially available microcentrifuge (SciSpin MINI Microfuge, model: SQ-6050) using low-cost additive manufacturing (3D printing) (Figure 5.1.C). The main goal was to ensure that the modified rotor spun at the same rated speed as the original microcentrifuge motor, resulting in high-speed centrifugation that can match the performance of the high-cost refrigerated centrifuge. 3D printing has emerged in recent years as a convenient method for the development of cost-effective and open-source scientific and diagnostic tools [317], [326]–[328]. This solution has been made open-source and all the manufacturing details are included for others to

replicate this work. This customization procedure could be beneficial to scientists in a low-resource environment [316]–[318], to scientists in need of a mobile centrifugation solution, or to educators. This developed setup can be customised from a widely accessible CE approved low-cost microcentrifuge, and its enclosed structure enables safe centrifugation of two widely used standard 9 mL S-Monovette blood collection tubes, while costing as little as $140. I report the effects of different parameters (size, mass, aerodynamic drag force) on the behaviour and performance of the 3D printed rotor using plasma yield, blood cell counts, cfDNA and albumin levels for biological characterisation. The work has been presented at International Conference on Additive Manufacturing (ICAM 2021) and a full manuscript is currently under review and the pre-print is published online [329].

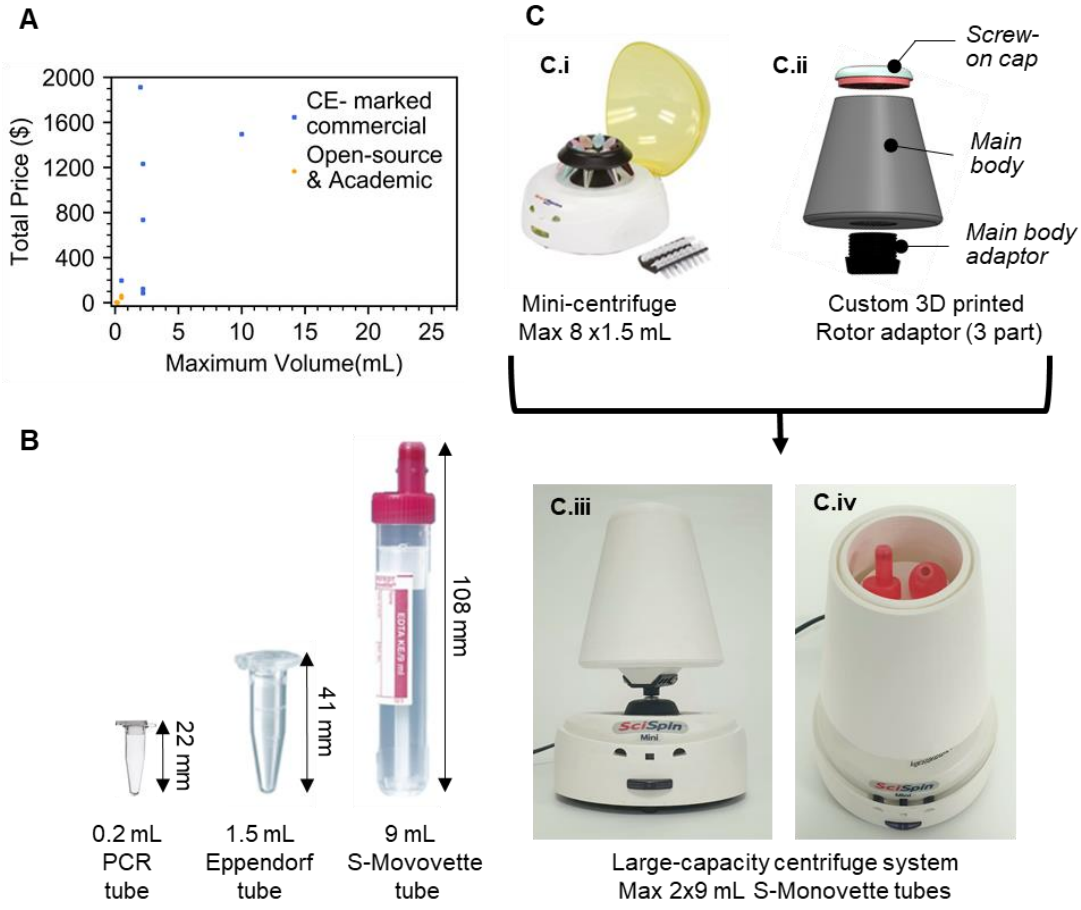

Figure 5.1: Developed 3D printed centrifuge setup (A) Sample processing volume vs price of available commercial and open source academic microcentrifuges, (B) Illustration of the different sized tubes used with the available microcentrifuges along with S-Monovette tube used in this project, (C) Adaptor concept: C.i) Commercial SciSpin MINI Microfuge, model: SQ-6050 with its original rotors C.ii) CAD schematic of the designed three-part rotor adaptor C.iii) Final 3D printed rotor adaptor mounted on the commercial microcentrifuge base C.iv) Top cover removed from the adaptor, showing inside part of the rotor adaptor that holds two standard 9mL S-Monovette tubes.

5.2 Material and methods

5.2.1 Theoretical background and design consideration

Centrifugation is a way to increase the gravitational field magnitude by spinning a sample around an axis which creates a relative centrifugal force (RCF, also called the "g" force) capable of pulling cells and other particles to the furthest position from the centre of rotation. The RCF is proportional to the square of the rotor speed and the radial distance and can be calculated using the following equation:

$$RCF = 1.118 \times 10^{-5} \times \bar{r} \times \omega^2 \qquad (5.1)$$

Where $\bar{r}$ is the average radial distance of the sample in the tube (in cm) and ω^2 is the rotor speed (in Revolutions Per Minute, RPM). The schematics of the tubes and dimensions are shown in Figure 5.2.A.

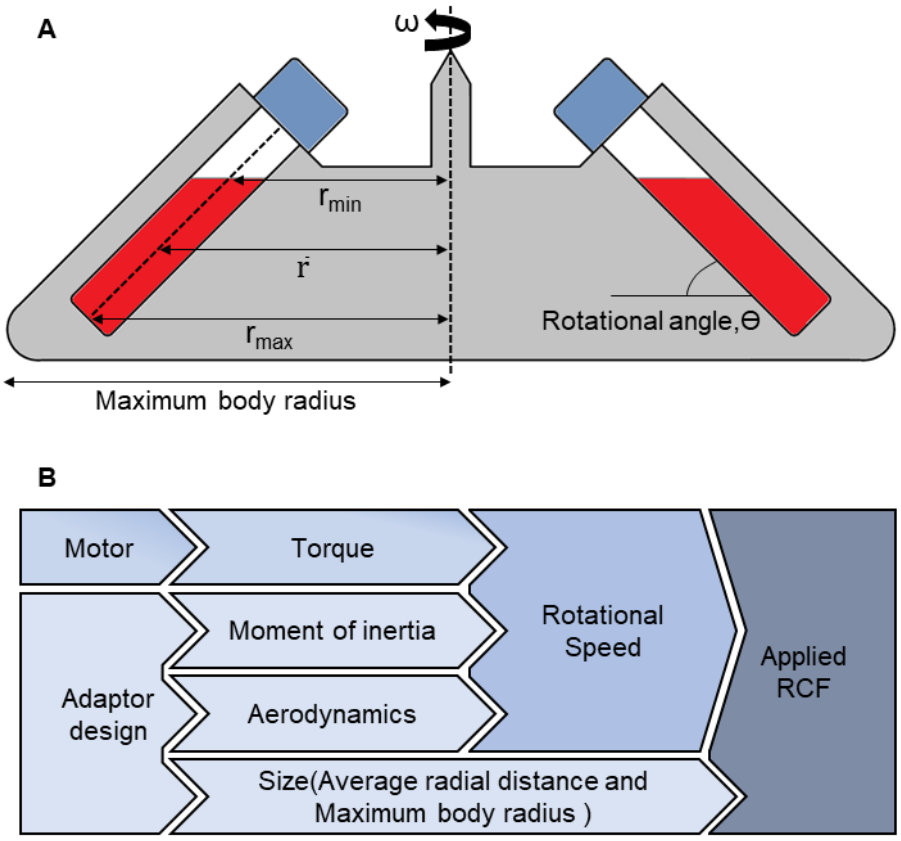

Figure 5.2: Parameters affecting the performance of centrifugation (A) Schematic illustration of the tubes on a fixed-angle adaptor and the radial dimensions (B) The influential parameters on the applied RCF on the sample in the tube mounted on the adaptor.

Although it seems from equation (5.1 that the RCF should increase with an increment in speed and the distance of the sample from the axis, other parameters must be considered to obtain the highest RCF. These parameters include the moment of inertia, torque, and

aerodynamics (Figure 5.2.B). As the original rotor is going to be replaced by the customised one, to meet this additional load demand, the torque of the motor will increase, which will force the speed to go down because of the inverse relationship between the torque and speed. As the RCF increases with the square of the rotor speed, halving the speed will result in a 4-fold decrement in RCF which will result in poor separation efficiency. The additional mass and larger size of the rotor adaptor to accommodate the S-Monovette tubes lead to a decrease in the speed because of the larger moment of inertia and higher aerodynamic drag force. Therefore, although the increment of radial distance increases the RCF, it can also decrease the rotational speed because of the increased moment of inertia and aerodynamic drag force. In this trade-off between speed and radial distance, the speed has been given priority because of its squared relationship with the RCF and every effort has been made to keep the design as small and light as possible. In addition to these discussed parameters, the rotational angle also plays a vital role in the separation process where most compact pellet after the separation usually forms with a higher rotational angle and therefore 45° fixed angled rotors are most common in commercial centrifuges that uses fixed-angle rotors. It should be noted that, among the two types of rotors, fixed-angle and swing-bucket rotors, the former one has many advantages like lower exposure to stress, higher RCF and not having any moving hanging parts; hence, adopted in our project. The effect of different angled rotors has been studied in different designs which will be discussed in the next sections.

5.2.2 Centrifuge hardware

The commercial microcentrifuge (SciSpin MINI Microfuge, model: SQ-6050) used in this project is widely available on mainstream purchasing platforms. To the best of my knowledge, this is the lowest cost CE-marked microcentrifuge on the market at the time of writing. It also has a higher rotational speed (7000 RPM), is lightweight and is more compact compared to other available devices. The full technical specifications of the microcentrifuge are provided in Table 5.1. A commercial benchtop refrigerated centrifuge (Allegra X-12R, Beckman Coulter) with a swinging bucket, (Modular Disk Adapters for Tubes (SX4750)) was used as the benchmark. The benchmark centrifuge was always run with an RCF of 3273×g (3750 RPM). The RCF for the benchmark was chosen as the maximum speed allowed on a swinging bucket configuration and close to the average first spin values used in cfDNA studies [330]. The maximum speed for the commercial Allegra centrifuge is respectively 3750 and 10,200 RPM for swinging bucket and fixed angle, (equivalent RCF respectively 3273 and 11,400 ×g). The second spin protocol

applied in plasma quality measurements was 12,000×g RCF for 10 minutes with a commercial high-speed microcentrifuge (5417 R, Eppendorf), also based on cfDNA studies [330].

Table 5.1: Technical specification of SciSpin MINI Microfuge, model: SQ-6050

Rotor Capacity	8 x 1.5 / 2.2 ml or 16 x 0.2ml PCR
Max Speed	7,000 RPM
Max RCF	2,680g
Timer	Continuous operation
Dimensions (DxWxH)	160mm x 170mm x 122mm
Weight	0.5kg
Noise level	45 dB
Power	100-240V- /50Hz/60Hz 20W
Rotor Capacity	8 x 1.5 / 2.2 ml or 16 x 0.2ml PCR

5.2.3 3D printed adaptor fabrication

All 3D printed rotor adaptors presented here were designed using 3D modelling CAD (SolidWorks, 2018) and fabricated using Fused Deposition Modelling (FDM) technology. The Anycubic i3 Mega (Anycubic, Shenzhen, China) 3D printer was employed for printing. Polylactic Acid (PLA) (Verbatim 1.75mm clear PLA) was used to print the rotor. The technical characteristic of the printer is provided in Table 5.2. The objects were sliced with Ultimaker Cura 4.4 [331] using the standard settings summarized in Table 5.3. All the design files are provided in .stl format in the online repository FigShare (https://doi.org/10.6084/m9.figshare.16762444.v2).

Table 5.2: Technical characteristics of Anycubic i3 Mega 3D printer

Technical Characteristics	Anycubic Mega I3 printer
Printing technology	Fused Deposition Modelling
Standard nozzle	0.4 mm
Printing bed size	210 x 210 x 205 mm
Extruder head temperature	275 °C (max)
Hot bed temperature	100 °C (max)
Printing materials diameter	1.75 mm
Printing material	PLA

Table 5.3: 3D printing setting for Ultimaker Cura 4.4

3D slicer settings print parameters	Ultimaker Cura 4.10
Quality: Layer height	0.2 – 0.3 mm
Infill density	20-25%
Infill pattern	Cubic
Print speed	50 mm/s
Extruder head temperature	220°C
Bed temperature	60°C
PLA filament: diameter	1.75 mm
Support	None

5.2.4 Simulation of critical speed

Any rotating system tends to vibrate in the absence of a driving force at certain frequencies called natural frequencies. When the frequency of the rotational speed matches with the natural frequencies of the system, there will be a resonance and the system will vibrate at that frequency. This natural frequency matching speed is commonly known as the critical speed of the system. The vibration of the rotating system can impose high shear stress on the blood cells and could potentially damage the cells, leading to hemolysis, the destruction of red blood cells, and erroneous analytical results [216]. Therefore, it is important to minimize the critical speed to ensure the minimum shear stress on blood cells. Industrial centrifuge systems operate below and above critical speeds and the critical speeds are controlled via damping in rotor shaft connection [332]. In this project, the critical speed of different designs was predicted in-silico using Ansys workbench modelling (2021 R1, student edition) with the purpose of minimising the model critical speed. During the simulation, modal analysis has been selected from the available analysis systems. The designed 3D model was then imported into the analysis using the geometry tab. The remaining configuration was then completed in the analysis' model tab. PLA material was assigned in this step and the threads present in the original design were removed to facilitate the meshing. Fine meshing was chosen which was the highest possible meshing setting available with the Ansys version used in this study. Later the connection point between the designed rotor and the centrifuge base was selected as a fixed support. To run the modal analysis under loaded condition (rotational velocity) and calculate the critical speed using Campbell diagram, the Coriolis effect, the Campbell

diagram and the damped condition were turned on, and the number of points was set to 15, allowing me to do the modal analysis for fifteen different speeds. Finally, from the environment tab, a rotating velocity was added to the analysis, and fifteen rotational speeds were employed, ranging from 0-7000 RPM with 500 RPM intervals. Following the computation, a Campbell diagram was created under the solution, displaying the design's critical speeds, with the one lower than 7000 RPM chosen as the model critical speed for the further analysis.

5.2.5 Deflection measurement

The deflections of each 3D printed adaptor were measured from video recordings using a code written in the Python OpenCV module. Three video recordings of each adaptor were taken, with a duration of 4 minutes (At 0 sec, Motor mains and video start; at 2 min, Motor mains stop; at 4 min, video stop). Prior to the deflection measurement, sizes of the video files were reduced using an online video converter (https://ezgif.com/). In the first module of the python code, the edge position of the adaptor was detected and transformed in pixel units for each frame of the video. Then these detected positions were compared with the initial reference and deflections in the pixel unit were incorporated into a final deflection matrix. Finally, the values of the deflection matrix were saved to an MS Excel file along with their corresponding pixel numbers. The code saved the screenshot of the processed video images from which a pixel per mm value was calculated from a known distance. This calculated pixel per mm value was then compared to the saved deflections values in the MS Excel file which provided the absolute deflection in mm for each design. The full deflection measurement procedure can be visualised with the help of Figure 5.3 and the required Python code is provided in Appendix B. All video recordings are available from the FigShare repository https://doi.org/10.6084/m9.figshare.16762444.v2.

A

Steps	Software	Action	Example illustration
1	Camera	Record three videos of each design in mp4 along with the speed measurement using USB techometer	I
2	Windows video editor	Open in Windows video editor and compress the video files down to less than 100MB	
3	Ezgif	Open in online video editor Ezgif ezgif.com and normalise video length for each design	
4	Python editor	Transform the video to grayscale	II
5	Python editor	Manually adjust edge detection	III
6	Python editor	Manually provide the reference line	IV
7	Python editor	Compute the edge deflections at reference line for each time frame (See Code supplied in Appendix B)	
8	Python editor	Export deflection from each time frame (in pixel unit) to an excel file	
9	Excel	Scale deflection to reference measurement and convert the pixel values of deflection to mm	
9	Excel	Align deflection measurement to tachometer speed measurements	
10	Python editor	Plot the rotational speed vs the deflection of each design	V

B

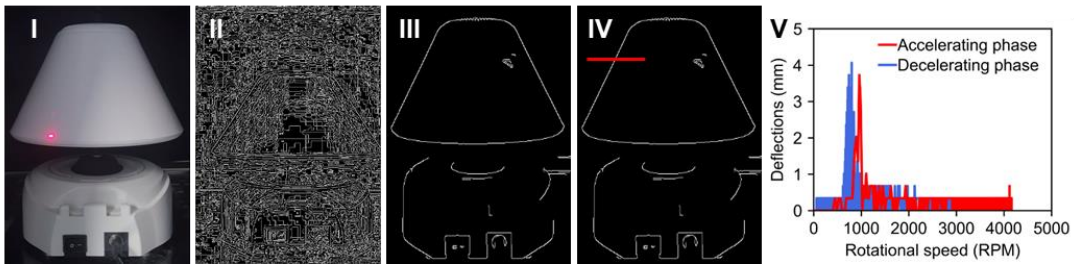

Figure 5.3: Deflection measurement from recorded video using Python code (A) Step-by-step guide for the deflection measurements (B) Corresponding illustration for steps annotated I-V in the process. All three video files for each design are available from FigShare https://doi.org/10.6084/m9.figshare.16762444.v1.

5.2.6 Sample material

Human blood samples were obtained under local ethical approval from the Scottish National Blood Transfusion Service (contract #18~06) and according to the Declaration of Helsinki. Samples were kept refrigerated (2°-8° degrees) before their use. Blood samples were ordered from the same group (O positive) and pooled. Upon arrival, they were mixed gently to save the RBCs from getting damaged via excessive shear stress. Prior to each experiment, 9 mL blood samples (from the same pool) were poured into 9

mL S-Monovette opened syringes using S1 Pipet Filler (Thermo Scientific) which enabled fatigue-free pipetting. The larger diameter of the pipette tip (~0.9 mm) ensured lower stress exerted during blood aspiration.

5.2.7 ImageJ analysis on yield calculation

Prior to the experiments, all the S-Monovette tubes were marked to indicate the area required for a 1 mL volume of plasma. After each experiment, photographs of the tubes in a fixed custom set-up were captured with a mobile camera (Samsung Galaxy Note9). Thereafter, the captured images were processed using ImageJ software to measure the yield of the separated plasma. During the analysis, the previously marked area was selected as the scale. The plasma volume separated after centrifugation was calculated from the position of the plasma limit. Finally, the yield was calculated by comparing this separated plasma volume with the total available plasma in the sample, known from the hematocrit (HCT) measurement (See section 5.2.8).

5.2.8 Blood cell counts

RBCs and platelets count, HCT, and hemoglobin (HGB) of all the pre-and post-centrifuged blood and plasma samples were measured by a hematology analyzer (Sysmex XP-300, Sysmex Corporation, Japan). These measurements were used to compare the separation efficiency and purity of different designs.

5.2.9 Characterisation of hemolysis via spectrophotometry

A centrifuge operates at a high centrifugal force and may exert a shear rate on the RBCs resulting in hemolysis. The reference for hemolysis rate during storage provided by the American Society for Clinical Pathology is 2% or less [333], the Council of Europe guidelines recommend not to exceed 0.8% [334] and the US FDA 1%. While these values provide a useful guide to interpret the effect of centrifugation on blood samples, it should be noted that they refer to hemolysis in blood and blood components intended for transfusion or further manufacture, not *in-vitro* diagnostics. During hemolysis, RBCs release their HGB content on the sample. Free HGB measurements in plasma provide an estimation of the overall hemolysis of a sample. In order to evaluate the hemolysis generated during the centrifugation with different devices, HGB concentration on the plasma was measured using the spectrophotometric Cripps method at 560, 576 and 592 nm wavelengths [335]. The percentage of hemolysis was estimated with equation (5.2 [336]:

$$Hemolysis\ Percentage(\%) = \frac{(100 - HCT) \times Free\ HGb}{Total\ Hgb} \quad (5.2)$$

where HCT and Total HGB represents the total hematocrit and total HGB content of the initial blood sample and free HGB is the estimation of HGB concentration using the Cripps method in an undiluted plasma sample. In this method, background absorption from other proteins, such as bilirubin, is automatically mitigated by the fractional absorbance between 576 nm and at 560 nm and 592 nm wavelengths. In order to quantify the absolute free HGB level in the samples, a standard curve was obtained by diluting human HGB powder (Sigma-Aldrich, USA) in human plasma (Cambridge Bioscience, UK) to make samples of 1, 0.5, 0.1, 0.05, 0.01, and 0.005 mg/dL. The absorbance of the plasma samples extracted after centrifugation of different devices along with the standard samples made from human plasma was measured with the 96 well plate reader (POLARstar Omega, BMG Labtech).

5.2.10 cfDNA extraction

To assess cfDNA levels in several designs and controls, total cfDNA was extracted from 3 mL of separated plasma using the QIAamp Circulating Nucleic Acid kit (QIAGEN) following manufacturer instructions. Extracted cfDNA samples were frozen until use. Real-time quantitative PCR was performed using 2x Power SYBR® Green PCR Master Mix (Thermo Fisher Scientific) to amplify 90 bp target with LINE primers (final concentration 200 nM): forward 5'-TGC CGC AAT AAA CAT ACG TG -3' and reverse 5'-GAC CCA GCC ATC CCA TTA C-3' [337]. A standard curve was created using a series of 5 dilutions of Human Genomic DNA. Thermal cycling conditions involved a 10-minute cycle at 95°C followed by 40 cycles with 15 seconds at 95°C and 60 seconds at 60°C. Samples were amplified in triplicates using Applied Biosystems StepOnePlus™ Real-Time PCR System (Applied Biosystems). A melting curve was performed as a control measure for non-specific amplification. Absolute amounts in each sample were obtained from the standard curve.

5.2.11 Protein load

Bromocresol Purple (BCP) Albumin Assay Kit (Sigma-Aldrich, Merck, Germany) performed as per manufacturer's instructions with plasma samples diluted 5-fold in ultrapure water. The kit utilizes bromocresol purple, which forms a coloured complex specifically with albumin. The intensity of the colour, which is directly proportional to the albumin concentration in the sample, was measured at 610 nm with a 96 well plate reader (POLARstar Omega, BMG Labtech).

5.2.12 Statistical Analysis

Statistical significance was determined by an unpaired parametric Student t-test. Unless specified, the p-value significance threshold was set at 0.05. When reporting on statistical significance symbols '*ns*' is used to indicate non-significance ($p>0.05$), while *, **, *** denotes $p<0.05$, $p<0.01$, $p<0.001$ as per conventional practice.

5.2.13 Safety Notice

To accommodate the large rotor adaptor, the original safety lid of the mini-centrifuge was removed. During the development phase, other safety measures were put into place in case of an adverse event (e.g., accidental detachment of rotor adaptor). Firstly, the base of the microcentrifuge was fixed with a 5 mm Perspex sheet with recessed screws. Secondly, all the experiments were performed under a custom 6 mm thick Perspex safety hood. All the designs went through a 30-minute continuous runtime without incident. None of the designs showed any overheating, rotor displacement/detachment. The motor power load was measured on C-E0 designs on a Bench Digital Multimeter (Keithley DMM6500, Tektronix, Beaverton, OR, USA) (Table 5.4) and found to operate well below the indicated power rating of the original instrument at full speed. Peak power loads within 10% of the original power rating were observed at the beginning of each cycle. Motor power load measurements are available on Figshare at https://doi.org/10.6084/m9.figshare.16762444.v2. While we are confident the adapted rotor can be safely operated, we recommend additional precautions, such as (i) performing a thorough visual inspection of the printed parts to ensure they have no defects (ii) ensuring the correct balance of the tubes prior to spin, and (iii) operating the instrument within an appropriate enclosure (we recommend at least 5 mm thick solid polycarbonate). Despite the fact that the final design provided equivalent performance to the control refrigerated centrifuge, users should keep in mind the customised setup's service life. Obviously, the customised setup will not be able to provide the same level of service life as the high-cost refrigerated centrifuge in operation.

Table 5.4: Motor power load of different designs at the loaded and unloaded condition

Design	Peak current (A)	Peak voltage (V)	Peak power (W)	Average current at full speed (A)	Average voltage at full speed (V)	Average power at full speed (W)
Design C unloaded	1.54	17.9	20.3	0.7	17.8	11.6
Design C loaded	1.52	17.9	20.3	0.7	17.7	11.6
Design D unloaded	1.54	19.9	21.6	0.6	19.6	12.5
Design D loaded	1.51	19.9	20.7	0.6	19.8	12.6
Design E0 unloaded	1.43	22.2	20.5	0.6	22.1	13.8
Design E0 loaded	1.53	17.9	20.5	0.7	17.6	11.5

5.3 Results and discussion

5.3.1 Design progression

A total of thirteen designs were manufactured and tested. Each design is presented in Table 5.5 alongside physical parameters. All the designs are capable of holding two 9 mL S-Monovette tubes. Parameters such as the size of the device, weight, radial distance, aerodynamic drag force around the device and the rotational angle were explored. Design A and B are the preliminary rotor designs planned without aerodynamic drag force considerations where the angles and radial distance of the two designs were varied while keeping the weight constant around 60 g to observe the radial distance effect on the RCF.

Table 5.5: Evolution of design and basic characterisation

Design	Schematic	Cross section	Tube Angle (°)	Rotor mass (g)	Average radial distance, $\bar{r}$ (cm)	Max. body radius (cm)	Rotat-ional speed (RPM)	Applied RCF (×g)
A		N/A	30	60.7	7.677	10.1875	1706	250
			37.5	59.9	8.337	10.925	1607	241
			45	60.5	7.979	10.55	1719	264
				60.33	8.979	11.55	1524	233
				60.8	9.979	12.55	1345	202
B	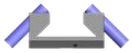	N/A	30	59.3	6.204	8.57	2101	307
			37.5	59.2	6.596	9.091	1990	293
			45	59.1	7.135	9.65	1909	291
C	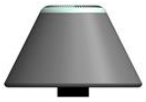	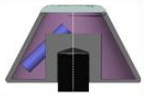	45	364.8	4.459	9.25	4160	864
D	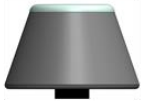	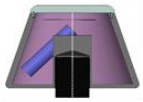	45	384	3.835	8.275	4505	871
E0		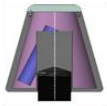	25	297.3	2.278	6.25	6392	1043
E2	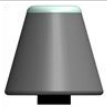	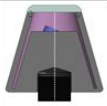	25	338.6	2.094	6.05	6725	1060
E5		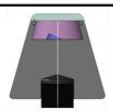	25	272.8	2.066	5.75	6884	1097

Although the radial distance of design A is higher than that of design B, the RCF of Design A is smaller because of the higher speed obtained by design B. A close inspection of angle variations also shows similar phenomena. The radial distance of higher angled designs is slightly higher than the smaller ones. As an example, the radial distance of design B-45° is 0.931 mm higher than that of B-30° design and the RCF value is 16×g lower. These designs' optimal speed is also substantially lower (3.5 times) than the motor's rated speed.

In the subsequent designs (C-E), the aerodynamic drag force was considered by making them truncated cone shape rotor. The speed of the truncated conical shape devices was over two folds that of the primary designs A-B. The relationship between the radial distance and speed for all designs is displayed Figure 5.4.A.

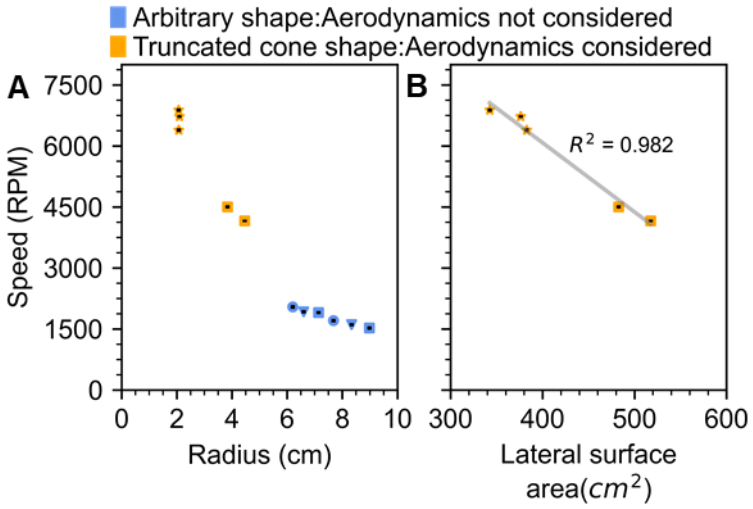

Figure 5.4:Influence of design shapes and sizes on speed (A) The radial distance of all designs vs their rotational speed (B) Lateral surface area of the truncated cone-shaped designs vs their rotational speed. NB: Both panels A and B share the same legend (Error bars in B and C are smaller than the pointer)

After achieving a higher speed (4160 RPM) with the initial truncated cone shape design C, speed was further increased with the later designs D-E by decreasing the lateral surface area (Figure 5.4.B). Design with a smaller lateral surface area provided the least air resistance during the rotation and less moment of inertia which increased the speed of these designs. The final design E5, achieved a rotational speed of 6884 RPM, almost the rated speed of the original mini-centrifuge, and an RCF value of around 1100×g. It can be noted that the final three designs (E0, E2 and E5) all possess a 25° rotational angle. Although a higher angle is recommended to ensure the most compact pellet, the trade-off has to be made to increase the speed and RCF of the designs.

5.3.2 Truncated cone shape design and vibrational analysis

In the previous section, it has been noticed that by considering the aerodynamic drag force with the first truncated cone shape design, Design C, the rotational speed was increased almost 2-fold compared to design B which is an arbitrary shaped design. However, with higher speeds, vibrations were observed during the ramping up or slowing down of the rotation. In order to understand the nature of these vibrations and reduce them, video analysis was used to measure their amplitude and duration (see Material and Methods section). Figure 5.5.A illustrates this process on Design C. Figure 5.5 A.i and A.ii show snapshots of the recorded video before, and after, the edge detection with the Python OpenCV code. Figure 5.5.A.iii shows the deflection measurements obtained from one of the Design C videos. A deflection around 4 mm was observed both in the accelerating

and decelerating phase at nearly 800 RPM, which by definition constitutes the critical speed of this design. These vibrations at high speed could damage the RBCs because of high stress, hence the primary target was to lower the critical speed of the later designs while ensuring higher rotational speed. To serve this purpose, the lateral surface area of the abovementioned designed devices has been decreased to boost the rotational speed while Ansys workbench modelling helped to predict the critical speed before printing the devices.

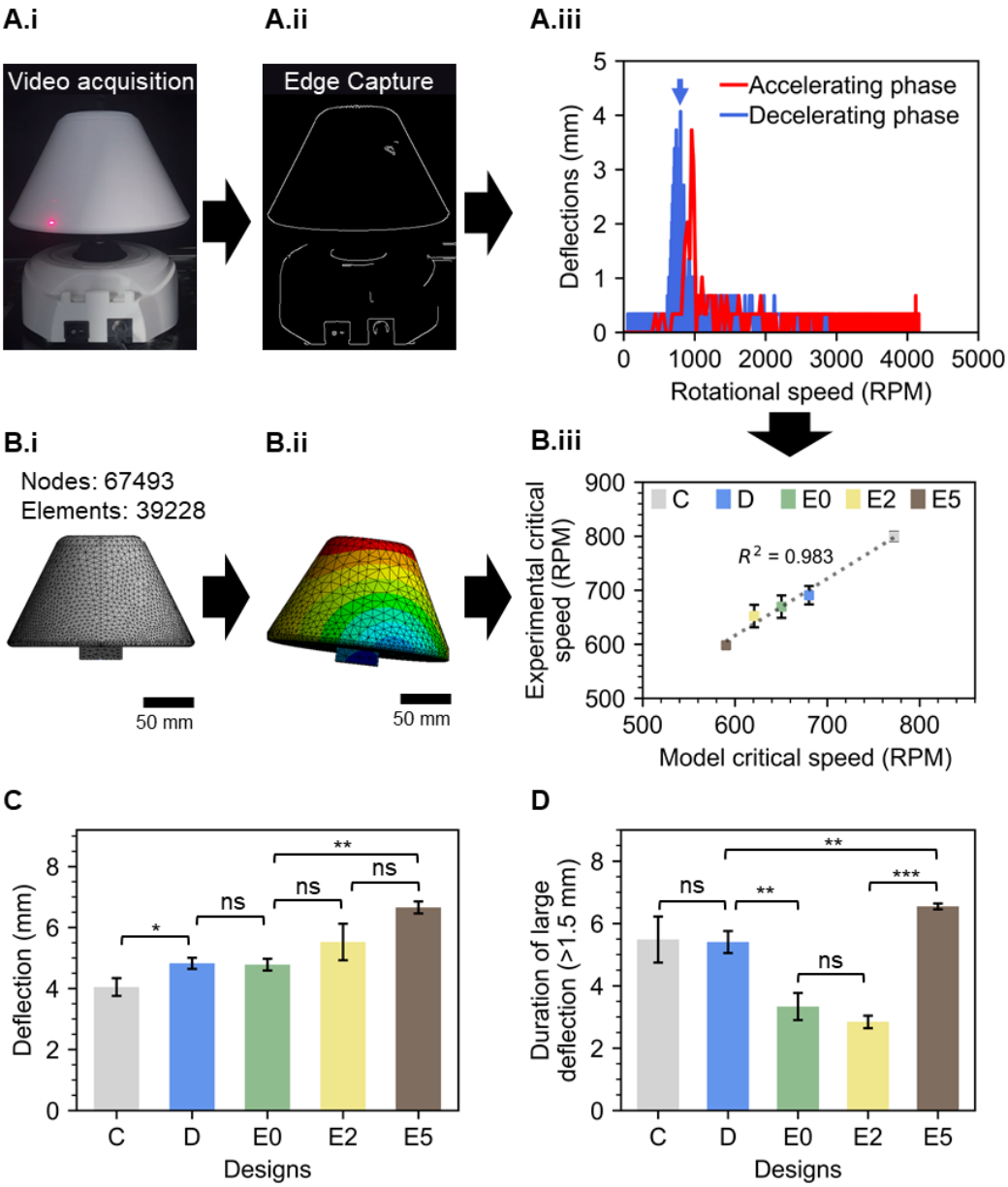

Figure 5.5: Experimental and simulated deflection measurement (A) Deflection measurement from the recorded video of conical Design C. A.i) Snapshot of one of the video recordings of Design C A.ii) Edge capturing from one of Design C videos using Canny, an edge detection operator in Python OpenCV module A.iii) Measured deflection of both acceleration and decelerating phase from the recorded video using python OpenCV module for Design C. All of the design's real-time deflection measurement from video recordings can be found in Appendix C (B) Critical speed measurement in Ansys workbench B.i) Meshing of Design C (Nodes: 6749, Elements: 39228) B.ii) Mode shape during natural frequency B.iii) Simulated (model) vs experimental critical speed of each conical shape design showing a good agreement between them with low percentage difference (1-5%) (C) Measured deflection of each conical shape design showing all designs experiencing deflection from 4 to 7 mm (D) Duration of deflection higher than 1.5 mm was decreasing the lowering of critical speed except design E5 which experienced higher deflection for longer times.

The fine meshing of design C and the mode shape during the deflection of the device can be observed from Figure 5.5.B.i and ii, for illustration. The Ansys model correctly predicted the critical speed of each model with high accuracy (model vs experimental measurement values in Figure 5.5.B.iii, R^2=0.983). The maximum deflection of each design at their critical speed can be found in Figure 5.5.C. The final design, E5 with the lowest critical speed of around 600 RPM provided a maximum deflection of around 7 mm whereas for the other designs the average deflection was limited within 4 to 5 mm. Figure 5.5.D illustrates the duration of deflection higher than 1.5 mm. The duration of large deflections was minimised from C to E2. However, design E5 appeared to be providing maximum deflection for about 7 seconds.

5.3.3 Plasma yield

The separation performance of a centrifuge can be described by the separation yield. The separation yield indicates how much volume of plasma the centrifuge can separate from the total volume of available plasma. To determine the plasma separation yield, 9 mL of pooled blood samples were centrifuged with each conical design (C, D, E0-2-5) and the full–scale centrifuge control for 3, 6 and 10 minutes and the separated plasma volume and full blood count were measured. Figure 5.6 shows photographs (panel A) and quantitative results of plasma yield in the initial sample and samples after 3,6-, and 10-minutes centrifugation on the adapted centrifuge and the control.

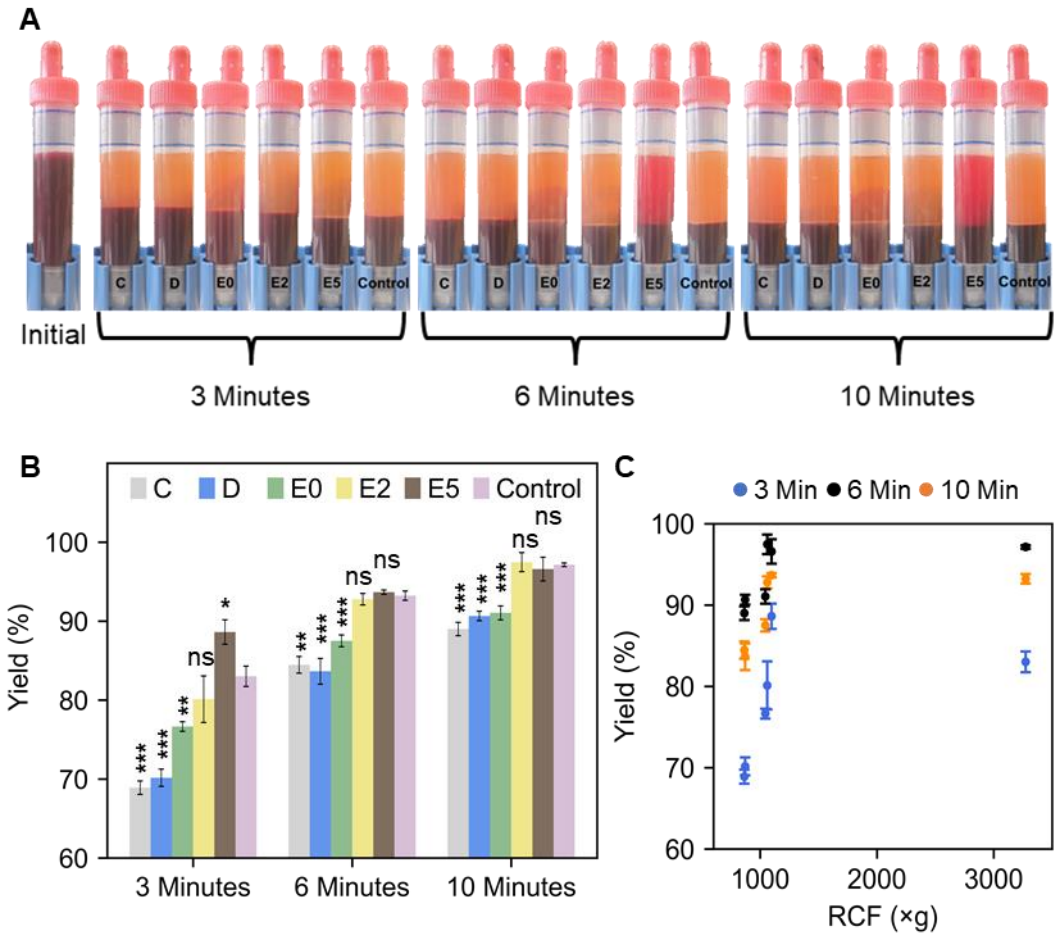

Figure 5.6: Plasma yield of different devices at different time instances (A) Images of the initial and post centrifugated (3,6,10 minutes) S-Monovette tubes showing that larger centrifugation times resulted in a higher volume of plasma separated from 9 mL sample. (B) Measured separation yield of different designs compared with the control centrifugation performance. Statistics: standard unpaired t-test between each column and the control. Design E2 and E5 were able to separate the same amount of plasma as the control at 6 and 10 minutes with no statistically significant difference (C) RCF vs yield of different designs at different time instances.

It is worth noting that most of the plasma gets separated within 3 minutes of centrifugation (minimum separation ~70% for Design C) and the separation volume further increases at 6 and 10 minutes. The single most striking observation is the decreased separation performance of Design E5 at 6 and 10 minutes which might be resulted from extended duration of intensive vibration. With device E2, it was possible to achieve almost 80% yield within 3 minutes which was almost equivalent to the performance of the control. The comparative yield of design E2, E5 (approximatively 95%) are not significantly different from the control after 10 minutes of centrifugation. Figure 5.6.C shows that the yield reaches the plateau position after around 1000 RCF.

5.3.4 Plasma quality: Residual blood cell count

Firstly, the total RBC count was measured each time the blood sample was remixed following centrifugation to investigate the integrity of the blood sample after centrifugation. Figure 5.7.A presents the pre-and post-centrifuged whole blood RBC count at 3, 6 and 10 minutes. It is apparent that there was no significant decrease in RBC count between centrifugations. Due to the removal of plasma (the hematology analyser removes around 50 μL of the sample during each measurement) at every time instance, a slight increment in the RBC count per litre of blood has been noticed on some of the designs (and control). The absence of hemolysis in most of the samples (see Section 5.3.5) corroborate this interpretation.

Secondly, a residual cell count can be used to establish the quality of the separated plasma. Figure 5.7.B shows the remaining RBC count on the separated plasma. The remaining RBCs in design E2 was significantly lower than that of the control at all time instances. Design E5 performed best at 3 minutes, however, due to the vibrations reported earlier in this work, the separation reversed at 6 minutes. The best cell separation performance was observed in the platelet counts (Figure 5.7.C). Notably, design E2 separated almost 4 times more platelets than the control, which could be of benefit in coagulation studies requiring platelet-poor plasma. As explained in Materials and Methods, the separation performance was investigated on pooled blood samples, which has the advantage of removing individual sample specificities and enables accurate comparison between designs and control. To investigate any notable differences between individual pools, the separation performance of designs E0, E2 and control was compared after 10 minutes of centrifugation with two different pools of blood (Figure 5.7.D). The two pools investigated were found to have significant differences in original HCT (Pool 1, HCT ≈ 45.5%; Pool 2, HCT ≈ 43.2%). However, in terms of relative difference post and pre-centrifugation, the pools showed no significant differences in RBC and platelet relative counts.

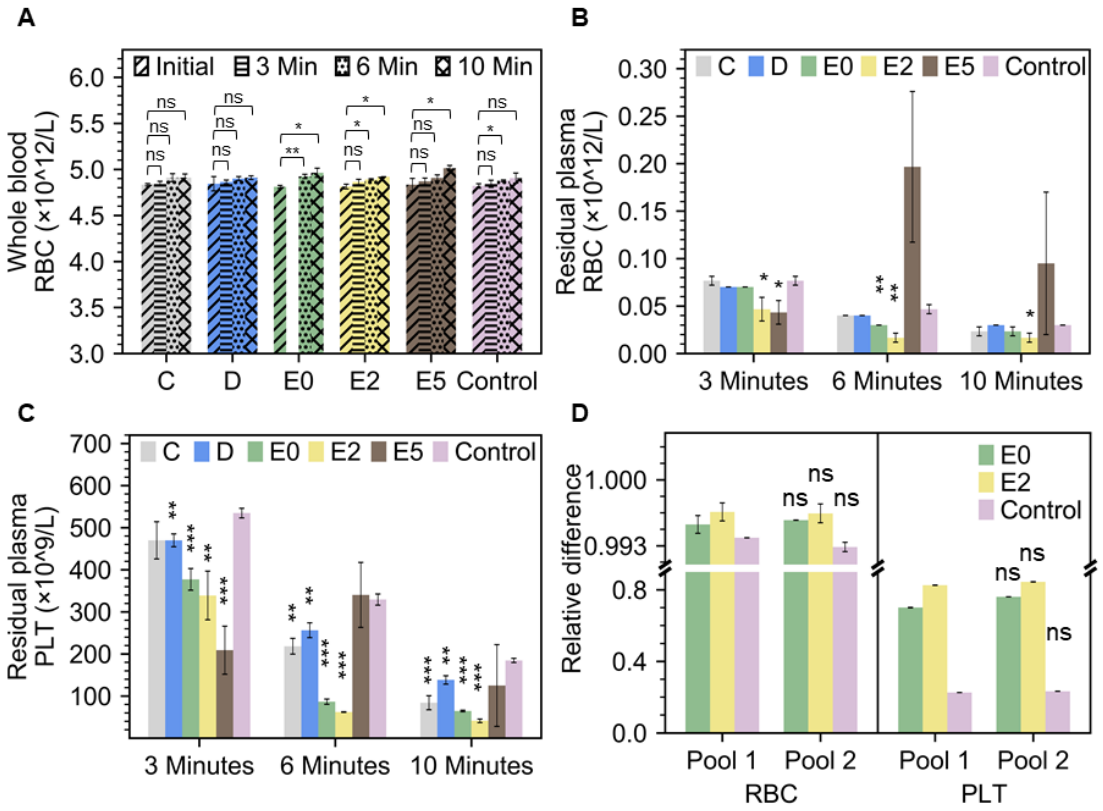

Figure 5.7: Blood count at 3, 6 and 10 minutes (A) The red blood cell counts of pre (initial) and post (3,6, 10 minutes) separated blood to show the integrity of the sample after centrifugation. The statistical indications relate to a non-paired t-test between the RBC counts between 0, 3, 6, and 10 minutes (B) The red blood cell (RBC) count on plasma after centrifugation shows RBC concentration with design E2 was significantly lower than the control in all periods. On the contrary, design E5, although performing well at 3 minutes was hampered by vibrations reversing the separation process. Here the statistics relate to a non-paired t-test between each of the designs and the control, for each time point (C) Platelet count (PLT) on separated plasma. Design E2 was able to separate almost 4 times higher platelet than the control within 10 minutes. Here the statistics relate to a non-paired t-test between each of the designs and the control for each time point (D) Relative RBC and Platelet counts after 10 minutes centrifugation from two different pools of blood. Here the statistics relate to a non-paired t-test between Pool 1 and Pool 2 for each experiment. No significant difference was observed between different pools of blood.

5.3.5 Plasma quality: Hemolysis detection

To assess the quality of the separated samples, the free-hemoglobin released after centrifugation was measured and derived a hemolysis percentage (See Materials and Methods). HGB levels from collected plasma samples of design E0, E2 and control (single and double centrifugation) were measured using Cripps method (See Materials and Methods). As reported in Figure 5.8.A, all the measured samples had an estimated

percentage of hemolysis between 1 to 1.7% corresponding to a free HGB concentration of 0.2-0.4 g/dL. Despite the deflections observed on Designs E0 and E2, the separated plasma is well below the threshold of hemolysis limit and similar to the control used in the experiment, which shows the adapted device is adequate for the general low-speed spin of clinical blood samples.

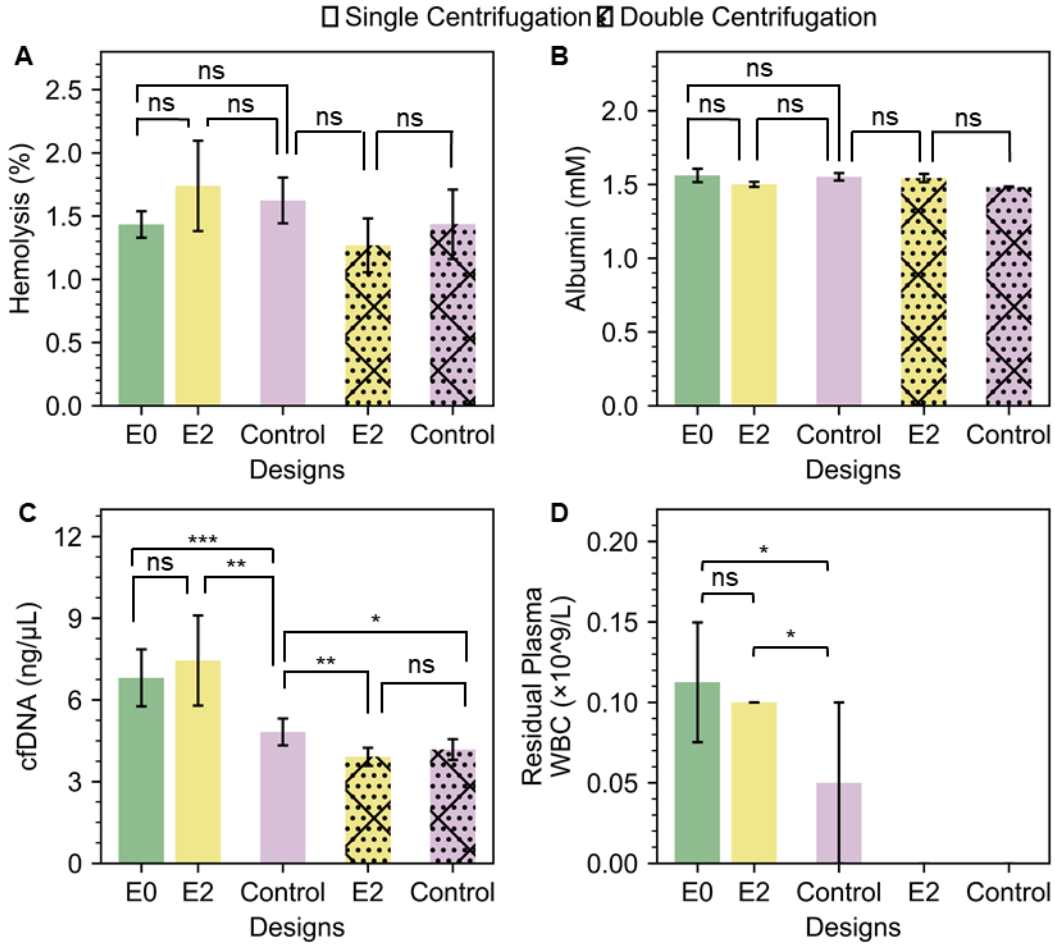

Figure 5.8: Biological characterization of the separated plasma (A) Percentage of hemolysis in separated plasma from E0, E2 and control. (B) Albumin concentration in E0, E2 and control (C) Cell-free DNA levels in E0, E2, and control after single centrifugation or with additional second separate centrifugation (D) WBC count on the residual plasma after single centrifugation (at the own respective speed, 10 minutes) and double centrifugation (12000 rpm, 10 minutes)

5.3.6 Plasma quality: Protein load

Albumin is known to be the most abundant plasma protein in humans which accounts for almost 60% of the total serum protein. It is an established biomarker of nutritional status [338] and reliable prognostic indicator for heart failure [339], pulmonary arterial hypertension [340], in acute surgical patients [341], morbidity and mortality [342] and many more diseases. The recovered plasma from the best designs (E0, and E2) and control

centrifugation (single and double) were analysed to quantify the concentration of albumin. The albumin quantification from the sample was obtained by directly measuring the absorbance at 610 nm when the available albumin in a sample provides a peak in the presence of reagent bromocresol purple (see Materials and Methods). As shown in Figure 5.8.B, E0 and E2 samples (single and double centrifugation) showed a similar concentration to the full-scale centrifuge control, around 1.5 mM (~2.5 g/dL) with no statistically significant difference which shows the adapted centrifuge is suitable for plasma protein studies.

5.3.7 Plasma quality: cfDNA extraction

As elaborately discussed in section 1.3, Cell-free DNA (cfDNA) are small (50-200 bp) DNA fragments that originate from cell apoptosis or necrosis. cfDNA overall levels or specific cfDNA regions can be used as biomarkers in the diagnosis, prognosis, or monitoring of fetal chromosomal abnormalities, various cancers, infectious diseases and organ transplants [71]. To assess the suitability of the adapted centrifuge for cfDNA-based assays, the levels of cfDNA was measured using a LINE PCR. Total cfDNA was extracted from 3 mL of separated plasma as per Material and Methods. After the first centrifugation, it has been found the cfDNA concentration from design E0 and E2 to be higher (6.5-8 ng/μL) compared to the control (~5 ng/μL) (Figure 5.8.C). This could be due to the substandard pelleting of white blood cells singe significantly more residual white blood cells (WBCs) were found in the adapted centrifugation, compared to the control (Figure 5.8.D). A second, higher speed centrifugation is often incorporated in cfDNA extraction protocols. This second spin at a higher speed (12,000×g RCF for 10 minutes), can be performed on smaller sample volumes using cheaper and smaller bench centrifuge. To test if cfDNA yields can be brought to the same level as the control, a second spin was applied to both design E2 and control samples. After this second centrifugation, both sample types showed a similar lower concentration of cfDNA with no statistically significant difference.

5.4 Discussion

In comparison to the subsequent truncated cone shape designs, the initial two arbitrary designs A and B experienced substantially stronger aerodynamic force around their bodies. This can be explained by the aerodynamic drag force acting during the rotation which is directly related to the drag coefficient (depends on the shape of the body), the frontal area and the square of the rotating velocity [343]. The frontal area of design A and B can be compared to a flat plate that is highly resistive to the surrounding air and have a

high drag coefficient of 1.17 to 1.98 [344], [345]. With a higher radial distance or angle, the frontal area becomes even bigger and minimize the speed and RCF value. It is also noteworthy that the maximum achievable speed of designs A and B is much smaller than the rated speed of the motor because of their high air resistive flat plate shape. Therefore, although these initial arbitrary shaped designs have some advantages such as the low material amount and low material cost, and fast printing time (<2 hours), the achieved speed and RCF are not capable of highly efficient centrifugal separation.

Whereas, the truncated cone shape designs have a drag coefficient of about 0.05 to 0.5 [344], [345]. As a result, they experience substantially less aerodynamic force, allowing them to achieve faster speeds. A schematic diagram of the aerodynamic drag force around the designs A-B and C-E is provided in Figure 5.9.

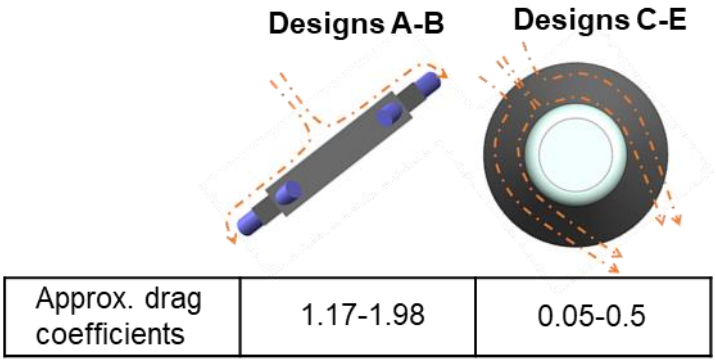

Figure 5.9: Schematic diagram showing an arbitrary shape design provides higher aerodynamic drag force than the truncated cone shape design by resisting much of the surrounding airflow. For simplicity, airflow is shown only in one direction instead of all sides.

One point of concern is that during the ramping up and down of the speed, the truncated cone shape designs introduced deflections from their axis of rotation. These deflections can be interpreted as impulsive vibrations which might exert excessive shear stress on the RBCs and cause hemolysis [346], [347]. The final degree of hemolysis depends on the shear stress exerted on RBCs and the exposure time of the impulse vibration [348]. This can be observed from the separation performance of Design E5. Because of the intensity and duration of the impulsive vibrations, despite having the maximum rotating speed and lowest critical speed, this device had a low separation efficiency.

This can be also interpreted from the separation yield of design E5 (Figure 5.6). The design showed much greater performance after 3 minutes centrifugation (~90% yield) compared to the control. However, during 6- and 10-minutes separation instances, the design failed to maintain this higher performance where it was unable to separate all RBCs present in the separated plasma. The internal shape of design E5 might be a reason

behind this poor separation efficiency. This design is comparatively the smallest of all the other designs and to accommodate this size, the sidewall was brought very close to the placed tube inside and furthermore, the tube was completely encased against the sidewall, unlike the other design where the tubes are hanging freely, away from sidewalls. Therefore, the high deflection and duration of deflection with design E5 might cause the sidewall to touch the S-Monovette tubes randomly at several instances and hinder the separation efficiency. Given the design's performance at 3 minutes, it's likely that if the vibration intensity and duration are reduced, this design will outperform the control.

Among the other designs, Design E2 maintained the same yield as the control in all time instances. As discussed previously, the overarching goal in this study was to customize a low-cost microcentrifuge in such a way that it could handle a large 9 mL clinical sample volume directly after the blood withdrawal without any extra blood handling steps. At the same time, the device should ensure at least similar separation performances as a benchtop refrigerated centrifuge. Our lab, and others in the field, have previously demonstrated microfluidic solutions as an alternative to traditional centrifugation [112], [113], [131], [132]. However, in previous chapters, I have concluded that for extremely low concentrated biomarker detection such as the detection of various fractions of circulating DNA, currently available microfluidic BPS devices are not viable because of their low separation yield and the difficulty to handle the large volume of the viscous whole blood sample. The main barrier in the available microfluidic BPS devices is the cell-cell interaction between red blood cells. When high volume fractional blood flows at a high flow rate, the cell interaction between a large number of RBCs in the microfluidic channel increases, which inhibits the cell-free zone formation and other deterministic effects, thus reducing the separation performance [138]. As a result, the use of high-volume fractional blood in the above comparative high-throughput studies has resulted in much lower separation yields. Comparatively, it can be observed, design E0 and E2 managed to secure more than 95% of the available plasma within 10 minutes of centrifugation. This high plasma yield is a valuable factor in low-level biomarker detection. Plasma yield has been seen to reach a plateau after around 1000×g RCF. This is why at least 1000×g RCF is recommended to run for 10 minutes to separate plasma from blood in clinical settings.

In platelet separation, all adaptors (except E5) outperformed the control. Because of the size and density of platelets, ultracentrifugation (high speed) is commonly employed in industry for platelet separation. All of the designed devices have faster speeds than the control, ensuring superior platelet separation performance.

The albumin concentration in all samples, including control samples, was slightly lower than the normal range of Albumin in plasma (3.4 to 5.4 g/dL). The total cfDNA levels in this study were also higher than levels reported elsewhere. Both of these are due to the age of the samples (three days old) which is sub-optimal for cfDNA-based diagnostic or in protein load studies, but adequate to characterise the performance of a device.

The only downside of the designs is their ability to separate WBCs within first centrifugation. The lysis of remaining WBCs during the cfDNA extraction has introduced genomic DNA, resulting in overall higher cfDNA levels. However, other studies also have reported higher cfDNA concentration after single centrifugation [330]. Although designs E0 and E2 showed similar RBCs separation and the yield compared to that of control, the low rotational angle of 25° resulted in lower buffy coat compaction and consequently higher WBC counts in the separated plasma, compared to the benchmark. This issue might be addressed by exploring the use of a higher rotational angle or longer spin duration. In the meantime, second high-speed centrifugation can remove remaining WBCs and lead to similar cfDNA levels in the adapted design and benchmark.

5.5 Conclusion

In this study, a mini-centrifuge costing <$130 was adapted to handle large volume (9 mL) standard clinical samples in S-Monovette collection tubes. The results showed that the air resistance was the most crucial parameter needed to be optimised to ensure an adequate centrifugal force for comparable cell separation to a commercial centrifuge. Following optimisation, the final design reached a speed of around 6725 RPM and RCF of 1060×g. Similar yield, cell counts (red blood cells, platelets), hemolysis and albumin levels were obtained from the optimised design and benchmark. Only the total cfDNA levels of the plasma separated in the adapted design were found to be significantly different to the benchmark, owing to a reduced separation performance for white blood cells. The nearest cheapest option for 9mL S-Monovette centrifugation cost over $1,500. The bill of material for the adapted centrifuge setup stands at around $140. The overall performance of the optimised adapted centrifuge, which costs a fraction of the total price of the commercial control centrifuge, was equivalent to a commercial centrifuge and superior to microfluidic approaches in yield, throughput and quality. Therefore, this developed centrifuge setup offers value and performance to the low-resource environment or could be further adapted to create portable diagnostic laboratories.

Chapter 6: Conclusion and future work

In this thesis, I have presented the findings of three years of research focused on high-volume blood plasma separation (BPS) techniques. The investigation focused on various key aspects influencing microfluidic BPS efficiency and yield of BPS devices was the main emphasis of the first two years. Although a developed microfluidic device in future with high yield and throughput will be critical in low to mid-volume BPS (<4 mL), I came to the conclusion that the devices will have several limitations for high volume BPS (>4 mL), which will be detailed further in the following paragraphs. In order to facilitate this high-volume BPS, the rotor of a commercially available micro-centrifuge was modified in the last year to allow centrifugation of large volumes of clinical blood samples (two 9 mL S-Monovette tubes).

The high HCT blood flow experiment (Chapter 3) demonstrated that blood with a high-volume fraction of red blood cells (RBCs) or hematocrit (HCT) (~90%) can flow through a microfluidic channel similar in size to that used in microfluidic BPS devices without any sample dilution, with caveats on distance and residence time. Therefore, it will be possible to provide a large number of bifurcations at the main channel to ensure high plasma yield and separation of samples with up to 90% HCT. I found that a flow rate of 19 mL/h may be achieved in an 11 mm long channel without hemolysis, this flow rate could be enhanced to 30 mL/h with the use of a new suggested ferrule system (Section 3.5.2). The proposed new ferrule system is simple to manufacture and greatly improves the high HCT blood flow. I hope that this research could aid future design engineers in making informed decisions about design parameters while developing a new BPS device. In addition, the design and fabrication of the straight microchannel used in this high HCT study are simple and can be used as a viscometer along with a pressure sensor and syringe pump.

The study investigating the effect of syringe pump fluctuation on cell-free zone width (CFZW) (Chapter 4), is the first study in this field to conclude that all commonly used low-cost syringe pumps are responsible for adding a high level of fluctuation to the CFZW and thus could degrade the separation efficiency of a microfluidic BPS device. Using different dilutions of milk samples, it was demonstrated that at high flow rates (>5 mL/h), the fluctuation could be 2% of the average pressure and that each 10 KPa fluctuation could be responsible for roughly 2 μm CFZW fluctuation. Moreover, using samples of varying viscosity, it has been verified that the 2% pressure fluctuation at high flow rates (>5 mL/h) is true for any shape of a microfluidic channel structure. These

findings should hold true in BPS as well. In future, only the 2 μm CFZW fluctuation that accounts for a 10 KPa pressure fluctuation can be verified by replicating that required specific experiment in BPS. In conclusion, despite the fact that this study was conducted with milk samples rather than blood, the results should be similar with blood samples, with the exception that the pressure gradient inside the channel and the CFZW fluctuation amplitude for whole blood samples will be substantially higher. This fluctuation effect can be reduced by utilising a pulseless syringe pump (e.g., neMESYS) or a stepper-motor based syringe pump with higher micro-steps per rotation (e.g., KD Legato). Both of these methods, however, are costly and thus unsuitable for low-cost settings. To perform BPS with commercial low-cost syringe pumps such as the Aladdin pump (~$700) or a custom-made Ender pump (~$200), designers must account for the syringe pump's fluctuation effects when designing their device and ensure that the CFZW is greater than the CFZW fluctuations that can occur for the designated flow rate at each bifurcation. This study could open up a practical approach for experimentalists wanting to simulate oscillating flows, for example in the context of rheological or haematology studies.

Experiments with a single bifurcation device should be done in order to improve future designs of microfluidic BPS devices. After each separation zone following plasma extraction, blood HCT often rises above physiological levels, resulting in a gradual decrease in the CFZW [102]. I also verified this phenomenon by plotting fluid velocity streamlines for different viscosity samples using COMSOL Multiphysics on the previously developed BPS device (August 15 C1) designed by our lab. This design was also employed in the syringe pump fluctuation experiment in Chapter 4. The results informed that when the flow rate ratio is the same (1^{st}-3^{rd} bifurcation: 1:22), the same viscosity samples (2 cP) maintain the same CFZW at each bifurcation, however, the CFZW for a higher viscosity sample (5 cP) decreases by around 10 μm compared to the lower viscosity sample (2 cP) (Figure 6.1). I hypothesize that increasing the flow rate ratio between the plasma extraction and main channel at each bifurcation is essential to maintain a constant CFZW, which will ultimately improve the BPS device's overall performance.

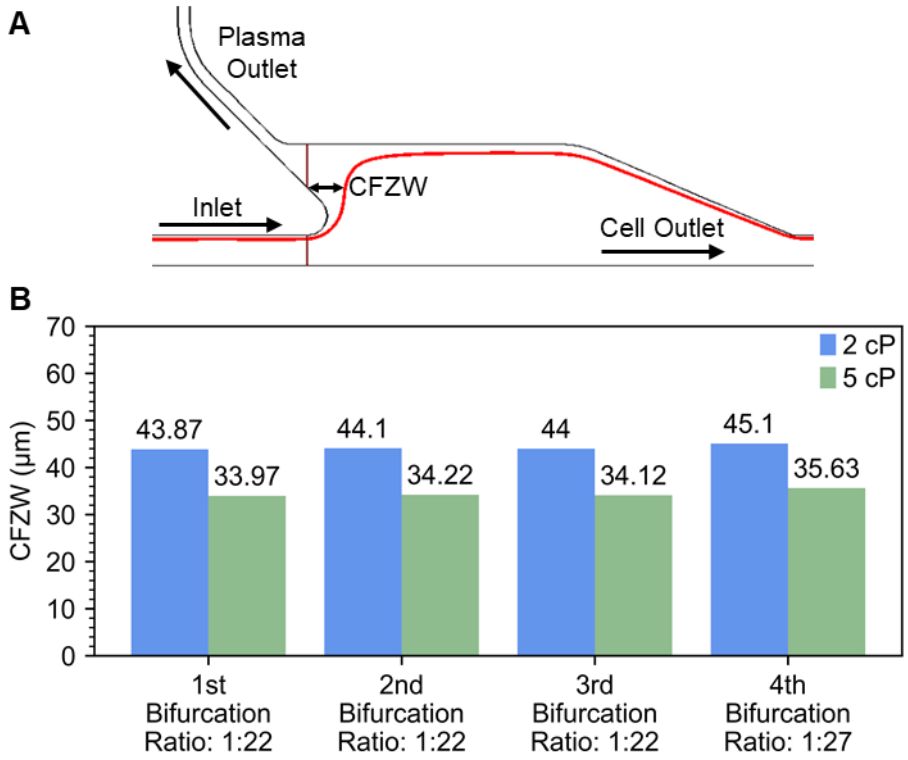

Figure 6.1: Effect of different viscosity samples on CFZW (A) Snapshot from COMSOL simulation which shows the velocity streamline from where the CFZW is measured for different viscosity samples. The streamline is computed at the channel centre (Z=10 µm, total height 20 µm), 4 µm far from the constriction upper boundary (Y=4 µm, constriction width 37.5 µm), 7 µm far from each constriction edge towards the expansion region. The YZ plane slice from where the CFZW is measured is 25 µm inside from each bifurcation bend. (B) Measured CFZW for different viscosity samples (Material: water). Viscosity values have been randomly chosen considering the average blood viscosity of 3 cP. For the first 3 bifurcations, the flow rate ratio is the same therefore CFZW for 2 cP and 5 cP samples are constant around 44 µm and 34 µm respectively. This shows the significance of increasing the flow rate ratio after each bifurcation in order to maintain a constant CFZW throughout all bifurcations. In the fourth bifurcation, where the flow rate ratio is increased, the CFZW is larger for both samples, which indicates the importance of increasing the flow rate ratio.

In hydrodynamic BPS, maintaining a constant substantial CFZW at each bifurcation is important because if the layer shrinks and the cell layer moves too close to the plasma extraction channel, RBCs have a strong possibility of invading the plasma extraction channel due to the syringe pump fluctuation effect, which can reduce separation efficiency significantly. However, if the flow rate ratio between the cell outlet and the plasma extraction channel is made too high to assure a large CFZW, the flow rate of the plasma extraction channel will be considerably lowered, which is not ideal for high yield BPS devices. Furthermore, raising the flow rate ratio will result in a higher overall

pressure gradient inside the device, which could damage the RBCs' quality and lead to hemolysis. The single bifurcation study would thus facilitate the investigation of these counterintuitive phenomena and the determination of the optimal CFZW size at each bifurcation. It will also inform about the total number of required bifurcations as well as the rate of flow rate ratio increment after each bifurcation. Figure 6.2 summarises the entire process chart of the investigation into the likely limiting factors that affect the yield and separation efficiency of a microfluidic BPS device, as well as how these findings will aid in the design of a high-performance BPS device.

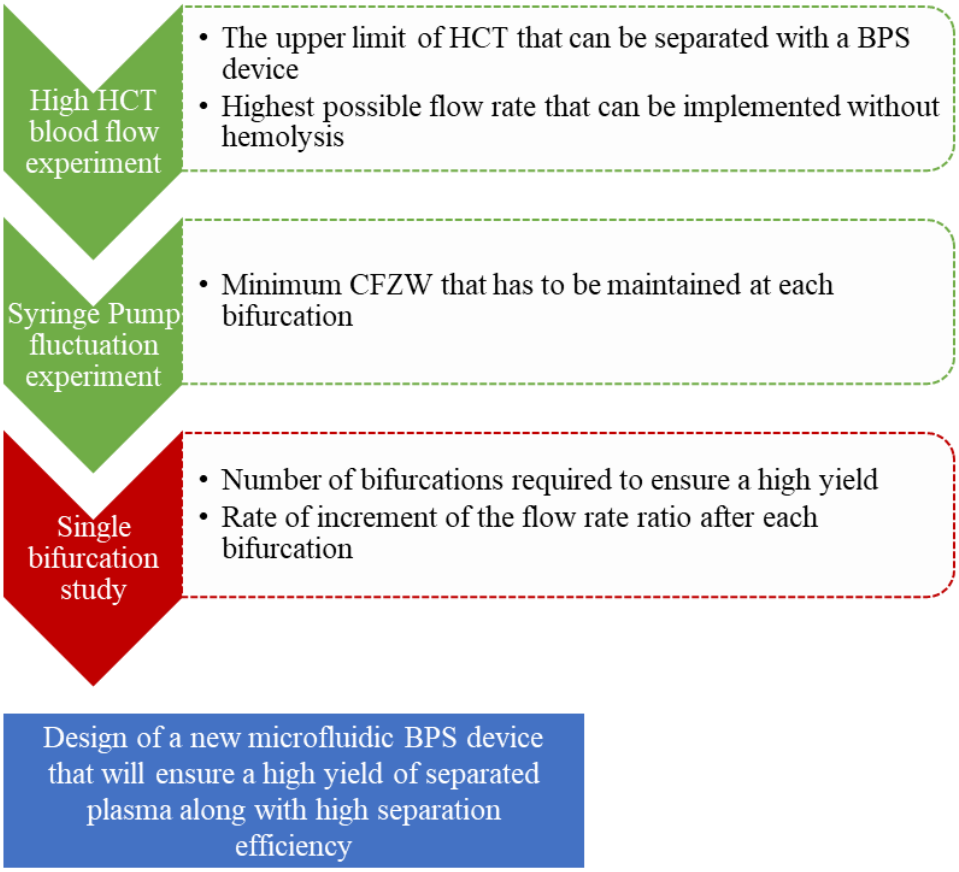

Figure 6.2: The process chart of designing a high-performance microfluidic BPS device. Studies coloured in green are already investigated and the red one is yet to be investigated in future.

Although microfluidic BPS has a number of advantages, including being less expensive because it requires lower sample sizes and reagent volumes, being portable, and being compatible with continuous flow operations, centrifugation remains the gold standard for BPS to date. The required amount of plasma in many diagnostic methods like plasma fibrinogen detection, monitoring organ transplantation, liquid biopsy and NIPT is in the range of 1 to 10 mL, or above [43], [50], [315], [349], [350]. Any requirement above 1mL of undiluted plasma is not deliverable in a fast manner by currently available microfluidic BPS (non-centrifugal) devices whose yield and flow rates are very low.

During my PhD, it was expected that a newly developed high-yield BPS device with a high throughput would be produced for integration into an automated cfDNA extraction platform. After investigating some of the key parameters that influence the performance of microfluidic BPS, it became apparent that a microfluidic device with a high yield and high flow rate (~20 mL/h) could be developed and coupled with low-cfDNA-required assays that only require 0.5 to 2 mL of plasma. A flow rate between 15 mL/h and 20 mL/h may seem high for a microfluidic setting, but such flow rates would not suffice to separate high volume blood (>4 mL) in a short period like within 10 minutes. For instance, several non-invasive cancer diagnosis procedures require 10 mL blood for analysis of the cfDNA present in plasma, therefore a microfluidic BPS device with a 20 mL/h flow rate will take 30 minutes to process this amount of blood, which is not feasible and would weigh down the entire procedure. Therefore, a parallel investigation has been conducted alongside the microfluidic approach to the development of a low-cost centrifugation system to facilitate high volume BPS (>4 mL).

The developed low-cost microcentrifuge rotor (version E2) (Chapter 5) is able to ensure comparable separation performance to the bulky, high-cost refrigerated centrifuge that is widely used to separate the large volume of plasma that is required in many blood-based biomarker detections including cfDNA analyses. This newly developed setup (microcentrifuge & custom printed rotor) costs only around $140 and is able to separate two 9 mL clinical blood samples in the same collection tube immediately after blood withdrawal. This cost-effective centrifugation method ensured 95% plasma yield within 10 minutes, the same as the refrigerated control centrifuge. The estimated percentage of hemolysis in the device is between 1 to 1.7% which is below the acceptable range provided by the American Society for Clinical Pathology [333]. To assess the quality of the plasma separated using the developed setup, a variety of observations and assays were performed and evaluated against the benchmark. The developed centrifuge is capable of extracting the same amount of Albumin as the control centrifuge and can be employed in plasma protein studies. Furthermore, the performance of this customised centrifuge in platelet separation is better than the control due to its high speed, which can be useful in coagulation studies. Only the cfDNA concentration was slightly higher than the control after 10 minutes of centrifugation which can be alleviated by further optimisation of vibration or potentially by a slightly longer time spin. In a nutshell, this developed centrifugation setup costs only a fraction of the total price of the commercial refrigerated centrifuge yet provides similar performance.

Three modifications are planned for the adapted centrifuge future development, which will considerably increase BPS performance as well as aid in the separation of other biological samples (e.g., algae). The first one is the centrifuge speed control, which will be accomplished by connecting a potentiometer to the centrifuge. This is necessary for lowering the centrifuge speed required for cultured cell pelleting, as high-speed centrifugation can induce cell damage in these situations [351], [352]. Secondly, falcon tubes with a capacity of 15 mL are commonly used in biological laboratories to handle a variety of biological materials, including blood. To be able to handle the 15 mL falcon tube using the same rotor used in S-Monovette tube handling, the lid can be replaced by additional two parts (connector and lid). Introducing these two parts will facilitate the separation of samples in 15 mL falcon tubes. Finally, the tubes inside the rotor will be prevented from touching the sidewall by making the fastest design, E5, hollow, which should improve separation performance over the control refrigerated centrifugation.

In conclusion, this thesis investigates the use of microfluidics and centrifugation as solutions to low to high-volume BPS (0.5 mL-10 mL). Future designers are expected to develop high-performance hydrodynamic BPS devices that can extract low and mid-volume plasma (typically 0.25-2 mL) in the lowest feasible time using the microfluidic technique presented here. In addition, the newly developed low-cost centrifuge system could make a positive contribution to near-patient, field applications that handle large volume biological samples. Figure 6.3 shows the best separation methods for analysing several blood-based molecular biomarkers based on their initial blood volume requirements.

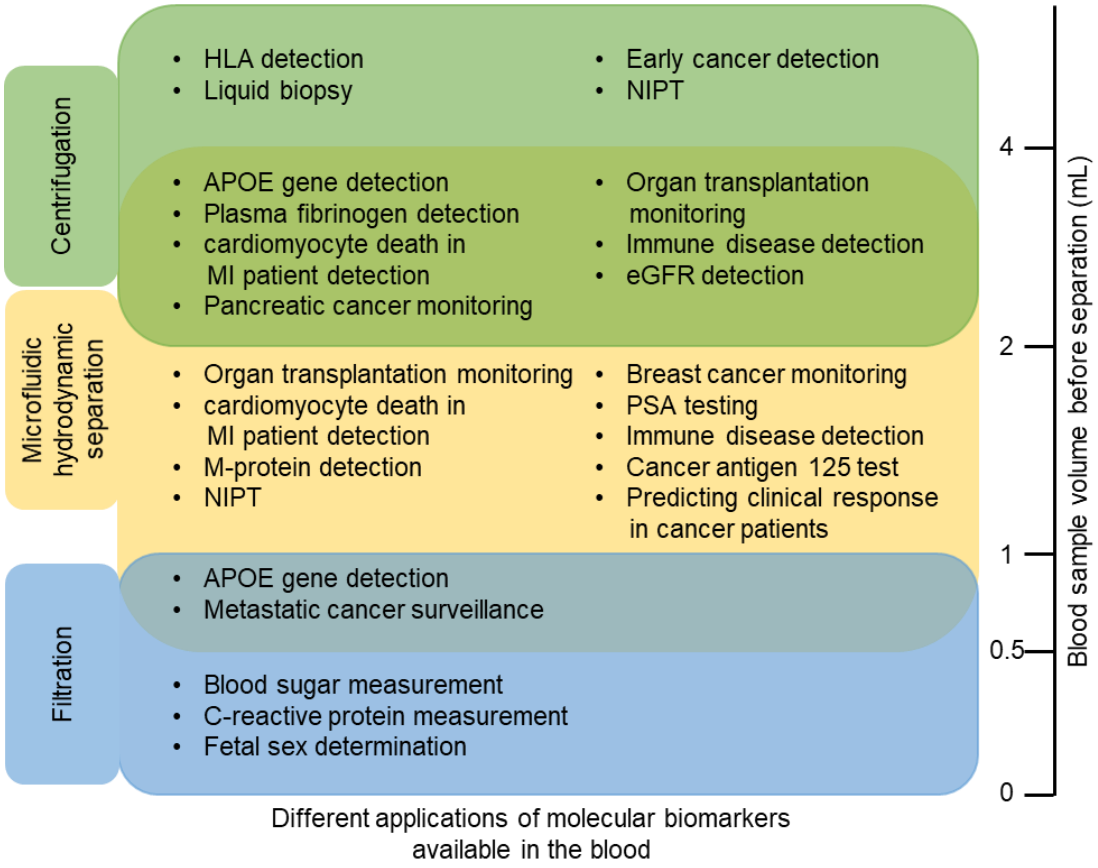

Figure 6.3: Suitable separation methods for different plasma-based diagnostics methods requiring different volumes of separated plasma after BPS [12], [15], [22]–[25], [29], [32], [35], [40]–[43], [50], [65], [68], [69], [315], [349], [350], [353]–[357]**.**

Appendix A

A.1

Raw data for CFZW (CCRM acquisition) and pressure (LabSmith pressure sensor acquisition) for 50% milk dilution. The dataset was aligned manually, since the image acquisition and the pressure acquisition could not be automatically synchronised. However, the CFZWperfectly mirror the pressure sensor acquisition. The pressure sensor provides 30 samples per second whereas the CCRM camera is able to capture 210 frames per second.

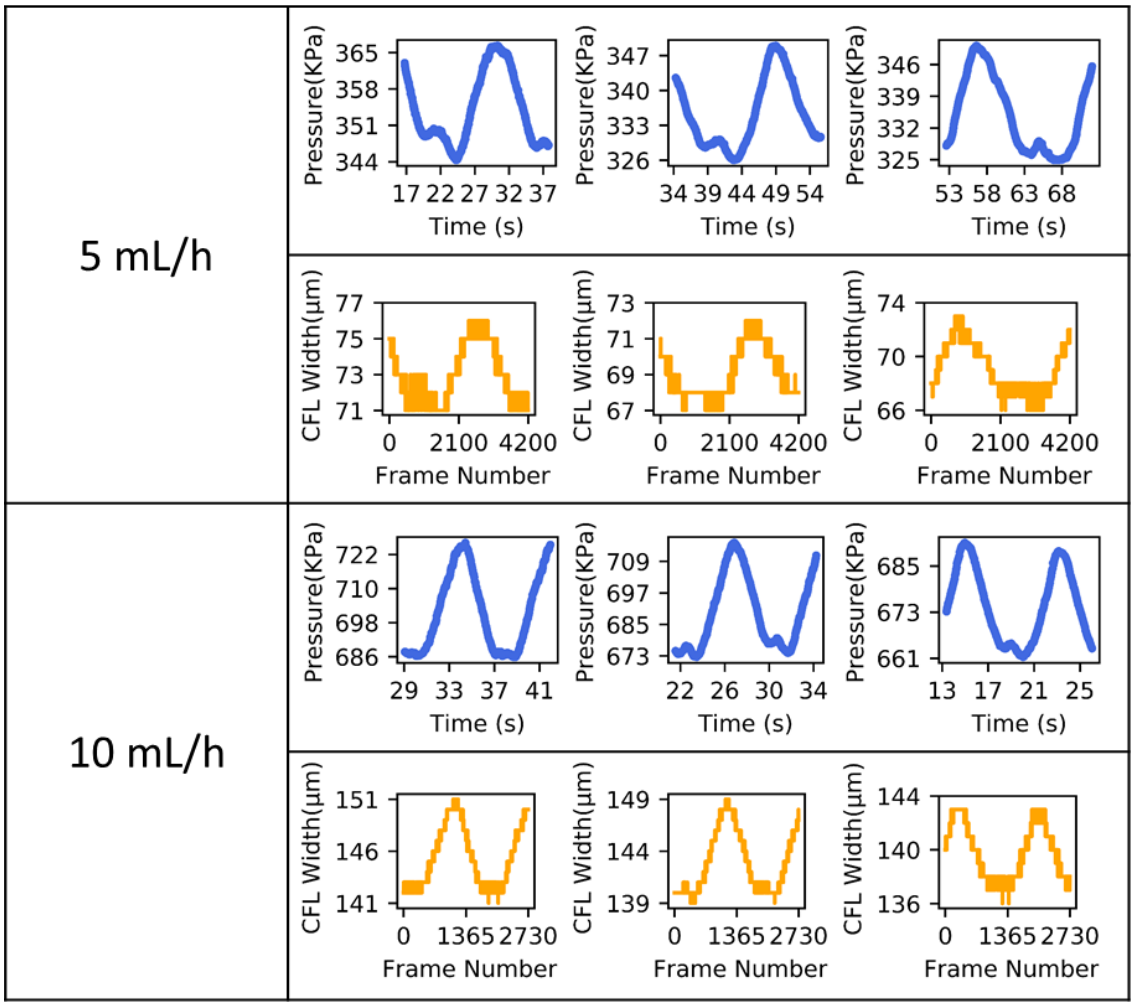

15 mL/h	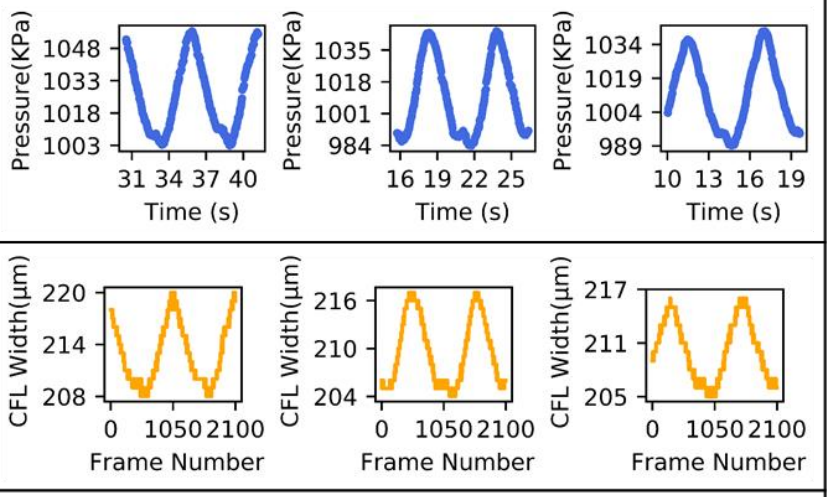
20 mL/h	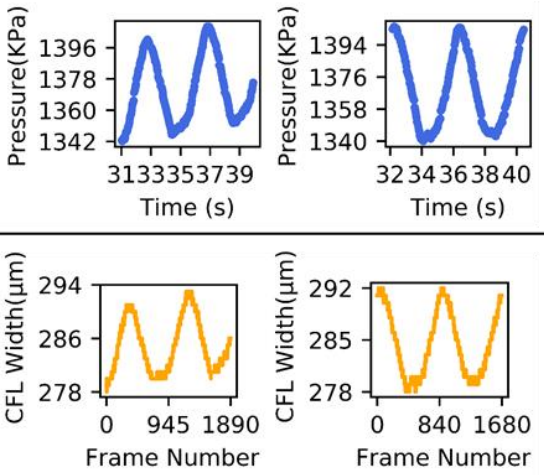
25 mL/h	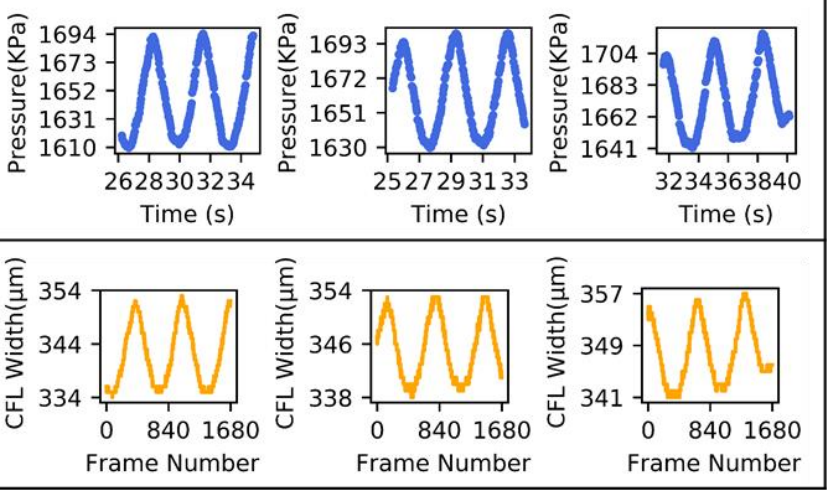

A.2

Raw data for CFZW (CCRM acquisition) and pressure (LabSmith pressure sensor acquisition) for 20% milk dilution. The dataset was aligned manually, since the image acquisition and the pressure acquisition could not be automatically synchronised. However, the CFZWperfectly mirror the pressure sensor acquisition. The pressure sensor provides 30 samples per second whereas the CCRM camera is able to capture 210 frames per second.

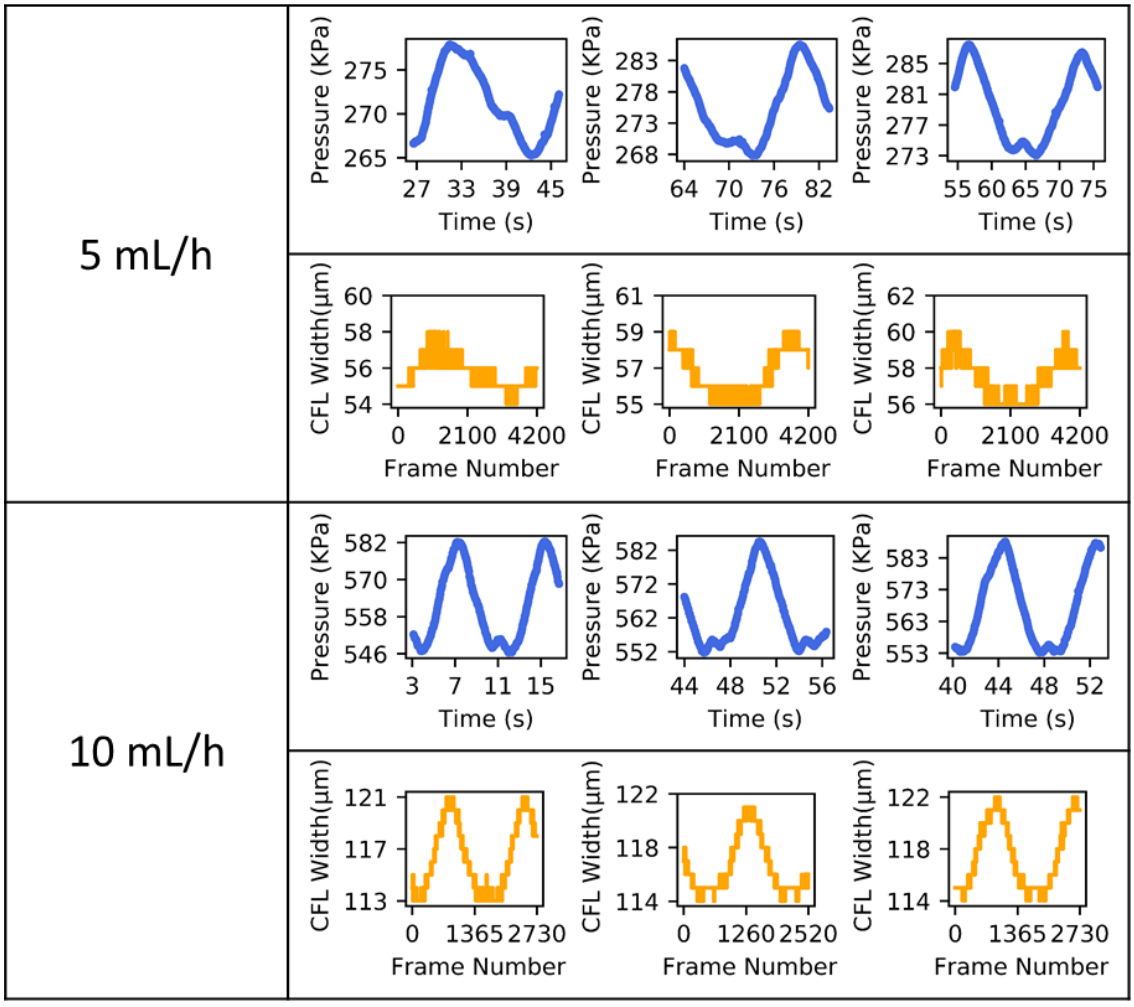

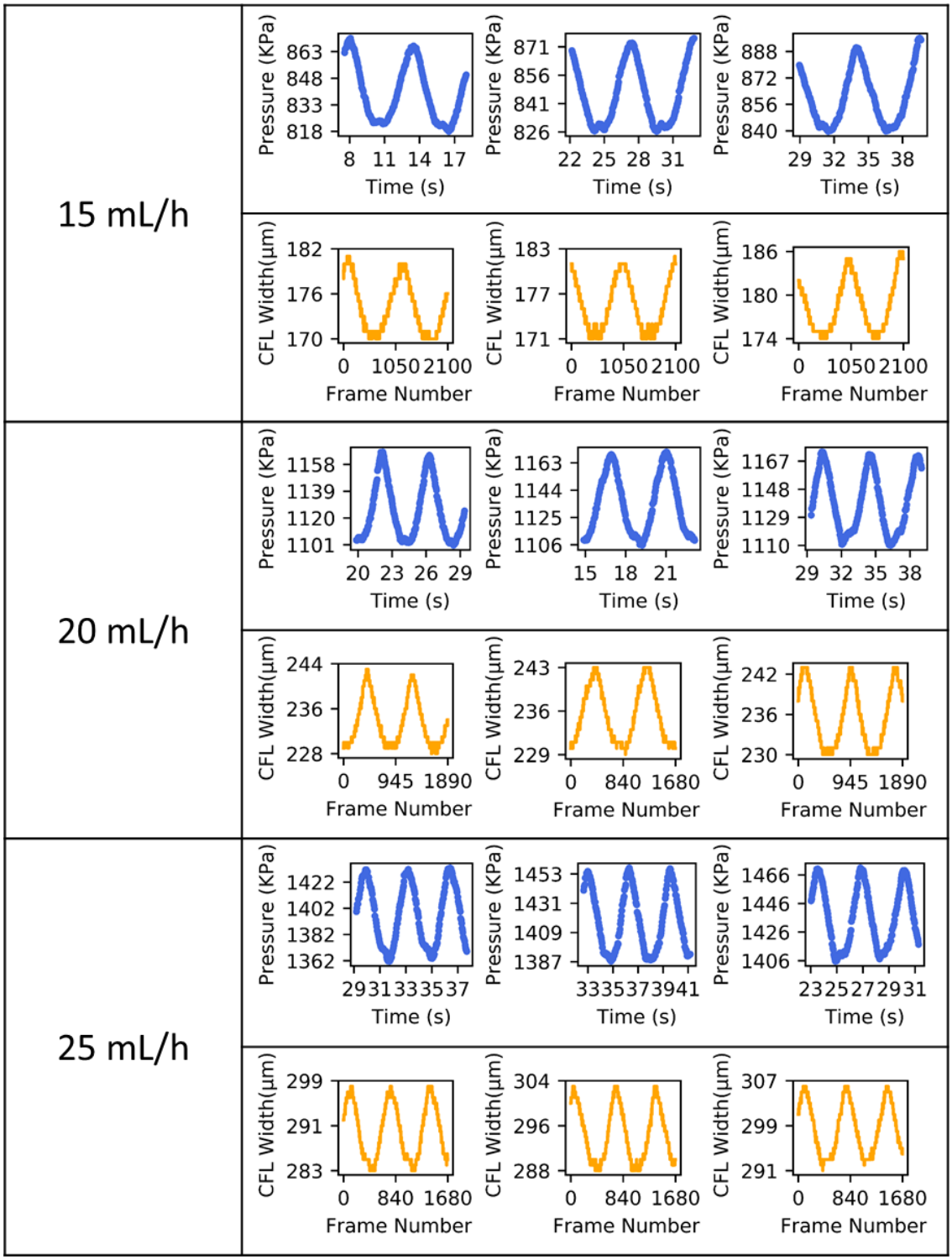
15 mL/h
Pressure (KPa)
863
848
833
818
8 11 14 17
Time (s)
Pressure (KPa)
871
856
841
826
22 25 28 31
Time (s)
Pressure (KPa)
888
872
856
840
29 32 35 38
Time (s)
CFL Width(μm)
182
176
170
0 1050 2100
Frame Number
CFL Width(μm)
183
177
171
0 1050 2100
Frame Number
CFL Width(μm)
186
180
174
0 1050 2100
Frame Number
20 mL/h
Pressure (KPa)
1158
1139
1120
1101
20 23 26 29
Time (s)
Pressure (KPa)
1163
1144
1125
1106
15 18 21
Time (s)
Pressure (KPa)
1167
1148
1129
1110
29 32 35 38
Time (s)
CFL Width(μm)
244
236
228
0 945 1890
Frame Number
CFL Width(μm)
243
236
229
0 840 1680
Frame Number
CFL Width(μm)
242
236
230
0 945 1890
Frame Number
25 mL/h
Pressure (KPa)
1422
1402
1382
1362
29 31 33 35 37
Time (s)
Pressure (KPa)
1453
1431
1409
1387
33 35 37 39 41
Time (s)
Pressure (KPa)
1466
1446
1426
1406
23 25 27 29 31
Time (s)
CFL Width(μm)
299
291
283
0 840 1680
Frame Number
CFL Width(μm)
304
296
288
0 840 1680
Frame Number
CFL Width(μm)
307
299
291
0 840 1680
Frame Number

A.3

Raw data for CFZW (CCRM acquisition) and pressure (LabSmith pressure sensor acquisition) for 10% milk dilution. The dataset was aligned manually, since the image acquisition and the pressure acquisition could not be automatically synchronised. However, the CFZWperfectly mirror the pressure sensor acquisition. The pressure sensor provides 30 samples per second whereas the CCRM camera is able to capture 210 frames per second.

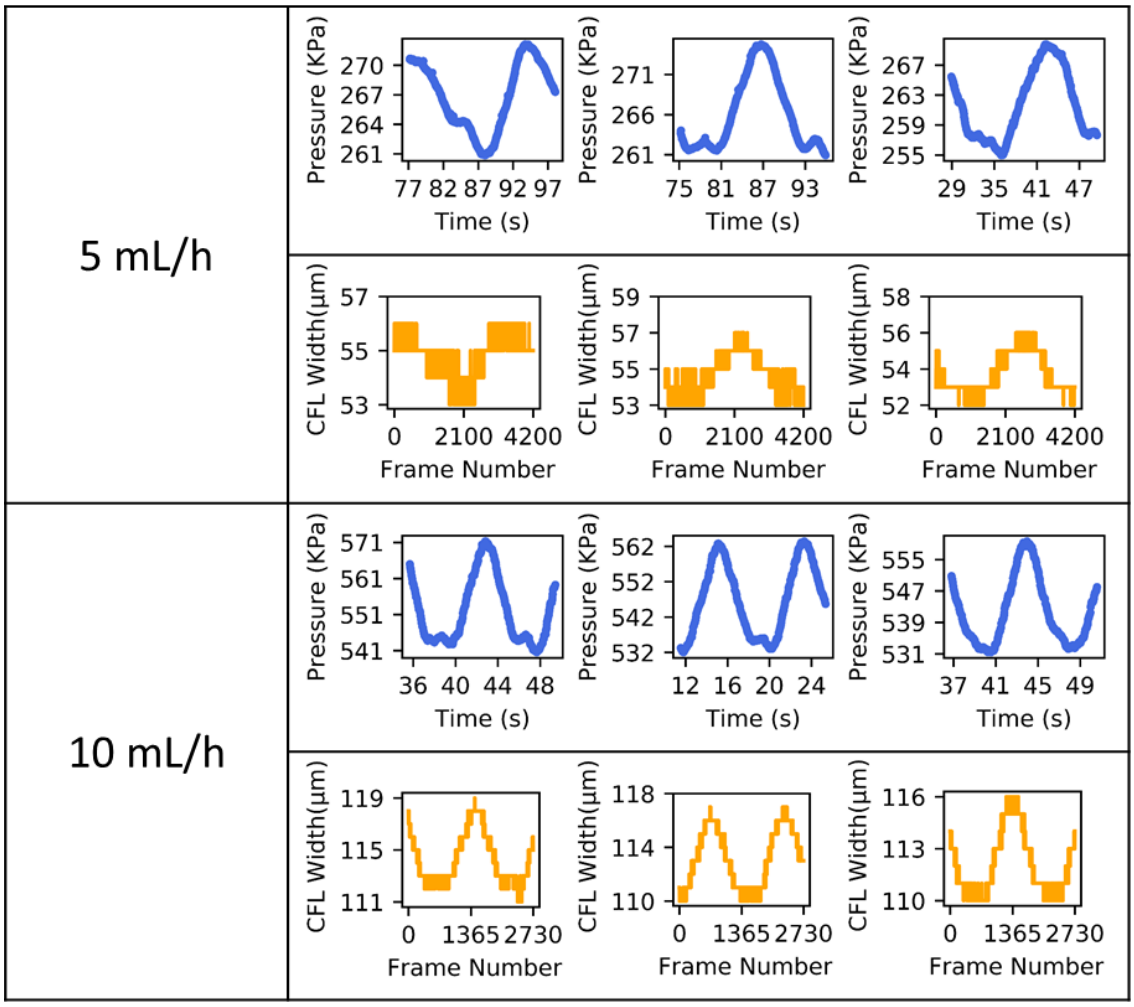

15 mL/h	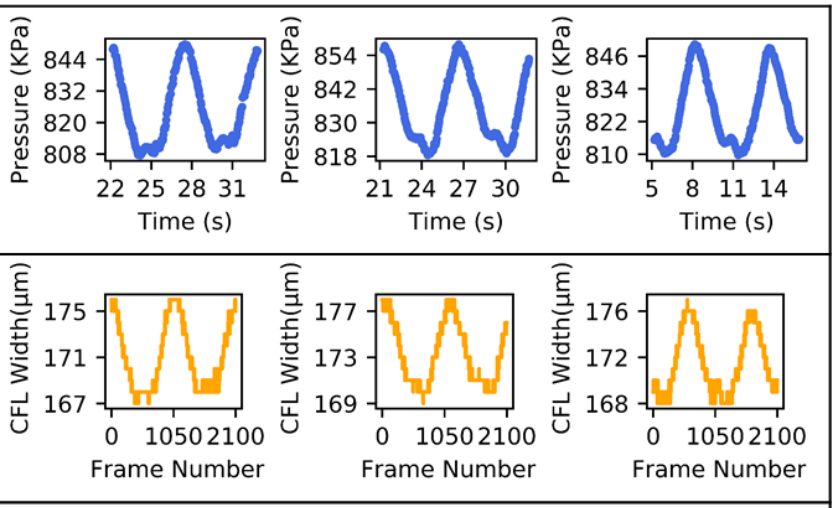
20 mL/h	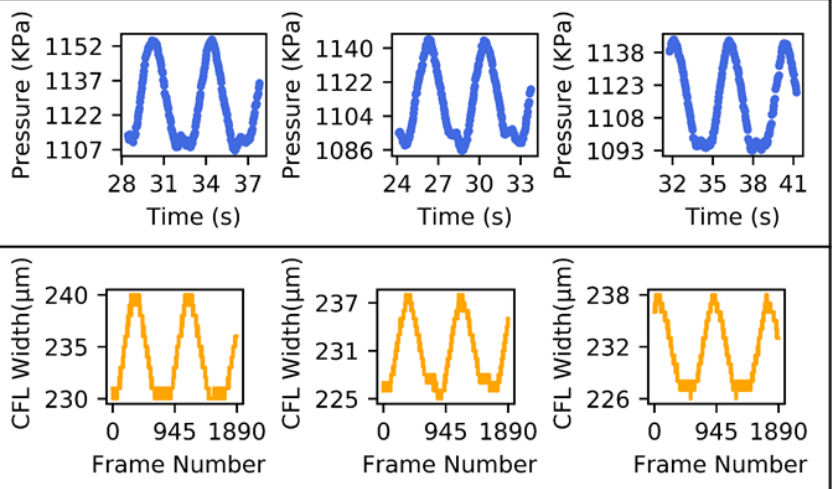
25 mL/h	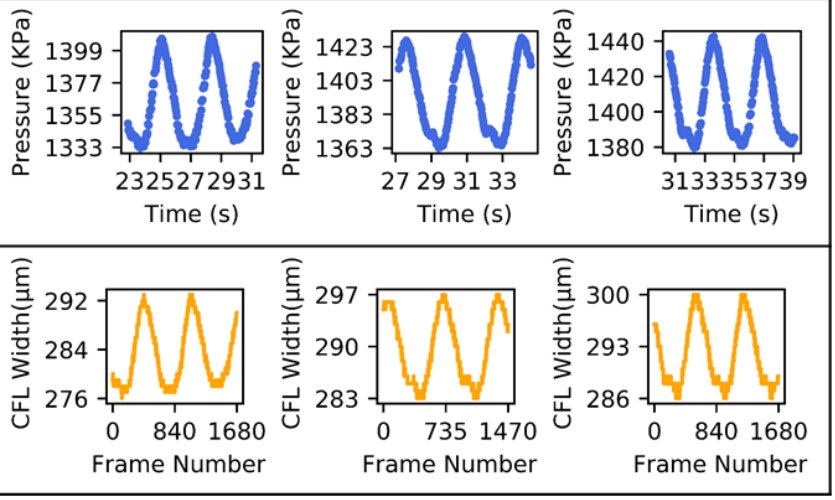

Appendix B

Python code for deflection measurement from recorded video.

```
#Matplotlib inline library
import cv2
import numpy as np
import time
import matplotlib.pyplot as plt
import os
import pandas as pd
from openpyxl import load_workbook

cv2.namedWindow("window")
def nothing(x):
    pass
# for finding optimal values
cv2.createTrackbar("upper", "window", 0, 255, nothing)
cv2.createTrackbar("lower", "window", 0, 255, nothing)
vid = cv2.VideoCapture('Documents/matplotlib/3rd phase/corrected/c2.mp4')
cap = cv2.VideoCapture('Documents/matplotlib/3rd phase/corrected/c2.mp4')
_, img = cap.read()
img = cv2.resize(img, (450, 700))
gray = cv2.cvtColor(img, cv2.COLOR_BGR2GRAY)
while True:

    # sets x and y which will be used later for edge detection
    x = cv2.getTrackbarPos('lower', 'window')
    y = cv2.getTrackbarPos('upper', 'window')

    edge = cv2.Canny(gray, x, y)
    cv2.imshow('window', edge)
    if cv2.waitKey(1) == 27:
        cv2.destroyAllWindows()
        break
```

```
orig = 76
diff = []
initial = False
while True:
    try:
        _, frm = vid.read()
        frm = cv2.resize(frm, (450, 700))
        gray = cv2.cvtColor(frm, cv2.COLOR_BGR2GRAY)
        img = cv2.Canny(gray, x, y)

        #saving one image for pixel calculation
        path = 'Documents/matplotlib/3rd phase/corrected/'
        cv2.imwrite(os.path.join(path , 'c2.jpg'), img)

        # thresholding to only have either pixel value 0 or 255
        _, img = cv2.threshold(img, 0, 255, cv2.THRESH_BINARY)
        cv2.imshow("winname", img)

        # refrence line
        gr = img[220, 115:170]
        #gr = img[233, 30:70]=255
        #cv2.imshow("gr", img)

        if not(initial):
            # setting refrence point
            ref = np.argmax(gr)
            initial = True

        # getting current positon
        curr_val = np.argmax(gr)

        print(gr)
        print(ref)
        print(curr_val)
        print(ref-curr_val)
```

```
        # getting and appending deflection from ref point
        if curr_val != 0:
            diff.append(ref-curr_val)
        else:
            diff.append(0)
    except:
        break
    if cv2.waitKey(1) == 27:
        break
cv2.destroyAllWindows()
print(diff)
t = np.arange(len(diff))
#writing to specific excel sheet using path & df to excel
path= r"Documents/matplotlib/3rd phase/corrected/3rd phase.xlsx"
book = load_workbook(path)
writer = pd.ExcelWriter(path, engine = 'openpyxl')
writer.book = book
#writer = pd.ExcelWriter(path, engine = 'xlsxwriter')
df = pd.DataFrame(diff)
df.to_excel(writer, sheet_name = 'C2_XY')
writer.save()
writer.close()
# plotting everything
plt.plot(t ,diff)
plt.show()
```

Appendix C

Real-time deflection measurement from the recorded video of Designs C, D, E0, E2, E5.

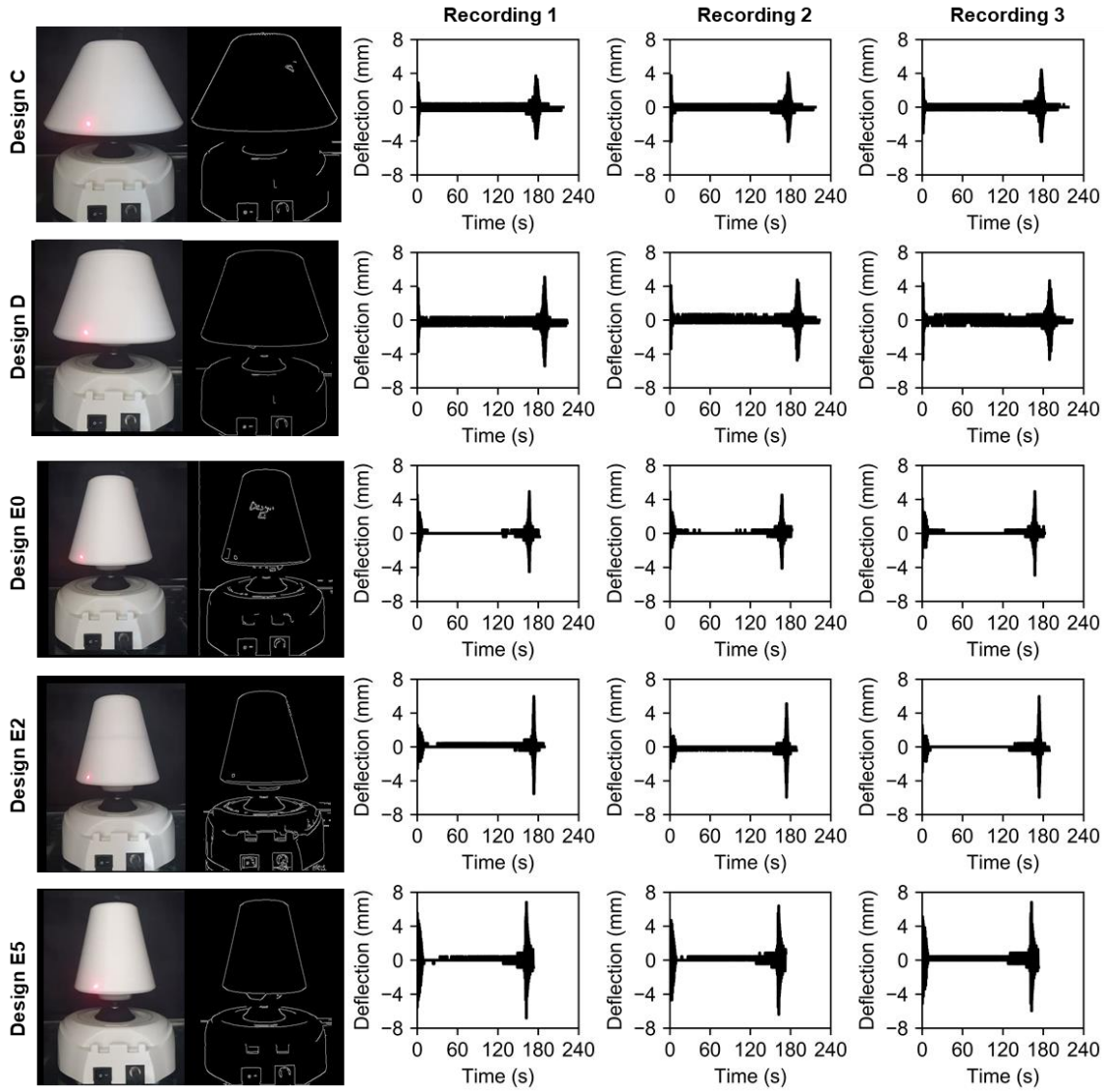

Bibliography

[1] A. St John and C. P. Price, "Existing and Emerging Technologies for Point-of-Care Testing.," *Clin. Biochem. Rev.*, vol. 35, no. 3, 2014.

[2] S. Sachdeva, R. W. Davis, and A. K. Saha, "Microfluidic Point-of-Care Testing: Commercial Landscape and Future Directions," *Frontiers in Bioengineering and Biotechnology*, vol. 8. 2021.

[3] P. B. Luppa, C. Müller, A. Schlichtiger, and H. Schlebusch, "Point-of-care testing (POCT): Current techniques and future perspectives," *TrAC - Trends in Analytical Chemistry*, vol. 30, no. 6. 2011.

[4] J. H. Nichols, "The future of point-of-care testing," *Point Care*, vol. 7, no. 4, pp. 271–273, Dec. 2008.

[5] D. Li, "Single-Phase Electrokinetic Flow in Microchannels," in *Heat Transfer and Fluid Flow in Minichannels and Microchannels*, 2013.

[6] W. H. Mueller, "Biological markers in epidemiology. Edited by B. S. Hulka, T. C. Wilcosky, and J. D. Griffith. xi + 236 pp. New York: Oxford University Press, 1990, $40.00 (cloth)," *Am. J. Hum. Biol.*, vol. 3, no. 2, 1991.

[7] FDA-NIH Biomarker Working Group, "BEST (Biomarkers, EndpointS, and other Tools) Resource Glossary," *Food Drug Adm. Natl. Institutes Heal.*, no. Md, 2016.

[8] P. E. Geyer, L. M. Holdt, D. Teupser, and M. Mann, "Revisiting biomarker discovery by plasma proteomics," *Mol. Syst. Biol.*, vol. 13, no. 9, p. 942, Sep. 2017.

[9] S. Mukherjee, T. G. Kang, Y. Chen, and S. Kim, "Plasma separation from blood: The lab-on-a-chip approach," *Critical Reviews in Biomedical Engineering*, vol. 37, no. 6. 2009.

[10] S. Lopez-Giacoman and M. Madero, "Biomarkers in chronic kidney disease, from kidney function to kidney damage," *World J. Nephrol.*, vol. 4, no. 1, pp. 57–73, Feb. 2015.

[11] G. Gentile and G. Remuzzi, "Novel Biomarkers for Renal Diseases? None for the Moment (but One)," *Journal of Biomolecular Screening*, vol. 21, no. 7. 2016.

[12] R. Kalyesubula *et al.*, "How to estimate glomerular filtration rate in sub-Saharan Africa: Design and methods of the African Research into Kidney Diseases (ARK) study," *BMC Nephrol.*, vol. 21, no. 1, 2020.

[13] T. J. Lyons and A. Basu, "Biomarkers in diabetes: hemoglobin A1c, vascular and tissue markers," *Transl. Res.*, vol. 159, no. 4, pp. 303–312, Apr. 2012.

[14] L. A. C. Wright and I. B. Hirsch, "The challenge of the use of glycemic biomarkers in diabetes: Reflecting on hemoglobin A1C, 1,5-anhydroglucitol, and the glycated

proteins fructosamine and glycated albumin," *Diabetes Spectrum*, vol. 25, no. 3. 2012.

[15] D. Pickering and J. Marsden, "How to measure blood glucose," *Community Eye Health Journal*, vol. 27, no. 87. 2014.

[16] G. Siravegna, S. Marsoni, S. Siena, and A. Bardelli, "Integrating liquid biopsies into the management of cancer," *Nat. Rev. Clin. Oncol.*, vol. 14, no. 9, pp. 531–548, 2017.

[17] D. A. Haber and V. E. Velculescu, "Blood-Based Analyses of Cancer: Circulating Tumor Cells and Circulating Tumor DNA," *Cancer Discov.*, vol. 4, no. 6, pp. 650 LP – 661, Jun. 2014.

[18] S. Zhang *et al.*, "Elevated Plasma cfDNA May be Associated with Active Lupus Nephritis and Partially Attributed to Abnormal Regulation of Neutrophil Extracellular Traps (NETs) in Patients with Systemic Lupus Erythematosus," *Internal medicine.*, vol. 53, no. 24. Tokyo, Japan :, pp. 2763–2771, 2014.

[19] M. Dunaeva, M. Derksen, and G. J. M. Pruijn, "LINE-1 Hypermethylation in Serum Cell-Free DNA of Relapsing Remitting Multiple Sclerosis Patients," *Mol. Neurobiol.*, vol. 55, no. 6, pp. 4681–4688, 2018.

[20] A. J. Vivanti *et al.*, "Optimal non-invasive diagnosis of fetal achondroplasia combining ultrasonography with circulating cell-free fetal DNA analysis," *Ultrasound Obstet. Gynecol.*, vol. 53, no. 1, pp. 87–94, Jan. 2019.

[21] X. Chen *et al.*, "Non-invasive early detection of cancer four years before conventional diagnosis using a blood test," *Nat. Commun.*, vol. 11, no. 1, 2020.

[22] S. Tug *et al.*, "Correlation between cell free DNA levels and medical evaluation of disease progression in systemic lupus erythematosus patients," *Cell. Immunol.*, vol. 292, no. 1–2, pp. 32–39, Nov. 2014.

[23] O. M. Hendy *et al.*, "Circulating cell free DNA as a predictor of systemic lupus erythematosus severity and monitoring of therapy," *Egypt. J. Med. Hum. Genet.*, vol. 17, no. 1, 2016.

[24] N. Kazachkova, J. Gontar, O. Verlinsky, and I. Ilyin, "Successful early fetal sex determination using cell-free fetal DNA isolated from maternal capillary blood: A pilot study," *Eur. J. Obstet. Gynecol. Reprod. Biol. X*, vol. 3, 2019.

[25] B. Vincze *et al.*, "Sex determination using circulating cell-free fetal DNA in small volume of maternal plasma in elephants," *Sci. Rep.*, vol. 9, no. 1, 2019.

[26] R. A. Kyle *et al.*, "A Long-Term Study of Prognosis in Monoclonal Gammopathy of Undetermined Significance," *N. Engl. J. Med.*, vol. 346, no. 8, pp. 564–569,

Feb. 2002.

[27] M. Zajec *et al.*, “Mass Spectrometry for Identification, Monitoring, and Minimal Residual Disease Detection of M-Proteins,” *Clinical chemistry*, vol. 66, no. 3. 2020.

[28] A. Gruber and J. Griffin, “Direct detection of activated protein C in blood from human subjects,” *Blood*, vol. 79, no. 9, 1992.

[29] O. Landgren *et al.*, “Monoclonal gammopathy of undetermined significance (MGUS) consistently precedes multiple myeloma: A prospective study,” *Blood*, vol. 113, no. 22, 2009.

[30] T. Ian *et al.*, “Guideline for the Management of Clinically Localized Prostate Cancer: 2007 Update,” *J. Urol.*, vol. 177, no. 6, pp. 2106–2131, Jun. 2007.

[31] S. H. M. and E. M. A., “Assessing and Treating Patients With Increasing Prostate Specific Antigen Following Radical Prostatectomy,” *J. Urol.*, vol. 178, no. 3S, pp. S20–S24, Sep. 2007.

[32] N. Hara *et al.*, “Reverse transcription-polymerase chain reaction detection of prostate-specific antigen, prostate-specific membrane antigen, and prostate stem cell antigen in one milliliter of peripheral blood: Value for the staging of prostate cancer,” *Clin. Cancer Res.*, vol. 8, no. 6, 2002.

[33] F. Gundogdu, F. Soylu, L. Erkan, O. Tatli, S. Mavi, and A. Yavuzcan, “The role of serum CA-125 levels and CA-125 tissue expression positivity in the prediction of the recurrence of stage III and IV epithelial ovarian tumors (CA-125 levels and tissue CA-125 in ovarian tumors),” *Arch. Gynecol. Obstet.*, vol. 283, no. 6, pp. 1397–1402, 2011.

[34] G. J. S. Rustin, M. Marples, A. E. Nelstrop, M. Mahmoudi, and T. Meyer, “Use of CA-125 to Define Progression of Ovarian Cancer in Patients With Persistently Elevated Levels,” *J. Clin. Oncol.*, vol. 19, no. 20, pp. 4054–4057, Oct. 2001.

[35] G. Wang *et al.*, “Nipple discharge of CA15-3, CA125, CEA and TSGF as a new biomarker panel for breast cancer,” *Int. J. Mol. Sci.*, vol. 15, no. 6, 2014.

[36] M. Del Re *et al.*, “The amount of activating EGFR mutations in circulating cell-free DNA is a marker to monitor osimertinib response,” *Br. J. Cancer*, vol. 119, no. 10, pp. 1252–1258, 2018.

[37] I. Lyskjær *et al.*, “Correlation between early dynamics in circulating tumour DNA and outcome from FOLFIRI treatment in metastatic colorectal cancer,” *Sci. Rep.*, vol. 9, no. 1, p. 11542, 2019.

[38] Y. Lo, “Presence of donor-specific DNA in plasma of kidney and liver-transplant

recipients," *The lancet.*, vol. 351, no. 9112. [London] , p. 1329, 1998.

[39] E. M. Gielis *et al.*, "Cell-Free DNA: An Upcoming Biomarker in Transplantation," *Am. J. Transplant.*, vol. 15, no. 10, pp. 2541–2551, Oct. 2015.

[40] H. Lee, C. Park, W. Na, K. H. Park, and S. Shin, "Precision cell-free DNA extraction for liquid biopsy by integrated microfluidics," *npj Precis. Oncol.*, vol. 4, no. 1, 2020.

[41] M. Toledano-Fonseca *et al.*, "Circulating cell-free dna-based liquid biopsy markers for the non-invasive prognosis and monitoring of metastatic pancreatic cancer," *Cancers (Basel).*, vol. 12, no. 7, 2020.

[42] P. M. K. Gordon *et al.*, "An Algorithm Measuring Donor Cell-Free DNA in Plasma of Cellular and Solid Organ Transplant Recipients That Does Not Require Donor or Recipient Genotyping," *Front. Cardiovasc. Med.*, vol. 3, 2016.

[43] M. Grskovic *et al.*, "Validation of a Clinical-Grade Assay to Measure Donor-Derived Cell-Free DNA in Solid Organ Transplant Recipients," *J. Mol. Diagnostics*, vol. 18, no. 6, 2016.

[44] S. G. Roberts, M. L. Blute, E. J. Bergstralh, J. M. Slezak, and H. Zincke, "PSA Doubling Time as a Predictor of Clinical Progression After Biochemical Failure Following Radical Prostatectomy for Prostate Cancer," *Mayo Clin. Proc.*, vol. 76, no. 6, pp. 576–581, Jun. 2001.

[45] L. Collette, T. M. De Reijke, F. H. Schröder, and G. Aus, "Prostate specific antigen: A prognostic marker of survival in good prognosis metastatic prostate cancer? (EORTC 30892)," *Eur. Urol.*, vol. 44, no. 2, 2003.

[46] G. K. Zagars, "Prostate-specific antigen as a prognostic factor for prostate cancer treated by external beam radiotherapy," *Int. J. Radiat. Oncol. Biol. Phys.*, vol. 23, no. 1, 1992.

[47] T. H. Kim, D. K. Oh, Y.-M. Oh, S. W. Lee, S. Do Lee, and J. S. Lee, "Fibrinogen as a potential biomarker for clinical phenotype in patients with chronic obstructive pulmonary disease," *J. Thorac. Dis.*, vol. 10, no. 9, pp. 5260–5268, Sep. 2018.

[48] B. E. Miller *et al.*, "Plasma Fibrinogen Qualification as a Drug Development Tool in Chronic Obstructive Pulmonary Disease. Perspective of the Chronic Obstructive Pulmonary Disease Biomarker Qualification Consortium," *Am. J. Respir. Crit. Care Med.*, vol. 193, no. 6, pp. 607–613, Jan. 2016.

[49] R. S. Rosenson, B. A. Staffileno, and C. C. Tangney, "Effects of tourniquet technique, order of draw, and sample storage on plasma fibrinogen," *Clin. Chem.*, vol. 44, no. 3, 1998.

[50] M. Blome *et al.*, “Relationship between factor XIII activity, fibrinogen, haemostasis screening tests and postoperative bleeding in cardiopulmonary bypass surgery,” *Thromb. Haemost.*, vol. 93, no. 6, 2005.

[51] S. Valpione *et al.*, “Plasma total cell-free DNA (cfDNA) is a surrogate biomarker for tumour burden and a prognostic biomarker for survival in metastatic melanoma patients,” *Eur. J. Cancer*, vol. 88, pp. 1–9, 2018.

[52] R. J. Hendriks *et al.*, “Epigenetic markers in circulating cell-free DNA as prognostic markers for survival of castration-resistant prostate cancer patients,” *Prostate*, vol. 78, no. 5, pp. 336–342, Apr. 2018.

[53] M. H. Hyun *et al.*, “Quantification of circulating cell-free DNA to predict patient survival in non-small-cell lung cancer,” *Oncotarget*, vol. 8, no. 55, 2017.

[54] N. Berka, J. M. Gill, A. Liacini, T. O’Bryan, and F. M. Khan, “Human leukocyte antigen (HLA) and pharmacogenetics: screening for HLA-B*57:01 among human immunodeficiency virus–positive patients from southern Alberta,” *Hum. Immunol.*, vol. 73, no. 2, pp. 164–167, 2012.

[55] A. R. Hughes *et al.*, “Pharmacogenetics of hypersensitivity to abacavir: From PGx hypothesis to confirmation to clinical utility,” *Pharmacogenomics Journal*, vol. 8, no. 6. 2008.

[56] J. M. Heward *et al.*, “ Linkage Disequilibrium between the Human Leukocyte Antigen Class II Region of the Major Histocompatibility Complex and Graves’ Disease: Replication Using a Population Case Control and Family-Based Study 1 ,” *J. Clin. Endocrinol. Metab.*, vol. 83, no. 10, 1998.

[57] M. Halonen *et al.*, “AIRE mutations and human leukocyte antigen genotypes as determinants of the autoimmune polyendocrinopathy-candidiasis-ectodermal dystrophy phenotype,” *J. Clin. Endocrinol. Metab.*, vol. 87, no. 6, 2002.

[58] S. Park, E. J. Lee, C. H. Rim, and J. Seong, “Plasma Cell-Free DNA as a Predictive Marker after Radiotherapy for Hepatocellular Carcinoma,” *ymj*, vol. 59, no. 4, pp. 470–479, May 2018.

[59] M. Yuan, L.-L. Huang, J.-H. Chen, J. Wu, and Q. Xu, “The emerging treatment landscape of targeted therapy in non-small-cell lung cancer,” *Signal Transduct. Target. Ther.*, vol. 4, no. 1, p. 61, 2019.

[60] P. Wang *et al.*, “Sensitive detection of mono- and polyclonal ESR1 mutations in primary tumors, metastatic lesions, and cell-free DNA of breast cancer patients,” *Clin. Cancer Res.*, vol. 22, no. 5, 2016.

[61] D. Fernandez-Garcia *et al.*, “Plasma cell-free DNA (cfDNA) as a predictive and

prognostic marker in patients with metastatic breast cancer," *Breast Cancer Res.*, vol. 21, no. 1, 2019.

[62] T. A. Pearson *et al.*, "Markers of Inflammation and Cardiovascular Disease," *Circulation*, vol. 107, no. 3, 2003.

[63] P. M. Ridker *et al.*, "Rosuvastatin to prevent vascular events in men and women with elevated C-reactive protein," *Obstetrical and Gynecological Survey*, vol. 64, no. 3. 2009.

[64] H. Peltola and M. Jaakkola, "C-reactive protein in early detection of bacteremic versus viral infections in immunocompetent and compromised children," *J. Pediatr.*, vol. 113, no. 4, 1988.

[65] J. S. Ahn *et al.*, "Development of a point-of-care assay system for high-sensitivity C-reactive protein in whole blood," *Clin. Chim. Acta*, vol. 332, no. 1–2, 2003.

[66] E. Genin *et al.*, "APOE and Alzheimer disease: A major gene with semi-dominant inheritance," *Mol. Psychiatry*, vol. 16, no. 9, 2011.

[67] A. C. Ferguson *et al.*, "Alzheimer's Disease Susceptibility Gene Apolipoprotein e (APOE) and Blood Biomarkers in UK Biobank (N=395,769)," *J. Alzheimer's Dis.*, vol. 76, no. 4, 2020.

[68] G. Kolovou *et al.*, "Association of apolipoprotein E polymorphism with myocardial infarction in Greek patients with coronary artery disease," *Curr. Med. Res. Opin.*, vol. 18, no. 3, 2002.

[69] V. B. Gupta *et al.*, "Plasma apolipoprotein e and Alzheimer disease risk: The AIBL study of aging," *Neurology*, vol. 76, no. 12, 2011.

[70] L. Gu *et al.*, "Association between the apolipoprotein E gene polymorphism and ischemic stroke in Chinese populations: New data and meta-analysis," *Exp. Ther. Med.*, vol. 5, no. 3, 2013.

[71] A. J. Bronkhorst, V. Ungerer, and S. Holdenrieder, "The emerging role of cell-free DNA as a molecular marker for cancer management," *Biomolecular Detection and Quantification*, vol. 17. 2019.

[72] A. N. Butt and R. Swaminathan, "Overview of Circulating Nucleic Acids in Plasma/Serum," *Ann. N. Y. Acad. Sci.*, vol. 1137, no. 1, 2008.

[73] P. Mandel and P. Metais, "Nuclear acids in human blood plasma," *C. R. Seances Soc. Biol. Fil.*, vol. 142, no. 3–4, pp. 241–243, 1948.

[74] K. Sun *et al.*, "Plasma DNA tissue mapping by genome-wide methylation sequencing for noninvasive prenatal, cancer, and transplantation assessments," *Proc. Natl. Acad. Sci.*, vol. 112, no. 40, pp. E5503–E5512, 2015.

[75] G. Perkins *et al.*, "Multi-Purpose Utility of Circulating Plasma DNA Testing in Patients with Advanced Cancers," *PLoS One*, vol. 7, no. 11, 2012.

[76] M. Fleischhacker and B. Schmidt, "Circulating nucleic acids (CNAs) and cancer-A survey," *Biochimica et Biophysica Acta - Reviews on Cancer*, vol. 1775, no. 1. 2007.

[77] G. A. Martins, M. T. Kawamura, and M. D. G. D. C. Carvalho, "Detection of DNA in the plasma of septic patients," in *Annals of the New York Academy of Sciences*, 2000, vol. 906.

[78] A. Rhodes, S. J. Wort, H. Thomas, P. Collinson, and E. D. David, "Plasma DNA concentration as a predictor of mortality and sepsis in critically ill patients," *Crit. Care*, vol. 10, no. 2, 2006.

[79] C. P. Y. Chang, R. H. Chia, T. L. Wu, K. C. Tsao, C. F. Sun, and J. T. Wu, "Elevated cell-free serum DNA detected in patients with myocardial infarction," *Clin. Chim. Acta*, vol. 327, no. 1–2, 2003.

[80] E. Sunami, A. T. Vu, S. L. Nguyen, A. E. Giuliano, and D. S. B. Hoon, "Quantification of LINE1 in circulating DNA as a molecular biomarker of breast cancer," in *Annals of the New York Academy of Sciences*, 2008, vol. 1137.

[81] D. Allen, A. Butt, D. Cahill, M. Wheeler, R. Popert, and R. Swaminathan, "Role of cell-free plasma DNA as a diagnostic marker for prostate cancer," in *Annals of the New York Academy of Sciences*, 2004, vol. 1022.

[82] S. Volik, M. Alcaide, R. D. Morin, and C. Collins, "Cell-free DNA (cfDNA): Clinical significance and utility in cancer shaped by emerging technologies," *Molecular Cancer Research*, vol. 14, no. 10. 2016.

[83] Y. van der Pol and F. Mouliere, "Toward the Early Detection of Cancer by Decoding the Epigenetic and Environmental Fingerprints of Cell-Free DNA," *Cancer Cell*, vol. 36, no. 4. 2019.

[84] "Cell-Free DNA (cfDNA) Testing Market Size Worth USD 22.41 Billion by 2027 | CAGR of 26.2%: Emergen Research." [Online]. Available: https://www.prnewswire.com/news-releases/cell-free-dna-cfdna-testing-market-size-worth-usd-22-41-billion-by-2027--cagr-of-26-2-emergen-research-301155883.html. [Accessed: 31-Oct-2021].

[85] M. Ikami *et al.*, "Immuno-pillar chip: a new platform for rapid and easy-to-use immunoassay," *Lab Chip*, vol. 10, no. 24, pp. 3335–3340, 2010.

[86] E. Stern *et al.*, "Label-free biomarker detection from whole blood," *Nat. Nanotechnol.*, vol. 5, no. 2, pp. 138–142, 2010.

[87] B. V. Chikkaveeraiah, V. Mani, V. Patel, J. S. Gutkind, and J. F. Rusling, "Microfluidic electrochemical immunoarray for ultrasensitive detection of two cancer biomarker proteins in serum," *Biosens. Bioelectron.*, vol. 26, no. 11, pp. 4477–4483, Jul. 2011.

[88] U. Y. Schaff and G. J. Sommer, "Whole Blood Immunoassay Based on Centrifugal Bead Sedimentation," *Clin. Chem.*, vol. 57, no. 5, pp. 753–761, May 2011.

[89] P. Wang, L. Ge, M. Yan, X. Song, S. Ge, and J. Yu, "Paper-based three-dimensional electrochemical immunodevice based on multi-walled carbon nanotubes functionalized paper for sensitive point-of-care testing," *Biosens. Bioelectron.*, vol. 32, no. 1, pp. 238–243, Feb. 2012.

[90] G. Garcia-Schwarz and J. G. Santiago, "Integration of on-chip isotachophoresis and functionalized hydrogels for enhanced-sensitivity nucleic acid detection," *Anal. Chem.*, vol. 84, no. 15, 2012.

[91] J. S. Jang *et al.*, "Quantitative miRNA Expression Analysis Using Fluidigm Microfluidics Dynamic Arrays," *BMC Genomics*, vol. 12, 2011.

[92] K. T. Kotz *et al.*, "Clinical microfluidics for neutrophil genomics and proteomics," *Nat. Med.*, vol. 16, no. 9, 2010.

[93] K. J. Liu, M. V. Brock, I. M. Shih, and T. H. Wang, "Decoding circulating nucleic acids in human serum using microfluidic single molecule spectroscopy," *J. Am. Chem. Soc.*, vol. 132, no. 16, 2010.

[94] C. Y. Zhang and J. Hu, "Single quantum dot-based nanosensor for multiple DNA detection," *Anal. Chem.*, vol. 82, no. 5, 2010.

[95] C. D. M. Campos *et al.*, "Microfluidic-based solid phase extraction of cell free DNA," *Lab Chip*, vol. 18, no. 22, 2018.

[96] A. Muck, T. Stelzner, U. Hübner, S. Christiansen, and A. Svatoš, "Lithographically patterned silicon nanowire arrays for matrix free LDI-TOF/MS analysis of lipids," *Lab Chip*, vol. 10, no. 3, pp. 320–325, 2010.

[97] M. Azahar Ali, S. Srivastava, P. R. Solanki, V. Varun Agrawal, R. John, and B. D. Malhotra, "Nanostructured anatase-titanium dioxide based platform for application to microfluidics cholesterol biosensor," *Appl. Phys. Lett.*, vol. 101, no. 8, p. 84105, Aug. 2012.

[98] S.-P. Chen, X.-D. Yu, J.-J. Xu, and H.-Y. Chen, "Lab-on-a-chip for analysis of triglycerides based on a replaceable enzyme carrier using magnetic beads," *Analyst*, vol. 135, no. 11, pp. 2979–2986, 2010.

[99] N. Ruecha, W. Siangproh, and O. Chailapakul, "A fast and highly sensitive

detection of cholesterol using polymer microfluidic devices and amperometric system," *Talanta*, vol. 84, no. 5, pp. 1323–1328, Jun. 2011.

[100] X. Chen *et al.*, "Determination of glucose and uric acid with bienzyme colorimetry on microfluidic paper-based analysis devices," *Biosens. Bioelectron.*, vol. 35, no. 1, pp. 363–368, May 2012.

[101] J. Sheng, L. Zhang, J. Lei, and H. Ju, "Fabrication of tunable microreactor with enzyme modified magnetic nanoparticles for microfluidic electrochemical detection of glucose," *Anal. Chim. Acta*, vol. 709, pp. 41–46, Jan. 2012.

[102] W. Mielczarek, "Microfluidic devices for the preparation of blood plasma samples in circulating nucleic acid based medical applications," vol. 84. Engineering and Physical Sciences, pp. 487–492, 2017.

[103] S. Karthick and A. K. Sen, "Improved Understanding of Acoustophoresis and Development of an Acoustofluidic Device for Blood Plasma Separation," *Phys. Rev. Appl.*, vol. 10, no. 3, 2018.

[104] R. Meddeb *et al.*, "Quantifying circulating cell-free DNA in humans," *Sci. Rep.*, vol. 9, no. 1, 2019.

[105] M. Kersaudy-Kerhoas, R. Dhariwal, M. P. Y. Desmulliez, and L. Jouvet, "Hydrodynamic blood plasma separation in microfluidic channels," *Microfluid. Nanofluidics*, vol. 8, no. 1, pp. 105–114, 2010.

[106] D. R. Reyes, D. Iossifidis, P. A. Auroux, and A. Manz, "Micro total analysis systems. 1. Introduction, theory, and technology," *Anal. Chem.*, vol. 74, no. 12, pp. 2623–2636, 2002.

[107] B. M. Dincau, Y. Lee, J. H. Kim, and W. H. Yeo, "Recent advances in nanoparticle concentration and their application in viral detection using integrated sensors," *Sensors (Switzerland)*, vol. 17, no. 10. 2017.

[108] M. Alshareef *et al.*, "Separation of tumor cells with dielectrophoresis-based microfluidic chip," *Biomicrofluidics*, vol. 7, no. 1, p. 11803, 2013.

[109] D. M. Whiley *et al.*, "Detection of novel influenza A(H1N1) virus by real-time RT-PCR," *J. Clin. Virol.*, vol. 45, no. 3, pp. 203–204, Jul. 2009.

[110] S. Suresh *et al.*, "Connections between single-cell biomechanics and human disease states: Gastrointestinal cancer and malaria," *Acta Biomater.*, vol. 1, no. 1, pp. 15–30, Jan. 2005.

[111] A. Lenshof *et al.*, "Acoustic whole blood plasmapheresis chip for prostate specific antigen microarray diagnostics," *Anal. Chem.*, vol. 81, no. 15, pp. 6030–6037, 2009.

[112] S. Tripathi, Y. V. B. Kumar, A. Agrawal, A. Prabhakar, and S. S. Joshi, "Microdevice for plasma separation from whole human blood using bio-physical and geometrical effects," *Sci. Rep.*, vol. 6, 2016.

[113] M. Kersaudy-Kerhoas, D. M. Kavanagh, R. S. Dhariwal, C. J. Campbell, and M. P. Y. Desmulliez, "Validation of a blood plasma separation system by biomarker detection," *Lab Chip*, vol. 10, no. 12, pp. 1587–1595, 2010.

[114] M. Hejazian, W. Li, and N. T. Nguyen, "Lab on a chip for continuous-flow magnetic cell separation," *Lab on a Chip*, vol. 15, no. 4. pp. 959–970, 2015.

[115] A. Homsy *et al.*, "Development and validation of a low cost blood filtration element separating plasma from undiluted whole blood," *Biomicrofluidics*, vol. 6, no. 1, 2012.

[116] C. Liu *et al.*, "Membrane-based, sedimentation-assisted plasma separator for point-of-care applications," *Anal. Chem.*, vol. 85, no. 21, pp. 10463–10470, 2013.

[117] T. Tachi, N. Kaji, M. Tokeshi, and Y. Baba, "Simultaneous separation, metering, and dilution of plasma from human whole blood in a microfluidic system," *Anal. Chem.*, vol. 81, no. 8, pp. 3194–3198, 2009.

[118] S. Q. Wang *et al.*, "Simple filter microchip for rapid separation of plasma and viruses from whole blood," *Int. J. Nanomedicine*, vol. 7, pp. 5019–5028, 2012.

[119] J. Chen *et al.*, "Blood plasma separation microfluidic chip with gradual filtration," *Microelectron. Eng.*, vol. 128, pp. 36–41, 2014.

[120] Y. C. Fung, "Stochastic flow in capillary blood vessels," *Microvasc. Res.*, vol. 5, no. 1, pp. 34–48, 1973.

[121] K. Svanes and B. W. Zweifach, "Variations in small blood vessel hematocrits produced in hypothermic rats by micro-occlusion," *Microvasc. Res.*, vol. 1, no. 2, pp. 210–220, 1968.

[122] S. Thorslund, O. Klett, F. Nikolajeff, K. Markides, and J. Bergquist, "A hybrid poly(dimethylsiloxane) microsystem for on-chip whole blood filtration optimized for steroid screening," *Biomed. Microdevices*, vol. 8, no. 1, pp. 73–79, 2006.

[123] T. A. Crowley and V. Pizziconi, "Isolation of plasma from whole blood using planar microfilters for lab-on-a-chip applications," *Lab Chip*, vol. 5, no. 9, pp. 922–929, Aug. 2005.

[124] P. Sajeesh and A. K. Sen, "Particle separation and sorting in microfluidic devices: A review," *Microfluid. Nanofluidics*, vol. 17, no. 1, pp. 1–52, Jul. 2014.

[125] M. S. Maria, P. E. Rakesh, T. S. Chandra, and A. K. Sen, "Capillary flow-driven microfluidic device with wettability gradient and sedimentation effects for blood

plasma separation," *Sci. Rep.*, vol. 7, 2017.

[126] D. Forchelet *et al.*, "Separation of blood microsamples by exploiting sedimentation at the microscale," *Sci. Rep.*, vol. 8, no. 1, 2018.

[127] Y. Xie, D. Chen, S. Lin, Z. Wang, and D. Cui, "A robust and easily integrated plasma separation chip using gravitational sedimentation of blood cells filling-in high-aspect-ratio weir structure," *RSC Adv.*, vol. 6, no. 36, pp. 30722–30727, 2016.

[128] X. B. Zhang *et al.*, "Gravitational sedimentation induced blood delamination for continuous plasma separation on a microfluidics chip," *Anal. Chem.*, vol. 84, no. 8, pp. 3780–3786, 2012.

[129] S. Tripathi, A. Prabhakar, N. Kumar, S. G. Singh, and A. Agrawal, "Blood plasma separation in elevated dimension T-shaped microchannel," *Biomed. Microdevices*, vol. 15, no. 3, pp. 415–425, 2013.

[130] S. Tripathi, Y. V. B. Varun Kumar, A. Prabhakar, S. S. Joshi, and A. Agrawal, "Performance study of microfluidic devices for blood plasma separation - A designer's perspective," *J. Micromechanics Microengineering*, vol. 25, no. 8, 2015.

[131] M. Faivre, M. Abkarian, K. Bickraj, and H. A. Stone, "Geometrical focusing of cells in a microfluidic device: An approach to separate blood plasma," *Biorheology*, vol. 43, no. 2, pp. 147–159, 2006.

[132] E. Sollier, M. Cubizolles, Y. Fouillet, and J. L. Achard, "Fast and continuous plasma extraction from whole human blood based on expanding cell-free layer devices," *Biomed. Microdevices*, vol. 12, no. 3, pp. 485–497, Jun. 2010.

[133] Y. C. Fung and R. Skalak, "Biomechanics: Mechanical Properties of Living Tissues," *J. Biomech. Eng.*, vol. 103, no. 4, pp. 231–298, 1981.

[134] E. P. Zilow and O. Linderkamp, "Viscosity reduction of red blood cells from preterm and full-term neonates and adults in narrow tubes (fahraeus-lindqvist effect)," *Pediatr. Res.*, vol. 25, no. 6, pp. 595–599, 1989.

[135] G. Coupier, B. Kaoui, T. Podgorski, and C. Misbah, "Noninertial lateral migration of vesicles in bounded Poiseuille flow," *Phys. Fluids*, vol. 20, no. 11, 2008.

[136] T. W. Secomb and A. R. Pries, "Blood viscosity in microvessels: Experiment and theory," *Comptes Rendus Physique*, vol. 14, no. 6. pp. 470–478, 2013.

[137] D. A. Fedosov, B. Caswell, A. S. Popel, and G. E. M. Karniadakis, "Blood Flow and Cell-Free Layer in Microvessels," *Microcirculation*, vol. 17, no. 8, pp. 615–628, 2010.

[138] M. E. Haque, A. Matin, X. Wang, and M. Kersaudy-Kerhoas, "Effects of syringe

pump fluctuations on cell-free layer in hydrodynamic separation microfluidic devices," *Phys. Fluids*, vol. 33, no. 7, Jul. 2021.

[139] S. Yang, A. Ündar, and J. D. Zahn, "A microfluidic device for continuous, real time blood plasma separation," *Lab Chip*, vol. 6, no. 7, pp. 871–880, 2006.

[140] T. M. Amin and J. A. Sirs, "THE BLOOD RHEOLOGY OF MAN AND VARIOUS ANIMAL SPECIES," *Q. J. Exp. Physiol.*, vol. 70, no. 1, pp. 37–49, Jan. 1985.

[141] R. D. Jäggi, R. Sandoz, and C. S. Effenhauser, "Microfluidic depletion of red blood cells from whole blood in high-aspect-ratio microchannels," *Microfluid. Nanofluidics*, vol. 3, no. 1, pp. 47–53, 2007.

[142] A. I. Rodríguez-Villarreal, M. Arundell, M. Carmona, and J. Samitier, "High flow rate microfluidic device for blood plasma separation using a range of temperatures," *Lab Chip*, vol. 10, no. 2, pp. 211–219, 2010.

[143] C. CHALMERS and W. J. RUSSELL, "WHEN DOES BLOOD HAEMOLYSE?: A Temperature Study," *Br. J. Anaesth.*, vol. 46, no. 10, pp. 742–746, 1974.

[144] T. A. Shatova, S. Lathwal, M. R. Engle, H. D. Sikes, and K. F. Jensen, "Portable, Constriction-Expansion Blood Plasma Separation and Polymerization-Based Malaria Detection," *Anal. Chem.*, vol. 88, no. 15, pp. 7627–7632, 2016.

[145] C. C. Chen, P. H. Lin, and C. K. Chung, "Microfluidic chip for plasma separation from undiluted human whole blood samples using low voltage contactless dielectrophoresis and capillary force," *Lab Chip*, vol. 14, no. 12, pp. 1996–2001, 2014.

[146] M. Robinson, H. Marks, T. Hinsdale, K. Maitland, and G. Coté, "Rapid isolation of blood plasma using a cascaded inertial microfluidic device," *Biomicrofluidics*, vol. 11, no. 2, 2017.

[147] L. R. Huang, E. C. Cox, R. H. Austin, and J. C. Sturm, "Continuous Particle Separation Through Deterministic Lateral Displacement," *Science (80-.).*, vol. 304, no. 5673, pp. 987–990, 2004.

[148] S. Tripathi, Y. V. B. Varun Kumar, A. Prabhakar, S. S. Joshi, and A. Agrawal, "Passive blood plasma separation at the microscale: A review of design principles and microdevices," *Journal of Micromechanics and Microengineering*, vol. 25, no. 8. 2015.

[149] D. Holmes *et al.*, "Separation of blood cells with differing deformability using deterministic lateral displacement," *Interface Focus*, vol. 4, no. 6, 2014.

[150] D. W. Inglis *et al.*, "Microfluidic device for label-free measurement of platelet

activation," *Lab Chip*, vol. 8, no. 6, pp. 925–931, 2008.

[151] J. A. Davis *et al.*, "Deterministic hydrodynamics: Taking blood apart," *Proc. Natl. Acad. Sci. U. S. A.*, vol. 103, no. 40, pp. 14779–14784, 2006.

[152] D. Di Carlo, "Inertial microfluidics," *Lab on a Chip*, vol. 9, no. 21. pp. 3038–3046, 2009.

[153] Z. T. F. Yu, K. M. Aw Yong, and J. Fu, "Microfluidic blood cell sorting: Now and beyond," *Small*, vol. 10, no. 9. Wiley-VCH Verlag, pp. 1687–1703, 14-May-2014.

[154] M. G. Lee *et al.*, "Inertial blood plasma separation in a contraction-expansion array microchannel," *Appl. Phys. Lett.*, vol. 98, no. 25, 2011.

[155] S. C. Hur, H. T. K. Tse, and D. Di Carlo, "Sheathless inertial cell ordering for extreme throughput flow cytometry," *Lab Chip*, vol. 10, no. 3, pp. 274–280, 2010.

[156] A. J. Mach and D. di Carlo, "Continuous scalable blood filtration device using inertial microfluidics," *Biotechnol. Bioeng.*, vol. 107, no. 2, pp. 302–311, 2010.

[157] M. E. Warkiani, A. K. P. Tay, B. L. Khoo, X. Xiaofeng, J. Han, and C. T. Lim, "Malaria detection using inertial microfluidics," *Lab Chip*, vol. 15, no. 4, pp. 1101–1109, 2015.

[158] T. H. Kim, H. J. Yoon, P. Stella, and S. Nagrath, "Cascaded spiral microfluidic device for deterministic and high purity continuous separation of circulating tumor cells," *Biomicrofluidics*, vol. 8, no. 6, 2014.

[159] M. E. brahim. Warkiani *et al.*, "Ultra-fast, label-free isolation of circulating tumor cells from blood using spiral microfluidics," *Nat. Protoc.*, vol. 11, no. 1, pp. 134–148, 2016.

[160] L. Liang, Kirby B.J., L. Liang, and Kirby B.J., "Particle Electrophoresis and Magnetophoresis in Microchannels," *All Theses, Clemson Univ. Tiger Prints*, p. 1699, 2013.

[161] L. Zheng, S. Li, J. P. Brody, and P. J. Burke, "Manipulating nanoparticles in solution with electrically contacted nanotubes using dielectrophoresis," *Langmuir*, vol. 20, no. 20, pp. 8612–8619, 2004.

[162] D. H. Kang, K. Kim, and Y. J. Kim, "An anti-clogging method for improving the performance and lifespan of blood plasma separation devices in real-time and continuous microfluidic systems," *Sci. Rep.*, vol. 8, no. 1, 2018.

[163] D. H. Kuan, C. C. Wu, W. Y. Su, and N. T. Huang, "A Microfluidic Device for Simultaneous Extraction of Plasma, Red Blood Cells, and On-Chip White Blood Cell Trapping," *Sci. Rep.*, vol. 8, no. 1, 2018.

[164] F. Yang *et al.*, "Extraction of Cell-Free Whole Blood Plasma Using a

Dielectrophoresis-Based Microfluidic Device," *Biotechnol. J.*, vol. 14, no. 3, p. 1800181, Mar. 2019.

[165] C. Szydzik, K. Khoshmanesh, A. Mitchell, and C. Karnutsch, "Microfluidic platform for separation and extraction of plasma from whole blood using dielectrophoresis," *Biomicrofluidics*, vol. 9, no. 6, pp. 1–16, 2015.

[166] H. Zhu, X. Lin, Y. Su, H. Dong, and J. Wu, "Screen-printed microfluidic dielectrophoresis chip for cell separation," *Biosens. Bioelectron.*, vol. 63, pp. 371–378, Jan. 2015.

[167] C. C. Chai, Z. H. Lee, P. Y. Toh, D. C. J. Chieh, A. L. Ahmad, and J. K. Lim, "Effects of dissolved organic matter and suspended solids on the magnetophoretic separation of microalgal cells from an aqueous environment," *Chem. Eng. J.*, vol. 281, pp. 523–530, 2015.

[168] P. Kim, E. H. Ong, K. H. H. Li, Y. J. Yoon, S. H. G. Ng, and K. Puttachat, "Low-cost, disposable microfluidics device for blood plasma extraction using continuously alternating paramagnetic and diamagnetic capture modes," *Biomicrofluidics*, vol. 10, no. 2, 2016.

[169] S. Vemulapati and D. Erickson, "Portable Resource-Independent Blood-Plasma Separator," *Anal. Chem.*, vol. 91, no. 23, pp. 14824–14828, 2019.

[170] L. Y. Yeo and J. R. Friend, "Ultrafast microfluidics using surface acoustic waves," in *Biomicrofluidics*, 2009, vol. 3, no. 1.

[171] J. Dual and T. Schwarz, "Acoustofluidics 3: Continuum mechanics for ultrasonic particle manipulation," *Lab Chip*, vol. 12, no. 2, pp. 244–252, 2012.

[172] J. Curie and P. Curie, "Phénomènes électriques des cristaux hémièdres à faces inclinées," *J. Phys. Théorique Appliquée*, vol. 1, no. 1, pp. 245–251, 1882.

[173] J. D. N. Cheeke, *Fundamentals and applications of ultrasonic waves, second edition*. CRC Press, 2017.

[174] L. Y. Yeo and J. R. Friend, "Surface acoustic wave microfluidics," *Annu. Rev. Fluid Mech.*, vol. 46, pp. 379–406, 2014.

[175] X. Ding *et al.*, "Standing surface acoustic wave (SSAW) based multichannel cell sorting," *Lab Chip*, vol. 12, no. 21, pp. 4228–4231, 2012.

[176] G. Destgeer, B. H. Ha, J. Park, J. H. Jung, A. Alazzam, and H. J. Sung, "Travelling surface acoustic waves microfluidics," in *Physics Procedia*, 2015, vol. 70, pp. 34–37.

[177] C. Campbell and J. C. Burgess, *Surface Acoustic Wave Devices and Their Signal Processing Applications*, vol. 89, no. 3. Academic Press, 1991.

[178] O.-A. K. Kavli, “Surface Acoustic Wave Acoustophoresis for Microfluidic Based Micron and Submicron Particle Separation,” *121*, no. May, 2016.

[179] M. Wu, A. Ozcelik, J. Rufo, Z. Wang, R. Fang, and T. Jun Huang, “Acoustofluidic separation of cells and particles,” *Microsystems and Nanoengineering*, vol. 5, no. 1. 2019.

[180] A. Lenshof, M. Evander, T. Laurell, and J. Nilsson, “Acoustofluidics 5: Building microfluidic acoustic resonators,” *Lab Chip*, vol. 12, no. 4, pp. 684–695, 2012.

[181] A. Lenshof, C. Magnusson, and T. Laurell, “Acoustofluidics 8: Applications of acoustophoresis in continuous flow microsystems,” *Lab on a Chip*, vol. 12, no. 7. pp. 1210–1223, 2012.

[182] A. A. Doinikov, “Theory of acoustic radiation pressure for actual fluids,” *Phys. Rev. E - Stat. Physics, Plasmas, Fluids, Relat. Interdiscip. Top.*, vol. 54, no. 6, pp. 6297–6303, 1996.

[183] A. P. Sarvazyan, O. V. Rudenko, and W. L. Nyborg, “Biomedical applications of radiation force of ultrasound: Historical roots and physical basis,” *Ultrasound in Medicine and Biology*, vol. 36, no. 9. pp. 1379–1394, 2010.

[184] A. A. Doinikov, “Acoustic Radiation Pressure on a Compressible Sphere in a Viscous Fluid,” *Journal of Fluid Mechanics*, vol. 267. pp. 1–22, 1994.

[185] A. Nilsson, F. Petersson, H. Jönsson, and T. Laurell, “Acoustic control of suspended particles in micro fluidic chips,” *Lab Chip*, vol. 4, no. 2, pp. 131–135, Apr. 2004.

[186] D. H. Yoon, J. B. Ha, Y. K. Bahk, T. Arakawa, S. Shoji, and J. S. Go, “Size-selective separation of micro beads by utilizing secondary flow in a curved rectangular microchannel,” *Lab Chip*, vol. 9, no. 1, pp. 87–90, Jan. 2009.

[187] J. Takagi, M. Yamada, M. Yasuda, and M. Seki, “Continuous particle separation in a microchannel having asymmetrically arranged multiple branches,” *Lab Chip*, vol. 5, no. 7, pp. 778–784, Jul. 2005.

[188] K. Lee, H. Shao, R. Weissleder, and H. Lee, “Acoustic purification of extracellular microvesicles,” *ACS Nano*, vol. 9, no. 3, pp. 2321–2327, 2015.

[189] R. Guldiken, M. C. Jo, N. D. Gallant, U. Demirci, and J. Zhe, “Sheathless size-based acoustic particle separation,” *Sensors*, vol. 12, no. 1, pp. 905–922, 2012.

[190] F. Petersson, A. Nilsson, C. Holm, H. Jönsson, and T. Laurell, “Separation of lipids from blood utilizing ultrasonic standing waves in microfluidic channels,” *Analyst*, vol. 129, no. 10, pp. 938–943, 2004.

[191] A. Urbansky, P. Ohlsson, A. Lenshof, F. Garofalo, S. Scheding, and T. Laurell,

"Rapid and effective enrichment of mononuclear cells from blood using acoustophoresis," *Sci. Rep.*, vol. 7, no. 1, 2017.

[192] T. S. Roukis, T. Zgonis, and B. Tiernan, "Autologous platelet-rich plasma for wound and osseous healing: A review of the literature and commercially available products," *Advances in Therapy*, vol. 23, no. 2. pp. 218–237, 2006.

[193] E. Gutierrez, B. G. Petrich, S. J. Shattil, M. H. Ginsberg, A. Groisman, and A. Kasirer-Friede, "Microfluidic devices for studies of shear-dependent platelet adhesion," *Lab Chip*, vol. 8, no. 9, pp. 1486–1495, 2008.

[194] J. Nam, H. Lim, D. Kim, and S. Shin, "Separation of platelets from whole blood using standing surface acoustic waves in a microchannel," *Lab Chip*, vol. 11, no. 19, pp. 3361–3364, 2011.

[195] Y. Chen *et al.*, "High-throughput acoustic separation of platelets from whole blood," *Lab Chip*, vol. 16, no. 18, pp. 3466–3472, 2016.

[196] S. Deshmukh, Z. Brzozka, T. Laurell, and P. Augustsson, "Acoustic radiation forces at liquid interfaces impact the performance of acoustophoresis," *Lab Chip*, vol. 14, no. 17, pp. 3394–3400, 2014.

[197] Y. Gu *et al.*, "Plastic-based acoustofluidic devices for high-throughput, biocompatible platelet separation," *Lab Chip*, vol. 19, no. 3, pp. 394–402, 2019.

[198] A. A. Tajudin *et al.*, "Integrated acoustic immunoaffinity-capture (IAI) platform for detection of PSA from whole blood samples," *Lab Chip*, vol. 13, no. 9, pp. 1790–1796, 2013.

[199] T. Li, Y. Fan, Y. Cheng, and J. Yang, "An electrochemical Lab-on-a-CD system for parallel whole blood analysis," *Lab Chip*, vol. 13, no. 13, pp. 2634–2640, 2013.

[200] S. Haeberle, T. Brenner, R. Zengerle, and J. Ducrée, "Centrifugal extraction of plasma from whole blood on a rotating disk," *Lab Chip*, vol. 6, no. 6, pp. 776–781, 2006.

[201] Y.-K. Cho, J.-G. Lee, J.-M. Park, B.-S. Lee, Y. Lee, and C. Ko, "One-step pathogen specific DNA extraction from whole blood on a centrifugal microfluidic device," *Lab Chip*, vol. 7, no. 5, pp. 565–573, 2007.

[202] J. Zhang, Q. Guo, M. Liu, and J. Yang, "A lab-on-CD prototype for high-speed blood separation," *J. Micromechanics Microengineering*, vol. 18, no. 12, p. 125025, 2008.

[203] T. Li, L. Zhang, K. M. Leung, and J. Yang, "Out-of-plane microvalves for whole blood separation on lab-on-a-CD," *J. Micromechanics Microengineering*, vol. 20, no. 10, p. 105024, 2010.

[204] T. H. Kim, H. Hwang, R. Gorkin, M. Madou, and Y. K. Cho, “Geometry effects on blood separation rate on a rotating disc,” *Sensors Actuators B Chem.*, vol. 178, pp. 648–655, Mar. 2013.

[205] F. Hu *et al.*, “Rapid isolation of cfDNA from large-volume whole blood on a centrifugal microfluidic chip based on immiscible phase filtration,” *Analyst*, vol. 144, no. 14, pp. 4162–4174, 2019.

[206] M. S. Bhamla, B. Benson, C. Chai, G. Katsikis, A. Johri, and M. Prakash, “Hand-powered ultralow-cost paper centrifuge,” *Nat. Biomed. Eng.*, vol. 1, no. 1, 2017.

[207] A. P. Wong, M. Gupta, S. S. Shevkoplyas, and G. M. Whitesides, “Egg beater as centrifuge: Isolating human blood plasma from whole blood in resource-poor settings,” *Lab Chip*, vol. 8, no. 12, 2008.

[208] A. K. Patel *et al.*, “Design and Development of Low-cost Portable Centrifuge using Additive Manufacturing,” 2019.

[209] S. S. Sule, A. L. Petsiuk, and J. M. Pearce, “Open Source Completely 3-D Printable Centrifuge,” *Instruments*, vol. 3, no. 2, p. 30, 2019.

[210] L. C. CERNY, F. B. COOK, and C. C. WALKER, “Rheology of blood,” *Am. J. Physiol.*, vol. 202, no. 6, pp. 1188–1194, Jun. 1962.

[211] Y. Çinar, G. Demir, M. Paç, and A. B. Çinar, “Effect of hematocrit on blood pressure via hyperviscosity,” *Am. J. Hypertens.*, vol. 12, no. 7, pp. 739–743, 1999.

[212] S. Chien, S. Usami, R. J. Dellenback, and M. I. Gregersen, “Blood viscosity: Influence of erythrocyte deformation,” *Science (80-.).*, vol. 157, no. 3790, pp. 827–829, Aug. 1967.

[213] D. Sampaio, D. Lopes, and V. Semiao, “Horse and dog blood flows in PDMS rectangular microchannels: Experimental characterization of the plasma layer under different flow conditions,” *Exp. Therm. Fluid Sci.*, vol. 68, pp. 205–215, 2015.

[214] C. Higgins, “Useful tips to avoid preanalytical errors in blood gas testing : pH , pCO 2 and pO 2,” *Acute Care Testing*, no. May, pp. 1–8, 2016.

[215] W. Chang, D. Trebotich, L. P. Lee, and D. Liepmann, “Blood flow in simple microchannels,” in *1st Annual International IEEE-EMBS Special Topic Conference on Microtechnologies in Medicine and Biology - Proceedings*, 2000, pp. 311–315.

[216] L. B. Leverett, J. D. Hellums, C. P. Alfrey, and E. C. Lynch, “Red Blood Cell Damage by Shear Stress,” *Biophys. J.*, vol. 12, no. 3, pp. 257–273, 1972.

[217] L. Moldovan, K. E. Batte, J. Trgovcich, J. Wisler, C. B. Marsh, and M. Piper,

"Methodological challenges in utilizing miRNAs as circulating biomarkers," *J. Cell. Mol. Med.*, vol. 18, no. 3, 2014.

[218] S. F. Green, "The cost of poor blood specimen quality and errors in preanalytical processes," *Clin. Biochem.*, vol. 46, no. 13–14, 2013.

[219] G. Lippi *et al.*, "Haemolysis: An overview of the leading cause of unsuitable specimens in clinical laboratories," *Clinical Chemistry and Laboratory Medicine*, vol. 46, no. 6. 2008.

[220] R. Fåhræus and T. Lindqvist, "the Viscosity of the Blood in Narrow Capillary Tubes," *Am. J. Physiol. Content*, vol. 96, no. 3, pp. 562–568, 1931.

[221] R. FÅHRŒUS., "The Suspension-stability of the Blood.," *Acta Medica Scandinavica*, vol. 55, no. 1, pp. 3–7, 1921.

[222] P. K. Panigrahi, *Transport Phenomena in Microfluidic Systems*. 2015.

[223] A. Peterson and E. Tobias, "Design and Properties of Microfluidic Surface Acoustic Wave Devices," 2016.

[224] J. Holman, *Heat Transfer*. 2010.

[225] University of Sydney, "Classification of Flows, Laminar and Turbulent Flows," *University of Sydney*, 2005. [Online]. Available: http://www-mdp.eng.cam.ac.uk/web/library/enginfo/aerothermal_dvd_only/aero/fprops/pipeflow/node8.html. [Accessed: 11-May-2020].

[226] C. Miller, "Predicting Non-Newtonian Flow Behavior in Ducts of Unusual Cross Section," *Ind. Eng. Chem. Fundam.*, vol. 11, no. 4, pp. 524–528, 1972.

[227] D. E. Brooks, J. W. Goodwin, and G. V. Seaman, "Interactions among erythrocytes under shear.," *J. Appl. Physiol.*, vol. 28, no. 2, pp. 172–177, 1970.

[228] S. Chien, S. Usami, H. M. Taylor, J. L. Lundberg, and M. I. Gregersen, "Effects of hematocrit and plasma proteins on human blood rheology at low shear rates.," *J. Appl. Physiol.*, vol. 21, no. 1, pp. 81–87, Jan. 1966.

[229] Y. Sui, Y. T. Chew, P. Roy, Y. P. Cheng, and H. T. Low, "Dynamic motion of red blood cells in simple shear flow," *Phys. Fluids*, vol. 20, no. 11, 2008.

[230] M. Abkarian, M. Faivre, and A. Viallat, "Swinging of red blood cells under shear flow," *Phys. Rev. Lett.*, vol. 98, no. 18, 2007.

[231] T. M. Fischer, M. Stöhr-Liesen, and H. Schmid-Schönbein, "The red cell as a fluid droplet: Tank tread-like motion of the human erythrocyte membrane in shear flow," *Science (80-.).*, vol. 202, no. 4370, pp. 894–896, 1978.

[232] T. Krüger, M. Gross, D. Raabe, and F. Varnik, "Crossover from tumbling to tank-treading-like motion in dense simulated suspensions of red blood cells," *Soft*

Matter, vol. 9, no. 37, pp. 9008–9015, 2013.

[233] J. Dupire, M. Socol, and A. Viallat, "Full dynamics of a red blood cell in shear flow," *Proc. Natl. Acad. Sci. U. S. A.*, vol. 109, no. 51, 2012.

[234] W. R. Dodson and P. Dimitrakopoulos, "Tank-treading of erythrocytes in strong shear flows via a nonstiff cytoskeleton-based continuum computational modeling," *Biophys. J.*, vol. 99, no. 9, pp. 2906–2916, 2010.

[235] P. R. Waghmare and S. K. Mitra, "Contact angle hysteresis of bovine serum albumin (BSA) solution/metal (Au-Cr) coated glass substrate," *Colloid Polym. Sci.*, vol. 291, no. 2, 2013.

[236] K. L. Wlodarczyk, D. P. Hand, and M. M. Maroto-Valer, "Maskless, rapid manufacturing of glass microfluidic devices using a picosecond pulsed laser," *Sci. Rep.*, vol. 9, no. 1, 2019.

[237] K. F. Jensen, "Silicon-based microchemical systems: Characteristics and applications," *MRS Bull.*, vol. 31, no. 2, 2006.

[238] A. W. Martinez, S. T. Phillips, M. J. Butte, and G. M. Whitesides, "Patterned paper as a platform for inexpensive, low-volume, portable bioassays," *Angew. Chemie - Int. Ed.*, vol. 46, no. 8, 2007.

[239] S. Wang *et al.*, "Paper-based chemiluminescence ELISA: Lab-on-paper based on chitosan modified paper device and wax-screen-printing," *Biosens. Bioelectron.*, vol. 31, no. 1, 2012.

[240] S. T. Sanjay, M. Li, W. Zhou, X. Li, and X. J. Li, "A reusable PMMA/paper hybrid plug-and-play microfluidic device for an ultrasensitive immunoassay with a wide dynamic range," *Microsystems Nanoeng.*, vol. 6, no. 1, 2020.

[241] Z. B. Qi *et al.*, "Disposable silicon-glass microfluidic devices: Precise, robust and cheap," *Lab Chip*, vol. 18, no. 24, 2018.

[242] S. T. Sanjay *et al.*, "Biomarker detection for disease diagnosis using cost-effective microfluidic platforms," *Analyst*, vol. 140, no. 21. 2015.

[243] R. Mukhopadhyay, "When PDMS isn't the best," *Analytical Chemistry*, vol. 79, no. 9. pp. 3249–3253, 01-May-2007.

[244] C. W. Tsao, L. Hromada, J. Liu, P. Kumar, and D. L. DeVoe, "Low temperature bonding of PMMA and COC microfluidic substrates using UV/ozone surface treatment," *Lab Chip*, vol. 7, no. 4, pp. 499–505, Apr. 2007.

[245] R. Truckenmüller, P. Henzi, D. Herrmann, V. Saile, and W. K. Schomburg, "Bonding of polymer microstructures by UV irradiation and subsequent welding at low temperatures," *Microsyst. Technol.*, vol. 10, no. 5, 2004.

[246] E. Nader *et al.*, “Blood rheology: Key parameters, impact on blood flow, role in sickle cell disease and effects of exercise,” *Frontiers in Physiology*, vol. 10, no. OCT. 2019.

[247] G. Késmárky, P. Kenyeres, M. Rábai, and K. Tóth, “Plasma viscosity: A forgotten variable,” in *Clinical Hemorheology and Microcirculation*, 2008, vol. 39, no. 1–4.

[248] H. Yamamoto *et al.*, “Measurement of human blood viscosity a using Falling Needle Rheometer and the correlation to the Modified Herschel-Bulkley model equation,” *Heliyon*, vol. 6, no. 9, 2020.

[249] G. D. O. Lowe, A. J. Lee, A. Rumley, J. F. Price, and F. G. R. Fowkes, “Blood viscosity and risk of cardiovascular events: The Edinburgh Artery Study,” *Br. J. Haematol.*, vol. 96, no. 1, 1997.

[250] B. Joob and V. Wiwanitkit, “Blood viscosity of COVID-19 patient: a preliminary report.,” *Am. J. Blood Res.*, vol. 11, no. 1, 2021.

[251] C. L. Maier, A. D. Truong, S. C. Auld, D. M. Polly, C. L. Tanksley, and A. Duncan, “COVID-19-associated hyperviscosity: a link between inflammation and thrombophilia?,” *The Lancet*, vol. 395, no. 10239. 2020.

[252] G. Schramm, *A practical approach to rheology and rheometry*. Haake Karlsruhe, 1994.

[253] B. J. Kim, S. Y. Lee, S. Jee, A. Atajanov, and S. Yang, “Micro-viscometer for measuring shear-varying blood viscosity over a wide-ranging shear rate,” *Sensors (Switzerland)*, vol. 17, no. 6, 2017.

[254] S. Arya, V. Sharma, and S. L. Shimi, “Design and fabrication of micro-channels based fluid viscosity sensor,” *ISSS J. Micro Smart Syst.*, vol. 6, no. 2, 2017.

[255] P. Zhu and L. Wang, “Passive and active droplet generation with microfluidics: a review,” *Lab Chip*, vol. 17, no. 1, pp. 34–75, 2017.

[256] L. Yobas, S. Martens, W. L. Ong, and N. Ranganathan, “High-performance flow-focusing geometry for spontaneous generation of monodispersed droplets,” *Lab Chip*, vol. 6, no. 8, pp. 1073–1079, 2006.

[257] D. R. Arifin, L. Y. Yeo, and J. R. Friend, “Microfluidic blood plasma separation via bulk electrohydrodynamic flows,” *Biomicrofluidics*, vol. 1, no. 1, 2007.

[258] H. Jang, M. R. Haq, J. Ju, Y. Kim, S. M. Kim, and J. Lim, “Fabrication of all glass bifurcation microfluidic chip for blood plasma separation,” *Micromachines*, vol. 8, no. 3, 2017.

[259] W. Saadi, S. J. Wang, F. Lin, and N. L. Jeon, “A parallel-gradient microfluidic chamber for quantitative analysis of breast cancer cell chemotaxis,” *Biomed.*

Microdevices, vol. 8, no. 2, pp. 109–118, 2006.

[260] T. Luo, L. Fan, R. Zhu, and D. Sun, "Microfluidic single-cell manipulation and analysis: Methods and applications," *Micromachines*, vol. 10, no. 2. 2019.

[261] J. Siegrist *et al.*, "Validation of a centrifugal microfluidic sample lysis and homogenization platform for nucleic acid extraction with clinical samples," *Lab Chip*, vol. 10, no. 3, pp. 363–371, 2010.

[262] M. Sonker, V. Sahore, and A. T. Woolley, "Recent advances in microfluidic sample preparation and separation techniques for molecular biomarker analysis: A critical review," *Analytica Chimica Acta*, vol. 986. pp. 1–11, 2017.

[263] A. Hatch *et al.*, "A rapid diffusion immunoassay in a T-sensor," *Nat. Biotechnol.*, vol. 19, no. 5, pp. 461–465, 2001.

[264] Z. Li, S. Y. Mak, A. Sauret, and H. C. Shum, "Syringe-pump-induced fluctuation in all-aqueous microfluidic system implications for flow rate accuracy," *Lab Chip*, vol. 14, no. 4, pp. 744–749, 2014.

[265] D. F. Crawford, C. A. Smith, and G. Whyte, "Image-based closed-loop feedback for highly mono-dispersed microdroplet production," *Sci. Rep.*, vol. 7, no. 1, 2017.

[266] W. Zeng, I. Jacobi, D. J. Beck, S. Li, and H. A. Stone, "Characterization of syringe-pump-driven induced pressure fluctuations in elastic microchannels," *Lab Chip*, vol. 15, no. 4, pp. 1110–1115, 2015.

[267] A. Kalantarifard, E. Alizadeh Haghighi, and C. Elbuken, "Damping hydrodynamic fluctuations in microfluidic systems," *Chem. Eng. Sci.*, vol. 178, pp. 238–247, Mar. 2018.

[268] Z. Jiao, J. Zhao, Z. Chao, Z. You, and J. Zhao, "An air-chamber-based microfluidic stabilizer for attenuating syringe-pump-induced fluctuations," *Microfluid. Nanofluidics*, vol. 23, no. 2, p. 26, Feb. 2019.

[269] Y. Zhou *et al.*, "Standing air bubble-based micro-hydraulic capacitors for flow stabilization in syringe pump-driven systems," *Micromachines*, vol. 11, no. 4, Apr. 2020.

[270] D. Di Carlo, J. F. Edd, D. Irimia, R. G. Tompkins, and M. Toner, "Equilibrium separation and filtration of particles using differential inertial focusing," *Anal. Chem.*, vol. 80, no. 6, pp. 2204–2211, 2008.

[271] J. Oakey, R. W. Applegate, E. Arellano, D. Di Carlo, S. W. Graves, and M. Toner, "Particle focusing in staged inertial microfluidic devices for flow cytometry," *Anal. Chem.*, vol. 82, no. 9, pp. 3862–3867, 2010.

[272] D. Di Carlo, D. Irimia, R. G. Tompkins, and M. Toner, "Continuous inertial

focusing, ordering, and separation of particles in microchannels," *Proc. Natl. Acad. Sci. U. S. A.*, vol. 104, no. 48, pp. 18892–18897, 2007.

[273] D. Yuan *et al.*, "Sheathless separation of microalgae from bacteria using a simple straight channel based on viscoelastic microfluidics," *Lab Chip*, vol. 19, no. 17, pp. 2811–2821, 2019.

[274] M. S. Syed *et al.*, "Selective separation of microalgae cells using inertial microfluidics," *Bioresour. Technol.*, vol. 252, pp. 91–99, 2018.

[275] D. W. Inglis, N. Herman, and G. Vesey, "Highly accurate deterministic lateral displacement device and its application to purification of fungal spores," *Biomicrofluidics*, vol. 4, no. 2, 2010.

[276] H. W. Hou *et al.*, "Deformability based cell margination - A simple microfluidic design for malaria-infected erythrocyte separation," *Lab Chip*, vol. 10, no. 19, pp. 2605–2613, 2010.

[277] Z. Wu, B. Willing, J. Bjerketorp, J. K. Jansson, and K. Hjort, "Soft inertial microfluidics for high throughput separation of bacteria from human blood cells," *Lab Chip*, vol. 9, no. 9, pp. 1193–1199, 2009.

[278] B. S. Cho, T. G. Schuster, X. Zhu, D. Chang, G. D. Smith, and S. Takayama, "Passively driven integrated microfluidic system for separation of motile sperm," *Anal. Chem.*, vol. 75, no. 7, pp. 1671–1675, 2003.

[279] J. P. Brody and P. Yager, "Diffusion-based extraction in a microfabricated device," *Sensors Actuators, A Phys.*, vol. 58, no. 1, pp. 13–18, 1997.

[280] S. Baas and V. Saggiomo, "Ender3 3D Printer Kit Transformed into Open, Programmable Syringe Pump Set," *ChemRxiv. Cambridge Cambridge Open Engag.*, vol. 2, 2021.

[281] A. Matin and X. Wang, "Compressive coded rotating mirror camera for high-speed imaging," *Photonics*, vol. 8, no. 2, pp. 1–12, Nov. 2021.

[282] T. P. Beresford, *Non-starter lactic acid bacteria (NSLAB) and cheese quality*. 2003.

[283] T. Truong, M. Palmer, N. Bansal, and B. Bhandari, "Effect of Milk Fat Globule Size on Functionalities and Sensory Qualities of Dairy Products," 2016, pp. 47–67.

[284] P. Walstra, "Physical Chemistry of Milk Fat Globules," in *Developments in Dairy Chemistry—2*, 1983, pp. 119–158.

[285] N. Norouzi, H. C. Bhakta, and W. H. Grover, "Sorting cells by their density," *PLoS One*, vol. 12, no. 7, 2017.

[286] R. Jenness, E. O. Herreid, W. J. Caulfield, L. H. Burgwald, E. L. Jack, and S. L. Tuckey, “The Density of Milk Fat: Its Relation to the Accuracy of the Babcock Test,” *J. Dairy Sci.*, vol. 25, no. 11, pp. 949–960, 1942.

[287] O. J. McCarthy and H. Singh, “Physico-chemical properties of milk,” in *Advanced Dairy Chemistry*, vol. 3, 2009, pp. 691–758.

[288] A. S. Hariyani, A. J. Thesiya, T. Hazra, J. B. Gol, and R. S. Chavan, “Novel Methods to Detect Adulteration of Ghee or Milk Fat,” in *Technological Interventions in Dairy Science*, 2019, pp. 207–239.

[289] R. Tsenkova, S. Atanassova, K. Toyoda, Y. Ozaki, K. Itoh, and T. Fearn, “Near-infrared spectroscopy for dairy management: Measurement of unhomogenized milk composition,” *J. Dairy Sci.*, vol. 82, no. 11, pp. 2344–2351, 1999.

[290] R. M. El-Abassy, P. J. Eravuchira, P. Donfack, B. Von Der Kammer, and A. Materny, “Fast determination of milk fat content using Raman spectroscopy,” *Vib. Spectrosc.*, vol. 56, no. 1, pp. 3–8, 2011.

[291] P. M. Korczyk, O. Cybulski, S. Makulska, and P. Garstecki, “Effects of unsteadiness of the rates of flow on the dynamics of formation of droplets in microfluidic systems,” *Lab Chip*, vol. 11, no. 1, pp. 173–175, 2011.

[292] A. Volk and C. J. Kähler, “Density model for aqueous glycerol solutions,” *Experiments in Fluids*, vol. 59, no. 5. Springer Verlag, p. 75, 01-May-2018.

[293] N. S. Cheng, “Formula for the viscosity of a glycerol-water mixture,” *Ind. Eng. Chem. Res.*, vol. 47, no. 9, pp. 3285–3288, May 2008.

[294] R. J. Schaefer, “Dynamic properties of rubber,” *Rubber World*, vol. 211, no. 4, pp. 16–18, 1995.

[295] G. S. Huang, Q. Li, and L. X. Jiang, “Structure and damping properties of polydimethylsiloxane and polymethacrylate sequential interpenetrating polymer networks,” *J. Appl. Polym. Sci.*, vol. 85, no. 3, pp. 545–551, 2002.

[296] H. Bourbaba, C. Ben Achaiba, and B. Mohamed, “Mechanical behavior of polymeric membrane: Comparison between PDMS and PMMA for micro fluidic application,” *Energy Procedia*, 2013. .

[297] L. Antiga and D. A. Steinman, “Rethinking turbulence in blood,” *Biorheology*, vol. 46, no. 2, pp. 77–81, 2009.

[298] S. C. Hur, N. K. Henderson-Maclennan, E. R. B. McCabe, and D. Di Carlo, “Deformability-based cell classification and enrichment using inertial microfluidics,” *Lab Chip*, vol. 11, no. 5, pp. 912–920, Mar. 2011.

[299] A. J. Mach and D. di Carlo, “Continuous scalable blood filtration device using

inertial microfluidics," *Biotechnol. Bioeng.*, vol. 107, no. 2, pp. 302–311, Oct. 2010.

[300] A. A. S. Bhagat, S. S. Kuntaegowdanahalli, and I. Papautsky, "Inertial microfluidics for continuous particle filtration and extraction," *Microfluid. Nanofluidics*, vol. 7, no. 2, pp. 217–226, Dec. 2009.

[301] A. A. S. Bhagat, S. S. Kuntaegowdanahalli, and I. Papautsky, "Continuous particle separation in spiral microchannels using dean flows and differential migration," *Lab Chip*, vol. 8, no. 11, pp. 1906–1914, 2008.

[302] C. Liu, G. Hu, X. Jiang, and J. Sun, "Inertial focusing of spherical particles in rectangular microchannels over a wide range of Reynolds numbers," *Lab Chip*, vol. 15, no. 4, pp. 1168–1177, Feb. 2015.

[303] D. Di Carlo, J. F. Edd, K. J. Humphry, H. A. Stone, and M. Toner, "Particle segregation and dynamics in confined flows," *Phys. Rev. Lett.*, vol. 102, no. 9, 2009.

[304] E. S. Asmolov, "The inertial lift on a spherical particle in a plane poiseuille flow at large channel Reynolds number," *J. Fluid Mech.*, vol. 381, pp. 63–87, 1999.

[305] T. R. Lee, M. Choi, A. M. Kopacz, S. H. Yun, W. K. Liu, and P. Decuzzi, "On the near-wall accumulation of injectable particles in the microcirculation: Smaller is not better," *Sci. Rep.*, vol. 3, 2013.

[306] G. Bugliarello and J. Sevilla, "Velocity distribution and other characteristics of steady and pulsatile blood flow in fine glass tubes.," *Biorheology*, vol. 7, no. 2, pp. 85–107, 1970.

[307] S. Kim, R. L. Kong, A. S. Popel, M. Intaglietta, and P. C. Johnson, "Temporal and spatial variations of cell-free layer width in arterioles," *Am. J. Physiol. - Hear. Circ. Physiol.*, vol. 293, no. 3, 2007.

[308] Y. K. Ha, H. Hong, E. Yeom, and J. M. Song, "Numerical study of the pulsatile flow depending on non-Newtonian viscosity in a stenosed microchannel," *J. Vis.*, vol. 23, no. 1, pp. 61–70, 2020.

[309] G. (丁光辉) Ding, K.-S. Choi, B. (马炳和) Ma, T. (加藤友規) Kato, and W. (苑伟政) Yuan, "Transitional pulsatile flows with stenosis in a two-dimensional channel," *Phys. Fluids*, vol. 33, no. 3, p. 34115, Mar. 2021.

[310] W. (최우락) Choi, J. H. (박준홍) Park, and S. J. (이상준) Lee, "Flow induced stress on vulnerable stenosis in tandem stenosed vessels," *Phys. Fluids*, vol. 32, no. 10, p. 101904, Oct. 2020.

[311] M. O. Bernabeu *et al.*, "Abnormal morphology biases hematocrit distribution in

tumor vasculature and contributes to heterogeneity in tissue oxygenation," *Proc. Natl. Acad. Sci. U. S. A.*, vol. 117, no. 45, pp. 27811–27819, Nov. 2020.

[312] W. G. Pitt *et al.*, "Rapid separation of bacteria from blood-review and outlook," *Biotechnol. Prog.*, vol. 32, no. 4, pp. 823–839, Jul. 2016.

[313] H. Lee, W. Na, C. Park, K. H. Park, and S. Shin, "Centrifugation-free extraction of circulating nucleic acids using immiscible liquid under vacuum pressure," *Sci. Rep.*, vol. 8, no. 1, p. 5467, 2018.

[314] Z. Berk, "Centrifugation," in *Food Process Engineering and Technology*, Elsevier, 2013, pp. 241–257.

[315] I. S. Haque and O. Elemento, "Challenges in Using ctDNA to Achieve Early Detection of Cancer," *bioRxiv*, 2017.

[316] A. Tsanni, "African scientists leverage open hardware," *Nature*, 2020. [Online]. Available: https://www.nature.com/articles/d41586-020-01606-z. [Accessed: 28-Jun-2020].

[317] M. Zastrow, "Open science takes on the coronavirus pandemic," *Nature*, vol. 581, no. 7806, pp. 109–110, 2020.

[318] A. Maia Chagas, L. L. Prieto-Godino, A. B. Arrenberg, and T. Baden, "The €100 lab: A 3D-printable open-source platform for fluorescence microscopy, optogenetics, and accurate temperature control during behaviour of zebrafish, Drosophila, and Caenorhabditis elegans," *PLoS Biol.*, vol. 15, no. 7, Jul. 2017.

[319] C. H. Liu *et al.*, "Blood Plasma Separation Using a Fidget-Spinner," *Anal. Chem.*, vol. 91, no. 2, pp. 1247–1253, 2019.

[320] I. Michael *et al.*, "A fidget spinner for the point-of-care diagnosis of urinary tract infection," *Nat. Biomed. Eng.*, vol. 4, no. 6, 2020.

[321] E. Li, A. Larson, A. Kothari, and M. Prakash, "Handyfuge-LAMP: Low-cost and electricity-free centrifugation for isothermal SARS-CoV-2 detection in saliva," *medRxiv*, 2020.

[322] J. Brown *et al.*, "A hand-powered, portable, low-cost centrifuge for diagnosing anemia in low-resource settings," *Am. J. Trop. Med. Hyg.*, vol. 85, no. 2, 2011.

[323] M. Bhupathi, G. Chinna, and R. Devarapu, "Mobilefuge: A low-cost, portable, open source, 3D-printed centrifuge that can be used for purification of saliva samples for SARS-CoV2 detection," *medRxiv*, 2021.

[324] Z. WareJoncas, C. Stewart, and J. Giannini, "An inexpensive, open-source mini-centrifuge," *Am. Biol. Teach.*, vol. 80, no. 6, 2018.

[325] "How To Build Your Own DIY Centrifuge." [Online]. Available:

https://www.popsci.com/diy/article/2013-07/how-build-your-own-diy-centrifuge/. [Accessed: 10-Feb-2022].

[326] J. Ford, T. Goldstein, S. Trahan, A. Neuwirth, K. Tatoris, and S. Decker, "A 3D-printed nasopharyngeal swab for COVID-19 diagnostic testing," *3D Print. Med. 2020 61*, vol. 6, no. 1, pp. 1–7, Aug. 2020.

[327] S. Ravindran, "How DIY technologies are democratizing science," *Nature*, vol. 587, no. 7834, pp. 509–511, Nov. 2020.

[328] S. Bhagia *et al.*, "Critical review of FDM 3D printing of PLA biocomposites filled with biomass resources, characterization, biodegradability, upcycling and opportunities for biorefineries," *Appl. Mater. Today*, vol. 24, p. 101078, Sep. 2021.

[329] M. E. Haque, L. Marriott, N. Naeem, T. Henry, A. J. Conde, and M. Kersaudy-Kerhoas, "Design, 3D-printing, and characterisation of a low-cost, open-source centrifuge adaptor for separating large volume clinical blood samples," *bioRxiv*, p. 2021.10.19.464959, Jan. 2021.

[330] R. M. Trigg, L. J. Martinson, S. Parpart-Li, and J. A. Shaw, "Factors that influence quality and yield of circulating-free DNA: A systematic review of the methodology literature," *Heliyon*, vol. 4, no. 7, pp. e00699–e00699, Jul. 2018.

[331] Ultimaker, "Ultimaker Cura: Powerful, easy-to-use 3D printing software," *Ultimaker*, 2020. [Online]. Available: https://ultimaker.com/software/ultimaker-cura. [Accessed: 04-Jul-2020].

[332] J. Fischer and J. Strackeljan, "Stability analysis of high speed lab centrifuges considering internal damping in rotor-shaft joints," 2006, pp. 131 – 147.

[333] G. Lowe *et al.*, "Nursing Blood Specimen Collection Techniques and Hemolysis Rates in an Emergency Department: Analysis of Venipuncture Versus Intravenous Catheter Collection Techniques," *J. Emerg. Nurs.*, vol. 34, no. 1, pp. 26–32, Feb. 2008.

[334] R. Cardigan, "Guide to the Preparation, Use and Quality Assurance of Blood Components (13th edn)," *Transfus. Med.*, vol. 17, no. 6, pp. 491–491, Dec. 2007.

[335] C. M. Cripps, "Rapid method for the estimation of plasma haemoglobin levels," *J. Clin. Pathol.*, vol. 21, no. 1, pp. 110–112, Jan. 1968.

[336] S. O. Sowemimo-Coker, "Red blood cell hemolysis during processing," *Transfus. Med. Rev.*, vol. 16, no. 1, pp. 46–60, 2002.

[337] B. S *et al.*, "Direct quantification of cell-free, circulating DNA from unpurified plasma," *PLoS One*, vol. 9, no. 3, Mar. 2014.

[338] T. Hirata *et al.*, "Associations of cardiovascular biomarkers and plasma albumin

with exceptional survival to the highest ages," *Nat. Commun.*, vol. 11, no. 1, p. 3820, 2020.

[339] W. Su *et al.*, "Serum albumin is a useful prognostic indicator and adds important information to NT-proBNP in a Chinese cohort of heart failure," *Clin. Biochem.*, vol. 45, no. 7, pp. 561–565, 2012.

[340] D. Snipelisky, J. Jentzer, O. Batal, Z. Dardari, and M. Mathier, "Serum albumin concentration as an independent prognostic indicator in patients with pulmonary arterial hypertension," *Clin. Cardiol.*, vol. 41, no. 6, pp. 782–787, Jun. 2018.

[341] K. SP, T. GJ, W. CW, and L. WY, "Serum albumin concentration as a prognostic indicator for acute surgical patients," *Zhonghua Yi Xue Za Zhi (Taipei).*, vol. 62, no. 2, pp. 61–67, Feb. 1999.

[342] L. YC *et al.*, "Preoperative serum albumin level is a prognostic indicator for adenocarcinoma of the gastric cardia," *J. Gastrointest. Surg.*, vol. 8, no. 8, pp. 1041–1048, Dec. 2004.

[343] F. Malizia, T. van Druenen, and B. Blocken, "Impact of wheel rotation on the aerodynamic drag of a time trial cyclist," *Sport. Eng.*, vol. 24, no. 1, p. 3, 2021.

[344] S. F. Hoerner, *Fluid Dynamic Drag: Practical Information on Aerodynamic Drag and Hydrodynamic Resistance*, 2nd ed. New Jersey: Hoerner Fluid Dynamics, 1965.

[345] W. E. (Wilfred E. Baker, *Explosion hazards and evaluation*, 1st Edition. Elsevier Scientific Pub. Co, 1983.

[346] R. M. Nerem, "Vibration-Induced Arterial Shear Stress," *Arch. Environ. Heal. An Int. J.*, vol. 26, no. 3, pp. 105–110, Mar. 1973.

[347] H. Ando, K. Nieminen, E. Toppila, J. Starck, and T. Ishitake, "Effect of impulse vibration on red blood cells in vitro," *Scand. J. Work. Environ. Heal.*, vol. 31, no. 4, 2005.

[348] T. Jing, Y. Cheng, F. Wang, W. Bao, and L. Zhou, "Numerical investigation of centrifugal blood pump cavitation characteristics with variable speed," *Processes*, vol. 8, no. 3, 2020.

[349] D. Wong *et al.*, "Optimizing blood collection, transport and storage conditions for cell free DNA increases access to prenatal testing," *Clin. Biochem.*, vol. 46, no. 12, pp. 1099–1104, Aug. 2013.

[350] R. B. Lanman *et al.*, "Analytical and clinical validation of a digital sequencing panel for quantitative, highly accurate evaluation of cell-free circulating tumor DNA," *PLoS One*, vol. 10, no. 10, 2015.

[351] Y. Xu, J. J. Milledge, A. Abubakar, R. A. R. Swamy, D. Bailey, and P. J. Harvey, “Effects of centrifugal stress on cell disruption and glycerol leakage from Dunaliella salina,” *Microalgae Biotechnol.*, vol. 1, no. 1, 2015.

[352] A. K. Upadhyay, R. Singh, J. S. Singh, and D. P. Singh, “Microalgae-assisted phyco-remediation and energy crisis solution: Challenges and opportunity,” in *New and Future Developments in Microbial Biotechnology and Bioengineering: Microbial Biotechnology in Agro-environmental Sustainability*, 2019.

[353] M. La Verde *et al.*, “Performance of cell-free DNA sequencing-based non-invasive prenatal testing: experience on 36,456 singleton and multiple pregnancies,” *BMC Med. Genomics*, vol. 14, no. 1, 2021.

[354] Y. Xue, G. Zhao, L. Qiao, J. Lu, B. Yu, and T. Wang, “Sequencing Shorter cfDNA Fragments Decreases the False Negative Rate of Non-invasive Prenatal Testing,” *Front. Genet.*, vol. 11, 2020.

[355] R. Gyanchandani *et al.*, “Whole genome amplification of cell-free DNA enables detection of circulating tumor DNA mutations from fingerstick capillary blood,” *Sci. Rep.*, vol. 8, no. 1, 2018.

[356] X. Zhou *et al.*, “Kinetics of plasma cfDNA predicts clinical response in non-small cell lung cancer patients,” *Sci. Rep.*, vol. 11, no. 1, 2021.

[357] H. Zemmour *et al.*, “Non-invasive detection of human cardiomyocyte death using methylation patterns of circulating DNA,” *Nat. Commun.*, vol. 9, no. 1, 2018.